

Electrodeposition of p-Type Cuprous Oxide and its Application in Oxide Solar Cells

by
Yiyi Yang

A thesis
presented to the University of Waterloo
in fulfillment of the
thesis requirement for the degree of
Doctor of Philosophy
in
Chemical Engineering

Waterloo, Ontario, Canada, 2017

© Yiyi Yang 2017

Examining Committee Membership

The following served on the Examining Committee for this thesis. The decision of the Examining Committee is by majority vote.

External Examiner	Prof. Alan Sellinger (Colorado School of Mines)
Supervisor(s)	Prof. Mark Pritzker Prof. Yuning Li
Internal Member	Prof. William Anderson Prof. Ting Tsui
Internal-external Member	Prof. Hany Aziz

Author's Declaration

I hereby declare that I am the sole author of this thesis. This is a true copy of the thesis, including any required final revisions, as accepted by my examiners.

I understand that my thesis may be made electronically available to the public.

Abstract

Cuprous oxide (Cu_2O) is a promising material for the fabrication of oxide solar cells due to its abundance, nontoxicity, stability and ability to be deposited under mild conditions. At the moment, the reported efficiencies for Cu_2O -based solar cells are well below its theoretical limit and most of the high performance devices are fabricated using energy-intensive processes. Electrodeposition of Cu_2O thin films is a well-known process although a systematic study of the dependence of Cu_2O film properties on the deposition conditions has not been reported, especially in the context of photovoltaic applications. The purpose of this study is to optimize the electrodeposited p-type Cu_2O film properties for the application in heterojunction solar cells through the manipulation of electrodeposition conditions.

A range of Cu_2O morphologies are formed by varying the parameters during the constant potential deposition of Cu_2O thin films from a copper-lactate electrolyte including applied potential, temperature, pH, copper concentration and lactate concentration. The variation in morphology is mostly attributed to the relative growth rates of $\langle 111 \rangle$ and $\langle 100 \rangle$ orientations. It is found that the variation in growth orientation is mostly due to the relative rates of reaction and transport. When reaction kinetics is the limiting factor, $\langle 100 \rangle$ growth is preferred when the conditions are close to thermodynamic equilibrium. On the other hand, when transport limitation in the system is significant, $\langle 111 \rangle$ -oriented growth and cubic grains are favored as the surface concentration of CuLac_2 is reduced. In other conditions, mixed orientations tend to be formed. Evidence of adsorption of lactate ions onto the (111) faces is also observed, promoting $\langle 100 \rangle$ directed growth at high lactate concentration. In addition, significant evidence of film dissolution during deposition is observed at high electrolyte pH of 13 and above.

The performance of Cu_2O thin films in photovoltaic devices is evaluated using an FTO/ Cu_2O /AZO cell structure. It is found that the electrolyte pH has the most prominent effect on the device performance among different electrodeposition parameters. Performance variables including J_{SC} , V_{OC} and FF all improve significantly as the Cu_2O deposition pH increases. An optimal cell efficiency of $\sim 1.55\%$ is obtained using Cu_2O thin films deposited at a high pH of 13.4, which exceeds the majority of previously

reported efficiencies using the same deposition technique. The reason for the improved efficiency is attributed to the dissolution and reformation of Cu_2O grains during deposition at high pH through the improvement of charge carrier mobility and band gap in the Cu_2O layer. Film orientation of Cu_2O also plays a minor role in cell efficiency.

Alternative electrodeposition procedures are investigated. Galvanostatic deposition is found to be less suitable than potentiostatic deposition for solar cell fabrication due to the difficulty in controlling Cu metal content in the film. Evidence of dissolution by oxidation is observed under both pulsed and stirred conditions. Different morphologies to the typical polyhedral shapes with higher carrier concentration and low carrier mobility are obtained in both cases. These effects are attributed to the lowering of diffusion limitations during the deposition process either by allowing more time for transport or by increasing transport rate. These processes result in lower device performance compared to potentiostatic deposition under similar conditions.

Finally, FTO/ Cu_2O /ZnO devices are fabricated by depositing ZnO onto electrodeposited Cu_2O layer through a seed-layer assisted chemical growth method in zinc nitrate-HMTA solution. Ordered ZnO nanorods are obtained using this technique and their dimensions can be controlled by adjusting bath compositions. Smooth ZnO thin films with no pin-hole defects are obtained although the performance of Cu_2O /ZnO devices is not as high as devices with AZO layers.

Acknowledgments

I would like to express my sincerest gratitude to my advisors, Dr. Mark Pritzker and Dr. Yuning Li. Their expertise and insights have helped me greatly during the course of this research work, and their patience and continuous encouragement allowed me to develop my research skills and gaining more confidence along the way.

I am thankful for the Giga-to Nano (G2N) Centre, where the majority of the device fabrication and characterization involved in this work was conducted. Special thanks to Richard Barber for his excellent management of the facilities and technical support. Also, a big thank you to Dr. Ting Tsui for granting me frequent access to his FE-SEM system, which allowed me to gather morphology data in a timely manner.

I am indebted to Jorge Vazques, Tanyakarn Treeratanaphitak, Graeme Williams, Bin Sun, Sibi Sutti, Minoli Pathirane, Elizabeth Salsberg, Guocheng Liu, Ruifeng Yang, Jesse Quinn, Ahmet Camlica, Muneendra Prasad, and Dr. Czang-Ho Lee for their training and support, which allowed me to overcome the many challenges I encountered at the various stages of this project. I would also like to thank all my committee members, Dr. William Anderson, Dr. Ting Tsui, Dr. Hany Aziz, and Dr. Alan Sellinger, for their time and interest.

Finally, I would like to acknowledge the funding sources, Natural Sciences and Engineering Research Council of Canada (NSERC) and Ontario Graduate Scholarship (OGS) for the financial support during the completion of this project.

Table of Contents

Examining Committee Membership.....	ii
Author's Declaration.....	iii
Abstract.....	iv
Acknowledgments.....	vi
Table of Contents.....	vii
List of Figures.....	x
List of Tables.....	xvi
List of Symbols.....	xvii
List of Abbreviations.....	xviii
Chapter 1. Introduction.....	1
1.1 Motivation.....	1
1.2 Structure of thesis.....	3
Chapter 2. Background.....	5
2.1 P-n junction photovoltaics.....	5
2.1.1 Device structure.....	5
2.1.2 Current generation process.....	6
2.1.3 Device output.....	7
2.1.4 Series and shunt resistance effect.....	10
2.2 Cu ₂ O-based photovoltaics.....	11
2.2.1 Cu ₂ O in photovoltaic applications.....	11
2.2.2 Techniques for efficiency enhancement.....	13
2.3 Cu ₂ O synthesis techniques.....	15
2.3.1 Overview.....	15
2.3.2 Electrodeposition of Cu ₂ O.....	17
2.3.3 Electrodeposited p-type Cu ₂ O in solar cells.....	19
Chapter 3. Experimental Methods.....	22
3.1 Materials.....	22
3.1.1 Chemicals.....	22
3.1.2 Fluorine-doped tin oxide (FTO).....	23
3.2 Deposition Techniques.....	24
3.2.1 Electrochemical experiments.....	24
3.2.2 Sputtering of Al-doped tin oxide (AZO).....	25

3.2.3	Thermal evaporation.....	26
3.3	Characterization Techniques.....	26
3.3.1	Film Morphology and Orientation.....	26
3.3.2	Electrical and Optical Properties.....	28
3.3.3	Photovoltaic Properties.....	34
Chapter 4.	Potentiostatic DC Deposition of Cu ₂ O.....	35
4.1	Introduction.....	35
4.2	Experimental details.....	35
4.3	Morphology of electrodeposited Cu ₂ O.....	36
4.3.1	XRD.....	36
4.3.2	Linear sweep voltammetry (LSV).....	37
4.3.3	Effect of applied potential.....	39
4.3.4	Effect of Temperature.....	40
4.3.5	Effect of CuSO ₄ concentration.....	42
4.3.6	Effect of pH.....	45
4.3.7	Effect of lactic acid concentration.....	54
4.4	Discussion.....	57
4.4.1	Factors affecting growth orientation.....	57
4.4.2	Role of transport limitation.....	60
4.4.3	Dissolution.....	62
4.5	Summary.....	64
Chapter 5.	Cu ₂ O/AZO Solar Cells with Electrodeposited Cu ₂ O Layer.....	66
5.1	Introduction.....	66
5.2	Experimental details.....	66
5.2.1	Device fabrication and characterization.....	66
5.2.2	Experimental design.....	67
5.3	Device performance.....	70
5.3.1	Overview of parameter effects.....	70
5.3.2	Effect of pH.....	74
5.3.3	Devices with deformed Cu ₂ O layer.....	76
5.3.4	Back-illumination.....	80
5.4	Discussion.....	84
5.4.1	Effect of high-electrolyte pH.....	84
5.4.2	Limitations.....	91
5.5	Summary.....	96
Chapter 6.	Alternative Procedures for Cu ₂ O Electrodeposition.....	98

6.1	Introduction.....	98
6.2	Galvanostatic Deposition.....	98
6.2.1	Background.....	98
6.2.2	Experimental.....	99
6.2.3	Results and Discussion	99
6.3	Pulsed Potential Deposition	102
6.3.1	Background.....	102
6.3.2	Experimental.....	103
6.3.3	Film morphology.....	104
6.3.4	Device performance.....	118
6.4	Use of Stirred Electrolytes	120
6.4.1	Background.....	120
6.4.2	Experimental.....	120
6.4.3	Film morphology.....	121
6.4.4	Device performance.....	124
6.5	Summary.....	127
Chapter 7.	Chemical Deposition of ZnO	129
7.1	Background.....	129
7.2	Experimental.....	131
7.3	Chemical growth of ZnO nanorods	133
7.3.1	XRD	133
7.3.2	Effect of seed layer.....	134
7.3.3	Effect of bath composition	135
7.4	Device performance	138
7.5	Summary.....	141
Chapter 8.	Conclusions and Future Outlook.....	142
8.1	Conclusions.....	142
8.2	Recommended future research.....	144
References	147

List of Figures

Figure 2-1: Energy band diagram for a p-n junction at thermodynamic equilibrium.....	5
Figure 2-2: Typical output characteristic curve of a photovoltaic device.....	8
Figure 2-3: Shockley–Queisser limit for a single heterojunction solar cell.....	8
Figure 2-4: Equivalent circuit model for a photovoltaic device.....	10
Figure 2-5: Effect of (a) series resistance and (b) shunt resistance on solar cell performance	10
Figure 2-6: Reported efficiency of Cu ₂ O-based solar cells by year	16
Figure 2-7: Relationship between Cu ₂ O crystallite shape and growth orientation.....	18
Figure 3-1: Properties of a FTO-coated glass substrate: (a) UV-visible light absorption profile, (b) X-ray diffraction profile, (c) surface morphology.	23
Figure 3-2: Typical plot of J vs V ² for a Cu ₂ O thin film.	32
Figure 3-4: Solar cell characterization setup: (a) front illumination, (b) back illumination.	34
Figure 4-1: (a) X-ray diffraction profile of typical electrodeposited Cu ₂ O films electrodeposited on FTO-glass substrate. The top spectrum shows a Cu ₂ O film containing a small amount of Cu. The middle spectrum shows a Cu ₂ O film with no significant Cu formation. The bottom spectrum shows the profile of the FTO glass slide used as substrates for all experiments in this work. (b) SEM image of a typical Cu ₂ O thin film containing clusters of Cu (indicated by arrows).	36
Figure 4-2: Linear sweep voltammetry curves obtained on FTO-coated glass substrates immersed in 0.2M CuSO ₄ -3M lactic acid solutions at pH 9.5 and 12.5 and 60°C.....	37
Figure 4-3: Applied potential range for Cu ₂ O deposition as functions of: (a) pH (0.2 M CuSO ₄ +3 M lactic acid, 60°C), (b) temperature (0.2 M CuSO ₄ +3 M lactic acid, pH 9.5), and (c) [CuSO ₄] (CuSO ₄ +3 M lactic acid, pH 9.5, 60°C). Dashed line indicates the minimum cathodic potential required for Cu formation.....	38
Figure 4-4: (a) Current transient curves and (b-e) SEM images of Cu ₂ O films electrodeposited at 60°C in electrolyte containing 0.2 M CuSO ₄ and 3 M lactic acid adjusted to pH 9.5 at applied potentials of (b) -0.3V, (c) -0.4V, (d) -0.5V and (e) -0.6V vs. SCE.. All samples formed after 15 min deposition time.	39
Figure 4-5: SEM images of Cu ₂ O films deposited from 0.2 M CuSO ₄ + 3 M lactic acid adjusted to pH 9.5 at different temperatures and cathodic potentials: (a-c) 45°C and -0.3, -0.5, -0.6V; (d-f) 60°C and -0.3, -0.5, -0.6V; (g-i) 75°C and -0.3, -0.5, -0.6V. Deposition time is 15 min in all cases.	40
Figure 4-6: Effect of deposition temperature on (111):(200) peak intensity ratio from the XRD patterns of Cu ₂ O films obtained by deposition on FTO-glass substrate at 60°C Cu ₂ O films deposited from 0.2 M CuSO ₄ + 3 M lactic acid electrolyte adjusted to pH 9.5.	42
Figure 4-7: SEM images of Cu ₂ O films deposited in CuSO ₄ + 3 M lactic acid adjusted to pH 9.5 at 60°C: (a-c) 0.1 M CuSO ₄ at -0.3, -0.5, -0.6V; (d-f) 0.2 M CuSO ₄ at -0.3, -0.5, -0.6V; (g-i) 0.4 M CuSO ₄ at -0.3, -0.5, -0.6V. Deposition time is 15 min in all cases.	43
Figure 4-8: Effect of [CuSO ₄] on (111):(200) peak intensity ratio from the XRD patterns of Cu ₂ O films obtained by deposition on FTO-glass substrate at 60°C Cu ₂ O films deposited from M CuSO ₄ + 3 M lactic acid electrolyte adjusted to pH 9.5.	44

Figure 4-9: SEM images of Cu ₂ O films deposited at 60°C in 0.2 M CuSO ₄ + 3 M lactic acid adjusted to different pH: (a) pH 8.5, -0.4V, 5.5 hours; (b) pH 9.5, -0.5V, 26 min; (c) pH 12.5, -0.6V, 35 min; (d) pH 13.5, -0.7V, 40 min. (e) Effect of pH on (111):(200) peak intensity ratio in the XRD patterns. All samples are ~2µm in thickness.	45
Figure 4-10: SEM images of Cu ₂ O films electrodeposited on FTO-glass substrate at 60°C for the following durations: (a) 3 min, (b) 10 min, (c) 20 min, (d) 60 min at an applied potential of -0.4V vs. SCE in electrolyte containing 0.2 M CuSO ₄ – 3 M lactic acid adjusted to pH 8.5.....	46
Figure 4-11: SEM images of Cu ₂ O films electrodeposited on FTO-glass substrate at 60°C for the following durations: (a) 1 min, (b) 3 min, (c) 5 min, (d) 10 min at an applied potential of -0.5V vs. SCE in electrolyte containing 0.2 M CuSO ₄ – 3 M lactic acid adjusted to pH 9.5.....	47
Figure 4-12: SEM images of Cu ₂ O films electrodeposited on FTO-glass substrate at 60°C for the following durations: (a) 1 min, (b) 3 min, (c) 5 min, (d) 10 min at an applied potential of -0.6V vs. SCE in electrolyte containing 0.2 M CuSO ₄ – 3 M lactic acid adjusted to pH 12.5.....	48
Figure 4-13: SEM images of Cu ₂ O films deposited from 0.2 M CuSO ₄ + 3 M lactic acid adjusted to pH 12.5 at the following temperature and applied potential: (a) 60°C, -0.5V; (b) 60°C, -0.65V; (c) 75°C, -0.5V; (d) 75°C, -0.65V.....	49
Figure 4-14: SEM images of Cu ₂ O films electrodeposited on FTO-glass substrate at 60°C for the following durations: (a) 0.5 min, (b) 1 min, (c) 2 min, (d) 3 min, (e) 5 min, (f) 10 min at an applied potential of -0.7V vs. SCE in electrolyte containing 0.2 M CuSO ₄ – 3 M lactic acid adjusted to pH 13.5.	50
Figure 4-15: (a) Current transients curves for Cu ₂ O electrodeposition on FTO-glass substrate at 60°C in electrolyte containing 0.2 M CuSO ₄ – 3 M lactic acid adjusted to pH 13.5 for 15 minutes, at different applied potentials between -0.42V and -0.70V vs. SCE. Corresponding SEM images formed at (b) -0.42V, (c) -0.50V, (d) -0.60V, (e) -0.70V are shown on the right.	51
Figure 4-16: SEM images of Cu ₂ O films deposited from 0.2 M CuSO ₄ + 3 M lactic acid adjusted to pH 13.5 at -0.5V: (a) 45°C, (b) 60°C, (c) 75°C and -0.7V: (d) 45°C, (e) 60°C, (f) 75°C. All samples deposited for 15 min.	52
Figure 4-17: Effect of pH on (111):(200) peak intensity ratio for Cu ₂ O films deposited from 0.2 M CuSO ₄ + 3 M lactic acid adjusted to pH 13.5 at -0.5V and -0.7V.....	53
Figure 4-18: SEM images of Cu ₂ O films deposited from electrolyte containing (a) 0.2 M, (b) 0.3 M and (c) 0.4 M CuSO ₄ and 3 M lactic acid adjusted to pH 13.5 at 60°C at -0.7V. All samples deposited for 15 minutes.	54
Figure 4-19: (a) Potential range for Cu ₂ O deposition and (b) effect of applied potential on Cu ₂ O film thickness after 15 min deposition at 60°C from 0.2 M CuSO ₄ electrolytes containing various amounts of lactic acid adjusted to pH 9.5.....	54
Figure 4-20: (a) Effect of lactic acid concentration on (111):(200) peak intensity ratio of Cu ₂ O films formed at 60°C from 0.2 M CuSO ₄ electrolytes adjusted to pH 9.5. SEM images of Cu ₂ O films deposited from electrolyte containing 0.2 M CuSO ₄ and different lactic acid concentrations adjusted to pH 9.5 at 60°C at -0.5V are shown on the right: (b) 1.9 M, (c) 3.0 M, (d) 4.5 M. All samples deposited for 15 minutes.	55
Figure 4-21: SEM images of Cu ₂ O films deposited from electrolyte containing 0.2M CuSO ₄ + 4.5M lactic acid at 60°C at -0.5V: (a) pH 9.5, (b) pH 12.5, (c) pH 13.5; at -0.7V: (d) pH 9.5, (e) pH 12.5, (f) pH 13.5. The effect of pH on (111):(200) peak intensity ratio for deposition in 4.5M lactic acid is shown in (g). All samples deposited for 15 minutes.	56

Figure 4-22: Effect of transport limitation on Cu ₂ O growth orientation (diagram is intended for qualitative purpose only).	61
Figure 4-23: Change in thickness of Cu ₂ O thin films (electrodeposited in 0.2 M CuSO ₄ + 3 M lactic acid adjusted to pH 12.5 at 60°C at -0.65V, film thickness ~2.2μm) after immersion for 3 hours in 3.0 M lactic acid solution adjusted to pH 12.5 or 13.5 using NaOH.	63
Figure 5-1: Correlation between J _{SC} and Cu ₂ O film orientation in Cu ₂ O/AZO devices consisting of Cu ₂ O films deposited at pH (a) 9.5 and (b) 12.5. Outliers are indicated by blue rectangles.	72
Figure 5-2: Illuminated J-V characteristics of solar cells fabricated using Cu ₂ O thin films deposited at different pH and applied potential (0.2 M CuSO ₄ + 3 M lactic acid, 60°C).	74
Figure 5-3: Device characteristics of solar cells fabricated using Cu ₂ O thin films deposited at different pH and applied potential (0.2 M CuSO ₄ + 3 M lactic acid, 60°C).	75
Figure 5-4: Shunt resistance and series resistance of solar cells fabricated using Cu ₂ O thin films deposited at different pH and applied potential (0.2 M CuSO ₄ + 3 M lactic acid, 60°C).	76
Figure 5-5: Effect of deposition temperature on device characteristics of solar cells fabricated using Cu ₂ O thin films produced in 0.2 M CuSO ₄ + 3 M lactic acid electrolyte adjusted to pH 13.5 at -0.7V.	77
Figure 5-6: Effect of deposition temperature on device characteristics of solar cells fabricated using Cu ₂ O thin films formed in electrolytes containing 3 M lactic acid and 0.3 or 0.4 M CuSO ₄ adjusted to pH 13.5 at -0.7V.	78
Figure 5-7: Effect of deposition pH (from ~ 12.7 to 13.7) and potential (from -0.65V to ~ -0.72V) on device characteristics of solar cells fabricated using Cu ₂ O thin films deposited at 65°C in 0.2 M CuSO ₄ + 3 M lactic acid electrolyte.	80
Figure 5-8: J-V characteristics of solar cells fabricated using Cu ₂ O thin films deposited at different pH, potential and temperature illuminated from the front or back of the device. The electrolyte contains 0.2 M CuSO ₄ + 3 M lactic acid in all cases.	81
Figure 5-9: Effect of deposition pH on device characteristics of solar cells fabricated using Cu ₂ O thin films formed in 0.2 M CuSO ₄ + 3M lactic acid illuminated from the front or back.	83
Figure 5-10: Effect of deposition pH on R _{sh} and R _s of solar cells fabricated using Cu ₂ O thin films formed in 0.2 M CuSO ₄ + 3 M lactic acid illuminated from the front or back of the device.	84
Figure 5-11: (a) UV-vis absorption spectra of Cu ₂ O films (~2μm) deposited at different electrolyte pH. Plots are normalized for comparison purpose. Absorption spectrum of FTO substrate is shown in the bottom. Tauc plots for bandgap calculation are presented in (b).	85
Figure 5-12: Cyclic voltammograms of Cu ₂ O films (~2μm) deposited at different electrolyte pH.	86
Figure 5-13: Charge carrier (a) concentration and (b) mobility of Cu ₂ O thin films deposited at different pH. Values are obtained using SCLC techniques with FTO/Cu ₂ O/Al structure.	88
Figure 5-14: Correlation between hole concentration and mobility of Cu ₂ O thin films deposited at different electrolyte pH. Values are obtained using SCLC techniques with FTO/Cu ₂ O/Al structure.	89
Figure 5-15: (a) SIMS profiles of Cu ⁺ and O ²⁻ intensities with sputter time and (b) Cu:O intensity ratios for samples deposited at pH 9.5 and 13.5.	90
Figure 5-16: (a) Measured charge carrier mobility using different contact materials and (b) electron and hole mobility of Cu ₂ O thin films deposited at different pH.	91

Figure 5-17: SEM images of Cu ₂ O and AZO surfaces used in devices with: (a, b) typical cubic Cu ₂ O morphology (0.2 M CuSO ₄ + 3 M lactic acid, pH 12.5, 60°C, -0.65V, thickness ~ 2µm) and (c, d) typical dissolved and reformed morphology (0.2 M CuSO ₄ + 3 M lactic acid, pH 13.5, 65°C, -0.72V, thickness ~ 2µm). AFM image for (a) is shown in (e).....	92
Figure 5-18: SIMS profiles of OH ⁻ and C ⁻ intensities with sputter time for Cu ₂ O films deposited at different electrolyte pH	94
Figure 5-19: The effect of deposition pH on device performance for back-illuminated solar cells with and without an Al top contact.	95
Figure 5-20: Effect of deposition pH on R _{sh} and R _s of back-illuminated solar cells with and without an Al top contact.	96
Figure 6-1: Potential transient curves during deposition of Cu ₂ O films in electrolyte containing 0.2 M CuSO ₄ + 3 M lactic acid adjusted to pH 12.5 at different applied current densities and (a) 40°C and (b) 60°C.....	100
Figure 6-2: Cell characteristics for devices fabricated using galvanostatic Cu ₂ O films deposited in electrolyte containing 0.2 M CuSO ₄ and 3 M lactic acid adjusted to pH 12.5 at different applied current densities (FTO/2 µm Cu ₂ O/250 nm AZO, front-illuminated)	102
Figure 6-3: (a) Current transients during pulsed Cu ₂ O electrodeposition on FTO-glass substrate at 60°C and 50% duty cycle in electrolyte containing 0.2 M CuSO ₄ – 3 M lactic acid adjusted to pH 9.5 at frequency 1, 1/10 and 1/600 Hz, respectively. Overall trends of the transients are shown in (b) by plotting the final current density during each individual pulse.....	104
Figure 6-4: SEM images of Cu ₂ O films obtained by deposition on FTO-glass substrate at 60°C in electrolyte containing 0.2 M CuSO ₄ – 3 M lactic acid adjusted to pH 9.5 with square-wave pulses of -0.5 V/OCP at frequencies: (a) 500, (b) 10, (c) 1, (d) 1/10, (e) 1/60, (f) 1/180, (g) 1/360, (h) 1/600 Hz. Cu ₂ O film deposited under DC conditions at -0.5 V for 15 min is shown in (i) for comparison.	106
Figure 6-5: SEM images of Cu ₂ O films obtained by deposition on FTO-glass substrate at 60°C in electrolyte containing 0.2 M CuSO ₄ - 3M lactic acid adjusted to pH 9.5 with square-wave pulses of -0.5 V/OCP and off-times t _{off} of (a-d) 50 ms and (e-h) 500 ms. Values of t _{on} are labelled on the images.	108
Figure 6-6: SEM images of Cu ₂ O films obtained by deposition on FTO-glass substrate at 60°C in electrolyte containing 0.2M CuSO ₄ - 3M lactic acid adjusted to pH 9.5 with square-wave pulses of -0.5 V/OCP vs. SCE at on-times t _{on} of (a-d) 50 ms and (e-h) t _{on} = 500 ms. Values of t _{off} are labelled on the images.	109
Figure 6-7: (a) Summary of effect of t _{on} and t _{off} on Cu ₂ O film morphology obtained by deposition on FTO-glass substrate at 60°C in electrolyte containing 0.2 M CuSO ₄ – 3 M lactic acid adjusted to pH 9.5 with square-wave pulses of -0.5 V/OCP vs. SCE; (b) schematic curve delineating conditions for spherical and cubic morphology (rectangular region indicated by the green dashed lines corresponds to the conditions covered in Figure 6-7a). Diagram is not to scale and is intended for qualitative purposes only.	110
Figure 6-8: SEM images of Cu ₂ O films obtained by deposition on FTO-glass substrate at 60°C in electrolytes containing 0.2 M CuSO ₄ – 3 M lactic acid adjusted to different pH with square-wave pulses of -0.5 V/OCP vs. SCE at the following on-/off-times: (a-e) 50 ms/50 ms and (f-j) 500 ms/500 ms. The cathodic and anodic current transients over the course of deposition at 500	

ms/500 ms obtained by plotting the final current density of each individual pulse are shown in (k).	112
Figure 6-9: SEM images of Cu ₂ O films obtained by deposition on FTO-glass substrate at 60°C in electrolyte containing 3 M lactic acid and different CuSO ₄ concentrations adjusted to pH 9.5 with square-wave pulses of -0.5 V/OCP vs. SCE at the following on-/off-times: (a-d) 50 ms/50 ms and (e-h) 500 ms/500 ms. The number above each image denotes the CuSO ₄ concentration.	114
Figure 6-10: (a) Effect of [CuSO ₄] on (111):(200) peak intensity ratio from the XRD patterns of Cu ₂ O films obtained by deposition on FTO-glass substrate at 60°C in electrolyte containing 3 M lactic acid adjusted to pH 9.5 with square-wave pulses of -0.5V/OCP vs. SCE and on-/off-times of 50 ms/50 ms and 500 ms/500 ms . (b) Effect of [CuSO ₄] on the cathodic and anodic current transients over the course of deposition at 500 ms/500 ms obtained by plotting the final current density of each individual pulse.....	115
Figure 6-11: SEM images of Cu ₂ O films obtained by deposition on FTO-glass substrate at 60°C in electrolytes containing 0.2 M CuSO ₄ – 3 M lactic acid adjusted to pH 9.5 with square-wave pulses having different cathodic potentials at the following on-/off-times: (a-d) 50 ms/50 ms and (e-h) 500 ms/500 ms. The potential during the off-time is maintained at the OCP. The number above each image denotes the cathodic potential.	116
Figure 6-12: Front- and back-illuminated J-V curves for devices fabricated using potentiostatic DC (-0.65 V) or pulsed waveform (-0.65 V/OCP, 500 ms/500 ms). Cu ₂ O films are deposited from electrolytes containing 0.2 M CuSO ₄ + 3.0 M lactic acid adjusted to pH 12.5 at 60°C.....	119
Figure 6-13: Current transient curves during electrodeposition of Cu ₂ O films at 60°C in electrolyte containing 0.2 M CuSO ₄ + 3 M lactic acid adjusted to pH 9.5 at -0.5 V vs. SCE under stirred or unstirred conditions.....	121
Figure 6-14: SEM images of Cu ₂ O films electrodeposited at 60°C in stirred electrolyte containing 0.2 M CuSO ₄ + 3 M lactic acid adjusted to pH 9.5 at applied potentials of (a) -0.3, (b) -0.4, (c) -0.5 and (d) -0.6V vs. SCE. Deposition time is 15 min in cases. The effect of deposition potential on (111):(200) peak ratio of Cu ₂ O films obtained under stirred and unstirred conditions is presented in (e).	122
Figure 6-15: : SEM images of Cu ₂ O films electrodeposited at -0.3 V and 60°C in stirred electrolyte containing 0.2 M CuSO ₄ + 3 M lactic acid adjusted to pH 9.5 for different durations: (a) 3, (b) 15, (c) 45 and (d) 60 min.....	123
Figure 6-16: Performance of devices fabricated using Cu ₂ O layers deposited in stirred and unstirred electrolytes (0.2M CuSO ₄ + 3.0M lactic acid) at different pH.	124
Figure 6-17: J-V curves for devices fabricated using Cu ₂ O layers deposited in stirred and unstirred electrolytes at pH 13.5 (0.2 M CuSO ₄ + 3.0 M lactic acid) at 65°C.	125
Figure 6-18: Effect of pH on the orientation of Cu ₂ O thin films deposited in stirred or unstirred electrolyte.	126
Figure 6-19: SIMS profiles of C ⁻ intensity for stirring and pulsing (500ms/500ms) electrodeposition conditions from the pH 9.5 electrolyte. Result for DC deposition in quiescent electrolyte is shown as comparison.	127
Figure 7-1: Linear sweep voltammogram obtained on FTO-coated glass substrates immersed in 0.05 M Zn(NO ₃) ₂ solution and 65°C	129

Figure 7-2: X-ray diffraction profile of a typical ZnO film chemically deposited on FTO-glass substrate. The bottom spectrum shows the profile of the FTO substrate for all experiments in this work. . 133

Figure 7-3: SEM images of ZnO thin films deposited on FTO-glass substrate from 0.025 M Zn(NO₃)₂ + 0.025 M HMTA solution at 85°C for 1 hour using different types of seed layer: (a) no seed layer, (b) ZnO powder (average diameter ~100nm), (c) ZnO colloids (average diameter ~120 nm). In each of the samples, 5 layers of seeds have been applied. 134

Figure 7-4: SEM images of ZnO thin films deposited on FTO-glass substrates at 85°C for 1 hour from 0.025 M Zn(NO₃)₂ + 0.025 M HMTA solution adjusted to pH:(a) 3, (b) 5, (c) 6.9 (unadjusted) with HNO₃. All samples dip-coated with 5 layers of ZnO colloids as seed layer. 135

Figure 7-5: SEM images of ZnO thin films deposited on FTO-glass substrates at 85°C for 1 hour from solution containing 0.025 M HMTA and different Zn(NO₃)₂ concentrations: (a) 0.01, (b) 0.025, (c) 0.05 and (d) 0.10M adjusted to pH 5 using HNO₃. The orientations of the resulting ZnO thin films are shown in (e). All samples dip-coated with 5 layers of ZnO colloids as seed layer. 136

Figure 7-6: SEM images of ZnO thin films deposited on FTO-glass substrates at 85°C for 1 hour from solution containing 0.025 M Zn(NO₃)₂ and different HMTA concentrations: (a) 0.01, (b) 0.025, (c) 0.05 and (d) 0.10M adjusted to pH 5 using HNO₃. The orientations of the resulting ZnO thin films are shown in (e). All samples dip-coated with 5 layers of ZnO colloids as seed layer. 137

Figure 7-7: Performance measures of Cu₂O/ZnO/Al devices fabricated using Cu₂O electrodeposited at 60°C and -0.65V from 0.2 M CuSO₄ + 3 M lactic acid at pH 12.5 and ZnO chemically deposited at 85°C from Zn(NO₃)₂ + 0.025 M HMTA with different Zn²⁺ concentrations. 139

Figure 7-8: Performance measures of Cu₂O/ZnO/Al devices fabricated using Cu₂O electrodeposited at 65°C and -0.72V from 0.2 M CuSO₄ + 3 M lactic acid at pH 13.4 and ZnO chemically deposited from Zn(NO₃)₂ + 0.025 M HMTA at 85°C with different Zn²⁺ concentrations. 140

Figure 8-1: Reported efficiencies of Cu₂O/ZnO (doped or undoped) solar cells fabricated using electrodeposited Cu₂O thin films as p-type material without additional interlayers. 143

List of Tables

Table 2-1: Application of p-type Cu ₂ O as active layer in photovoltaic devices	12
Table 2-2: Reported efficiencies of heterojunction solar cells using electrochemically deposited Cu ₂ O as p-type material.....	19
Table 3-1: Summary of reagents	22
Table 4-1: Estimated thickness of Cu ₂ O films galvanostatically deposited from 0.2M CuSO ₄ – 3M lactic acid electrolyte adjusted to pH 13.5 at different applied potentials.....	52
Table 5-1: Factorial design conditions	68
Table 5-2: Summary of Cu ₂ O electrodeposition conditions, morphology and Cu ₂ O/AZO device performance.....	69
Table 5-3: F-statistics for the effects of Cu ₂ O electrodeposition parameters and two-factor interactions on solar cell performance.....	71
Table 5-4: Summary of front- and back-illuminated Cu ₂ O/AZO device performance	82
Table 5-5: Bandgap of Cu ₂ O thin films as measured by different techniques	86
Table 6-1: Estimated thickness of Cu ₂ O films galvanostatically deposited from 0.2 M CuSO ₄ + 3 M lactic acid electrolyte adjusted to pH 9.5.....	99
Table 6-2: Performance measures of devices fabricated with Cu ₂ O layers deposited using	118

List of Symbols

$[XXX]$	concentration of XXX	Lac^-	lactate ion
A	area	m	mass
Abs	absorbance	M	molar mass
c	speed of light	n	ideality factor
$Cu(0)$	copper species at 0 oxidation state	N	charge carrier concentration
$Cu(I)$	copper species at +1 oxidation state	n_0	charge carrier concentration (average in a film)
$Cu(II)$	copper species at +2 oxidation state	$NaOH$	sodium hydroxide
Cu_2O	cuprous oxide	OH^-	hydroxide ion
CuO	cupric oxide	P_{in}	incident power
$CuSO_4$	cupric sulfate	Q	electric charge
D	diffusion coefficient	R_s	series resistance
d	film thickness	R_{sh}	shunt resistance
E	electric field	T	temperature
e	charge of an electron	t_{off}	off-time (pulsed deposition)
E_C	conduction band	t_{on}	on-time (pulsed deposition)
E_F	Fermi level	t_T	transit time
E_g	band gap	V	voltage
E_V	valence band	V_{bi}	built-in bias
F	Faraday constant	V_M	voltage at maximum power point
FF	fill factor	V_{OC}	open-circuit voltage
h	Planck constant	z	number of electrons transferred (during redox reaction)
i	current density (during electrodeposition)	$Zn(NO_3)_2$	zinc nitrate
J	current density	ZnO	zinc oxide
J_0	reverse saturation current	α	absorption coefficient
$J_{diffusion}$	diffusion current	ϵ	permittivity
J_{drift}	drift current	λ	photon wavelength
J_M	current at maximum power point	μ	charge carrier mobility
J_{ph}	photogenerated current	ν	photon frequency
J_{SC}	short circuit current		
k_B	Boltzmann constant		

List of Abbreviations

<i>AC</i>	alternating current
<i>AFM</i>	atomic force microscopy
<i>ALD</i>	atomic layer deposition
<i>AZO</i>	Al-doped ZnO
<i>CIGS</i>	copper indium gallium selenide (solar cell)
<i>CV</i>	cyclic voltammetry
<i>CVD</i>	chemical vapor deposition
<i>DC</i>	direct current
<i>DI</i>	de-ionized (water)
<i>DMSO</i>	dimethyl sulfoxide
<i>EQE</i>	external quantum efficiency
<i>FTO</i>	fluorine-doped tin oxide
<i>HMTA</i>	hexamethylenetetramine
<i>ITO</i>	indium-doped tin oxide
<i>LSV</i>	linear sweep voltammetry
<i>OCP</i>	open-circuit potential
<i>PCE</i>	power conversion efficiency
<i>PEDOT</i>	poly(3,4-ethylenedioxythiophene)
<i>PLD</i>	pulsed-layer deposition
<i>RF</i>	radio-frequency (sputtering)
<i>SCE</i>	saturated calomel electrode
<i>SCLC</i>	space-charge limited current
<i>SEM</i>	scanning electron microscopy
<i>SILAR</i>	successive ionic layer adsorption and reaction
<i>SIMS</i>	secondary ions mass spectroscopy
<i>TOF</i>	time-of-flight (measurement techniques)
<i>XRD</i>	X-ray diffraction

Chapter 1. Introduction

1.1 Motivation

In order to keep up with the rapidly increasing world energy demand, much attention over the last few decades has been focused on the development of alternative energy systems. Among the different options, solar energy shows great promise as a sustainable, non-polluting and benign source of energy. Photovoltaic devices or photovoltaics, more commonly referred to as solar cells, operate by making use of the photovoltaic effect to convert solar energy directly to electrical energy.

Different types of photovoltaic devices have been developed and commercialized over the years. Up to this date, first-generation solar cells based on crystalline semiconductors such as silicon and GaAs, commercialized in the 1970s, still achieve the highest performance [1]. However, the strict requirement for material purity results in a high material and fabrication cost. Therefore, one of the goals in the design of new photovoltaic cells is to reduce the cost of energy generation to an amount comparable to conventional electric energy [2]. This calls for the development of photovoltaic devices based on cheap materials and low-cost fabrication methods. Emerging photovoltaics during the last two decades have provided many promising alternatives to conventional solar cells. Excitonic solar cells such as dye-sensitized solar cells have already achieved over 11% efficiency on the laboratory scale [3]. Devices based on organic materials such as polymers [4,5] and small molecules [6] have been widely investigated. Furthermore, recently-developed halide perovskite cells have also demonstrated promises as high efficiency solar cells [7].

In the last few years, devices based entirely on metal oxides have emerged as promising alternatives. These devices take full advantage of the cheap and green nature of common oxide materials and hold promise for fabrication of ultra-low cost solar cells [8]. The concept of oxides in photovoltaic applications, mostly Cu_2O Schottky junction devices, was investigated in the 1970s following the oil crisis in 1973 [9–

11] although limited results were obtained due to difficulty in preventing Cu formation during sputtering [11,12]. Research interest in this topic has been renewed in the last decade with the demonstration of much better device performance of heterojunction oxide solar cells [13–16].

The main advantage of oxide solar cells compared to other alternatives is their stability under ambient conditions, which gives them much longer lifetime than devices based on organic materials. While metal oxides have been widely used in solar cells as the electron acceptor or hole-transport layer, only a few oxide semiconductors have shown potential as the sensitizing material due to their relatively large band gaps. Small-bandgap metal oxides such as Cu_2O , CuO [17], Co_3O_4 [18] and Fe_2O_3 [19] have been investigated as light absorbing materials. Alternatively, ternary or composite oxides have also been proposed as semiconductor materials due to their desirable band structures [20]. The basic idea here is to fabricate the band edges of the material by combining different metallic elements through a combinatorial design approach. An example of a ternary oxide used for light absorption is BiFeO_3 [21,22]. Although its bandgap is much larger than desired, its use proved successful enough to validate the concept behind this approach.

Among those choices, copper oxides attract the most attention due to their abundance and nontoxicity. Cupric oxide (CuO) has bandgap of 1.4eV, which is ideal for photovoltaic applications. Unfortunately, its low carrier concentration and high resistivity limits its potential. Efforts have been made to reduce the sheet resistance and to improve the charge transport properties of the CuO absorber layer [23]. On the other hand, cuprous oxide (Cu_2O) was one of the earliest semiconductors investigated for photovoltaic applications, long before Si and Ge devices were successfully fabricated [24]. Cu_2O is a p-type semiconductor with a direct bandgap of 1.9-2.2eV, which is larger than desired for photovoltaic applications. However, some rather attractive properties such as natural p-type conductivity, high absorption in the visible region and high carrier mobility make it a promising material for the fabrication of oxide solar cells.

At the moment, the reported efficiencies for Cu₂O-based solar cells are well below their theoretical limit. Furthermore, most of the high performance devices have been fabricated using vacuum processes, making them both energy-intensive and difficult for large scale production. On the other hand, electrodeposition of Cu₂O is a well-known technique for the synthesis of Cu₂O thin films. Although it has been applied often for the fabrication of oxide solar cells, a systematic study of the dependence of Cu₂O film properties on the deposition conditions has not been reported to date, especially in the context of photovoltaic applications. Furthermore, in cases where the solar cells consist of electrodeposited Cu₂O thin films, their performance has often been low and inconsistent [25].

The main objective of this study is to optimize the electrodeposited p-type Cu₂O film properties for the application in heterojunction solar cells through the manipulation of electrodeposition conditions. By achieving this goal, a deeper understanding can be gained in the Cu₂O electrodeposition system and the efficiency of oxide solar cells based on electrodeposited Cu₂O can be improved and consistently achieved.

1.2 Structure of thesis

The thesis is organized as follows:

Chapter 2 provides a review on the background of this study, including some theories behind heterojunction solar cells and a description of the current state of research on Cu₂O-based photovoltaics and the synthesis of Cu₂O thin films by electrodeposition and other techniques. In Chapter 3, the experimental methods used in this study are explained in detail. This is followed by a systematic study of the effect of constant potential deposition conditions on the morphology Cu₂O thin films from copper-lactate electrolyte, with detailed analysis of the mechanisms affecting film morphology in Chapter 4. In Chapter 5, the efficiency of Cu₂O/Al-doped ZnO (AZO) solar cells using electrodeposited p-type Cu₂O is optimized by varying Cu₂O deposition conditions, including the effect of electrodeposition conditions on the optical and electrical properties of Cu₂O thin films which directly influences device performance. Chapter 6 describes efforts to improve the efficiency of Cu₂O/AZO solar cells using less common

electrodeposition procedures including galvanostatic deposition, pulsed electrodeposition and deposition from stirred electrolytes. In Chapter 7, the possibility of replacing sputtered AZO with chemically grown ZnO thin films as the n-type material in the $\text{Cu}_2\text{O}/\text{AZO}$ devices is analyzed. Finally, the thesis concludes with a summary of the main results and contributions of this study and recommendations for future research in Chapter 8.

Chapter 2. Background

2.1 P-n junction photovoltaics

2.1.1 Device structure

The basic structure of a p-n junction solar cell is a photodiode consisting of a donor (p-type) and an acceptor (n-type) semiconductor directly adjacent to each other. In conventional solar cells such as silicon solar cells, the p-type and n-type semiconductors are the same material doped differently, namely a homojunction. For the devices investigated in this study, the p-n junction consists of two different oxide semiconductors forming a heterojunction.

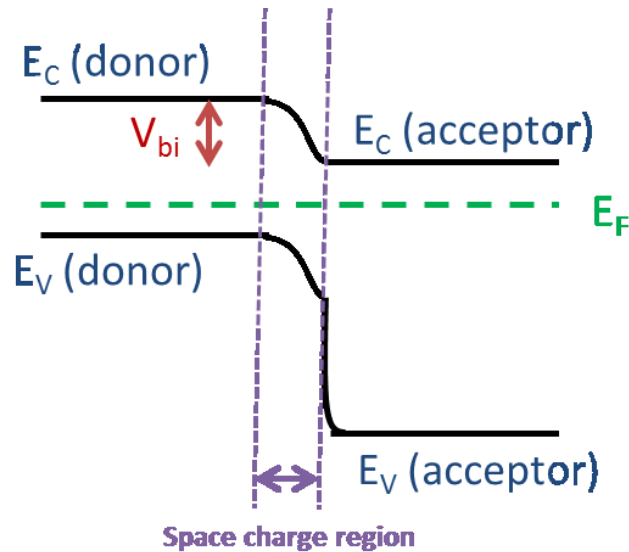


Figure 2-1: Energy band diagram for a p-n junction at thermodynamic equilibrium

In order for the photocurrent generation to occur effectively, the electronic bands at the p-n junction must have a staggered arrangement. The energy band diagram of a heterojunction at equilibrium is given in Figure 2-1. The electrons and holes close to the junction diffuse across the junction and recombine with each other, leaving ionized donors and acceptors behind. This forms a region at the p-n junction where no mobile charge carriers are present, termed the space charge region (or depletion region) as identified in the diagram. An electric field is generated by the ionized donor and acceptors across the space charge region, causing a drift current to flow in the opposite direction of the carrier diffusion. At equilibrium, the

magnitude of the drift current is equal to the diffusion current, causing no net current to flow. The potential difference between the conduction bands of p-type and n-type material at equilibrium is termed the built-in bias (V_{bi}) [26].

2.1.2 Current generation process

Charge generation in a p-n junction solar cell can occur in 4 steps:

1. Photon absorption

When light reaches the semiconductor, a portion of it is absorbed by the material. The fraction of light that can be absorbed at each wavelength depends on the properties of the material. In a solar cell, at least one side of the device must have good transparency in order for the maximum amount of the irradiated light to reach the active layer.

2. Charge carrier generation

If the absorbed photon has higher energy than the bandgap of the semiconductor, an electron from the valence band will be excited to the conduction band, leaving a free hole on the valence band. The free charge carriers can only be generated in a semiconductor if the absorbed photon has greater energy than the bandgap of the material.

3. Carrier transport

The transport of photogenerated charge carriers occurs as a combined effect of drift and diffusion. In the space charge region of the diode, charge carriers moves predominantly by drift:

$$J_{drift} = Ne\mu E \quad (2-1)$$

where N is the concentration of charge carriers, e is the charge of an electron, μ is the charge carrier mobility and E is the electric field. In particular, the charge carrier mobilities are especially important for the performance of a photovoltaic device since drift is usually considered to have a greater effect in charge transport than diffusion. Outside the space charge region, diffusion is the main mode of charge carrier transport:

$$J_{diffusion} = eD \frac{dN}{dx} \quad (2-2)$$

where D is the diffusion coefficient and the differential term denotes the concentration gradient of the corresponding charge carrier.

4. Charge collection

In addition to the p-n junction, conductive materials (typically metallic thin films) are also present on either side of the junction in a photovoltaic device in order for the generated current to be collected. The collection efficiency depends on the work function and contact quality of the contact electrodes. For efficient charge collection, the work function of the anodic contact should be high and close to the energy of the valence band of the p-type material, while the cathodic contact should have a low work function close to the conduction band of the n-type material.

On a macroscopic scale, the electrons move towards the cathode and the holes towards the anode, opposite to that of the forward diode when a load is connected to the device. However, not all photogenerated charge carriers can be converted to usable current from the above process since it is energetically favorable for free electrons and holes to recombine with each other. This recombination process is primarily assisted by trap states within the device, such as impurities in the semiconductor crystals and defects at the interfaces at p-n junction or between semiconductors and contacts.

2.1.3 Device output

The performance of a photovoltaic device is primarily characterized by the illuminated current-voltage (J-V) curve. The typical shape of a current-voltage curve is shown in Figure 2-2. It should be noted that, while the current J is typically shown as being positive in these curves, the forward diode current is taken to be positive by convention, thereby making the actual photocurrent negative as it flows in the opposite direction of the forward diode current.

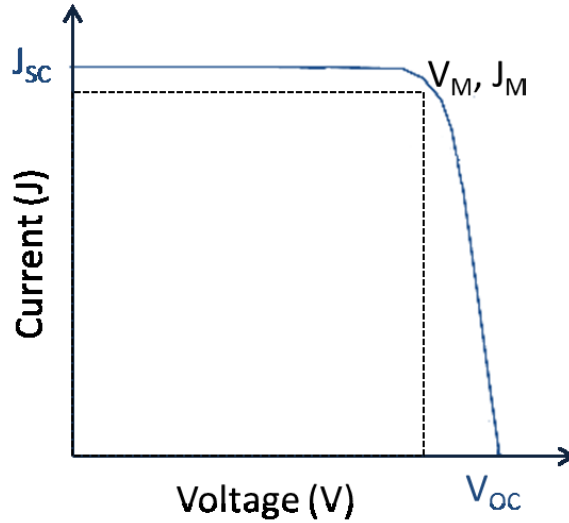


Figure 2-2: Typical output characteristic curve of a photovoltaic device

The performance of a photovoltaic device is usually indicated by its power conversion efficiency (PCE), which is the fraction of incident solar power (P_{in}) that is converted into electricity. This value is calculated from the open-circuit voltage (V_{oc}), short-circuit current (J_{sc}) and fill factor (FF) as follows:

$$PCE = \frac{J_{sc}V_{oc}FF}{P_{in}} \quad (2-3)$$

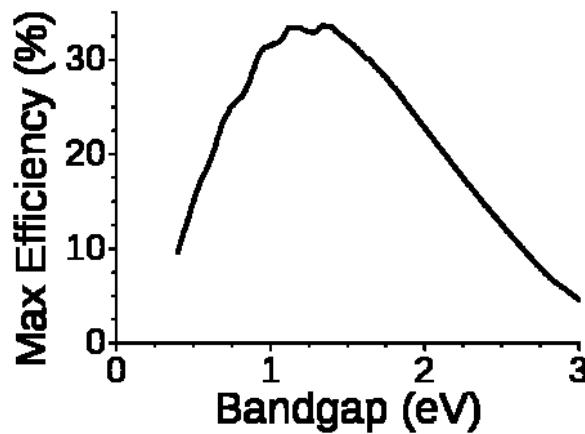


Figure 2-3: Shockley–Queisser limit for a single heterojunction solar cell

The theoretical maximum PCE obtainable by a standard p-n heterojunction photovoltaic device can be obtained from the bandgap of the light absorbing material, as shown in Figure 2-3 [27]. This value is referred to as the detailed balance limit or Shockley-Queisser limit and often serves as the guideline for

selecting the optimal sensitizer material. However, this limit can be exceeded by using advanced device structures such as tandem cells [28] or by generation of multiple-excitons from a single photon [29].

J_{SC} is the photocurrent density generated under illumination under short-circuit conditions and depends on the incident light intensity and absorption spectrum of the active layer:

$$J_{SC} = -\frac{e}{hc} \int_{\lambda_{min}}^{\lambda_{max}} EQE \times P(\lambda) \lambda d\lambda \quad (2-4)$$

where EQE is the external quantum efficiency, $P(\lambda)$ is the power of incident photons, λ_{min} and λ_{max} define the frequency range absorbed by the sensitizer. EQE refers to the number of electron-hole pairs successfully collected per photon reaching the solar cell. It is determined by the combined efficiency of light absorption, carrier diffusion, charge transport and charge collection.

V_{OC} is the maximum attainable voltage obtained when the electrodes are not connected. For a heterojunction photovoltaic device, the maximum obtainable open-circuit potential ($V_{OC, max}$) can be estimated from the band edge alignment of the materials:

$$V_{OC, max} = \left| \frac{1}{e} (E_C^{Acceptor} - E_V^{Donor}) \right| \quad (2-5)$$

FF is a measure of the squareness of the J-V curve for the device. It is calculated from the J-V curve using the maximum power point (V_M, J_M) and is an indicator of the deviation of the solar cell from ideal behaviour, i.e.,

$$FF = \frac{J_M V_M}{J_{SC} V_{OC}} \quad (2-6)$$

This parameter is strongly related to the ideality of the diode, series resistance and shunt resistance, as will be discussed in the following section.

2.1.4 Series and shunt resistance effect

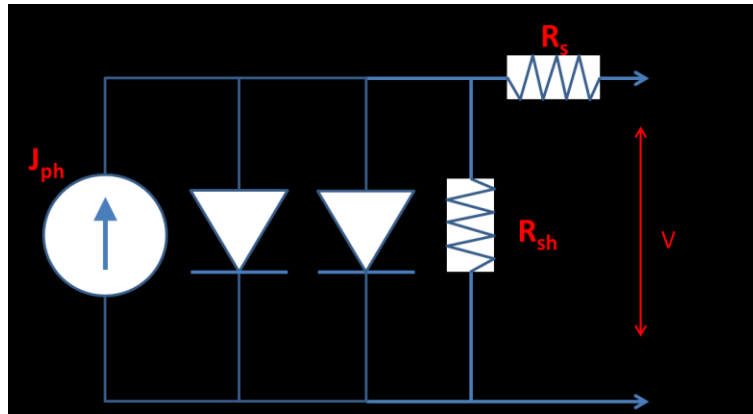


Figure 2-4: Equivalent circuit model for a photovoltaic device

A photovoltaic device can also be viewed as a current source in parallel with two diodes, as shown in Figure 2-4. The first diode represents recombination by a trap-assisted mechanism with an ideality factor 1, while the second represents recombination in the space-charge region with an ideality factor 2. Also, a non-ideal solar cell contains a series resistance (R_s) and parallel (shunt) resistance (R_{sh}), both of which contribute to the lowering of device PCE. The series resistance R_s arises from the combination of the resistivities of both the bulk materials and the interfaces. R_{sh} arises from the fraction of current leaking through the device surfaces and edges and grain boundaries instead of the external load.

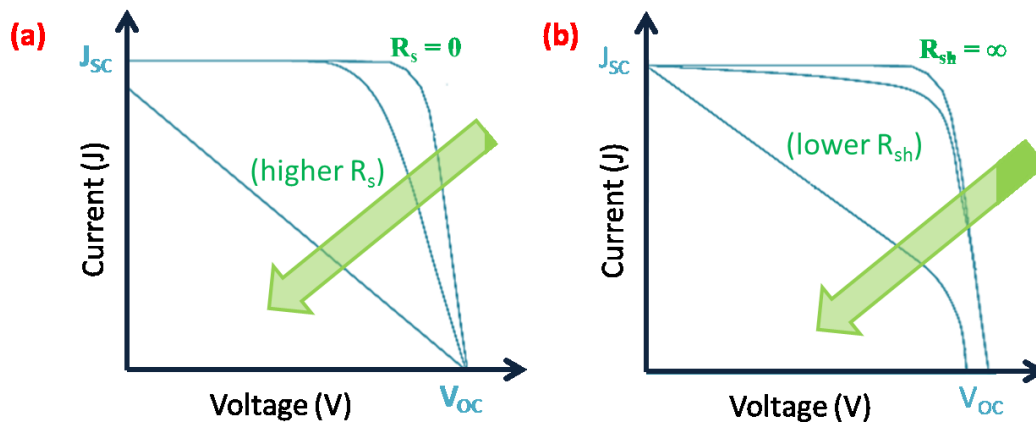


Figure 2-5: Effect of (a) series resistance and (b) shunt resistance on solar cell performance

In general, a low R_s and high R_{sh} values are preferred in solar cell operation. Figure 2-5 shows the effect of series and shunt resistance on a photovoltaic device, as represented by the deviation from an ideal J-V

curve. Both variables primarily affect FF, but J_{SC} and V_{OC} values are also reduced in the case of very high R_s and R_{sh} , respectively.

In the presence of R_s and R_{sh} , the J-V relationship in a solar cell can be written as:

$$J = J_0 \left\{ \exp \left[\frac{e(V - JR_s A)}{nk_B T} \right] - 1 \right\} + \frac{V - JR_s A}{R_{sh} A} - J_{ph} \quad (2-7)$$

where V and J are the output voltage and current, J_{ph} is the photogenerated current, k_B the Boltzmann constant, T the temperature, e the charge of an electron, A the device area, n the ideality factor of the diode and J_0 the reverse saturation current density, which reflects the number of charges that can overcome the energy barrier in the reverse direction (dark current).

2.2 Cu₂O-based photovoltaics

2.2.1 Cu₂O in photovoltaic applications

Cu₂O is a natural p-type semiconductor due to Cu vacancies [30,31] and possible O interstitials [32] although it can also be doped to be n-type by inducing O vacancies during the fabrication process. Table 2-1 presents some examples of solar cells using Cu₂O as the photon absorbing layer. Among the different types of solar cells, the performance of homojunction Cu₂O solar cells are limited by the difficulty in controlling the film properties of electrodeposited n-type Cu₂O, resulting in PCE below 1% despite recent report of relatively high J_{SC} being achieved [33]. Schottky barrier cells are mostly limited by the tendency to form ohmic contacts with high work function metals such as Au [11], although recently it has been reported that the addition of hexagonal boron nitride as a passivation layer can largely resolve this issue [34].

On the other hand, heterojunction solar cells with p-type Cu₂O with another inorganic semiconductor, especially ZnO, have shown great promises. At the moment, the highest efficiency demonstrated by a Cu₂O-based solar cell is 5%-6% obtained by using a Na-doped Cu₂O as absorbing layer, a Ga₂O₃ interlayer between Na-Cu₂O and an n-type AZO layer and additional electron- and hole- extracting layers

(n^+ and p^+) on either side of the device [35–37]. All of these devices are fabricated using thermally oxidized Cu_2O . With undoped Cu_2O , a high PCE of 3.8% has been achieved using a bilayer heterojunction of AZO and a thermally oxidized Cu_2O thin film [38]. Compared to $\text{Cu}_2\text{O}/\text{ZnO}$ heterojunctions, devices using other n-type materials have shown limited success in obtaining high PCEs in Cu_2O -based solar cells because of a non-ideal band structure and low carrier mobility. A $\text{Cu}_2\text{O}/\text{InP}$ device has been reported to have over 1.5% efficiency [39], while the highest PCE of $\text{Cu}_2\text{O}/\text{TiO}_2$ devices has been only 0.35% due to low carrier mobility in TiO_2 [40].

Table 2-1: Application of p-type Cu_2O as active layer in photovoltaic devices

Type of solar cells		References
Schottky junction		[34,41]
Homojunction		[33,42–44]
Liquid junction		[45]
Heterojunction	ZnO	[13,37,38,46–83]
	Al:ZnO (AZO)	[15,16,35,84–101]
	Mg:ZnO	[81]
	Ga:ZnO	[102]
	TiO_2	[40,103–108]
	Fe_xO	[109]
	InP	[39]
	In_2S_3	[110]
	ITO	[15]
	Si	[111,112]
PCBM		[113]

In addition to its use as a p-type absorption layer, Cu_2O has also been used in other types of photovoltaic device for performance improvement. Because of its excellent hole mobility, Cu_2O has been introduced as the hole transport layer in organic [114,115], perovskite [116–120] and CdTe solar cells [121] to reduce recombination and improve device stability. It has also been added to copper indium gallium selenide (CIGS) tandem solar cells [122] and polymer solar cells [123] as the interlayer for the purpose of junction tunnelling and absorption enhancement, respectively. Finally, it has been demonstrated that Cu_2O heterojunction solar cells can be fabricated on plastic [96] or templated NiW [97] substrates for the potential application in flexible solar cells.

2.2.2 Techniques for efficiency enhancement

Modifications of film properties

As mentioned previously, the most significant limitation on Cu₂O-based solar cells is the larger than desired band gap. The Shockley-Queisser limit for a Cu₂O/ZnO heterojunction is approximately 20% [98], much lower than the ~40% calculated for silicon-based solar cells. Consequently, attempts to modify the Cu₂O bandgap have been reported with different degrees of success. The most effective by far is bandgap narrowing by doping Cu₂O thin films with Na, which can be done for both thermally oxidized and electrodeposited Cu₂O films [35,94,111]. On the other hand, doping Cu₂O with nitrogen has been shown to widen the bandgap to ~2.5eV or larger [88]. Although this is not desired in a photo-absorption layer, it is able to achieve better charge collection efficiency through an improved semiconductor-metal contact [124]. Theoretical calculations have also been done for the doping of Cu₂O films with Zn [125,126], Se [125], S [127] and combinations of these [128] in order to reduce the band gap, although experimental results are not yet available. Extrinsicly doped Cu₂O or ZnO can be used on its own or in combination with pure Cu₂O and ZnO as electron and hole transporting layers [35] in order to further optimize the device architecture. In addition to doping, the bandgap of Cu₂O has also been reduced by chemical treatment with hydrogen peroxide [129], possibly through partial oxidation to CuO. Furthermore, similar to some other inorganic sensitizers, Cu₂O has been reported to also exhibit a strong quantum confinement effect. Because of this effect, the band gap of the material can be tuned to be as low as 1.2eV by decreasing the film thickness [130], which provides another potential approach to improve light absorption in photovoltaic application, although no research on this topic has been reported in the literature at the moment.

Aside from the band structure, the carrier concentration and mobility in p-type Cu₂O also play a significant role in oxide photovoltaics. In the case of p-type semiconductors, an extra acceptor level exists close to the valence band. Electrons on the valence band can be easily thermally excited to this level, leaving behind free holes on the valence band which determine the hole concentration of the material. On

the other hand, the mobility of charge carriers directly influences the drift velocity, which is the main mode of carrier transport in the space charge region in the solar cell. In general, it is preferable for both carrier concentration and mobility to be high in Cu₂O-based solar cells. However, a trade-off usually exists between these values since Cu vacancies in the crystal structure increases the carrier concentration, but also increases the rate of recombination due to traps and thus reduces the charge carrier mobility. Both values are reported to be highly dependent on the deposition method and conditions of the Cu₂O thin films. Although Cu₂O films with either high carrier mobility (over 50 cm²/Vs) or high carrier concentration (over 10¹⁶ cm⁻³) have been formed in previous research, the deposition of Cu₂O films having both high carrier mobility and concentration has been very challenging in the field, usually involving epitaxial growth on a single-crystalline substrate [131]. Extrinsic doping of Cu₂O with Na [111,132] or Ag [133] has been reported to increase the hole concentration, while Mg-doped Cu₂O shows improved hole mobility [83,104]. In addition, chemical treatment by crown ether cyanide has also been reported as a possible method to improve the hole concentration in sputtered Cu₂O thin films [134].

Interfacial control

The formation of nanostructured interfaces has long been accepted as an effective method to improve the J_{SC} values in excitonic solar cells since it increases the interfacial area between the p-type and n-type materials and thus minimizes the required travel length of excitons. Similar attempts have been made to improve the performance of Cu₂O-based solar cells. The use of ZnO thin films composed of nanowires has been demonstrated to effectively increase the interfacial area of Cu₂O/ZnO heterojunctions [63,68]. Nanocolumns have also been synthesized by adjusting the conditions for sputtering Cu₂O [62]. In addition, core-shell architectures of both Cu₂O/ZnO and Cu₂O/TiO₂ heterojunctions have been successfully fabricated for photovoltaic applications [67,91,108].

However, despite these various techniques, the PCEs of nanostructured Cu₂O solar cell devices remain lower than those of planar heterojunctions. This is attributed to the different length scales that are ideal for optimal V_{OC} and J_{SC} [63]. While the required transport length for carriers is reduced in a nanostructured

interface, it also inhibits the development of a built-in bias across the space charge region and hence allows a larger dark current to flow. Consequently, Cu_2O devices with nanostructured interfaces tend to have larger J_{SC} , but smaller V_{OC} , than planar heterojunction and therefore do not exhibit improved charge transport properties when operating as solar cells.

On the other hand, interlayers have been introduced between Cu_2O and ZnO in order to improve device performance. The V_{OC} of the $\text{Cu}_2\text{O}/\text{ZnO}$ has been reported to increase through modification of the interfacial band alignment by adding a thin layer of S-doped ZnO [86] or TiO_2 [71] at the p-n interface. Similarly, Ga_2O_3 [37,80,87] and $\text{Mg}:\text{ZnO}$ [93] layers have been introduced to improve band alignment and reduce interfacial defects between AZO and thermally oxidized Cu_2O . Additionally, the V_{OC} in devices based on a nanostructured $\text{Cu}_2\text{O}/\text{ZnO}$ interface can be improved by functionalizing the interface with polymers such as poly(3,4-ethylenedioxythiophene) (PEDOT) and polypyrrole [77].

Furthermore, it has been noted that the best-performing devices ($\text{PCE} > 2.0\%$) typically contain heterojunctions formed under vacuum that are fabricated using techniques such as pulsed-layer deposition (PLD) [35,38,87,94] and atomic layer deposition (ALD) [36] for the deposition of n-type semiconductors. This is explained by the tendency of Cu_2O surface to oxidize and form CuO [25,81] if no steps to eliminate oxygen are taken. Some techniques have been developed to reduce the formation of surface CuO under mild conditions. For example, Wilson et al demonstrated the possibility of interface stoichiometry control through the careful modification of the conditions during ZnO sputtering onto Cu_2O thin films [135]. Lin et al reported some success with a piezotropic approach involving the application of a compressive strain during ZnO deposition onto the Cu_2O layer [55].

2.3 Cu_2O synthesis techniques

2.3.1 Overview

For the fabrication of photovoltaic devices, p-type Cu_2O thin films can be synthesized using a variety of physical and chemical methods including ALD [36], anodization [41], chemical vapor deposition

(CVD) [70,136], e-beam evaporation [91], PLD [97], sputtering [39,62,88,89,134,137], successive ionic layer adsorption and reaction (SILAR) [46,48], sol-gel [95], spray pyrolysis [103,104], thermal oxidation [15,35,53,81,94,110] and electrodeposition. Although not commonly used in solar cells, a large variety of nano-morphologies can be obtained using different synthesis routes [124]. Examples include chemical reduction [138] and solvothermal [139] methods which can produce a range of nanocrystal shapes depending on the synthesis conditions. Template-based methods have also been used to produce more complex structures [140,141].

Figure 2-6 presents the reported efficiencies of $\text{Cu}_2\text{O}/\text{ZnO}$ (doped or undoped) solar cells which are by far the most efficient oxide solar cell structure, sorted by deposition method. While both thermal oxidation and electrodeposition have been extensively applied for the fabrication of Cu_2O -based solar cells, the plot shows that the highest device PCE have been achieved by optimizing the device architecture of cells fabricated using thermally oxidized Cu_2O sheets.

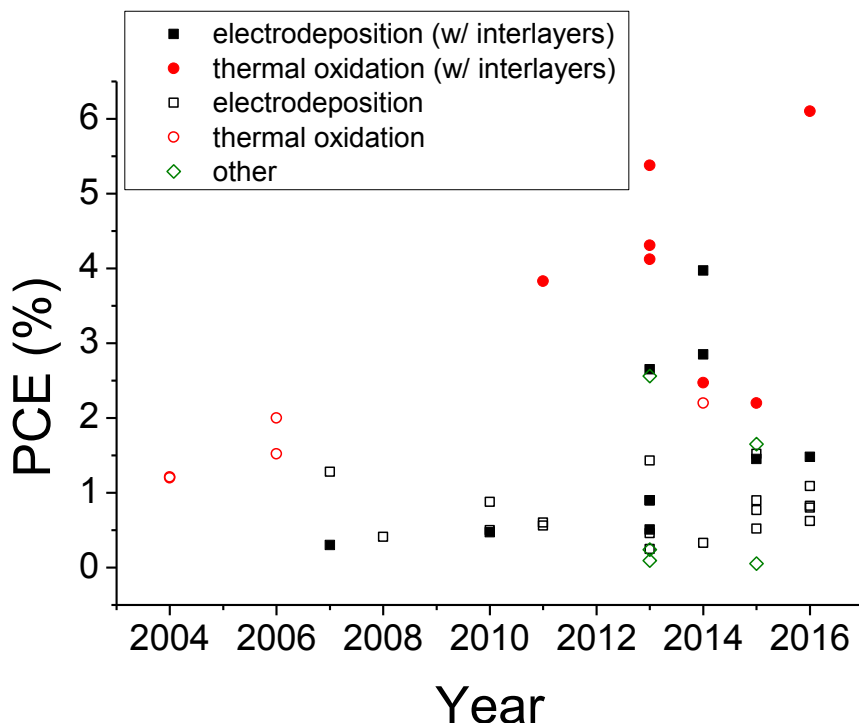


Figure 2-6: Reported efficiency of Cu_2O -based solar cells by year

The properties of Cu₂O thin films, including charge carrier concentration and mobility, are dependent on the synthesis technique and conditions. For example, the hole density in p-type films is typically on the order of 10¹⁴ cm⁻³ when formed by electrodeposition, 10¹⁶ cm⁻³ when produced by sputtering and 10²⁰ cm⁻³ when obtained by thermal oxidation. This difference is considered to be one of the main reasons why thermally oxidized Cu₂O thin films have exhibited the highest PCE in oxide photovoltaics, as described in the previous section. Annealing has been reported to improve the properties of the interfaces between Cu₂O and other oxides [142]. Cu₂O is usually annealed at temperatures between 200 °C and 300°C as CuO tends to form at higher temperatures [64].

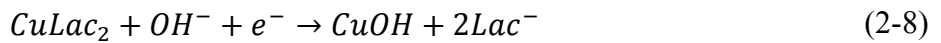
Despite current success at the laboratory scale, thermal oxidation of thin copper foil is challenging due to the thermal expansion and crystallization behavior of the metal [34]. On the other hand, in addition to being energy intensive and difficult to scale up, techniques such as RF sputtering also lead to the simultaneous formation of both CuO and Cu₂O phases, which is a major problem for the fabrication of Cu₂O thin films [143]. It is known that Cu(I) is less stable than Cu(II) and Cu(0) both in air and in aqueous conditions, making the preparation of highly pure Cu₂O very difficult. However, for most of the applications mentioned above, CuO or Cu impurities are detrimental and so highly pure Cu₂O is desired to obtain optimal electrical properties [76].

2.3.2 Electrodeposition of Cu₂O

First introduced by Stareck [144] in 1943, electrochemical deposition of Cu₂O has been widely investigated because of its simplicity, low cost, mild operating temperature and ease of scale-up. A particularly attractive feature of electrodeposition is its ability to produce highly pure Cu₂O by the appropriate control of its operating conditions. Furthermore, it may be possible to tune the conditions to control Cu₂O morphology and crystal structure, which can significantly affect its electrical properties. Both p-type and n-type films can be electrodeposited by adjusting solution composition although the doping level is difficult to control during the deposition of n-type Cu₂O thin films, as mentioned in Section 2.2.1. Furthermore, since electrodeposited Cu₂O material is usually highly crystalline with a

controllable growth direction, it does not require further heat treatment and therefore requires lower processing costs.

Typically, p-type Cu₂O thin films are deposited from an alkaline electrolyte containing cupric ions. A stabilizing agent such as lactate is required in these solutions to prevent the precipitation of Cu(OH)₂. When enough lactate (Lac⁻) is present, soluble copper lactate complexes form. Based on thermodynamic calculations, the predominant complex is CuLac₂ [145]. The electrochemical reduction of Cu(II) to Cu₂O involves the formation and dehydration of a CuOH intermediate [146]:



Cu₂O has a cubic crystal structure and typically forms cubic or octahedral shaped grains when produced by electrodeposition. The habits of these crystals are related to the relative growth rates in the <111> and <200> directions [147]. As shown in the structure on the left of Figure 2-7, when the growth rate in the <111> direction is faster than that in the <200> direction, cubic shaped grains are likely to form. On the other hand, when <200>-oriented growth dominates, octahedral grains form (structure on the right in Figure 2-7). When the growth rates in the two directions are similar, truncated grains will be present. Although uncommon when produced by electrodeposition, crystallites with <110>-oriented growth have also been observed [148,149]. Electrodeposition of Cu₂O onto substrates of other oxide nanostructures such as TiO₂ to form core-shell nanostructures has also been reported [108,150–152].

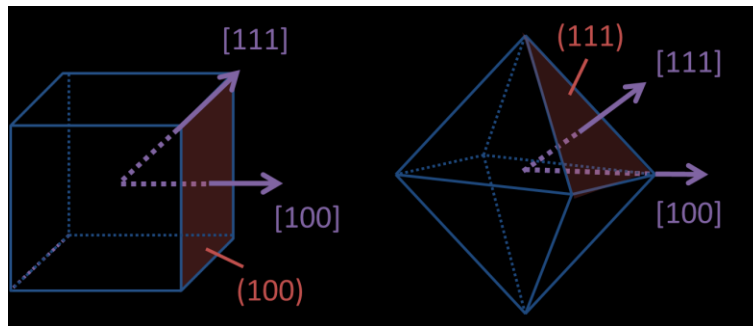


Figure 2-7: Relationship between Cu₂O crystallite shape and growth orientation

Most of the studies on Cu₂O use either potentiostatic or galvanostatic techniques and have shown that the morphology and crystal orientation of the resulting Cu₂O can be finely tuned by controlling operating

conditions such as applied potential and current [90,153–155], solution temperature, pH [147,149,155–165] and solution composition [74,154,155]. Beside lactate, citrate [167–169] and acetate [167] have also been used as stabilizing agents, leading to the formation of vastly different Cu₂O morphologies. The effect of additives on the orientation of crystal structures formed by electrochemical and other solution processes has been studied [148,170,171]. Electrodeposition in a non-aqueous electrolyte such as dimethyl sulfoxide (DMSO) [172] using an oxygen precursor has also been reported.

2.3.3 Electrodeposited p-type Cu₂O in solar cells

Table 2-2: Reported efficiencies of heterojunction solar cells using electrochemically deposited Cu₂O as p-type material

n-type material	Anode	J _{SC} (mA/cm ²)	V _{OC} (mV)	FF (%)	PCE (%)	Year	Reference
AZO	Ag	4.85	277	38.78	0.52	2015	[99]
	FTO	7.12	290	29.2	0.603	2011	[90]
	Au	6.97	280	41.5	0.824	2016	[84]
	Au	6.82	300	43.9	0.897	2015	[96]
	Au	6.21	350	50	1.09	2016	[85]
	Au	5.67	630	41.56	1.48	2016	[86]
ZnO	Au	7.03	150	33	0.33	2014	[78]
	Au	2.69	316	48	0.41	2008	[71]
	Ag	3.19	310	44.2	0.46	2013	[59]
	Au	4.4	280	39	0.47	2010	[66]
	Au	6.33	240	34.5	0.51	2013	[58]
	Ag	2.64	514	41.5	0.56	2011	[65]
	Au	4.38	340	41	0.62	2014	[54]
	Ag	4.28	431	42	0.77	2015	[47]
	Au	1.12-2.4	660-710	~47	0.4-0.8	2016	[53]
	Au	8.2	290	37	0.88	2010	[68]
	Au	6.32	320	45	0.9	2013	[57]
	SnO₂	3.8	590	58	1.28	2007	[72]
	Au	4.47	535	59.6	1.43	2013	[79]
	Pt	9.07	390	41	1.45	2015	[50]
Au	9.89	420	37	1.52	2015	[51]	
Fe _x O	In	0.74-1.58	38-108	26-35	0.02	2015	[109]
Si	Pt	1.85	460	37	0.31	2014	[112]
	Pt	2.2	480	47	0.45	2016	[111]
TiO ₂	Au	0.33	100	27	0.01	2011	[108]

Electrodeposition is one of the most common techniques for the fabrication of Cu₂O-based solar cells. Table 2-2 summarizes the device performances of representative Cu₂O-based heterojunction solar cells without additional interlayers and extraction layers. Most reported devices with significant efficiency consist of heterojunctions of Cu₂O and ZnO (Al-doped or undoped) and a high work-function metal such as gold (Au) as the anode contact.

Unlike the case of devices made up of thermally oxidized Cu₂O which often have PCEs of 2% or above, the reported efficiencies of devices containing electrodeposited Cu₂O rarely exceed 1% [50,51,72,79,85,86]. The V_{OC} values in devices based on electrodeposited Cu₂O typically range between 270 and 350 mV. High V_{OC} values up to 720 mV have been achieved by modifying the ZnO morphology at the interface although the device PCE is limited by the relatively low J_{SC} (~2.4 mA/cm²) that stem from the same modification [53]. Similarly, devices with high J_{SC} values of 8 mA/cm² or higher have been reported also by manipulating the interfacial morphology; however, the V_{OC} of these devices was at most ~ 420 mV [50,51,68].

Effects of deposition parameters such as copper concentration [78], applied potential and current density [72,90] on the device performance have been investigated. Furthermore, it has been established that both the Cu₂O film orientation [50,99,173] and interfacial morphology [58,59] have large impacts on the device performance. An improvement in V_{OC} by using Li⁺ as the counter-ion in the electrolyte during electrodeposition instead of Na⁺ has also been reported [79]. However, systematic studies on the influences of electrodeposition conditions on the performance of Cu₂O-based solar cells are few and incomplete. As shown in Table 2-2, while an efficiency exceeding 1.2% has already been achieved in 2007 [72] through the modification of deposition parameters, most reported PCE in the following years for devices with electrodeposited Cu₂O layer fall well below this value.

A major limitation of electrodeposited Cu₂O films in solar cells is that they usually have very low carrier density. This value is strongly dependent on the concentration of crystalline defects in the semiconductor oxide, which are largely determined by the deposition methods and conditions.

Unfortunately, the carrier density in electrodeposited Cu_2O films is two to three orders of magnitude lower than that in sputtered Cu_2O which has a typical carrier density of approximately 10^{16}cm^{-3} , already below the optimal level for photovoltaic devices. High hole concentrations above 10^{16}cm^{-3} have been reported for electrodeposited Cu_2O films [85,96], comparable to the typical values from Cu_2O films deposited by sputtering or PLD [97,134,137]. However, the effect of deposition conditions on carrier concentration is still unclear from the limited amount of information available. Similarly, the carrier mobility of electrodeposited Cu_2O thin films in photovoltaic devices has been rarely measured although its improvement using seed layer-assisted electrodeposition has been reported [112].

Chapter 3. Experimental Methods

3.1 Materials

3.1.1 Chemicals

In this study, all chemicals are used as purchased without further treatment unless specified otherwise. Aqueous solutions are mixed using de-ionized (DI) water and the solution pH is measured with a pH meter calibrated prior to measurement. A list of chemicals used in this study is provided in Table 3-1.

Table 3-1: Summary of reagents

Chemical	Physical form	Purity/composition	Company
Cupric sulfate pentahydrate $\text{CuSO}_4 \cdot 5\text{H}_2\text{O}$	Blue powder	98%-102%	BDH
Lactic acid $\text{C}_3\text{H}_6\text{O}_3$	Clear viscous solution	85%-90%	VWR
Sodium hydroxide NaOH	White pellet	>97%	BDH
Zinc acetate dehydrate $(\text{CH}_3\text{CO}_2)_2\text{Zn} \cdot 2\text{H}_2\text{O}$	White powder	98%	ACROS Organics
Potassium hydroxide KOH	White powder	>85%	BDH
Reagent alcohol (90% ethanol)	Clear solution	Ethanol (88 to 91%) Methanol (4.0 to 5.0%) Isopropanol (4.5 to 5.5%)	Fisher Chemical
Zinc oxide powder ZnO	White powder, average particle size ~120nm, surface area ~9m ² /g	99.9%	ZoChem
Zinc nitrate hexahydrate $\text{Zn}(\text{NO}_3)_2 \cdot 6\text{H}_2\text{O}$	White powder	98%	ACROS Organics
Hexamethylenetetramine (HMTA) $\text{C}_6\text{H}_{12}\text{N}_4$	White powder	98.5%	ACROS Organics
Nitric acid HNO_3	Clear viscous solution	70% (1.0M solution is used in experiments)	BDH

3.1.2 Fluorine-doped tin oxide (FTO)

In a photovoltaic device, one or both electrode must have high transparency in order for the light irradiation to reach the active layer. Common transparent conducting thin films used in photovoltaic applications include oxides and organic materials such as carbon nanotubes and PEDOT. In this study, all solar cells are fabricated using FTO-coated glass slides as the substrate and anode. Compared with the more common indium-doped tin oxide (ITO), FTO thin films are much cheaper and can be heated up to over 400°C without significant loss of conductivity. It should also be noted that FTO is an inherently n-type oxide, but it has been shown to have a high work function of ~5.0 eV, which makes it suitable as anode material in a photovoltaic device [174].

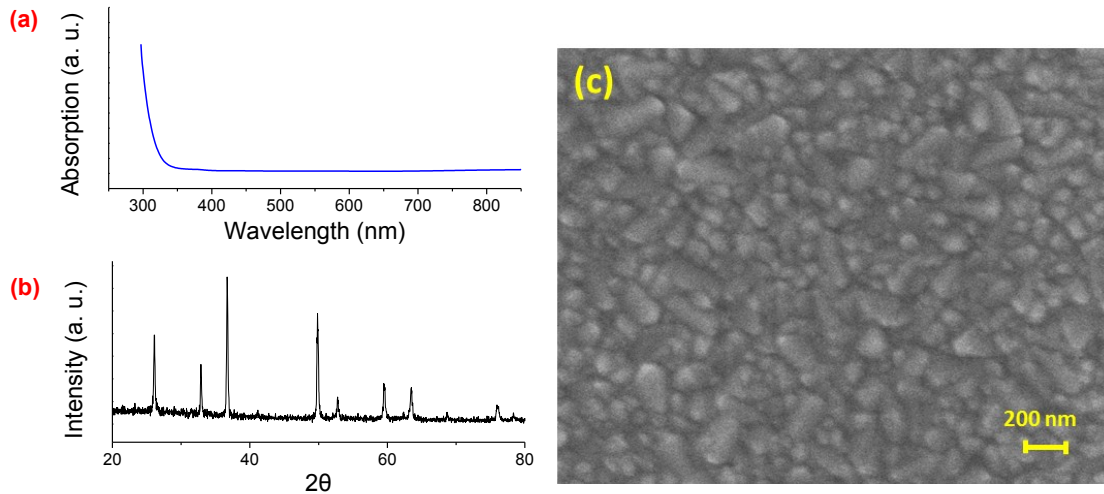


Figure 3-1: Properties of a FTO-coated glass substrate: (a) UV-visible light absorption profile, (b) X-ray diffraction profile, (c) surface morphology.

FTO glass slides (TEC15 glass, 100mm x 100mm x 2.2mm) with surface resistivity ~ 15 Ω /sq have been purchased from Dyesol Company. For thin film deposition as well as device fabrication, the glass slides are cut into small ~3 cm x 1 cm pieces. The UV-visible light absorption profile, X-ray diffraction (XRD) profile and surface morphology of a typical FTO substrate are presented in Figure 3-1. The absorption in the substrate is minimal in the visible range as shown in Figure 3-1a. No overlaying peaks are found with Cu_2O and ZnO in the XRD profile (Figure 3-1b). Scanning electron microscopy (SEM)

reveals the size of the FTO particles making up the substrate are between ~50 nm and ~200 nm (Figure 3-1c).

3.2 Deposition Techniques

3.2.1 Electrochemical experiments

All electrochemical experiments in this study including electrodeposition and voltammetry are performed in a standard 3-electrode setup. Each of the electrodes used for the experiments is inserted through one of the ports in a 3-neck flask. For experiments performed at elevated temperature, the temperature is maintained using a silicone oil bath. The FTO-glass substrate is connected to the working electrode using a modified alligator clip to ensure good contact between the wire lead and conductive surface and partially submerged in the electrolyte during deposition. The exact area for deposition is measured afterward and is usually ~1.5 cm². A graphite rod is used as the counter electrode and immersed in the electrolyte to provide at least ~3.5 cm² active surface area during the electrochemical process. A saturated calomel electrode (SCE) is used as the reference electrode. Prior to the experiments, each FTO-glass substrate is cleaned by ultrasonication sequentially in isopropanol, DI water and acetone. Electrochemical experiments are performed using a potentiostat (EPP-4000, Princeton Applied Research). The applied voltage/current or waveform is defined using software provided with the unit. The potential, current and total charge transferred during each experiment is also measured/controlled by the potentiostat. For linear scan voltammetry and cyclic voltammetry, the scan rate is kept at 20 mV/s for all experiments.

The mass of Cu₂O deposited during electrochemical deposition is estimated using Faraday's Law of electrolysis:

$$m = \left(\frac{Q}{F}\right) \left(\frac{M}{z}\right) \quad (3-1)$$

where m is the deposited mass, Q is the total electric charge transferred during the experiment, F is the Faraday constant, M is the molar mass of Cu₂O, and z is the number of electrons transferred during the

redox reaction ($z = 1$ for Cu_2O electrodeposition according to Eq. 2-8). The calculated mass from Faraday's Law can be compared to the actual mass of deposition obtained by measuring the initial and final mass of the substrate. The difference in these two measures of mass provides some insights on the deposition process such as the current efficiency for Cu_2O deposition and whether any dissolution occurs. Assuming that no side reaction or dissolution occurs, the mole fraction x of copper that is present as metallic Cu in the electrodeposit can be estimated by:

$$m_{actual} = \left(\frac{Q}{F}\right) \left[\frac{x}{1+x} M_{Cu} + \frac{1-x}{1+x} \left(M_{Cu} + \frac{1}{2} M_O \right) \right] \quad (3-2)$$

where M_{Cu} and M_O are the molar masses of Cu and O atoms, respectively, and m_{actual} is the deposited mass calculated from the difference between the initial and final masses of the working electrode.

3.2.2 Sputtering of Al-doped tin oxide (AZO)

For device fabrication (Chapters 5 and 6), AZO is deposited on top of a Cu_2O thin film by radio-frequency (RF) sputtering to serve as both the n-type material and transparent cathode in the solar cells. Sputtering is a physical vapor deposition technique that involves bombarding the target (AZO powder) in an inert atmosphere with a high energy ion beam. The material to be deposited is then ejected from the target surface and coated onto the substrate. The electrical and optical properties of the resulting AZO film are heavily influenced by the sputtering conditions such as Ar gas flow rate, process pressure and temperature. For this study, a process pressure of 5×10^{-3} Torr and an Ar flowrate of 15 sccm are used with a plasma power of 80W and the substrate is placed ~ 8.5 cm away from the target.

The temperature used during AZO sputtering is one of the critical parameters for device fabrication since it affects both AZO and Cu_2O film properties. As the temperature increases, the sputtered AZO films become more crystalline and so become more highly conducting [175]. On the other hand, the resistivity of the Cu_2O layer rises when the film is heated to 150°C or above [176]. The optimal temperature is therefore determined from a trade-off between these AZO and Cu_2O properties. For this study, a target temperature of 250°C (corresponding to a substrate temperature of $\sim 150\text{-}200^\circ\text{C}$) is selected

for all AZO sputtering experiments based on a previous report on the fabrication of a device with similar architecture [74]. The sheet resistance of a ~250 nm AZO thin film on glass is measured to be 150 Ω /sq. The sheet resistance may be higher for a rough thin film deposited onto Cu₂O due to unevenness of the AZO film, as discussed later in Chapter 5.

3.2.3 Thermal evaporation

Aluminium thin films are deposited by thermal evaporation on top of FTO as the electrodes to improve probe contact. Aluminium is also deposited on top of AZO thin films as the top contact for some back-illuminated devices, as discussed in Section 5.4.4. In addition, both gold and aluminium have been used as top contact for measurement of charge carrier concentration and mobility (Section 3.3.2).

During thermal evaporation, metal pellets are placed in high-resistance tungsten boats which heat up when a large current is applied. The generated heat evaporates the pellets which then deposits onto the sample surface. A high vacuum in both the evaporation and substrate chambers is required to deposit uncontaminated thin films.

In this study, the evaporation pressure is held at $2 \times 10^{-6} \sim 5 \times 10^{-6}$ Torr for Al deposition, and 5×10^{-5} for Au deposition. The deposition rate is maintained at 2 -3 $\text{\AA}/\text{s}$ for Al and $\sim 0.7 \text{\AA}/\text{s}$, in order to obtain the best film quality.

3.3 Characterization Techniques

3.3.1 Film Morphology and Orientation

Scanning electron microscopy (SEM)

In this study, the morphology of the thin films is examined using a model LEO 1550 field-emission scanning electron microscopy (FE-SEM). SEM provides information on the surface characteristics of a sample in the form of high resolution images. Compared to optical microscopes, electron microscopes can

achieve much higher spatial resolution and depth of focus because of the much shorter wavelength of an electron beam than that of visible light to probe the surface.

The operation of SEM involves the projection of a focused electron beam onto the surface of the sample. The electron beam is scanned on the sample by varying the current through the raster scanners. For each point of the sample surface, the intensities of the secondary and backscattered electrons reaching the detectors are measured. These data are then converted into optical intensities that can be viewed on the display screen. Non-conductive samples (including semiconductors) must be pre-coated with a thin conductive layer before viewing in order to prevent sample charging by the electron beam. In this project, oxide samples are sputtered with approximately 10 nm of gold before the SEM analysis. Some images have been post-processed for presentation purposes, but no further modifications of the presented figures have been made beyond adjustment of image brightness and contrast.

Atomic Force Microscopy (AFM)

In addition to SEM, atomic force microscopy (AFM) is also used in some cases for surface morphology characterization. In particular, the information gathered from AFM analysis is used to estimate the surface roughness. Similar to SEM in which an electron beam is used to scan a sample, AFM uses a nanoscale cantilever for the same purpose. The cantilever which is made to vibrate close to its resonant frequency by an alternating current (AC) is moved to a given location on the substrate surface and allowed to approach the surface using a micro-positioner. The interaction between the cantilever tip and surface causes a change in the vibration frequency and amplitude of the cantilever that is detected by a laser beam. The distance between the tip and the surface is then adjusted to maintain the vibration frequency fixed and the adjusted distance is recorded as the height at the corresponding position. Once this height is determined, the cantilever is moved to an adjacent location and the process is repeated. A map of the sample roughness can then be obtained by rastering the cantilever tip across a portion of the surface.

X-ray diffraction (XRD)

Since the electrical properties of semiconductor oxides are highly dependent on their crystallinity, photovoltaic devices must be fabricated using metal oxides with preferred crystalline structure. In this project, the crystalline orientations of oxide films are determined using XRD (D8 Discover Diffractometer System). XRD is an analytical technique most commonly used to identify the crystal structure of a material. The sample being analyzed can be in the form of a fine powder or a thin film.

During XRD characterization, a monochromatic X-ray beam is directed onto the sample where it is diffracted by the sample depending on its crystal lattice spacing. The sample is scanned with X-rays over a range of incident angles in order to attain all possible diffraction directions of the crystalline lattice. When conditions satisfy Bragg's Law (which relates the incident wavelength to the diffraction angle and the lattice spacing in the sample), the X-rays leaving the sample after diffraction interfere constructively and can be detected and counted. Diffraction peaks are observed at incident angles that are unique to each crystalline material and so serve as a fingerprint for that material. The identity of the crystalline compound can be obtained by comparison with information provided in reference data bases.

Note that the XRD equipment used in this project is not calibrated for thin film measurements. Consequently, the resulting spectra are usually offset by a small amount depending on the thickness of the substrate. Therefore, the data are further adjusted by shifting each spectrum so that the peak positions for Cu_2O and ZnO match the accepted angles for these compounds reported in the literature. This adjustment has already been made to all XRD profiles presented in the following chapters.

3.3.2 Electrical and Optical Properties

UV-visible absorption (UV-vis)

Measurement of UV-visible absorption spectra is used to determine the efficiency of light absorption in semiconductors and the bandgap of Cu_2O films in this study. The UV-visible absorption measurements are performed using a Thermo Scientific GENESYS 20 Spectrophotometer.

A spectrophotometer consists of a spectrometer to produce light of any selected wavelength and a photometer to measure light intensity. When a light beam strikes a surface, it may be reflected, transmitted, diffused, absorbed, refracted or polarized. In the case of a solid semiconductor, most of the incident light is absorbed, reflected or transmitted. The absorbance of monochromatic light is calculated from the difference between the intensity of the incident light and that of the reflected and transmitted light measured as described below:

$$Abs = 100\% - \%Reflectance - \%Transmittance \quad (3-3)$$

The absorption spectrum is constructed by tabulating the result over a range of wavelengths generated sequentially by the spectrometer.

For the measurement of transmittance, the sample is positioned between the incident light beam and the photometer which measures the amount of light that passes through the sample. The % transmittance is then obtained by dividing the transmitted intensity by the incident intensity. When the incident beam reaches the sample, the beams reflected by the sample in all directions strike the internal reflective surface of the sphere before reaching the detectors at the centre of the sphere.

The bandgap of the thin films is estimated using a Tauc plot. It was originally introduced to estimate the bandgap of amorphous materials [177] although it has also been successfully applied to crystalline materials with high accuracy [178]. Typically, a Tauc plot shows the relationship between absorbance and the photon energy which can be described in terms of the following semi-empirical expression:

$$(\alpha h\nu)^{1/r} = B(h\nu - E_g) \quad (3-4)$$

where:

h = Planck's constant

v = photon frequency

α = absorption coefficient

E_g = optical band gap

B = proportionality constant

The value of the exponent r can be 0.5, 1.5, 2, or 3 depending on the nature of the electronic transition [179]. For Cu_2O , r is taken to be 1.5 indicating a direct forbidden transition. For bandgap calculation, a plot of $(\alpha h\nu)^{1/r}$ versus photon energy ($h\nu$) is drawn based on the absorption data. The linear portion of the plot is then extrapolated and the bandgap E_g is estimated from the x-intercept.

Cyclic voltammetry (CV)

The Tauc plots do not provide information on the specific energy levels of the valence and conduction bands in a semiconductor. However, these energy levels can be estimated using cyclic voltammetry (CV). The transfer of electrons to the conduction band is registered as a reduction process in a voltammogram. Similarly, the removal of electrons from the valence band appears as an oxidation process. The oxidation and reduction peaks identified during the CV process can be correlated to the energy levels of the valence and conduction band of the semiconductor according to the following relations [180]:

$$E_v = -e(E_{oxidation} + 4.4) \quad (3-5)$$

$$E_c = -e(E_{reduction} + 4.4) \quad (3-6)$$

where e is the elemental charge, E_v and E_c are the electrochemical valence and conduction band levels, respectively, and $E_{oxidation}$ and $E_{reduction}$ correspond to the potentials of the oxidation and reduction peaks (or onset) identified from the cyclic voltammogram.

During the excitation of an electron by photons, a strongly bound electron-hole pair is created by exciting an electron from the valence band to the conduction band, whereas during a CV measurement electrons are injected into (or removed from) the system. The bandgap determined from a CV is in general larger than the bandgap since extra energy is required to overcome the coulombic interaction in the system. In addition, the positions of the peaks do not correspond exactly with the band position since the measurement is performed in solution rather than in air, and other factors such as solvation energies also play an important role during the measurement. However, some information can still be gathered by comparing the band potentials between different samples that are measured under the same conditions. In

this study, the CV experiments for Cu₂O thin films are performed in a 3M lactic acid solution adjusted to pH 10.

Space-charge limited current (SCLC) method

For thin film samples, the charge carrier concentration and mobility are most commonly measured by making use of the Hall effect, which involves determination of the voltage drop across an electromagnetic field. However, in this study, since all Cu₂O thin films are deposited onto a conductive FTO substrate, they are very difficult to remove without damaging them. Multilayer models are available for the estimation of the carrier concentration (n_0) and mobility (μ) in similar cases although certain limitations on the sample thickness and surface conductivity of the substrate exist in order to obtain unbiased results [181]. Consequently, alternative techniques are employed in this study to measure n_0 and μ . The space-charge limited current (SCLC) method is one technique for the estimation of both the carrier concentration and mobility in p-type Cu₂O thin films.

In a semiconductor material, the SCLC phenomenon occurs when the number of injected charge carriers exceeds the defect concentration in the sample. At low applied voltage, the material exhibits ohmic behavior where the current changes linearly with the applied potential. At voltages where the number of injected charges becomes comparable to that of thermally excited ones, the semiconductor current-voltage characteristic changes from ohmic to SCLC. With a further increase in voltage, the trap-free regime appears since the number of injected charge carriers far exceeds that of thermally excited ones. In the SCLC regime, the thin film behavior follows the Mott-Gurney law where the current is proportional to the square of the applied voltage [182]:

$$J = \frac{9\varepsilon\mu}{8d^3} V^2 \quad (3-7)$$

where:

ε = permittivity

μ = charge carrier mobility

d = film thickness

This permits the carrier mobility to be estimated from the linear portion of a J vs V^2 plot. The charge carrier density is estimated using the voltage at which the film behavior enters the SCLC regime under the assumption that it is similar in quantity to the defect density:

$$V_{SCLC} = \frac{en_0d^2}{\epsilon} \quad (3-8)$$

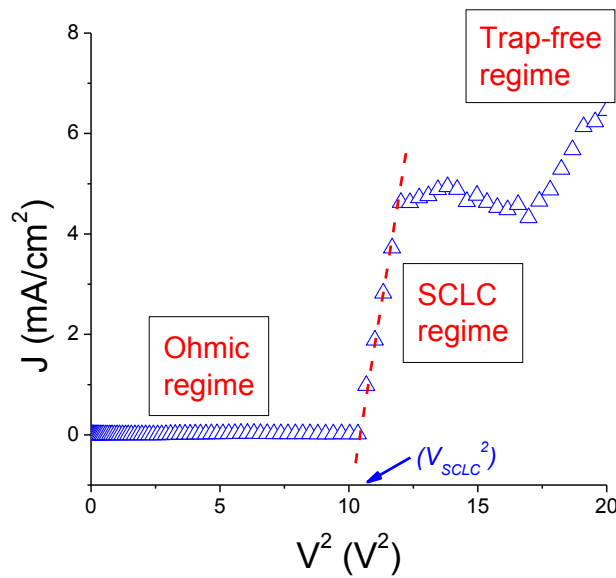


Figure 3-2: Typical plot of J vs V^2 for a Cu₂O thin film.

A typical plot of J vs V^2 used for the above calculations in this study is shown in Figure 3-2 obtained for a Cu₂O thin film sandwiched between FTO substrate and $\sim 1 \text{ mm}^2$ Al contacts.

This method for carrier concentration and mobility is typically used for organic material with thickness in the nanometer range. It has been demonstrated in previous literature that the SCLC behavior may deviate from the Mott-Gurney model for thicker oxide films [183], thus making the method less accurate for oxide semiconductors such as Cu₂O. On the other hand, previously reported SCLC results for sputtered CuO thin films show good agreement with the Hall effect [182], indicating that the method is still relatively reliable for the purpose of this study.

For this study, SCLC measurements are performed with either Al or Au as the top contact for the Cu₂O thin films deposited on FTO-glass substrate. With FTO/Cu₂O/Au structure, it is assumed that electron injection into the thin film is prevented by the high work function of Au contact, making holes the only type of charge carrier present in the system during measurement. Therefore, the carrier mobility obtained using Eq. 3-7 is an estimation of the hole mobility in the system. On the other hand, since Al has a much lower work function, both electrons and holes are being injected into the thin film with an FTO/Cu₂O/Al structure. When the J-V characteristics are located in the SCLC regime where contribution of intrinsic conductivity is negligible, one type of charge carrier would be dominant over the other in the bulk of the thin film [184]. Charge carriers with higher mobility are more likely to move a longer distance into the film before recombination. As such, recombination tends to occur in regions close to the injection layer of the lower-mobility charge carrier, and the SCLC mobility obtained in this case will reflect the mobility of the high-mobility species. A comparison between the results obtained using Al and Au contact would determine which species is being measured.

Secondary ions mass spectroscopy (SIMS)

The secondary ions mass spectroscopy (SIMS) is a technique that identifies the type and amount of different elements on the surface of a thin film sample and is typically used for the measurement of doping levels. This technique is highly sensitive and can detect elemental surface concentrations as low as ppm levels. During a SIMS measurement, an internally generated beam of either positive or negative ions (primary ion beam) is focused on the sample surface. This provides enough energy to slowly sputter away the surface and ionize the ejected species (secondary ions) which are then transferred across a high electric field to a mass spectrometer for collection according to their mass-to-charge ratio. In the time-of-flight (TOF) SIMS experiment, this process is continued to sputter as much as 10 μm of the surface and thus provide an elemental composition depth profile of the film.

In this study, SIMS (IonTOF SIMS-5) is used to obtain information on the defect concentration in the Cu₂O thin films using a Cs⁺ primary ion beam (1 keV) and ~350 μm² sputtering area. A depth of ~300 nm is analyzed to ensure that the portion of the film below the oxidized layer is sampled and characterized. The hole concentrations of different samples are compared based on the ratio of the Cu and O intensities since a sample with a higher hole concentration should have more Cu vacancies and a lower Cu:O ratio.

3.3.3 Photovoltaic Properties

For the measurement of solar cell performance, a solar simulator (ABET Sun 3000 Class AAA) with a Xe arc lamp is used to provide global AM1.5 simulated solar radiation (1000mW/cm²). The light intensity is calibrated by using a Si reference cell with PCE ~ 3.3%. A multimeter is connected to the system to provide a bias for the device and the current-voltage characteristics are recorded using measurement software. The device performance parameters (J_{SC} , V_{OC} , FF, PCE, R_{sh} , and R_s) as discussed in Section 2.1 are calculated automatically by the software.

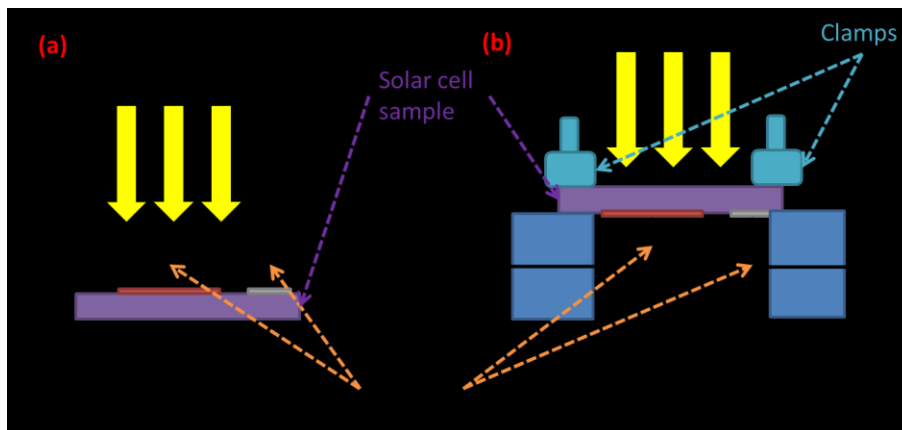


Figure 3-3: Solar cell characterization setup: (a) front illumination, (b) back illumination.

During measurement, probe needles connect the multimeter to the anode and cathode of the solar cell. Depending on the direction of illumination (discussed in more detail in Chapter 5), the samples are placed differently on the test stage to ensure that the active cell area is fully illuminated and the probes properly contact the electrodes, as illustrated in Figure 3-4. For each testing configuration, the illumination intensity is calibrated with the reference cell placed at the same height of the sample.

Chapter 4. Potentiostatic DC Deposition of Cu₂O

4.1 Introduction

The majority of studies concerning the electrodeposition of Cu₂O for photovoltaic applications have involved direct current (DC) potentiostatic electrodeposition which often enables good control of deposit morphology and properties. The purpose of this chapter is to study the effect of different electrodeposition parameters on film morphology during Cu₂O electrodeposition using constant applied potential in a typical copper-lactate electrolyte. Attention is paid to possible mechanisms controlling Cu₂O morphology and crystal orientation formation mechanisms.

A portion of the results presented in this chapter (Figures 4-4 b-e, 4-11) are adapted from published work [185].

4.2 Experimental details

The electrodeposition of Cu₂O is performed on an FTO-coated glass substrate using a standard three-electrode setup, as described in Section 3.2.1. The electrodeposition of Cu₂O is conducted in a typical Cu-lactate system discussed in Section 2.3.2. The electrolyte composition is varied over the range 0.1M – 0.4M CuSO₄ and 1.9M – 4.5M lactic acid, with pH adjusted to values between 8.5 and 13.7 using NaOH pellets. All deposition experiments are carried out at a temperature between 45°C and 85°C. LSV is conducted at each electrolyte concentration and temperature to determine the range of potentials where Cu₂O forms. The deposition time is kept at 15 minutes unless otherwise specified. The current transients are recorded during electrodeposition. All potentials are reported with reference to the SCE scale.

After deposition, the samples are rinsed with DI water and dried in air. The mass of each deposited film is calculated using Faraday's Law from the total charge measured during electrodeposition and compared with their net weight measured directly at the end of the experiment. Film thickness is estimated using deposit mass and area as measured after electrodeposition assuming 100% current

efficiency. The samples are examined by XRD measurement to characterize the growth orientations of the Cu_2O films. The morphology of the samples is examined using SEM.

4.3 Morphology of electrodeposited Cu_2O

4.3.1 XRD

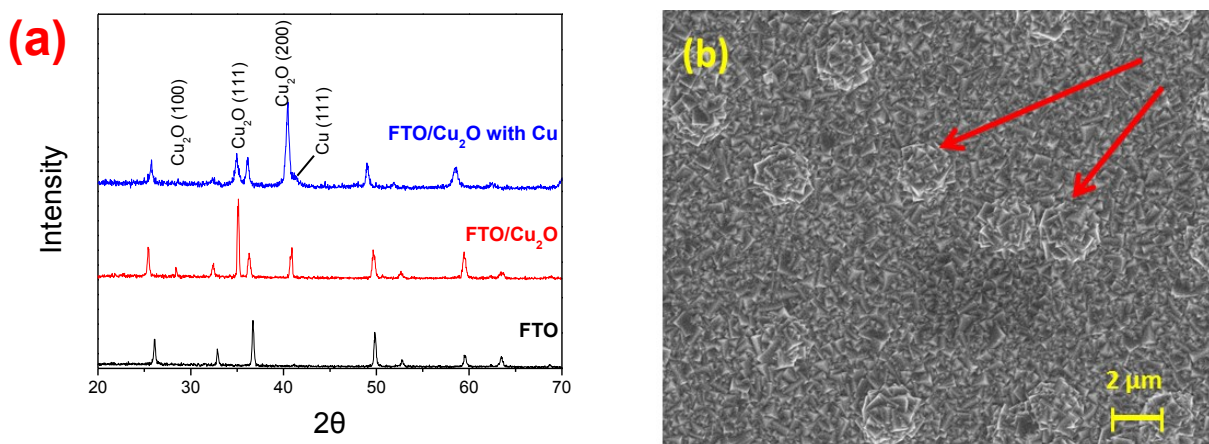


Figure 4-1: (a) X-ray diffraction profile of typical electrodeposited Cu_2O films electrodeposited on FTO-glass substrate. The top spectrum shows a Cu_2O film containing a small amount of Cu. The middle spectrum shows a Cu_2O film with no significant Cu formation. The bottom spectrum shows the profile of the FTO glass slide used as substrates for all experiments in this work. (b) SEM image of a typical Cu_2O thin film containing clusters of Cu (indicated by arrows).

Figure 4-1a presents the typical XRD patterns of Cu_2O thin films electrodeposited on FTO obtained for samples discussed in Chapters 4 through 7. For most of the samples obtained in this work, XRD analysis yields spectra similar to the middle one shown above, in which no peaks corresponding to CuO or Cu are observed. On the other hand, in some cases, a small peak corresponding to Cu (111) phase is observed (top spectrum in Figure 4-1). A Cu peak can only be observed in an XRD profile when the amount in the film is significant (typically ~ 2 wt% for powdered samples). Indirect evidence of Cu formation is also observed in SEM images in the form of micron-sized clusters on the surface of the Cu_2O thin films, as reported in previous literature [90]. An example from our study is presented in (Figure 4-1b). Interestingly, such clusters appear even when the amount of Cu formed is less than 2 wt%. The

appearance of these clusters in SEM images is taken as the primary indication of Cu formation in this work.

Furthermore, three major Cu_2O peaks corresponding to the crystallographic orientations (100), (111) and (200) can be observed in the XRD patterns. Among the three major peaks, the (100) peak is always noticeably smaller than the other two, whereas the intensities of (111) and (200) peaks vary depending on the conditions applied. The ratio of the intensities of the (111) and (200) peaks can therefore be used to estimate the relative growth rates in these directions during Cu_2O electrodeposition. As powdered Cu_2O samples usually exhibit a (111):(200) peak intensity ratio of ~ 3 based on previous reports [162], we consider samples with a measured peak ratio between 1 and 6 to have mixed $\langle 111 \rangle$ and $\langle 100 \rangle$ orientations.

4.3.2 Linear sweep voltammetry (LSV)

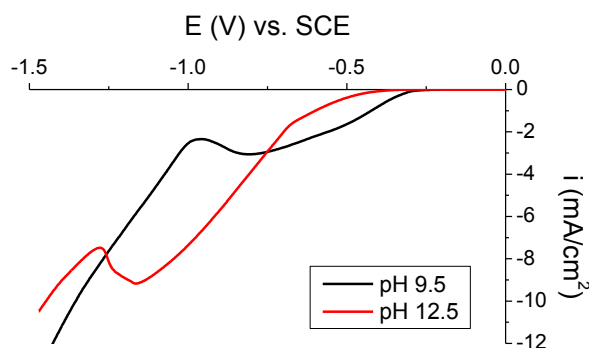


Figure 4-2: Linear sweep voltammetry curves obtained on FTO-coated glass substrates immersed in 0.2M CuSO_4 -3M lactic acid solutions at pH 9.5 and 12.5 and 60°C.

Linear sweep voltammetry (LSV) has been conducted at all electrolyte compositions and temperatures investigated in this chapter in order to determine the deposition window for Cu_2O . Figure 4-2 shows LSV obtained at 60°C in electrolyte solutions containing 0.2M CuSO_4 and 3M lactic acid at pH values of 9.1 and 12.5. The shapes of the LSV curves shown in the figure are typical for the conditions investigated in this work and consistent with those previously reported in similar electrolytes [90,147,154]. The lower potential limit for Cu_2O formation is obtained from the peak positions in the LSVs (-0.82 V at pH 9.5, -1.16 V at pH 12.5), whereas the upper limit is taken to be the onset of cathodic current in these curves (-

0.25 V at pH 9.5, -0.33 V at pH 12.5). Similarly, LSV is also performed for other electrolytes and temperature, and the range of applied potentials in which Cu₂O deposition occurs is plotted in Figure 4-3 (between red and black lines) for the various conditions investigated.

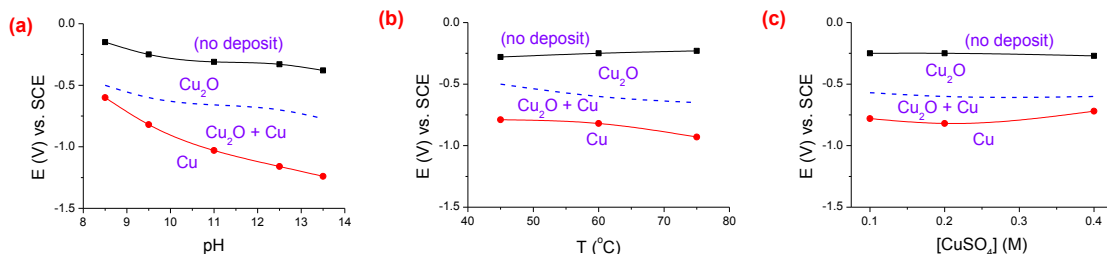


Figure 4-3: Applied potential range for Cu₂O deposition as functions of: (a) pH (0.2 M CuSO₄+3 M lactic acid, 60°C), (b) temperature (0.2 M CuSO₄+3 M lactic acid, pH 9.5), and (c) [CuSO₄] (CuSO₄+3 M lactic acid, pH 9.5, 60°C). Dashed line indicates the minimum cathodic potential required for Cu formation.

Cu formation occurs at a potential more positive than the lower limits above for Cu₂O formation, as observed in the XRD and SEM data, which indicates that a mixture of Cu₂O and Cu may be formed within the estimated deposition window. The most positive potentials at which Cu formation are obtained on the basis of the SEM images and are shown as the dashed lines in Figure 4-3. In order to ensure that Cu forms during Cu₂O electrodeposition, the applied potentials used to produce the Cu₂O films in this study are always maintained between the dashed lines and the upper limits shown in Figure 4-3.

The effects of pH, temperature and [CuSO₄] on the potential range for Cu₂O electrodeposition in the CuSO₄-lactate acid system are shown in Figure 4-3. As the electrolyte pH increases, the potential range shifts in the negative direction (Figure 4-3a). The potential range becomes wider when either the deposition temperature (Figure 4-3b) or [CuSO₄] (Figure 4-3c) increases, although the effect of the latter does not appear to be very large.

4.3.3 Effect of applied potential

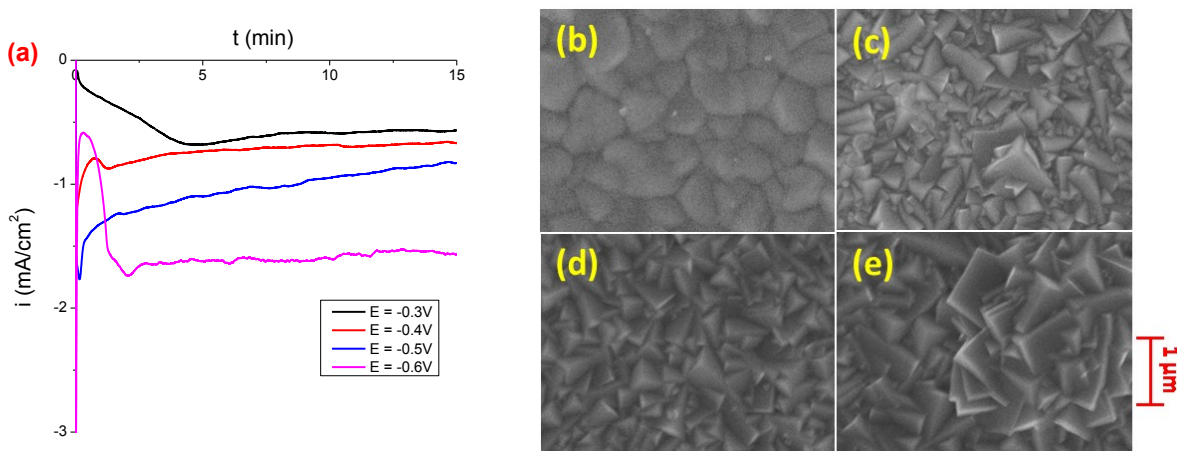


Figure 4-4: (a) Current transient curves and (b-e) SEM images of Cu₂O films electrodeposited at 60°C in electrolyte containing 0.2 M CuSO₄ and 3 M lactic acid adjusted to pH 9.5 at applied potentials of (b) -0.3V, (c) -0.4V, (d) -0.5V and (e) -0.6V vs. SCE.. All samples formed after 15 min deposition time.

The current transients and surface morphology of Cu₂O films electrodeposited at 60°C in electrolyte containing 0.2M CuSO₄ and 3M lactic acid adjusted to pH 9.5 at different applied potentials are shown in Figure 4-4. The overall shapes of the current transients appear similar during deposition at applied potentials from -0.4V to -0.6V (Figures 4-4 a). The current density dips to a minimum within the first minute before rising to a small peak between 1 and 2 minutes. Thereafter, the current either quickly levels off to a steady state value (at -0.6 V) or gradually decreases toward a steady state value over the remaining 13-14 minutes. Both the peak and steady state current densities increase as the potential becomes more cathodic, indicating a faster deposition rate. Well defined cubic particles make up the deposits formed at -0.4, -0.5 and -0.6 V (Figures 4-4 c-e), which are commonly observed in Cu₂O films electrodeposited under similar conditions [90,156,160]. The coatings deposited at -0.4 V and -0.5 V are relatively uniform, whereas clusters of cubic particles with diameters up to a few microns are formed on the film obtained at -0.6 V. As shown earlier in Figure 4-3a, an applied potential of -0.6 V is beyond the potential range for pure Cu₂O formation in pH 9.5 electrolyte and the appearance of these clusters signify the beginning of the formation of Cu metals [90].

On the other hand, at a lower cathodic potential of -0.3V , the peak current density is not observed until ~ 5 minutes after the process begins and levels off to the steady state value soon afterward (Figure 4-4a). The steady state current is lower than that obtained at the more cathodic potentials. In contrast to the cubic grains observed in the other samples, the Cu_2O film formed at -0.3V contains irregularly shaped grains with more rounded features and no sharp angles after 15 minutes of deposition (Figure 4-4b). From these observations, it appears that the formation of cubic grains is promoted as the potential becomes more cathodic. This observation is consistent with those of previous studies on Cu_2O deposition at pH 9 under galvanostatic or potentiostatic conditions which showed the shift in morphology from octahedral to cubic as the applied current or overpotential is increased [147,155,158].

4.3.4 Effect of Temperature

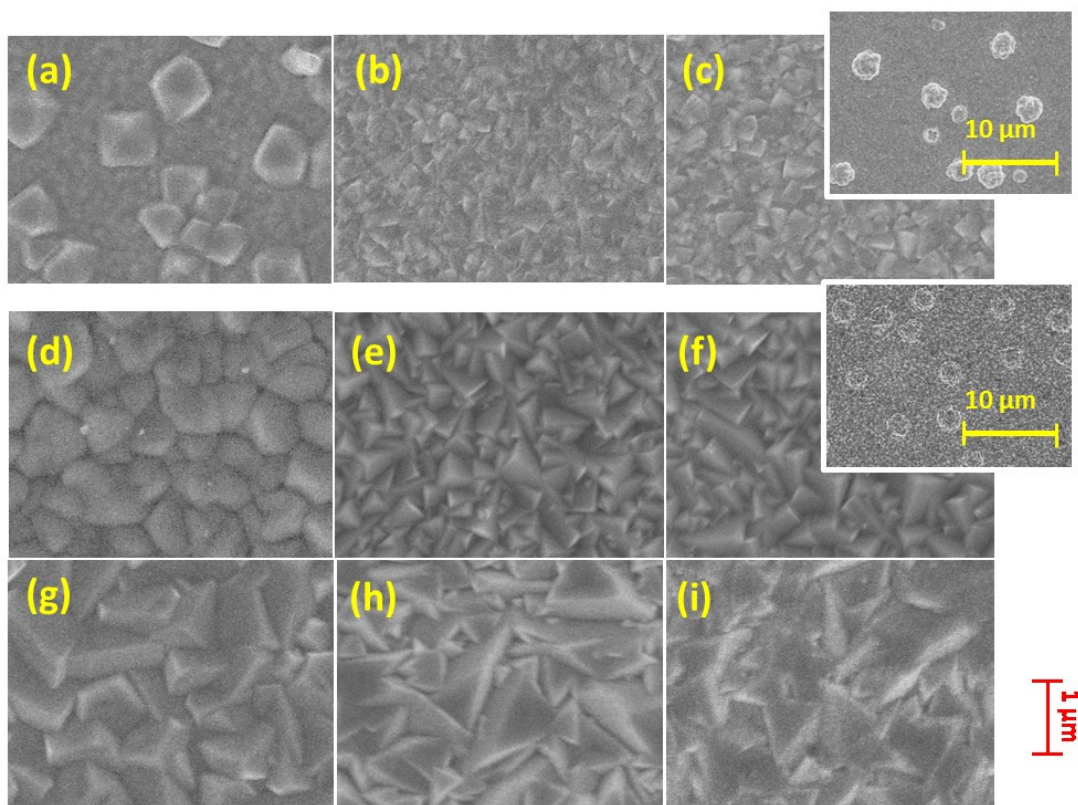


Figure 4-5: SEM images of Cu_2O films deposited from $0.2\text{ M CuSO}_4 + 3\text{ M}$ lactic acid adjusted to pH 9.5 at different temperatures and cathodic potentials: (a-c) 45°C and $-0.3, -0.5, -0.6\text{V}$; (d-f) 60°C and $-0.3, -0.5, -0.6\text{V}$; (g-i) 75°C and $-0.3, -0.5, -0.6\text{V}$. Deposition time is 15 min in all cases.

Figure 4-5 shows the effect of deposition temperature on Cu_2O film morphology in an electrolyte containing 0.2M CuSO_4 and 3M lactic acid adjusted to pH 9.5 at different applied potentials. In general, the deposition rate and Cu_2O grain size increase with temperature, in agreement with previous reports on both potentiostatic and galvanostatic deposition from Cu-lactate electrolytes with similar compositions [156,159].

It is also evident that the deposition temperature has a large effect on grain shape. At an applied potential of -0.5V or -0.6V, the grains appear as irregular polyhedrons with no well-defined shapes at 45°C, cubic grains at 60°C and truncated cubes at 75°C. The formation of regular and truncated cubic grains suggests a preferred growth orientation of $\langle 111 \rangle$, as confirmed by the XRD results shown in Figure 4-6. Furthermore, this orientation becomes increasingly favoured as the temperature is raised. It is worth noting that some Cu forms at -0.6V in both the 45°C and 60°C electrolytes (insets), but not at 75°C. This indicates that a rise in deposition temperature promotes the formation of Cu_2O over Cu. On the other hand, at a low cathodic potential of -0.3V, well-defined octahedral grains are observed at a deposition temperature of 45°C, indicating a preferred growth in the $\langle 100 \rangle$ direction. As the temperature increases, the grains become more irregular and no clear orientation can be determined from the shape of the Cu_2O grains. XRD results reveal that the (200) peak intensity drops dramatically when deposition is conducted at -0.3V and 75°C (Figure 4-6).

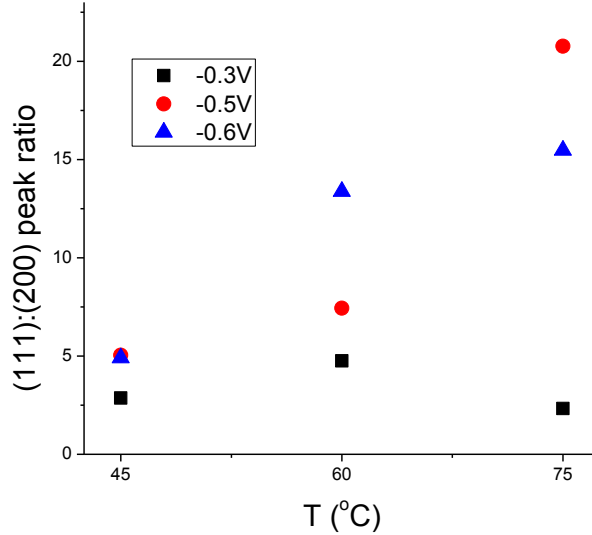


Figure 4-6: Effect of deposition temperature on (111):(200) peak intensity ratio from the XRD patterns of Cu_2O films obtained by deposition on FTO-glass substrate at 60°C Cu_2O films deposited from 0.2 M CuSO_4 + 3 M lactic acid electrolyte adjusted to pH 9.5.

4.3.5 Effect of CuSO_4 concentration

The effect of CuSO_4 concentration on Cu_2O film morphology in an electrolyte containing 3M lactic acid adjusted to pH 9.5 at different applied potentials is shown in Figure 4-7. Note that Cu clusters are observed at -0.6V in the 0.1M and 0.2M electrolytes as shown in the inset of Figures 4-7 c and f, whereas pure Cu_2O formed at 0.4M.

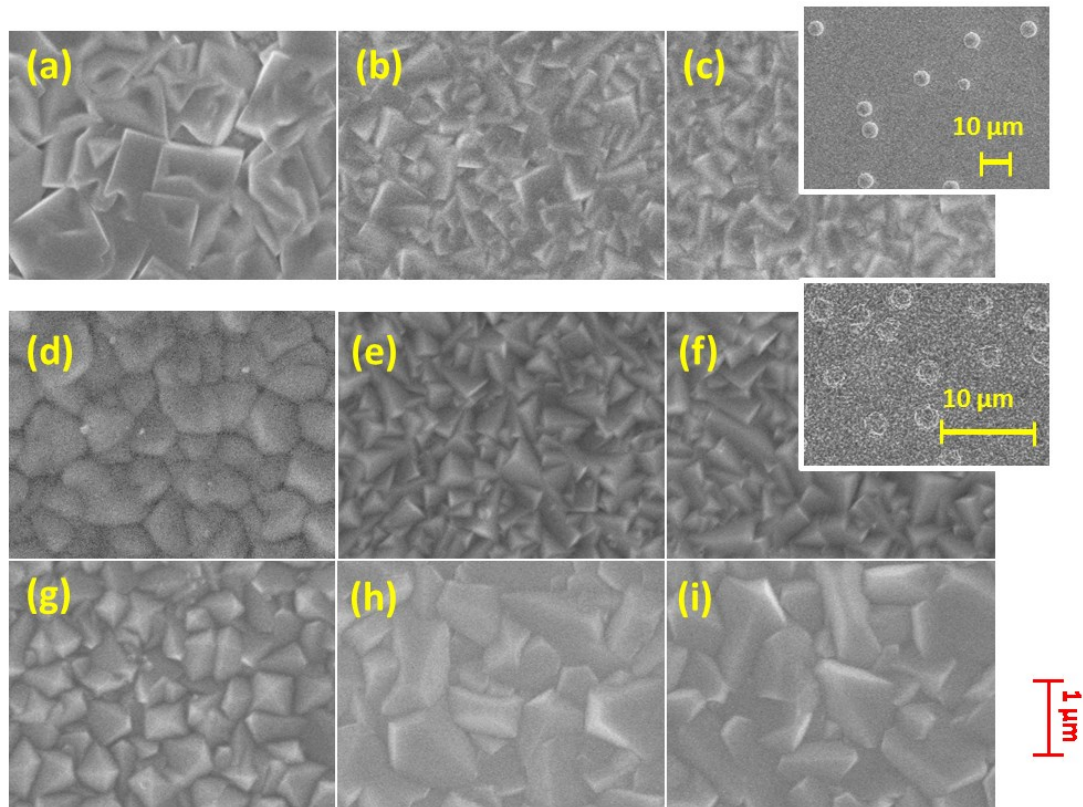


Figure 4-7: SEM images of Cu_2O films deposited in $\text{CuSO}_4 + 3 \text{ M}$ lactic acid adjusted to pH 9.5 at 60°C : (a-c) 0.1 M CuSO_4 at -0.3, -0.5, -0.6V; (d-f) 0.2 M CuSO_4 at -0.3, -0.5, -0.6V; (g-i) 0.4 M CuSO_4 at -0.3, -0.5, -0.6V. Deposition time is 15 min in all cases.

Similar to the effect of temperature, the effect of CuSO_4 concentration is different at -0.3V than at the more cathodic potentials. At -0.5V and -0.6 V, the grains change from cubic shapes to irregular polyhedra as the bulk CuSO_4 concentration increases from 0.1M to 0.4M. However, XRD results show that the films still have predominant $\langle 111 \rangle$ orientation (Figure 4-8) despite no longer exhibiting distinct cubic grains.

At -0.3V, the opposite trend appears to occur as the CuSO_4 concentration is increased from 0.2M to 0.4M. Whereas rounded grains with mixed orientation are formed in 0.2M solutions (Figure 4-7d), octahedral grains are observed at 0.4 M (Figure 4-7g). This indicates a transition to $\langle 100 \rangle$ rather than $\langle 111 \rangle$ orientation, as confirmed by comparison of their XRD peak intensities (Figure 4-8). On the other hand, when the concentration of Cu(II) is reduced to 0.1M, the morphology in the SEM image suggest that some dissolution of the grains occurs during deposition at an applied potential of -0.3V. Partial formation of cubic or octahedral grains is observed in Figure 4-7a, where the corners growing

perpendicular to the substrate appear to be etched off, leaving behind flat rectangular disks parallel to the surface. A comparison of the actual measured deposit mass with the amount expected based on the total charge passed during deposition shows that they do not differ significantly, indicating that either a dissolution process involving charge transfer occurs, or that the amount dissolved is not significant compared to deposit mass. Evidence of dissolution is also found at 0.2M CuSO_4 where the grains are noticeably more rounded than typical samples. The observation that dissolution would lead to more rounded deposit features is reasonable since it would be expected to occur preferentially at high energy sites such as edges and angles of a grain. The dissolution of Cu_2O during electrodeposition has not been reported previously in Cu-lactate systems.

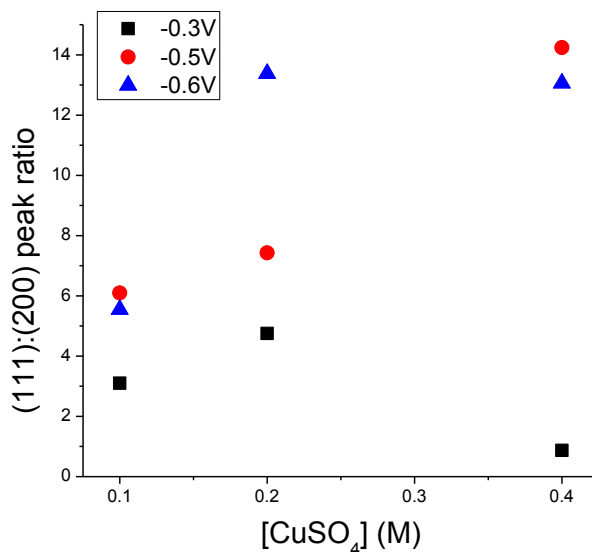


Figure 4-8: Effect of $[\text{CuSO}_4]$ on (111):(200) peak intensity ratio from the XRD patterns of Cu_2O films obtained by deposition on FTO-glass substrate at 60°C Cu_2O films deposited from M CuSO_4 + 3 M lactic acid electrolyte adjusted to pH 9.5.

4.3.6 Effect of pH

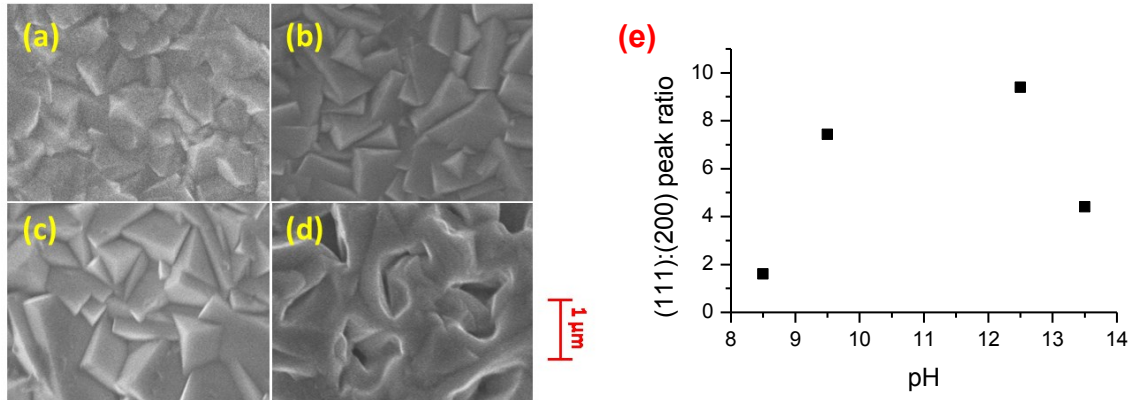


Figure 4-9: SEM images of Cu₂O films deposited at 60°C in 0.2 M CuSO₄ + 3 M lactic acid adjusted to different pH: (a) pH 8.5, -0.4V, 5.5 hours; (b) pH 9.5, -0.5V, 26 min; (c) pH 12.5, -0.6V, 35 min; (d) pH 13.5, -0.7V, 40 min. (e) Effect of pH on (111):(200) peak intensity ratio in the XRD patterns. All samples are ~2μm in thickness.

As shown from the LSV experiments, the deposition range for Cu₂O shifts in the negative direction as the pH increases (Figure 4-3a). Consequently, for each pH, a different applied potential is selected to be ~0.1V above the minimum cathodic potential for Cu formation.

Figure 4-9 presents SEM images of Cu₂O deposited at different pH values between 8.5 and 12.5 and the effect of pH on the I(111):I(200) ratio obtained from the XRD spectra of 2-micron Cu₂O films formed at different pH. At pH 8.5 (-0.4V), the grains are found to be irregular polyhedra with mixed orientations. At both pH 9.5 (-0.5V) and pH 12.5 (-0.6V), cubic grains growing predominantly in the <111> direction are formed. As shown in Figure 4-9e, <111>-oriented growth becomes increasingly dominant as the pH is raised up to ~ 12.5, as has been previously reported [147,149,157,159,160,162–165]. On the other hand, at pH 13.5 (-0.7V), so much dissolution of the grains appears to occur that a polyhedral grain structure is no longer evident. At the same time, the ratio of I(111):I(200) decreases and, in fact, exhibits no preferred orientation. To the best of our knowledge, this effect has not been reported to date possibly because deposition at pH 13.5 has not received much attention.

It is also worth noting that the actual mass of the deposit formed at pH 13.5 weighed directly is less than the mass expected from Faraday's Law assuming that the reduction of Cu(II) to Cu₂O is the only cathodic reaction occurring during the experiment, while the mass of the films produced at the other pH

values closely match the amount expected on the basis of the cathodic charge passed. This agrees well with the conclusion that a portion of the deposited oxide is being chemically dissolved during the electrodeposition process, from a mechanism that does not involve charge transfer, since this would lead to a lower final deposit mass on the substrate surface than the total amount formed by the cathodic reaction. The cause for this mismatch may also be due to a cathodic side reaction that forms a lower mass per charge transfer (such as the formation of Cu metal), although this possibility is less likely due to the fact that no evidence for the formation of metallic Cu or other materials is identified in either XRD or SEM result.

The Cu_2O films deposited at these pH are investigated in more detail in the following subsections.

pH 8.5

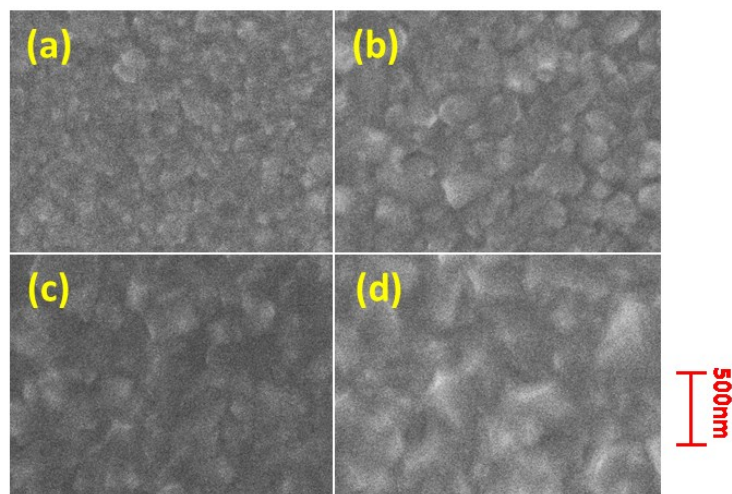


Figure 4-10: SEM images of Cu_2O films electrodeposited on FTO-glass substrate at 60°C for the following durations: (a) 3 min, (b) 10 min, (c) 20 min, (d) 60 min at an applied potential of -0.4V vs. SCE in electrolyte containing $0.2\text{ M CuSO}_4 - 3\text{ M}$ lactic acid adjusted to pH 8.5.

Figure 4-10 shows SEM images of Cu_2O films formed at an applied potential of -0.4 V vs. SCE in a $0.2\text{M CuSO}_4 - 3\text{M}$ lactic acid solution at pH 8.5 after different amounts of deposition time. The shape of the grains does not vary noticeably as deposition time increases. Irregular polyhedra are formed during the early stages of the deposition process, as shown in Figure 4-10a.

The average particle size is estimated to be less than 100 nm at 3 min and gradually grows to a few hundred nanometers after 1 hour. No preferred orientation can be clearly identified from the images, although XRD measurement shows a I(111)/I(200) peak ratio of 0.94 at 60 min deposition time, indicating a <100>-preferred growth. As shown in Figure 4-9e, the I(111)/I(200) peak ratio for a film formed over a longer deposition time of 5.5 hours, but under otherwise identical conditions, is found to be 1.61, which lies within the mixed-orientation regime. A comparison of the ratios suggests that the growth orientation at pH 8.5 gradually shifts towards <111> as the process continues.

It is also noted that the substrate is completely covered by Cu₂O after 1 minute of deposition (not included in the figures), at which point the calculated film thickness is less than 100nm. This suggests that Cu₂O nucleation is a relatively rapid process under this condition, despite the fact that the overall deposition rate is slow.

pH 9.5

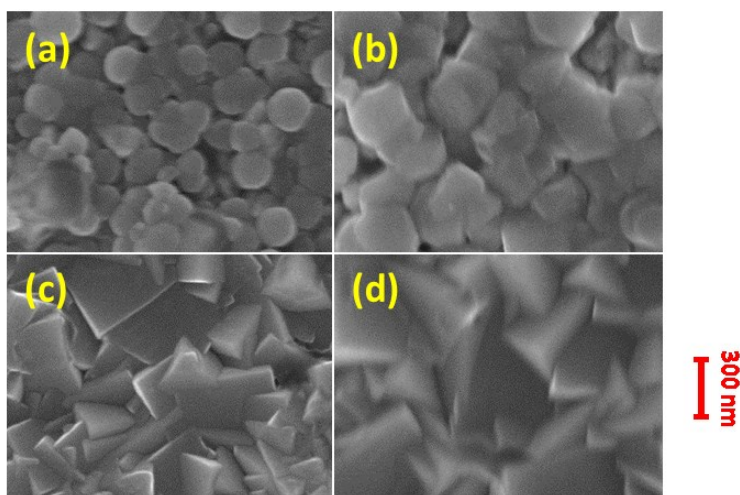


Figure 4-11: SEM images of Cu₂O films electrodeposited on FTO-glass substrate at 60°C for the following durations: (a) 1 min, (b) 3 min, (c) 5 min, (d) 10 min at an applied potential of -0.5V vs. SCE in electrolyte containing 0.2 M CuSO₄ – 3 M lactic acid adjusted to pH 9.5.

Figure 4-11 shows the morphology evolution of Cu₂O films formed at an applied potential of -0.5 V vs. SCE in a 0.2M CuSO₄ - 3M lactic acid solution at pH 9.5. A clear transformation of particle shape with time can be observed. After 1 minute deposition time, the film consists of loosely packed spherical

particles with diameters up to ~ 180 nm (Figure 4-11a). The particles then become more angular and closely packed as the deposition process continues. Irregular polyhedral particles are observed after 3 minutes (Figure 4-11b), while distinct cubic shapes appear by 5 minutes (Figure 4-11c). The size of the particles continues to increase after the formation of cubic particles, exceeding ~ 1 μm (edge length) after prolonged electrodeposition. Similar evolution of Cu_2O morphology over the course of deposition has been previously reported [171,186].

pH 12.5

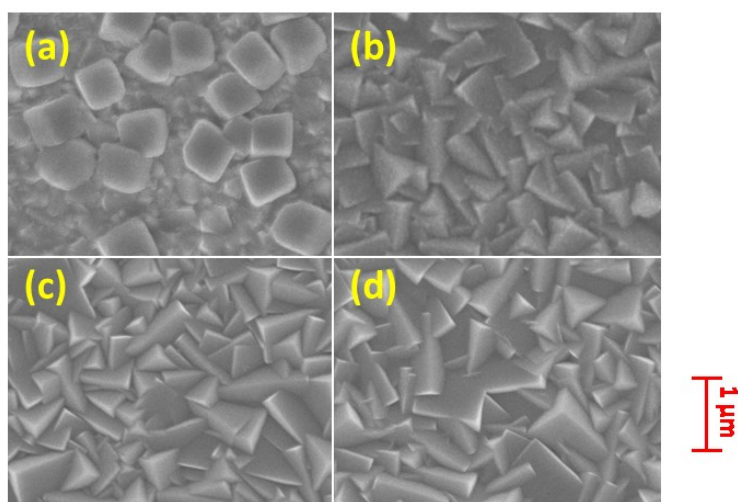


Figure 4-12: SEM images of Cu_2O films electrodeposited on FTO-glass substrate at 60°C for the following durations: (a) 1 min, (b) 3 min, (c) 5 min, (d) 10 min at an applied potential of -0.6V vs. SCE in electrolyte containing $0.2\text{ M CuSO}_4 - 3\text{ M}$ lactic acid adjusted to pH 12.5.

The morphology evolution of Cu_2O films formed at pH 12.5 and -0.6V , under otherwise identical conditions, is shown in Figure 4-12. While the final film morphologies after prolonged deposition time are found to be similar at pH 9.5 and 12.5, the evolution of film formation appears to occur differently. At pH 9.5, cubic crystals are only observed after ~ 5 min deposition time. However, at pH 12.5, cubic particles are formed at the very beginning of the process and long before they completely cover the FTO substrate surface.

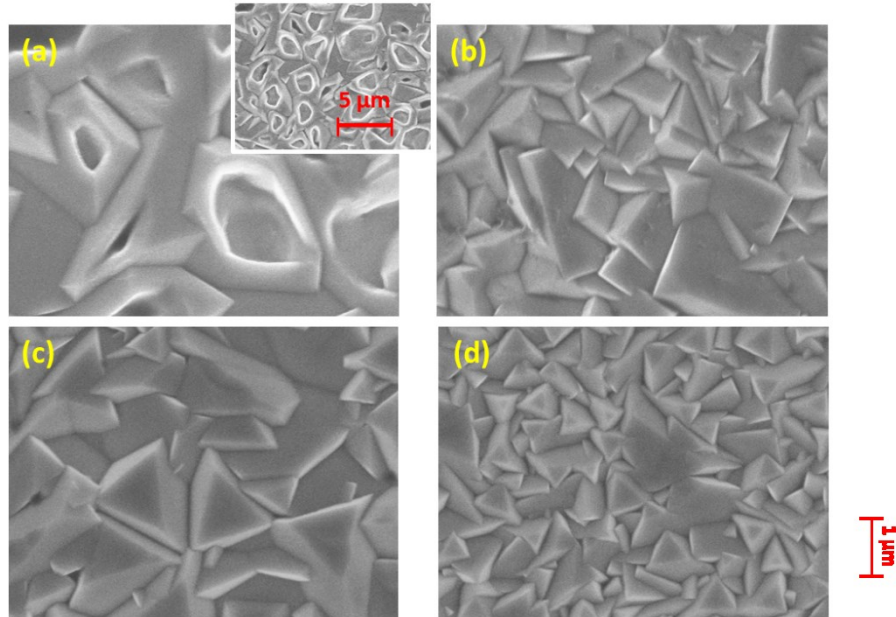


Figure 4-13: SEM images of Cu_2O films deposited from 0.2 M CuSO_4 + 3 M lactic acid adjusted to pH 12.5 at the following temperature and applied potential: (a) 60°C, -0.5V; (b) 60°C, -0.65V; (c) 75°C, -0.5V; (d) 75°C, -0.65V.

The morphology of Cu_2O films deposited at pH 12.5 is also affected by the deposition temperature and applied potential, as shown in Figure 4-13. At 75°C, truncated cubic grains are formed at both -0.5V and -0.65V (Figures 4-13 c, d). XRD reveals that both samples exhibit mixed orientation and faster growth in the $\langle 100 \rangle$ direction than the $\langle 111 \rangle$ -dominant film produced at 60°C at -0.65V. This differs from the effect observed at pH 9.5, where an increase in temperature tends to favor a $\langle 111 \rangle$ orientation at high cathodic potential.

The image in Figure 4-13a of a film deposited at pH 12.5, 60°C and -0.5V shows evidence that some dissolution of the coating likely occurs during deposition. However, the amount of dissolution is probably not as extensive compared to the cases shown in Figures 4-7a and 4-9d. Although the top corners of the grains have been attacked, the majority of the truncated cubic morphology remains visible. From the extent of the deformation, it appears that the dissolution process is faster at pH 13.5 (Figure 4-9d) than at lower pH and that the dissolution process preferentially starts at high energy sites such as corners of the as-formed grains.

pH 13.5

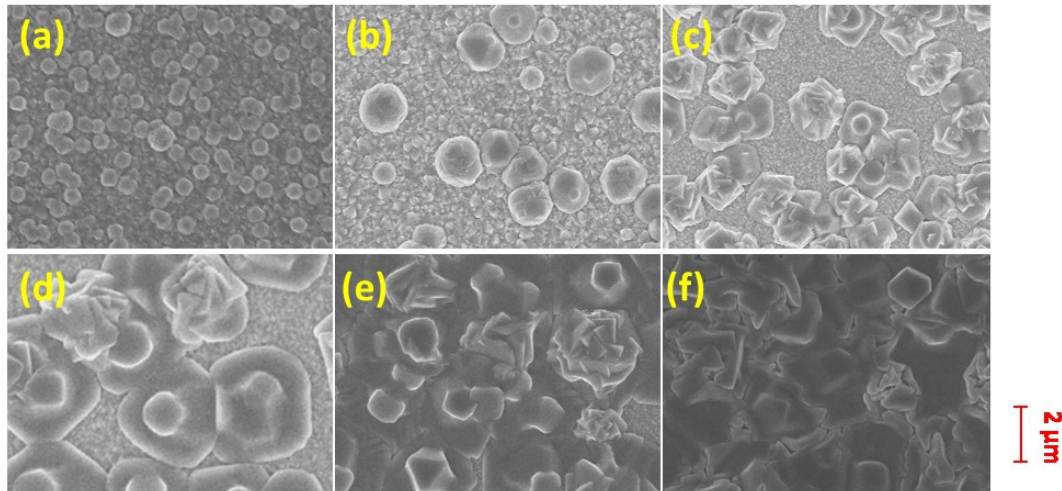


Figure 4-14: SEM images of Cu_2O films electrodeposited on FTO-glass substrate at 60°C for the following durations: (a) 0.5 min, (b) 1 min, (c) 2 min, (d) 3 min, (e) 5 min, (f) 10 min at an applied potential of -0.7V vs. SCE in electrolyte containing $0.2\text{ M CuSO}_4 - 3\text{ M lactic acid}$ adjusted to pH 13.5.

Figure 4-14 shows the morphology evolution of Cu_2O films formed at an applied potential of -0.7 V vs. SCE in a $0.2\text{M CuSO}_4 - 3\text{M lactic acid}$ solution at pH 13.5. At the beginning of the deposition process, spherical particles of a few hundred microns in diameter can be observed (Figure 4-14a). Unlike the situation at pH 9.5 (Figure 4-11) in which spherical particles are also observed at the initial stage, these particles do not evolve into well-defined cubic grains. Instead, micron-sized clusters with some visible angles and edges can be found after ~ 2 minutes of deposition (Figure 4-14c). At the same time, as the diameter of the particles becomes larger, the top portion of each particle shows noticeable evidence of dissolution, forming a disk-like morphology close to the substrate (Figure 4-14d). As the process continues, the disks appear to expand and merge together, forming a continuous film, while the vertical features becomes less defined (Figure 4-14 d-f). As a result, after ~ 10 min of electrodeposition, few edges and angles are observed in the film.

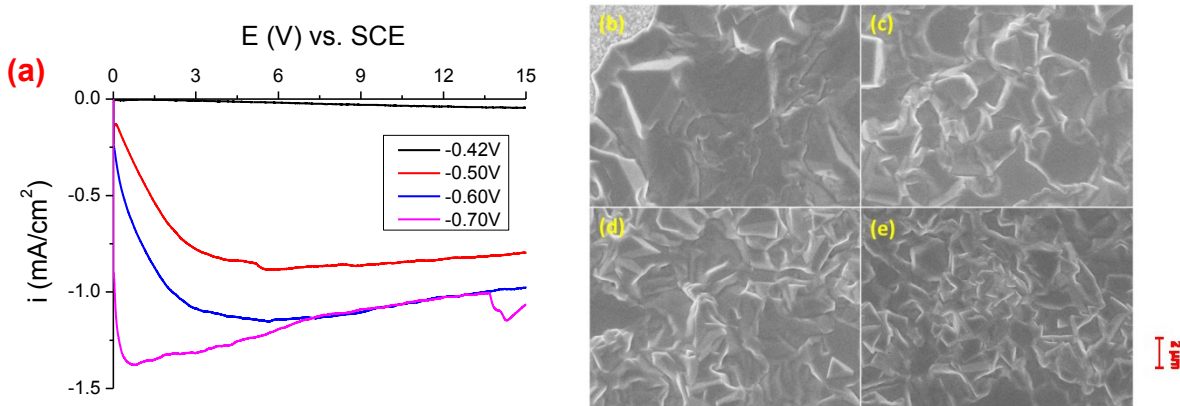


Figure 4-15: (a) Current transients curves for Cu₂O electrodeposition on FTO-glass substrate at 60°C in electrolyte containing 0.2 M CuSO₄ – 3 M lactic acid adjusted to pH 13.5 for 15 minutes, at different applied potentials between -0.42V and -0.70V vs. SCE. Corresponding SEM images formed at (b) -0.42V, (c) -0.50V, (d) -0.60V, (e) -0.70V are shown on the right.

The effect of applied potential on Cu₂O electrodeposition in the same pH 13.5 electrolyte is shown in Figure 4-15. Note that only minimal deposition occurs at -0.4V vs. SCE, which is expected from the deposition range predicted from the LSV curves (Figure 4-3a).

Similar to deposition at lower pH, the rate of electrodeposition increases as the applied potential becomes more negative (Figure 4-15a). Except at -0.42V for which only a small current is recorded through the process, the current transients for electrodeposition at -0.5V to -0.7V have similar shape over 15 min deposition time. The current density initially rises to a peak value and then gradually diminishes over the remainder of the deposition period. Unlike the case at lower pH, a steady state current is not reached by the end of 15 minutes of deposition. As shown in Table 4-1, the actual mass of deposit is less than the amount predicted from total charge using Faraday's Law. As discussed previously, either a side cathodic reaction is occurring that lowers the current efficiency or a portion of the film is chemically dissolving during the process. Again, only pure Cu₂O is identified from XRD analysis which does not support the presence of other cathodic side reactions. The fact that the same mismatch between measured and calculated mass occurs at potentials close to the upper limit of Cu₂O formation potential also indicates that the formation of Cu metal is very unlikely.

Table 4-1: Estimated thickness of Cu₂O films galvanostatically deposited from 0.2M CuSO₄ – 3M lactic acid electrolyte adjusted to pH 13.5 at different applied potentials.

E (V vs. SCE)	d_{Faraday} (nm)	d_{actual} (nm)	% difference
-0.42	1093	965	-11.7%
-0.50	996	883	-11.3%
-0.60	1079	1051	-11.9%
-0.70	1545	1333	-13.7%

The film morphologies obtained at the different potentials all show evidence of dissolution (Figures 4-15 b-e). Films deposited at less cathodic potentials appear smoother than those at higher potentials. At -0.6 or -0.7V, some evidence of cubic grain formation is still visible in the form of short straight edges, while at -0.42V only a large flat sheet of oxide is observed.

No clear trends are observed from the XRD analysis although all four samples above exhibit similar I(111):I(200) peak ratios between 3 and 5 (within the mixed orientation regime).

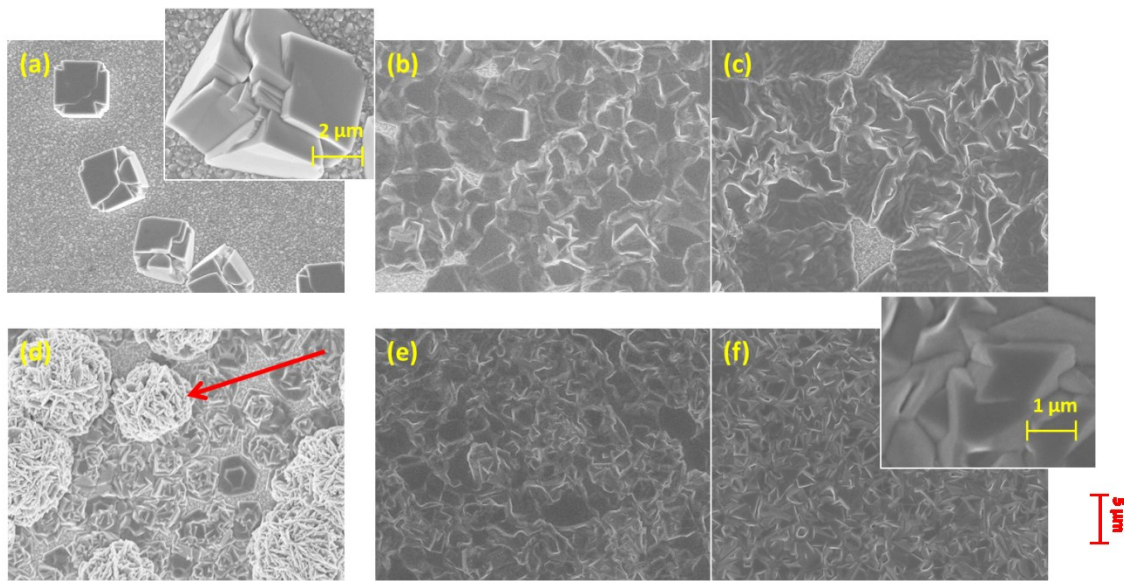


Figure 4-16: SEM images of Cu₂O films deposited from 0.2 M CuSO₄ + 3 M lactic acid adjusted to pH 13.5 at -0.5V: (a) 45°C, (b) 60°C, (c) 75°C and -0.7V: (d) 45°C, (e) 60°C, (f) 75°C. All samples deposited for 15 min.

Figure 4-16 shows the effect of temperature and potential on the morphology of Cu₂O films deposited from 0.2M CuSO₄ + 3M lactic acid at pH 13.5. At 45°C, electrodeposition at an applied potential of -0.7V results in the formation of Cu clusters (indicated by arrow), due to the narrower Cu₂O deposition range at lower temperature, similar to that observed at pH 9.5 (Figure 4-3b). The Cu₂O grains deposited in this condition also show evidence of dissolution, similar to the early stage morphology obtained in the same

electrolyte at 60°C (Figure 4-14d). This suggests that the same mechanism is occurring at the two temperatures, though at a slower rate at 45°C than at 60°C. Furthermore, at an applied potential of -0.7V, the film formed at 75°C shows more evidence of cubic/truncated cubic grain formation (see inset of Figure 4-16f) than at 60°C (Figure 4-16e). The less degradation of the grain structure when the temperature changes in either direction from 60°C may be due to either a slower dissolution rate or a faster deposition rate, both of which would lead to a larger portion of the original polyhedral grains being retained.

On the other hand, at an applied potential of -0.5V, the films produced at both 60°C and 75°C are almost completely deformed (Figure 4-16 b, c). However, temperature still plays an important role at this potential since individual cubic particles a few microns in size with deformed corners and edges are found at 45°C (Figure 4-16a). A layered structure on each particle is clearly evident, as shown in the inset, suggesting that deposition and dissolution are occurring simultaneously, but at a much slower rate at this temperature. The film orientation is also found to be <111>-dominant, whereas films that undergo more dissolution tend to exhibit mixed growth orientation, as shown in Figure 4-17.

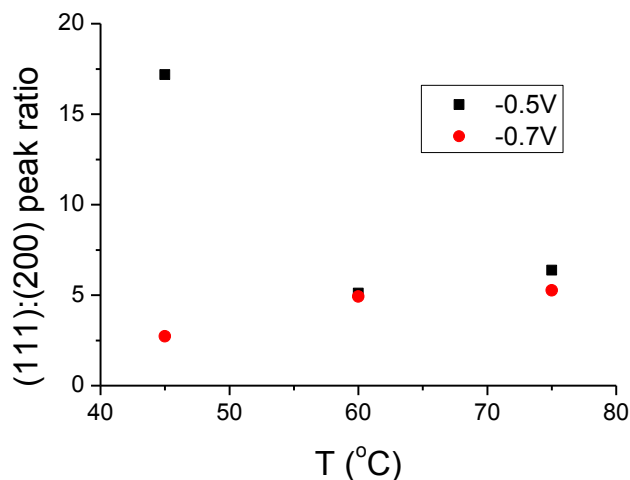


Figure 4-17: Effect of pH on (111):(200) peak intensity ratio for Cu₂O films deposited from 0.2 M CuSO₄ + 3 M lactic acid adjusted to pH 13.5 at -0.5V and -0.7V.

Finally, the effect of CuSO₄ concentration on the morphology of Cu₂O films deposited from the same system at pH 13.5 is presented in Figure 4-18. Again, all films show evidence of dissolution although the

extent appears to diminish as the CuSO_4 concentration increases so that truncated cubic grains still are mostly visible (Figure 4-18 b, c).

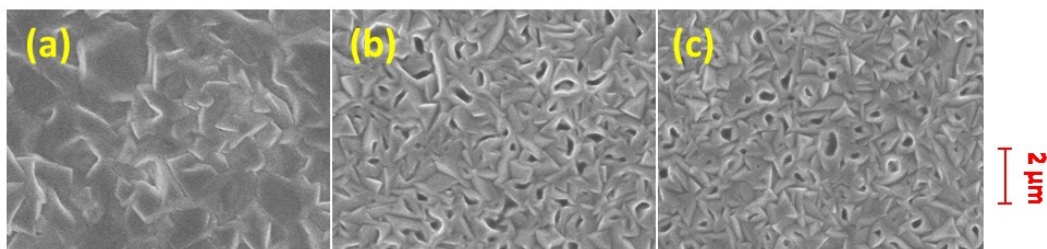


Figure 4-18: SEM images of Cu_2O films deposited from electrolyte containing (a) 0.2 M, (b) 0.3 M and (c) 0.4 M CuSO_4 and 3 M lactic acid adjusted to pH 13.5 at 60°C at -0.7V . All samples deposited for 15 minutes.

4.3.7 Effect of lactic acid concentration

In order to study the role of lactate ions during Cu_2O electrodeposition, solutions with different concentrations between 1.9 M and 4.5 M and the same CuSO_4 concentration have been prepared. When the lactic acid concentration drops below 1.5M at pH 9.5, a precipitate, presumably in the form of $\text{Cu}(\text{OH})_2$ immediately forms in the plating bath.

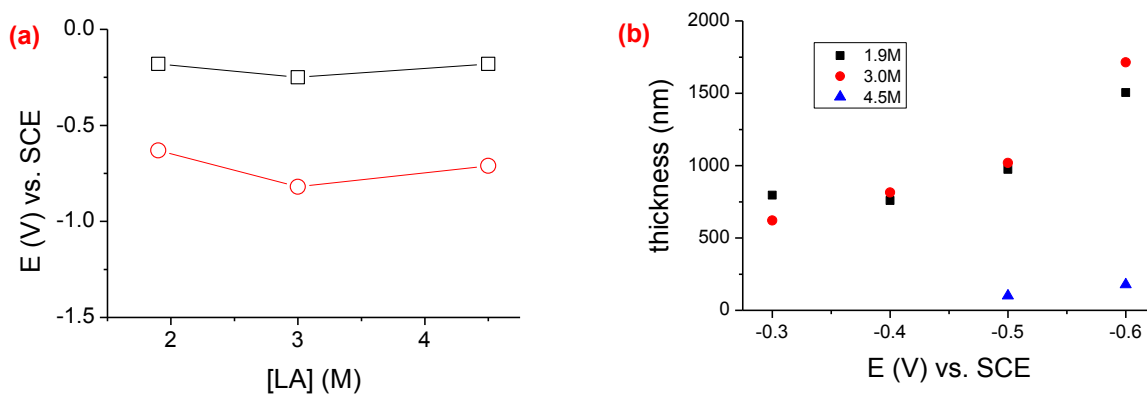


Figure 4-19: (a) Potential range for Cu_2O deposition and (b) effect of applied potential on Cu_2O film thickness after 15 min deposit at 60°C from 0.2 M CuSO_4 electrolytes containing various amounts of lactic acid adjusted to pH 9.5.

Interestingly, the deposition range of Cu_2O as estimated from the LSV curves does not change monotonously with lactic acid concentration, as shown in Figure 4-19a. The deposition range is most cathodic at a concentration of 3.0M, but becomes less so when [lactic acid] is either 1.9M or 4.5M. In addition, Cu clusters are found at a potential of -0.6V potential at all three lactic acid concentrations.

On the other hand, the deposition rate shows a different trend with respect to lactic acid concentration. This is shown in terms of the mass of Cu_2O film produced after 15 minutes of deposition in Figure 4-19b. The deposition rate at 1.9 M lactic acid increases monotonically as the potential becomes more cathodic and is similar to that observed at 3.0 M. On the other hand, the deposition rate remains very low at 4.5 M regardless of the potential. At a potential of -0.4V or more positive, very little deposition on the substrate occurs at a lactic acid concentration of 4.5 M although LSV suggests that this potential is well within the Cu_2O deposition range.

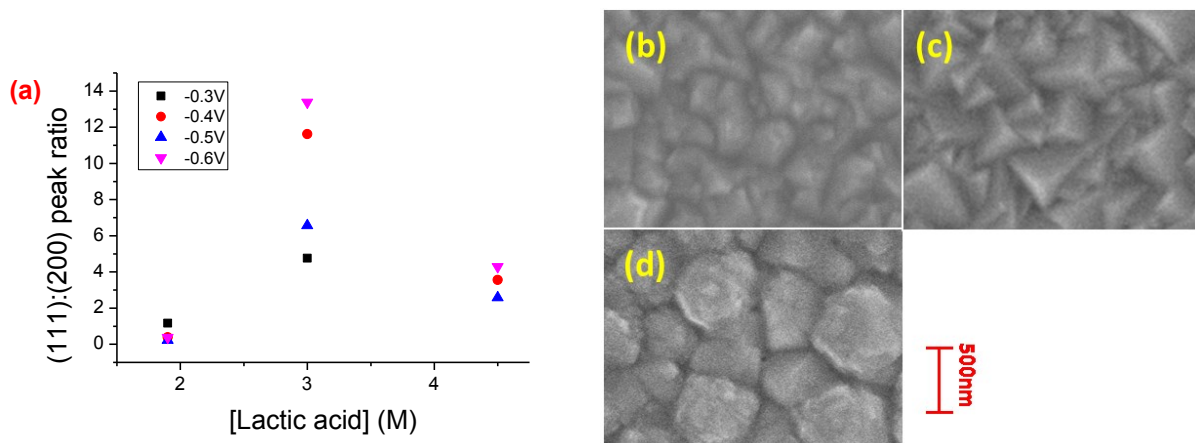


Figure 4-20: (a) Effect of lactic acid concentration on (111):(200) peak intensity ratio of Cu_2O films formed at 60°C from 0.2 M CuSO_4 electrolytes adjusted to pH 9.5. SEM images of Cu_2O films deposited from electrolyte containing 0.2 M CuSO_4 and different lactic acid concentrations adjusted to pH 9.5 at 60°C at -0.5V are shown on the right: (b) 1.9 M, (c) 3.0 M, (d) 4.5 M. All samples deposited for 15 minutes.

Furthermore, the XRD patterns reveal that the growth orientation also does not change monotonously with lactic acid concentration, as shown in Figure 4-20a. The films are found to favor $\langle 111 \rangle$ orientation at 3.0 M lactic acid. However, as the concentration changes in either direction, the $\langle 111 \rangle$ -dominance diminishes. In fact, $\langle 100 \rangle$ -oriented growth is preferred at 1.9 M, while mixed orientation is found at 4.5 M. SEM examination shows that neither samples formed at 1.9 M or 4.5 M contain cubic grains at an applied potential of -0.5V, agreeing with the XRD results. At 1.9 M lactic acid, the grains are irregular polyhedra with some $\langle 100 \rangle$ preference shown in the form of 4-sided pyramids (Figure 4-20b). Little difference is found in the film morphologies formed at different applied potentials and a lactic acid concentration of 1.9M, for which 4-sided pyramidal grains are prominent in the resulting morphology at

all potentials between -0.3V and -0.6V (SEM images not included here). At 3.0M lactic acid, on the other hand, a shift from mixed orientation to cubic grains is observed as the applied potential becomes more cathodic (Figures 4-4 b-e). The trend observed at 1.9 and 3.0 M lactic acid agrees with that reported by Zhu et al who found that a higher lactic acid concentration tends to promote faster $\langle 111 \rangle$ -oriented growth. However, it is important to note that Zhu et al only investigated lactic concentrations up to 3.0M [167]. In our study, when the lactic acid concentration to 4.5 M, we find that this trend changes. At the highest lactic acid level, large irregular grains hundreds of nm in size are observed (Figure 4-20d). The grains do not have straight edges, suggesting that some dissolution may have occurred during the process. It is also noted that the grain size increases with lactic acid concentration, despite the slow deposition rate observed at 4.5 M.

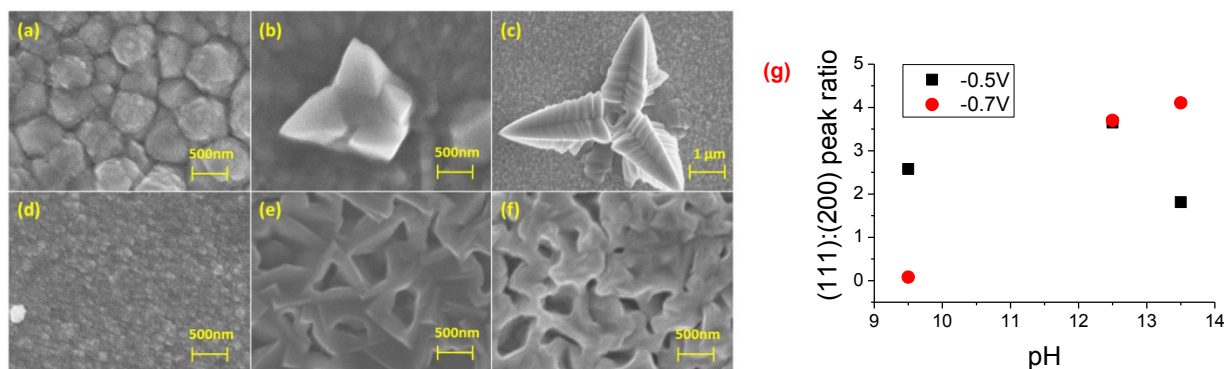


Figure 4-21: SEM images of Cu₂O films deposited from electrolyte containing 0.2M CuSO₄ + 4.5M lactic acid at 60°C at -0.5V: (a) pH 9.5, (b) pH 12.5, (c) pH 13.5; at -0.7V: (d) pH 9.5, (e) pH 12.5, (f) pH 13.5. The effect of pH on (111):(200) peak intensity ratio for deposition in 4.5M lactic acid is shown in (g). All samples deposited for 15 minutes.

The variation in film morphology at different pH and applied potential for Cu₂O films deposited in electrolytes containing 0.2 M CuSO₄ and 4.5 M lactic acid is presented in Figure 4-21. It is noted that Cu peaks are identified at -0.7 V in pH 9.5 and 12.5. These results show that the film morphology depends strongly on both pH and applied potential.

At an applied potential of -0.5V, large particles are deposited at all pH, although their shapes differ greatly. At pH 9.5, the particles are rounded and a few hundred nm in diameter, as described before (Figure 4-21a). At a higher pH of 12.5, the average size of the particle increases to ~1μm and the shape

resembles that of a cube or octahedron with corners protruding outward (Figure 4-21b). In this case, only a few large particles scattered across the substrate surface are formed so that the substrate surface between them remains exposed. At pH 13.5, the corners appear to extend even further than at pH 12.5 so that the particle has a star-like shape a few microns in diameter (Figure 4-21c). XRD patterns reveal mixed growth orientation for all three samples obtained at -0.5 V, as shown in Figure 4-21g. Similar star-like particles as that observed in Figure 4-21c have been reported previously for galvanostatic electrodeposition at low applied current in low [Cu(II)] systems containing sodium dodecyl sulfate (SDS), for which $\langle 100 \rangle$ orientation was identified [148].

On the other hand, Cu_2O films deposited at -0.7V are much smoother despite Cu formation at pH 12.5 or lower. At pH 9.5, small grains with an average diameter less than 100nm (Figure 4-21d) and a $\langle 100 \rangle$ -dominant growth direction (Figure 4-21g) are deposited. At pH 12.5 and 13.5, a partially dissolved morphology is formed (Figures 4-21 e, f), similar to that observed in 3.0 M lactic acid at 0.3M-0.4M $[\text{CuSO}_4]$ and pH 13.5 (Figures 4-18 b, c). Both samples have mixed orientation, also similar to previous observation (Figure 4-21g).

4.4 Discussion

From the results presented in the above sections, it is clear that the morphology of electrodeposited Cu_2O films from alkaline CuSO_4 -lactate electrolytes is very sensitive to the change in deposition conditions. In many cases, the effects of different parameters appear to compete with each other, further complicating the electrodeposition mechanism. The combined effect of these factors on Cu_2O film morphology is discussed in detail in this section.

4.4.1 Factors affecting growth orientation

Surface energy

Shinagawa et al have explained the growth orientation in terms of the surface energies of Cu_2O on the different faces [155]. In general, since faces with higher surface energy are less stable at equilibrium,

growth in the perpendicular direction is favored. In the case of Cu_2O with a cubic cuprite structure, the polar (100) plane has a higher surface energy than that of the nonpolar (111) plane [187–189]. Thus, for conditions close to thermodynamic equilibrium, $\langle 100 \rangle$ -oriented growth is preferred over $\langle 111 \rangle$. As the conditions shift away from the equilibrium state, $\langle 111 \rangle$ -oriented growth becomes more significant and $\langle 100 \rangle$ -dominant growth is no longer observed. This explains the fact that films deposited at low overpotential tend to favor $\langle 100 \rangle$ -oriented growth, as observed in the XRD peak ratio analysis shown in Figures 4-6 and 4-8.

The effect of surface energy does not explain the different orientations of samples deposited at similar rates, such as the case for films deposited in 1.9M and 3.0M lactic acid at pH 9.5 at 60°C (Figure 4-20 b and c). Also, the fact that predominantly $\langle 111 \rangle$ -oriented growth is observed in some cases when the system is far from equilibrium also cannot be entirely explained in terms of surface energy effects. If surface energy is the only factor determining growth orientation, then mixed orientation would be expected when the system is far from equilibrium instead of deposition on low-energy faces being completely replaced by deposition on high-energy faces.

Atomic density

Another factor that may be determining orientation is the atomic density of Cu and O on each face. As proposed by Wang et al. [149], deposition in the $\langle 100 \rangle$ direction leads to a repeating sequence of 2 layers – one containing Cu only adjacent to one containing O only. Crystal growth in the $\langle 111 \rangle$ direction proceeds by the formation of a 3-layer sequence made up of a Cu layer sandwiched between two O layers. The number of O atoms required in each of the O layers parallel to the (111) plane is estimated to be 8.83 nm^{-2} , whereas it is only 2.78 nm^{-2} in the O layer parallel to the (100) plane. Consequently, when a relatively small amount of OH^- is available at the electrode surface, the growth rate in the $\langle 111 \rangle$ direction would be low since the source of O for Cu_2O formation is lower. On the other hand, when the surface concentration of OH^- is high, $\langle 111 \rangle$ -oriented growth becomes easier since the source of oxygen from the

reactants is now larger. This agrees with our observation that the $\langle 111 \rangle$ orientation becomes more significant as pH increases up to pH 12.5 (Figure 4-9e).

Wu et al [190] proposed a similar explanation based on the ratio of O to Cu that makes up each of the crystal faces. The number of atoms required in the Cu layers parallel to the (111) and (100) planes are 14.62 nm^{-2} and 7.76 nm^{-2} , respectively. If these densities are combined with those for O along the same planes, then the atomic ratios O/Cu are 0.604 on the (111) face and 0.358 on the (100) face. Thus, the (111) plane is O-rich/Cu-lean and the (100) plane is O-lean/Cu-rich with respect to the bulk O/Cu ratio of 0.5 based on volumetric packing. This use of the O/Cu ratio as a criterion to select the preferred growth direction is consistent with the argument presented in the previous section concerning the effect of the pH since it correctly predicts that the orientation should shift toward the O-rich (111) plane as the pH rises. However, it does not agree with the observation that an increase in the CuSO_4 bulk concentration still results in a $\langle 111 \rangle$ -oriented film (Figure 4-8) although it is possible that a higher concentration is required to observe a change in orientation.

Adsorption of lactate

As discussed in Section 4.4.1, the stability of different Cu_2O planes plays an important role in determining the growth orientation. It is also known that surfactants can modify the surface energy by preferentially adsorbing onto specific surfaces. In previous studies, additives have been introduced into the electrolyte as capping agents for both the electrochemical and chemical syntheses of Cu_2O [170,171,191–193]. It has been demonstrated that different Cu_2O faces, including (100), (111) and (110), can be stabilized by using different types of surfactants. The type of complexing agent, such as lactate, acetate, and citrate, also has a large effect on Cu_2O grain structure in similar electrodeposition systems [167].

Therefore, any adsorption of lactate during deposition would be expected to affect the morphology of the resulting Cu_2O films. Furthermore, this effect is expected to become more significant as the lactate concentration increases. As demonstrated in Figure 4-21 b and c, star-like particles with $\langle 100 \rangle$

orientation similar to that observed in SDS-containing electrolyte [148] are formed in electrolytes containing 4.5M lactic acid at -0.5V. Although the exact reason is unknown, this suggests that lactate ions may have a similar surface stabilizing function as SDS, which preferentially adsorbs onto the (111) faces and hinders <111>-oriented growth, thus favoring growth in the <100> orientation. It also appears that a very high concentration of lactate is required for the effect of adsorption to become significant, which may be the reason why this has not been previously reported.

4.4.2 Role of transport limitation

In DC electrodeposition from a non-agitated electrolyte, the transport of reactants to the working electrode may become rate limiting, especially at higher overpotential when the rate of consumption at the electrode surface is high. In the case of the CuSO_4 -lactic acid system, the transport of large CuLac_2 complexes may become hindered due to the buildup of lactate ions that must diffuse away from the surface as Cu_2O deposition proceeds. Therefore, the surface Cu(II) concentration is likely to decrease over time.

This effect of the transport limitation can be used to explain the evolution of morphology shown in Figures 4-10, 4-11 and 4-12. For deposition from pH 9.5 electrolytes, any limitations of Cu(II) transport in the early stages would be counteracted by the fact that the bulk $[\text{OH}^-]$ is low. Thus, no preferred orientation would be observed and both <111> and <100> oriented growth would occur. However, if as the process continues, $[\text{Cu(II)}]$ diminishes at a faster rate than $[\text{OH}^-]$, the $[\text{OH}^-]:[\text{Cu(II)}]$ ratio at the surface would increase and favor <111> oriented growth. By comparison, at a lower pH of 8.5 where the bulk concentration of OH^- is lower, <100>-oriented growth is dominant at the start of deposition and the shift toward <111>-oriented growth is much slower, resulting in mixed growth orientation even after prolonged deposition time. On the other hand, at pH 12.5 where the bulk concentration of OH^- is much higher, the effect of Cu(II) depletion would become significant earlier during the process since the $[\text{OH}^-]:[\text{Cu(II)}]$ ratio that allows <111>-oriented growth would be reached at an earlier point, as reflected in cubic grains appearing formation even after only ~ 1 min (see Figure 4-12a).

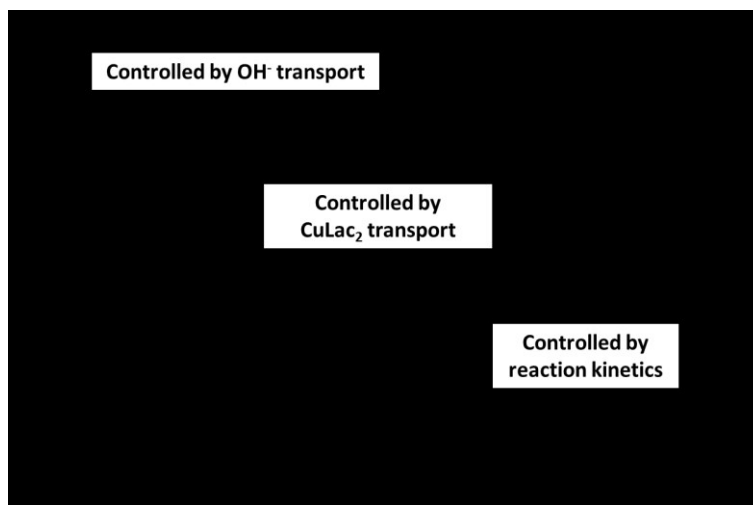


Figure 4-22: Effect of transport limitation on Cu₂O growth orientation (diagram is intended for qualitative purpose only).

It is proposed that the growth orientation is determined by the relative rates of the reduction reaction (Eq. 2-8) and the transport of reactant species to the working electrode, as summarized in Figure 4-22. For conditions where transport rate is significantly faster than the reaction, the deposition process is controlled by the reaction kinetics. In this regime, $\langle 100 \rangle$ orientation becomes more preferred as the conditions become closer to thermodynamic equilibrium. On the other hand, when the transport rate is slow compared to the rate of reaction, the deposition is limited by the availability of [Cu(II)] at the electrode surface. Within this regime, the growth orientation is mostly determined by the ratio of [Cu(II)] and [OH⁻] at the electrode surface. Mixed growth orientations may be found in either regime away from the limiting cases. In addition, the formation of Cu(0) at higher applied potential could occur when the system becomes limited by the diffusion of OH⁻ when the consumption rate is sufficiently high.

The relative rates of transport and reduction can be used to explain some observations that cannot be explained by a single factor. For example, the formation of $\langle 100 \rangle$ oriented films is only observed when the potential is relatively low. At higher applied potential, the transport of CuLac₂ becomes the limiting factor and so surface energy plays a less significant role than the atomic ratio of Cu to O. This argument also explains why the effect of temperature may depend on pH such as pH 9.5 and 12.5 (Figures 4-6 and 4-13). As the solution temperature increases, both reduction and diffusion occur more readily. As a result,

while Cu(II) is being consumed at a faster rate, its transport to the electrode surface also occurs more rapidly at the same time. Therefore, depending on which rate is affected more, the $[\text{OH}^-]:[\text{Cu(II)}]$ ratio at the electrode surface may increase or decrease and affect the orientation of the resulting crystals.

4.4.3 Dissolution

From results presented earlier, some conclusions regarding the dissolution of Cu_2O during the electrodeposition process can be drawn. Dissolution is more prominent at a high pH of 13.5, well beyond the typically studied range for electrodeposition in the CuSO_4 -lactic acid system, explaining why it has not been previously studied in detail. At lower pH, evidence of dissolution is only found at low applied potentials, such as in Figures 4-4b, 4-7a and 4-13a. Dissolution typically occurs at high energy sites such as edges and corners of polyhedral grains, thereby promoting either rounded or deformed morphology. In addition, samples which show evidence of significant dissolution usually have mixed growth orientation.

We can obtain further insight into this effect by immersing pre-deposited Cu_2O films with cubic morphology (0.2 M CuSO_4 + 3 M lactic acid adjusted to pH 12.5 at 60°C at -0.65V , film thickness $\sim 2.2\mu\text{m}$) in high pH solutions containing 3 M lactic acid solution without any CuSO_4 . This would allow dissolution of the films to occur without any Cu_2O deposition simultaneously occurring.

The effect of temperature on the amount of film dissolved after immersion in a 3 M lactic acid solution for 3 hours is presented in Figure 4-23. The change in thickness is calculated from the difference in sample mass before and after immersion. As shown, the amount of dissolution increases with solution temperature. No measurable dissolution is observed at room temperature at either pH. On the other hand, the rate of dissolution appears to be much faster at pH 13.5 than at pH 12.5 at 60°C . This agrees with the evidence from the SEM images of the Cu_2O deposits of more extensive dissolution at pH 13.5 than at 12.5 (Figures 4-12 and 4-14). These results also suggest that this dissolution is chemical rather than electrochemical in nature since no applied potential is required.

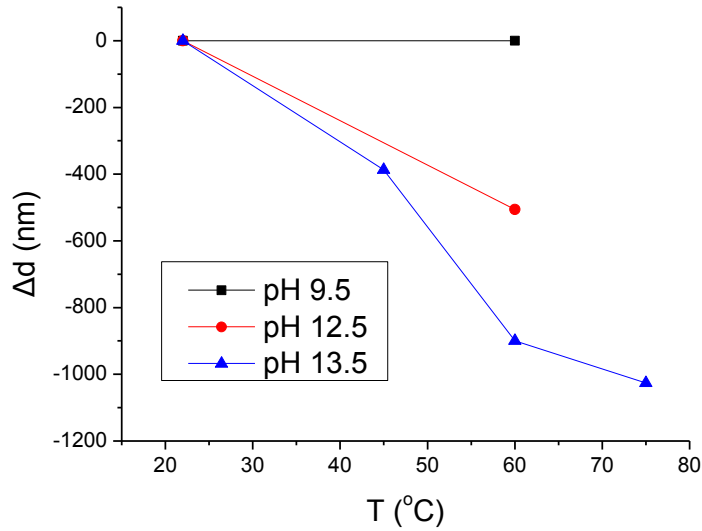
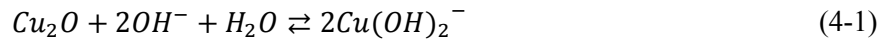


Figure 4-23: Change in thickness of Cu₂O thin films (electrodeposited in 0.2 M CuSO₄ + 3 M lactic acid adjusted to pH 12.5 at 60°C at -0.65V, film thickness ~2.2μm) after immersion for 3 hours in 3.0 M lactic acid solution adjusted to pH 12.5 or 13.5 using NaOH.

Dissolution occurring in this system may occur according to the reaction:



The formation of Cu(OH)₂⁻ is promoted at higher pH as this reaction indicates. The equilibrium constants for this reaction at 25, 45, 60 and 75°C are 1.41x10⁻⁶, 3.28x10⁻⁶, 5.87x10⁻⁶, and 9.86x10⁻⁶, respectively, which suggests that dissolution is promoted by increasing temperature, also agreeing with the above results [194,195]. Additionally, the kinetics of this reaction should increase with temperature, leading to more alteration of the deposit structure, which is consistent with the trend shown in Figure 4-16.

Therefore, the extent of deformation observed in the previous sections can be explained by the relative rates of reduction and dissolution (Eq. 2-8 and 4-1). Degradation of Cu₂O grains becomes more significant when either the deposition of Cu₂O becomes slower (at lower [CuSO₄], lower overpotential, higher [lactic acid], etc.) or when its dissolution becomes faster (higher pH, etc.). Similar to the effect of temperature on growth orientation (as discussed in Section 4.4.2), its effect on dissolution is also difficult to predict as a higher temperature promotes faster deposition and dissolution of Cu₂O. Likely, a temperature exists at which grain deformation is most favored.

For example, in 0.2 M CuSO_4 + 3M lactic acid electrolyte adjusted to pH 13.5 at -0.7V, grains formed at 60°C appear to be the most altered (Figure 4-16e). When the temperature is reduced to 45°C, the rate of dissolution appears to decrease relative to that of deposition so that less deformation of Cu_2O grains occurs, as observed in our experiments (Figure 4-16d). On the other hand, an increase in the temperature from 60°C to 75°C may cause the deposition rate to increase more than that of dissolution, thus leading to faster grain growth relative to grain reformation and explaining why the overall morphology appears less deformed in Figure 4-16f.

4.5 Summary

In this chapter, the effect of parameters including applied potential, temperature, pH, copper concentration and lactate concentration on the morphology of potentiostatically deposited Cu_2O film from a copper-lactate electrolyte is investigated in detail and possible explanations for the observed trends are discussed. A range of Cu_2O morphologies including cubic, octahedral, truncated and irregular polyhedral shapes, branched particles, as well as reformed shapes due to dissolution can be formed depending on the deposition conditions.

The variation in morphology is mostly attributed to the relative growth rates of $\langle 111 \rangle$ and $\langle 100 \rangle$ orientations. It is found that the variation in growth orientation is mostly due to the relative rates of reaction and transport. When reaction kinetics is the limiting factor, $\langle 100 \rangle$ growth is preferred when the conditions are close to thermodynamic equilibrium. On the other hand, when transport limitation in the system is significant, $\langle 111 \rangle$ -oriented growth and cubic grains are favored as the surface concentration of CuLac_2 is reduced. In other conditions, mixed orientations tend to be formed. It is also speculated that lactate ions may preferentially adsorb onto the (111) faces based on the results obtained from deposition in electrolytes containing high lactate concentration.

In addition, dissolution is observed at high electrolyte pH of 13 and above. It appears that some dissolution of the deposit occurs at all conditions at this pH although the effect becomes significant only when the rate of dissolution is comparable to the rate of Cu_2O formation.

Chapter 5. Cu₂O/AZO Solar Cells with Electrodeposited Cu₂O Layer

5.1 Introduction

To study of the effect of a Cu₂O layer on solar cell performance, we investigate solar cells based on a Cu₂O/AZO heterojunction prepared by electrodepositing a Cu₂O layer on an FTO-glass substrate followed by the sputtering of an AZO layer. The simple FTO/Cu₂O/AZO architecture is selected in order to minimize the deposition steps required for device fabrication. This architecture is identical to that reported in ref. [90] that typically exhibits an efficiency on the order of 0.1% - 1.0%.

The purpose of this chapter is to:

1. investigate the effect of different Cu₂O deposition parameters on the solar cell performance
2. optimize the efficiency of Cu₂O/AZO solar cells by varying Cu₂O deposition conditions
3. identify the limitations in devices based on electrodeposited Cu₂O/sputtered AZO heterojunctions.

5.2 Experimental details

5.2.1 Device fabrication and characterization

The electrodeposition of Cu₂O is carried out as described in Section 4.2, except by varying the deposition time to control thickness. It is well known that an optimal Cu₂O thickness exists for this type of solar cell. If the active layer becomes too thin, the device V_{OC} tends to be lower due to insufficient length of the space charge region, while J_{SC} tends to be lower due to lower light absorption in the long wavelength region. On the other hand, if the device becomes too thick, the buildup of series resistance will also cause a drop in J_{SC} and FF. Preliminary experiments have shown that a Cu₂O layer thickness of ~2 μm yields optimal device efficiency. Therefore, all devices fabricated in this section have a Cu₂O thickness between 1.85 μm and 2.25 μm .

AZO deposition is sputtered onto the Cu₂O surface as described in Section 3.2.2. The optimal thickness of this AZO layer for solar cells in this study is determined to be ~250 nm for maximum PCE

based on preliminary experiments. The device area is defined using Kapton thermal tape, which is stable at high process temperatures, adheres well to Cu_2O surfaces and leads to much smaller edge effects on sputtered AZO thin films than using a stainless steel shadow mask. All devices reported in this section have an area of $\sim 0.03\text{-}0.05\text{ cm}^2$, above which a noticeable drop in device FF is observed. Approximately 15 cells are fabricated on a single Cu_2O sheet by depositing separate AZO contacts. Very little variation in the performance of these 15 cells is observed. Also, comparison of the device performances of each of these cells depending on whether the other cells are covered or uncovered during characterization shows that no evidence of interaction between the cells using this set-up. In addition to the fact that at least 15 cells are fabricated and tested on the same substrate, typically 3 independent replicate experiments under identical deposition conditions are also performed for the majority of reported devices in order to ensure reproducibility.

After AZO deposition, Al contact is deposited onto the portion of the FTO substrate not covered by Cu_2O thin film as the back contact (cathode), as described in Section 3.2.3. For some samples (discussed in Section 5.4.4), it is also deposited on top of the AZO layer as the top contact.

The film morphology and orientation are characterized using SEM and XRD. Illuminated J-V characteristics for both front- and back-illuminated devices are obtained as described in Section 3.3.3. To characterize their optical and electric properties, $2\text{ }\mu\text{m}$ thick Cu_2O thin films are deposited using identical conditions as in the corresponding devices deposited onto FTO, unless otherwise stated. The bandgap values are measured by UV-vis spectroscopy and CV. The charge carrier concentration is estimated using the SCLC method and SIMS. The charge carrier mobility is estimated using the SCLC method and TOF mobility measurements. Surface roughness of Cu_2O is estimated from AFM examination.

5.2.2 Experimental design

In the previous chapter, the morphology of electrodeposited p-type Cu_2O thin film has been shown to strongly depend on the deposition conditions. Thus, in order to determine the optimal deposition

conditions, a factorial design is first used to determine the significance of each deposition parameter on device performance.

Preliminary investigation shows that the purer is the Cu_2O layer, the better is the device performance. When the metallic Cu level is higher than ~ 3 mol% (calculated using Eq. 3-2), the performance of the resulting devices noticeably degrades as J_{SC} , V_{OC} and FF all drop significantly. With a Cu level of $\sim 5\%$ or above, the resulting devices no longer exhibit photovoltaic properties. Hence in this chapter, conditions are selected so that pure Cu_2O is deposited without Cu formation.

A 2-level full factorial design is performed to investigate the effects of $[\text{Cu(II)}]$, pH, temperature and applied potential (Table 5-1). Note that the applied potential is different at each pH due to the shift in the deposition range for Cu_2O , as discussed in Section 4.6 and presented in Figure 4-3a. The applied potentials are selected so that the (-) level is approximately 0.05V higher than the minimum Cu formation potential, and the (+) level is 0.15V lower than the minimum Cu_2O formation potential, in order to ensure that only pure Cu_2O is deposited.

Table 5-1: Factorial design conditions

Parameter	(-) Level	(+) Level
$[\text{CuSO}_4]$ (M)	0.2	0.4
pH	9.5	12.5
Temperature ($^{\circ}\text{C}$)	60	75
Applied potential (V vs. SCE)	-0.55 (pH 9.5) -0.65 (pH 12.5)	-0.4 (pH 9.5) -0.5 (pH 12.5)

Table 5-2: Summary of Cu₂O electrodeposition conditions, morphology and Cu₂O/AZO device performance

Sample	Deposition conditions				Morphology		Cell Performance					
	[CuSO ₄] (M)	pH	E vs SCE (V)	T (°C)	(111):(200) peak ratio	Grain shape	J _{sc} (mA/cm ²)	V _{oc} (mV)	FF (%)	PCE (%)	R _{sh} (ohm.cm ²)	R _s (ohm.cm ²)
1-1	0.2	9.5	-0.4	60	5.96	cubic	0.346	218.5	23.3	0.018	1.10E+04	5.83E+02
1-2				75	10.14	truncated cubic	0.228	200.9	24.5	0.011	2.00E+04	7.80E+02
1-3			-0.55	60	5.07	cubic	0.197	197.1	23.5	0.009	3.07E+04	1.06E+03
1-4				75	17.12	truncated cubic	0.274	185.7	23.6	0.012	1.57E+04	6.60E+02
2-1	0.2	12.5	-0.5	60	2.84	deformed cubic	2.760	240.7	32.6	0.217	4.55E+03	3.55E+01
2-2				75	3.34	truncated cubic	2.488	199.8	29.2	0.145	3.98E+03	5.31E+01
2-3			-0.65	60	9.39	cubic	3.170	200.4	28.0	0.178	2.79E+03	4.51E+01
2-4				75	5.75	truncated cubic	1.403	161.5	22.6	0.051	3.29E+03	1.40E+02
3-1	0.4	9.5	-0.4	60	15.99	polyhedral	0.310	241.6	23.9	0.018	1.53E+04	7.35E+02
3-2				75	0.36	truncated octahedral	0.116	146.0	24.7	0.004	5.33E+04	1.04E+03
3-3			-0.55	60	14.94	truncated cubic	0.377	186.2	24.5	0.017	1.43E+04	6.23E+02
3-4				75	1.44	polyhedral	0.517	220.7	25.3	0.029	9.27E+03	3.48E+02
4-1	0.4	12.5	-0.5	60	3.89	truncated cubic	1.678	198.9	33.4	0.112	5.42E+03	3.81E+01
4-2				75	2.52	truncated octahedral	0.507	201.4	31.5	0.032	1.40E+04	1.32E+02
4-3			-0.65	60	5.09	truncated cubic	2.632	176.2	27.8	0.129	1.99E+03	4.72E+01
4-4				75	12.98	cubic	3.091	212.4	29.2	0.192	1.92E+03	5.03E+01

5.3 Device performance

5.3.1 Overview of parameter effects

Table 5-2 summarizes the deposition conditions and performance of the samples fabricated according to the factorial design described above. Overall, the film morphology observed for the conditions presented in this table is consistent with the results in Chapter 4, and the effects of each deposition parameters on the film orientation also agrees with previous findings. For the majority of the Cu₂O films, polyhedral grains are observed. The grain shapes vary from the typical cubic grains to octahedral. Evidence of dissolution and reformation of grains is found in Sample 2-1, for which the deposition conditions involve low [CuSO₄], low applied potential and high pH. This is consistent with the findings in Chapter 4 that these conditions favor dissolution of Cu₂O grains (Section 4.4.4). The preferred orientation of the Cu₂O films as indicated by the (111):(200) peak intensity ratio mostly corresponds to that of mixed growth (peak ratio between 1 and 6) or <111>-dominant growth (peak ratio > ~6), with one exception (Sample 3-2) which exhibits truncated octahedral grains, as also reflected in the XRD data.

The device performance including estimated R_s and R_{sh} values are also presented in the table. The PCE of the above devices is found to vary from 0.004% to 0.217%. The values of J_{SC}, V_{OC} and FF all vary significantly depending on the deposition conditions of Cu₂O thin film. Among the three quantities, J_{SC} shows the greatest variation, with the largest (~3.170 mA/cm²) being more than one order of magnitude greater than the lowest measured value (~0.116 mA/cm²).

Table 5-3 shows the F statistics for the effect of each deposition parameter and two-factor interaction on device performance calculated using the data in Table 5-2. Using a one-tailed F-test with 90% confidence ($F_{1, 14, 0.10} = 3.10$), electrolyte pH during Cu₂O deposition is identified as the parameter with the most significant impact on device performance, as highlighted in the table. This is evident from the values presented in Table 5-2, where device PCE is on the order of 0.01% at pH 9.5, but increases to ~ 0.1% when the pH is raised to 12.5 in all samples examined. J_{SC} is especially affected by pH since it remains

below 1 mA/cm² in all samples where the Cu₂O layer is deposited at pH 9.5, but rises to ~2-3 mA/cm² when deposition is conducted at pH 12.5. On the other hand, the effects of other parameters and interactions are found to be much less significant. Overall, lower [CuSO₄], higher applied voltage and lower temperature tend to improve device PCE, as shown in Table 5-3 although the effects are relatively minor compared to that of the deposition pH. The effects of two-factor interactions are also calculated, though no significant effect is found, as presented in Table 5-3. The fact that pH has a more significant impact on device performance than other effects indicates that orientation is not the only factor affecting device efficiency.

Table 5-3: F-statistics for the effects of Cu₂O electrodeposition parameters and two-factor interactions on solar cell performance

Variable / Interaction	J _{sc}	V _{oc}	FF	PCE
pH	4.168	0.000	2.147	3.161
[CuSO ₄]	0.014	0.005	0.103	0.015
V	0.056	0.141	0.224	0.005
T	0.043	0.220	0.024	0.065
pH-[CuSO ₄]	0.025	0.000	0.022	0.027
pH-V	0.033	0.060	0.208	0.001
pH-T	0.035	0.027	0.078	0.055
[CuSO ₄]-V	0.111	0.169	0.016	0.137
[CuSO ₄]-T	0.009	0.084	0.046	0.041
V-T	0.002	0.330	0.000	0.018

In order to gain further insight into the system, the correlation between Cu₂O film orientation and device performance is examined. Figure 5-1 presents the correlation between the film orientation and device J_{sc} depending on whether electrodeposition of the Cu₂O layer is conducted pH 9.5 or 12.5. The analysis shows a positive correlation between J_{sc} and the (111):(200) peak ratio at each pH, which suggests that <111> orientation is preferred over <100> orientation in Cu₂O thin films for application in Cu₂O/AZO solar cells. This effect of film orientation agrees with previous reports for Cu₂O/ZnO devices and can be attributed to either better charge carrier mobility [79] or better lattice matching between the

Cu₂O (111) and ZnO (002) orientations at the p-n interface [50,99]. However, some anomalies are found in this study, as with the data indicated by blue rectangles in Figure 5-1. The outliers in the plots corresponds to Samples 1-1 and 3-4 at pH 9.5 and Samples 2-1 and 2-2 at pH 12.5, and the results are found reproducible upon repeated trials.

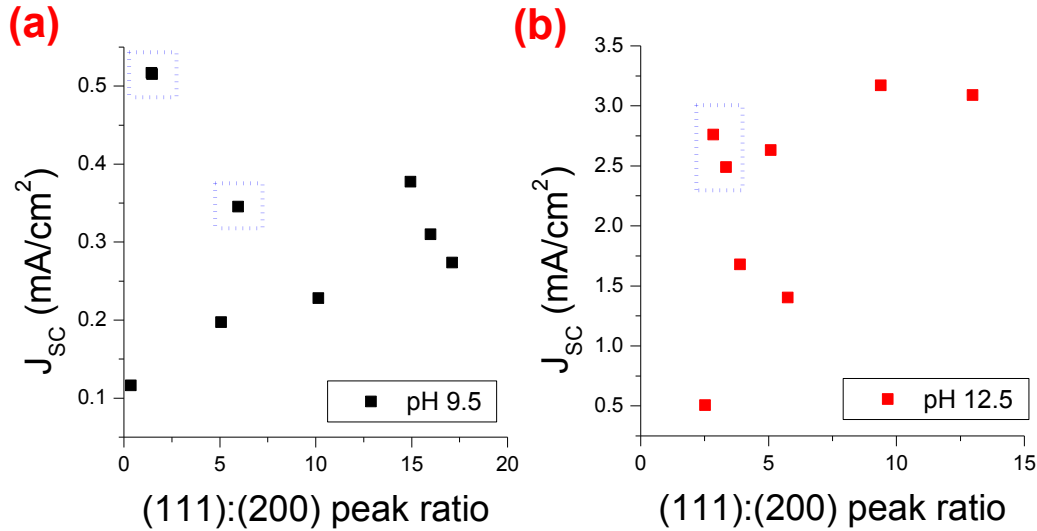


Figure 5-1: Correlation between J_{sc} and Cu₂O film orientation in Cu₂O/AZO devices consisting of Cu₂O films deposited at pH (a) 9.5 and (b) 12.5. Outliers are indicated by blue rectangles.

The Cu₂O film in Sample 3-4 has been deposited at low pH, high [CuSO₄], high applied potential and high temperature. As discussed previously, this set of conditions leads to fast deposition, which is further supported by our observation that the deposition rates of Cu₂O is highest in the cases of Samples 3-4 and 4-4. It is known that electrodeposited thin films grown at a high deposition rate usually have higher vacancy concentration since atomic movement cannot keep pace with crystal formation, resulting in a high amount of unfilled lattice sites [196,197]. Consequently, the higher-than-expected J_{sc} value may be attributed to the higher Cu vacancy concentration, which in turn correlates directly to the charge carrier concentration in the p-type Cu₂O films. It is noted that the other sample for which the Cu₂O deposition rate is high (Sample 4-4) also exhibits a high J_{sc} value although the effect is not as clear-cut since it also has high (111):(200) peak ratio.

On the other hand, the other outliers from the trend shown in Figure 5-1 (Samples 2-1 and 2-2) are both deposited at high pH, low [Cu(II)] and low applied potential. As shown in Section 4.4.4, these conditions favor the formation of Cu₂O films with a high fraction of deformed grains. Similarly, Sample 1-1 is deposited at low [Cu(II)] and low applied potential as well, although the pH is low. As shown in Figure 4-4b, the Cu₂O film deposited in the same electrolyte (0.2M CuSO₄ + 3M lactic acid at pH 9.5) and temperature, at slightly lower applied potential (-0.4V), also shows evidence of a small degree of dissolution in the form of rounded corners. Therefore, the improved J_{SC} in these samples may be attributed to the dissolution and reformation of grains during the electrodeposition of Cu₂O thin films although only Sample 2-1 shows clear evidence of this behavior in the SEM images. This is also consistent with the fact that samples with Cu₂O films deposited at high pH exhibit much higher J_{SC} and that pH is the parameter with most significant impact on dissolution rate.

By comparison, the effects of orientation on V_{OC} and FF are not as obvious. However, it is noted that the smallest V_{OC} value is observed in Sample 3-2, which has the lowest (111):(200) ratio and the only sample with a predominantly <100>-oriented Cu₂O film.

Based on the above discussions, three possible approaches to further optimize Cu₂O deposition have been identified:

- (1) increase the relative rate of <111>-oriented growth relative to that of <100>-oriented growth;
- (2) increase the defect concentration in the Cu₂O films;
- (3) increase the rate of dissolution during Cu₂O film deposition.

However, as shown in Figure 5-1, the effect of orientation on J_{SC} becomes less significant when the films have a clear <111>-dominant orientation. As such, improvements by using a more <111>-oriented film are expected to be relatively minor. On the other hand, in addition to increasing the deposition rate, different techniques can be used to increase the defect concentration in electrodeposited films although they usually require additives or different potential waveforms. Some of those procedures will be

discussed in Chapter 6. In the next sections, the device performance will be improved mainly through pH adjustment.

5.3.2 Effect of pH

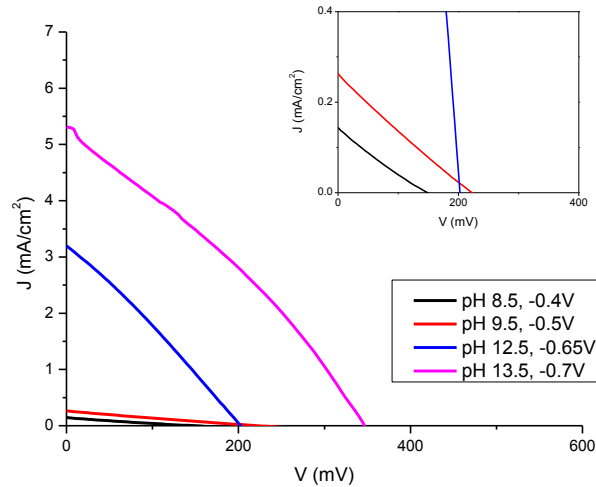


Figure 5-2: Illuminated J-V characteristics of solar cells fabricated using Cu_2O thin films deposited at different pH and applied potential (0.2 M CuSO_4 + 3 M lactic acid, 60°C).

Figure 5-2 presents the illuminated J-V curves of solar cells fabricated using Cu_2O thin films deposited at different pH between 8.5 and 13.5. As discussed in Section 4.3.6, different applied potentials are selected at each pH, typically $\sim 0.1\text{V}$ more positive than the minimum cathodic potential for Cu formation. The results clearly show that the device performance increases as the pH used for Cu_2O deposition rises, especially at pH 12.5 and 13.5.

The variation of the individual performance characteristics with deposition pH is plotted in Figure 5-3. Overall, an increase in the deposition pH has a positive impact on all performance variables, further indicating that high solution pH is preferable for Cu_2O thin films in $\text{Cu}_2\text{O}/\text{AZO}$ devices. In particular, an especially significant increase in PCE from 0.18% to 0.72% is observed when the deposition pH is increased from pH 12.5 to pH 13.5. The PCE of 0.72% observed for the devices fabricated using the pH 13.5 electrolyte is 0.72%, which exceeds the performance of all devices fabricated at pH 12.5 or lower as

presented in Table 5-2. This agrees with our previous hypothesis regarding dissolution and deformation of deposited Cu_2O grains which becomes most significant at pH 13.5 (Section 4.3.6).

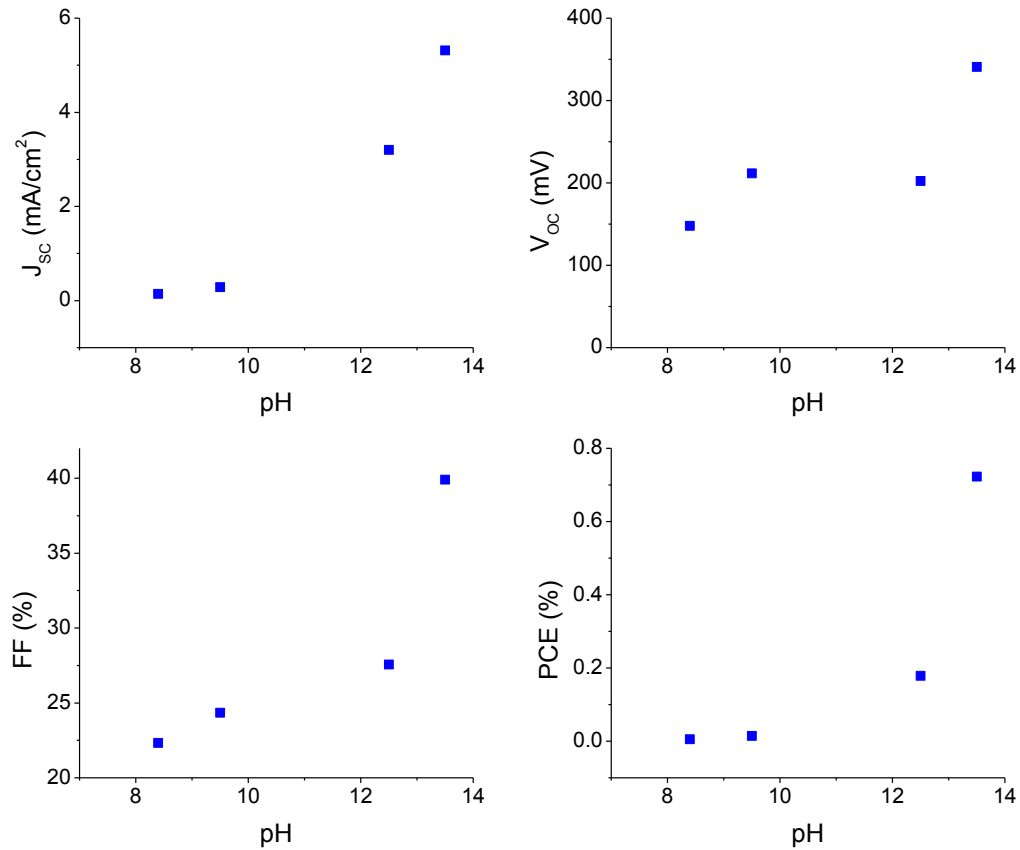


Figure 5-3: Device characteristics of solar cells fabricated using Cu_2O thin films deposited at different pH and applied potential (0.2 M CuSO_4 + 3 M lactic acid, 60°C).

Furthermore, the effect of Cu_2O deposition pH on series and shunt resistance of the resulting devices is plotted in Figure 5-4. R_s decreases dramatically with solution pH, which is consistent with the trend observed for the device FF. This also indicates that the device performance at lower pH values of 8.5 and 9.5 is mainly limited by R_s which is expected to reduce both FF and J_{sc} values and further suggests that charge carrier transport within the Cu_2O films formed at low pH is slow.

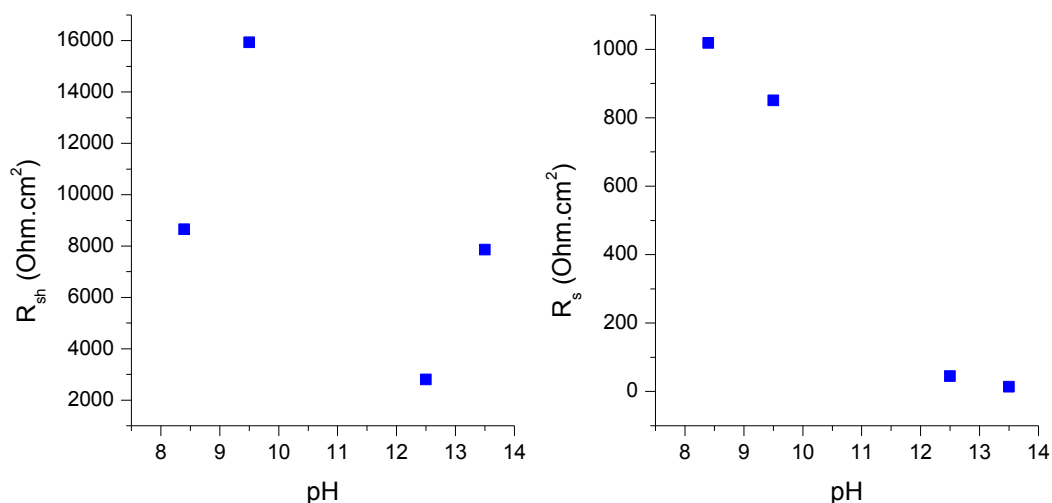


Figure 5-4: Shunt resistance and series resistance of solar cells fabricated using Cu_2O thin films deposited at different pH and applied potential (0.2 M CuSO_4 + 3 M lactic acid, 60°C).

5.3.3 Devices with deformed Cu_2O layer

Results in the previous section have demonstrated that $\text{Cu}_2\text{O}/\text{AZO}$ cells fabricated using Cu_2O layers which have partially dissolved and altered morphology show superior performance. In this section, the devices are further optimized by determining the deposition conditions that lead to the highest PCE. The deposition parameters investigated include temperature, $[\text{CuSO}_4]$, pH (pH > 12.5) and applied potential are investigated.

Figure 5-5 shows the effect of Cu_2O deposition temperature on the performance of $\text{Cu}_2\text{O}/\text{AZO}$ cells. Overall, the optimal deposition temperature is found to be $\sim 65^\circ\text{C}$. The Cu_2O films formed at 85°C tend to be easily detached from the FTO-glass substrate so that most of the resulting devices are too damaged to show photovoltaic properties. For those devices that do function, all three performance measures are extremely low. Furthermore, the corresponding R_s are very high ($\sim 1000 \text{ ohm cm}^2$) and comparable to those of devices with Cu_2O layers deposited from lower pH electrolytes (Figure 5-4).

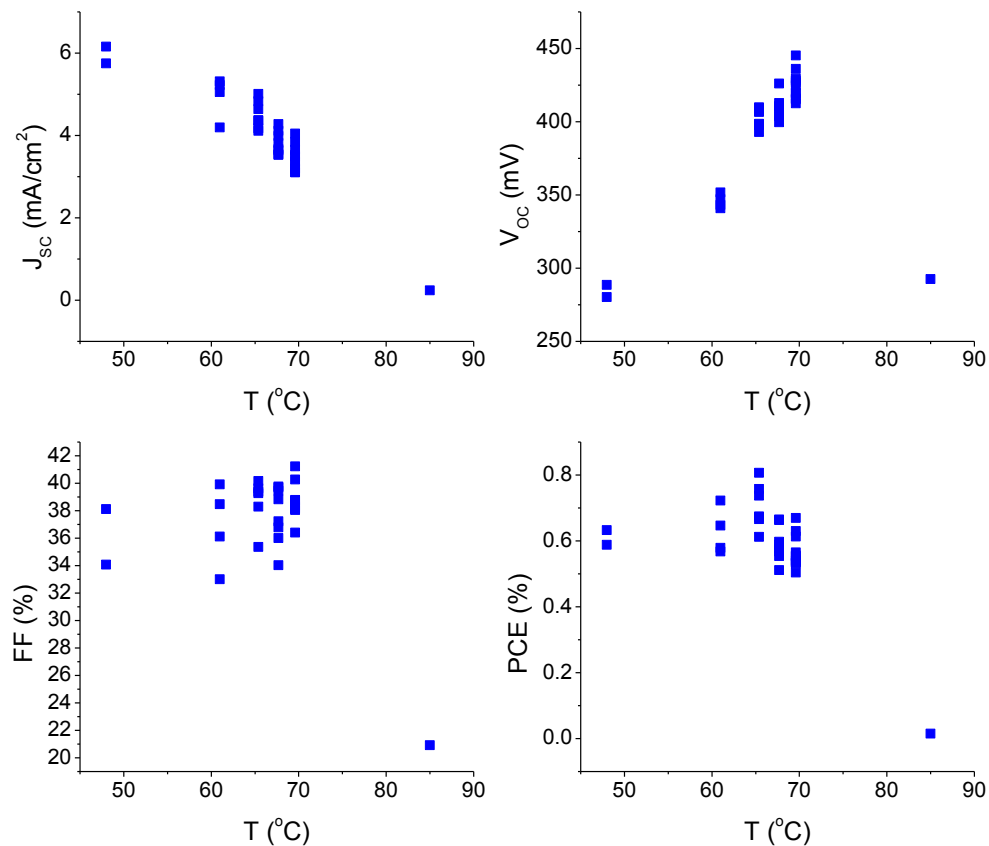


Figure 5-5: Effect of deposition temperature on device characteristics of solar cells fabricated using Cu_2O thin films produced in 0.2 M CuSO_4 + 3 M lactic acid electrolyte adjusted to pH 13.5 at -0.7V.

The device J_{sc} clearly decreases as the deposition temperature rises from 50°C to 85°C. Devices fabricated with Cu_2O films deposited at 50°C exhibit the highest J_{sc} values of $\sim 6 \text{ mA/cm}^2$, whereas they achieve values of $\sim 3\text{-}4 \text{ mA/cm}^2$ at 70°C and $\sim 0.24 \text{ mA/cm}^2$ at 85°C. The morphology of the Cu_2O layers (not included here) show a deformed grain structure when formed at all these temperatures, while no evidence of Cu formation is observed. Furthermore, as previously shown in Figure 4-16, Cu_2O films show higher degree of dissolution when formed at a lower temperature of 60°C. This agrees with the hypothesis presented in Section 5.3.1 that dissolution during Cu_2O deposition has a positive impact on device J_{sc} .

On the other hand, V_{oc} shows the exact opposite trend as it increases almost linearly with Cu_2O deposition temperature up to 70°C. The max V_{oc} observed up to this point is $\sim 450 \text{ mV}$, much higher than the other levels obtained for this system ($\sim 200\text{-}300 \text{ mV}$) that are shown in Table 5-2. This can be

attributed to either an improved $\text{Cu}_2\text{O}/\text{AZO}$ interface or a significant change in the electronic band structure. This second possible cause should also lead to the higher J_{SC} values observed for this system since a smaller bandgap should also improve the light absorption efficiency in the Cu_2O layer.

The device fill factor does not show a strong dependence on temperature. Most measured FF values with Cu_2O layer deposited at $50\text{--}70^\circ\text{C}$ are between 35% and 40%. The R_{sh} and R_{s} values in this temperature range also do not vary significantly, consistent with the effect on FF.

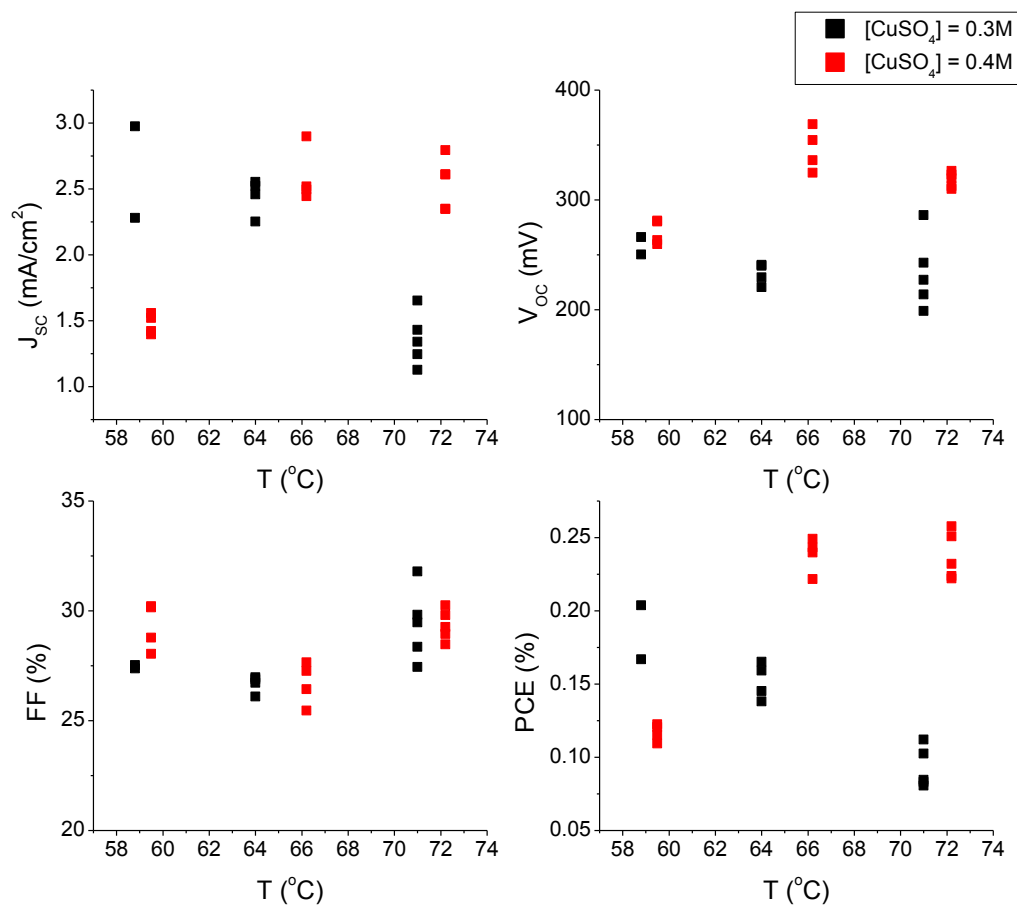


Figure 5-6: Effect of deposition temperature on device characteristics of solar cells fabricated using Cu_2O thin films formed in electrolytes containing 3 M lactic acid and 0.3 or 0.4 M CuSO_4 adjusted to pH 13.5 at -0.7V .

On the other hand, devices with Cu_2O layers deposited from electrolytes containing 0.3 or 0.4 M CuSO_4 show poorer performance than the ones containing Cu_2O formed in 0.2M CuSO_4 . Figure 5-6 shows the performance of devices containing Cu_2O deposited from 0.3 and 0.4 M CuSO_4 at temperatures from $\sim 58^\circ\text{C}$ to $\sim 72^\circ\text{C}$. The J_{sc} , V_{oc} and FF values are all lower than the ones presented in Figure 5-5. In

particular, the trend in which V_{OC} increases with Cu_2O deposition temperature is no longer observed and the maximum V_{OC} is ~ 370 mV and ~ 290 mV in 0.3M and 0.4M $CuSO_4$ electrolytes, respectively. These values are lower than the ones observed in devices containing Cu_2O formed at 0.2 M $CuSO_4$, but still higher than the typical V_{OC} formed using Cu_2O films deposited at lower pH as shown in Table 5-2, showing an increasing trend with the degree of deformation in the morphology, opposite to the trend observed from Figure 5-5. This suggests that the effect of dissolution on the Cu_2O band structure proposed above is likely not the only factor causing the improvement in the performance of devices containing Cu_2O formed at 0.2 M $CuSO_4$. It is also noted that the partially deformed Cu_2O films, as presented in Figure 4-18, are similar to the one observed for Sample 2-1 (pH 12.5, 0.2 M $CuSO_4$ +3M lactic acid, $60^\circ C$), for which the performance measures and PCE also lie within the same range of values. This is consistent with the argument that the degree of grain deformation is strongly correlated with performance improvement.

The combined effects of Cu_2O deposition pH and applied potential in high pH electrolytes are presented in Figure 5-7. Evidence of Cu formation is found at -0.75V (not included in the contour plots above) when the pH is 13.0 or lower and the resulting device performance is not comparable to those obtained at the same pH when the potential is more positive. Overall, an optimum PCE of 0.96% is obtained at pH 13.4 and applied potential of -0.72V. A strong dependence of performance variables on both parameters is observed. On the other hand, both V_{OC} and FF reach maximum values at pH 13.4 and a voltage of -0.7 ~ -0.72V. The maximum V_{OC} obtained is improved to ~ 550 mV, which is among the highest reported for devices with electrodeposited Cu_2O layer and similar to those obtained using alternative techniques such as PLD or thermal oxidation [87] and exceeding those using sputtering [71]. Some possible causes for this improvement are identified in literature, including improved interfacial morphology [53,65] and band alignment [86], as well as higher charge carrier mobility [79].

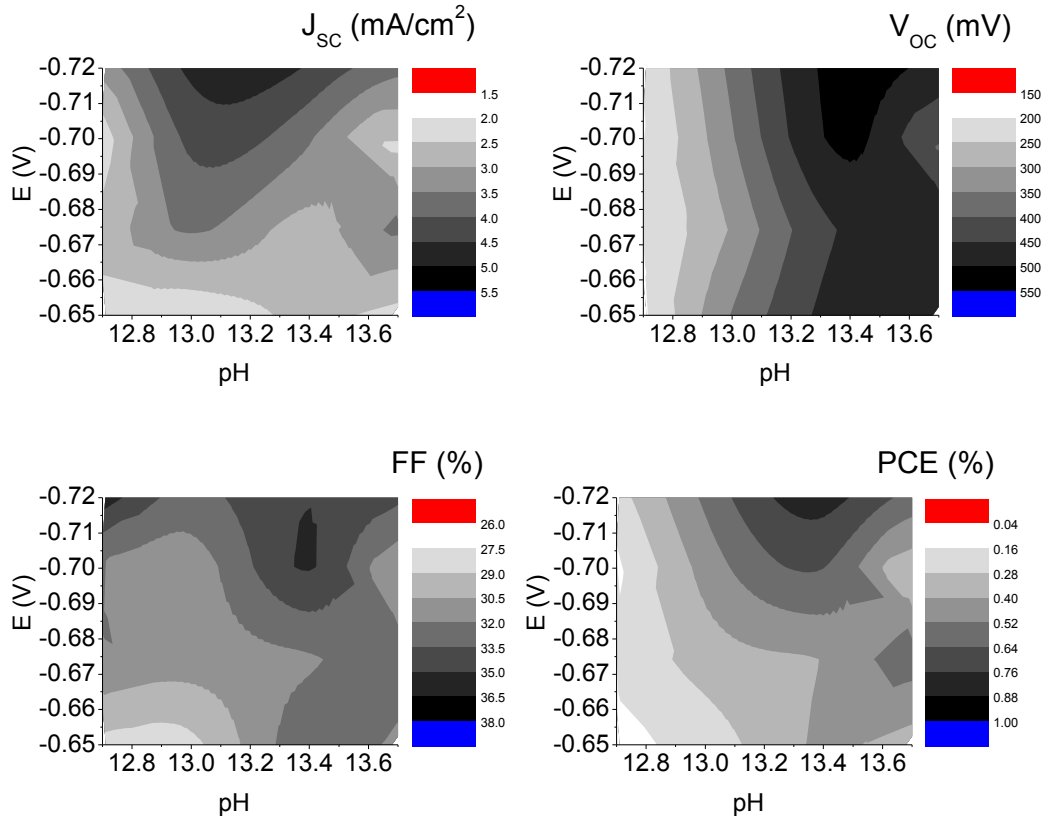


Figure 5-7: Effect of deposition pH (from ~ 12.7 to 13.7) and potential (from -0.65V to ~ -0.72V) on device characteristics of solar cells fabricated using Cu_2O thin films deposited at 65°C in 0.2 M $\text{CuSO}_4 + 3$ M lactic acid electrolyte.

5.3.4 Back-illumination

Up to this point, all solar cell samples are tested by illuminating from the front (n-type) side. However, it is well-known that the cell performance can vary significantly with the direction of the incident light relative to the device depending on the absorption spectrum of the active layer, as well as the electron and hole mobilities. Figure 5-8 shows the typical J-V curves of devices containing Cu_2O formed at pH 9.5, 12.5 and 13.4 and illuminated from either the front or back. It appears that the difference between back-illuminated and front-illuminated cell performance is heavily dependent on the Cu_2O film properties. The behavior of device with a Cu_2O layer deposited at pH 9.5 is not very different for front-illumination and back-illumination. On the other hand, when Cu_2O is deposited at pH 12.5, both performance variables are

noticeably lower when illuminated from the back. At pH 13.5, back-illumination leads to much better performance, with a PCE as high as 1.55% being achieved by the top-performing device (pH 13.4, -0.72V, 65°C). This is by far the highest PCE reported for Cu_2O -based solar cells fabricated using electrodeposited Cu_2O thin films, with no additional interlayer and extraction layer in the device structure. The same trend where the back-illumination PCE is found to be similar to that achieved using front-illumination at pH 9.5 and much lower at pH 12.5, is also observed in all devices presented in Section 5.2.2, as summarized in Table 5-4.

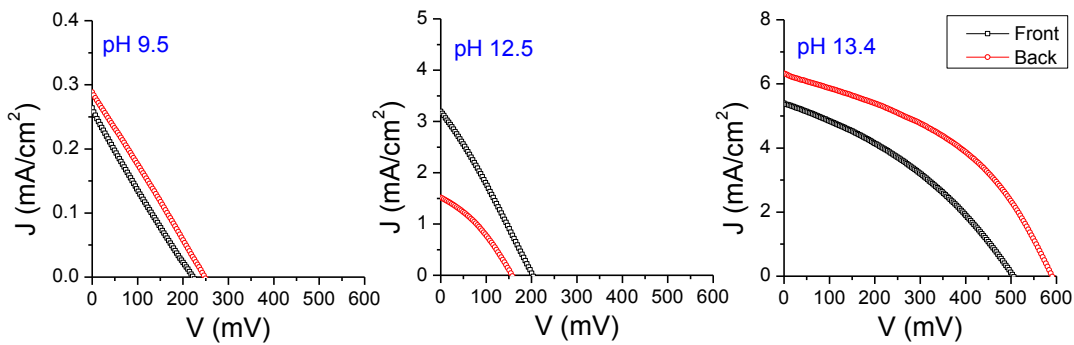


Figure 5-8: J-V characteristics of solar cells fabricated using Cu_2O thin films deposited at different pH, potential and temperature illuminated from the front or back of the device. The electrolyte contains 0.2 M CuSO_4 + 3 M lactic acid in all cases.

Table 5-4: Summary of front- and back-illuminated Cu₂O/AZO device performance

Sample	Deposition conditions				Cell performance							
	$[CuSO_4]$ (M)	pH	E vs SCE (V)	T (°C)	Front Illumination				Back illumination			
					J_{sc} (mA/cm ²)	V_{oc} (mV)	FF (%)	PCE (%)	J_{sc} (mA/cm ²)	V_{oc} (mV)	FF (%)	PCE (%)
1-1	0.2	9.5	-0.4	60	0.346	218.5	23.3	0.018	0.346	174.5	26.7	0.016
1-2				75	0.228	200.9	24.5	0.011	0.105	141.0	27.3	0.004
1-3			-0.55	60	0.197	197.1	23.5	0.009	0.111	149.3	27.7	0.005
1-4				75	0.274	185.7	23.6	0.012	0.223	150.7	27.6	0.009
2-1	0.2	12.5	-0.5	60	2.760	240.7	32.6	0.217	1.141	195.7	36.3	0.081
2-2				75	2.488	199.8	29.2	0.145	1.017	147.9	35.0	0.053
2-3			-0.65	60	3.170	200.4	28.0	0.178	1.519	156.7	33.6	0.080
2-4				75	1.403	161.5	22.6	0.051	0.735	102.9	27.6	0.021
3-1	0.4	9.5	-0.4	60	0.310	241.6	23.9	0.018	0.286	255.5	25.7	0.019
3-2				75	0.116	146.0	24.7	0.004	0.093	94.8	24.8	0.002
3-3			-0.55	60	0.377	186.2	24.5	0.017	0.112	168.4	25.0	0.005
3-4				75	0.517	220.7	25.3	0.029	0.252	172.0	27.4	0.012
4-1	0.4	12.5	-0.5	60	1.678	198.9	33.4	0.112	0.562	147.7	33.9	0.028
4-2				75	0.507	201.4	31.5	0.032	0.089	110.3	27.7	0.003
4-3			-0.65	60	2.632	176.2	27.8	0.129	1.025	139.7	34.1	0.049
4-4				75	3.091	212.4	29.2	0.192	0.851	156.3	35.9	0.048

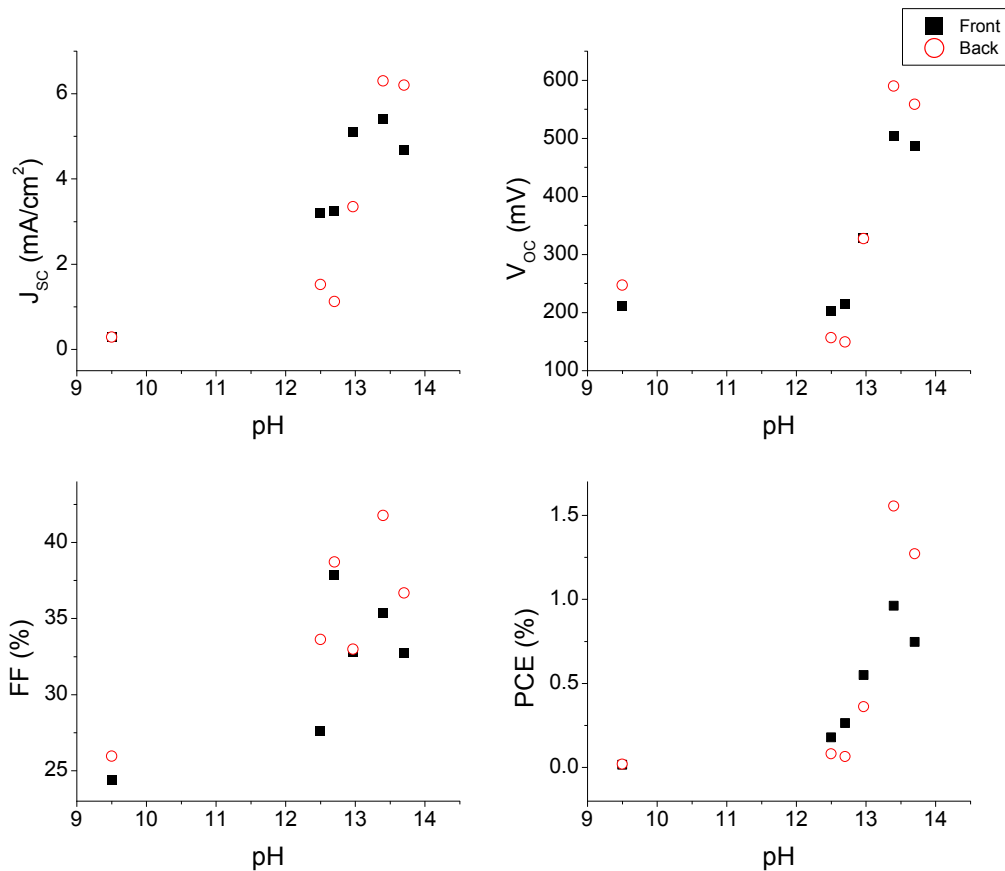


Figure 5-9: Effect of deposition pH on device characteristics of solar cells fabricated using Cu_2O thin films formed in 0.2 M CuSO_4 + 3M lactic acid illuminated from the front or back.

The effect of back-illumination is further examined by comparing the effect of deposition pH on the individual performance variables (Figure 5-9). Overall, the PCE of back-illuminated devices is less than front-illuminated devices at pH values below 13, but superior at higher pH values. An abrupt increase in both front- and back-illuminated PCE is observed when electrolyte pH increases beyond 12.5, although the improvement is steeper in back-illuminated devices. In particular, J_{sc} of front-illuminated devices increases almost linearly with pH from pH 9.5 to 13.5, whereas back-illuminated J_{sc} shows less improvement between pH 9.5 and 12.5, but increases sharply and exceeding front-illuminated J_{sc} at higher pH. Similarly, V_{oc} also exhibits a larger increase in back-illuminated devices at the pH is raised to 12.5 or higher so that it is higher than that for front-illumination above pH 13. V_{oc} for the device containing Cu_2O deposited at pH 12.5 is found to be much lower than at pH 9.5 for back-illuminated

devices, contributing to the inferior performance observed. On the other hand, back-illuminated devices tend to have better FF overall than front-illuminated devices at all pH investigated although the exact reason cannot be determined at this point as both R_s and R_{sh} appear to be influencing the device behavior (Figure 5-10). As shown in the plots, when the device is back-illuminated, an improved shunt resistance is observed below pH 13.4, whereas the improvement in series resistance is more significant above pH 13.4.

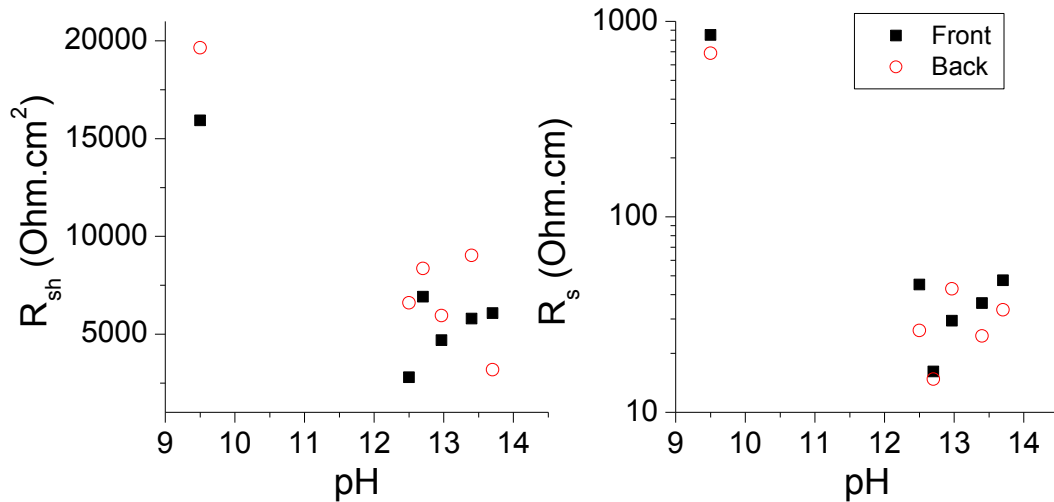


Figure 5-10: Effect of deposition pH on R_{sh} and R_s of solar cells fabricated using Cu_2O thin films formed in 0.2 M $CuSO_4$ + 3 M lactic acid illuminated from the front or back of the device.

5.4 Discussion

5.4.1 Effect of high-electrolyte pH

The above results present the influence of Cu_2O morphology on device performance. The films fabricated with Cu_2O layers deposited from electrolytes with pH above 13, when partial dissolution of the Cu_2O is observed, lead to far superior cell performance than the other samples. The purpose of this section is to identify some key properties that may be responsible for the observed improvement in order to determine the origin of this effect as well as identify some limitation of the devices presented in this section.

Band gap

Figure 5-11a shows the UV-vis absorption spectra of Cu_2O thin films (corresponding to devices presented in Section 5.3.2). The Cu_2O films deposited at pH 9.5 and 12.5 show similar absorption profiles. A drop in the absorption intensity is observed at ~ 500 nm in the film deposited at pH 9.5, whereas the drop in absorption occurs at a slightly longer wavelength of ~ 540 nm for the one deposited at pH 12.5. On the other hand, a more gradual change in absorptivity is observed in the Cu_2O thin film deposited at pH 13.5, beginning at a much shorter wavelength of ~ 350 nm. This indicates that the bandgap in Cu_2O formed at pH 13.5 where some dissolution occurs is smaller than that of the typical film with cubic Cu_2O grains.

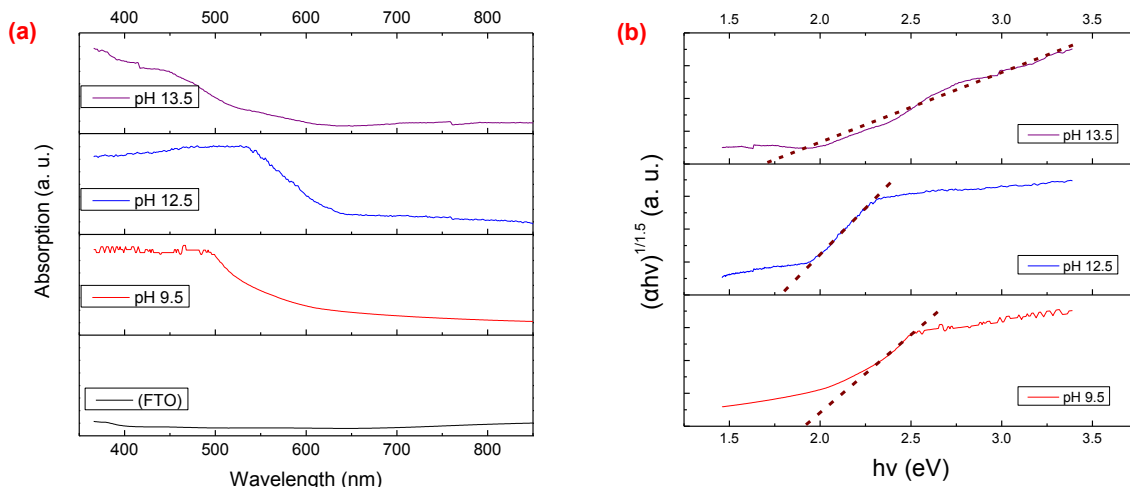


Figure 5-11: (a) UV-vis absorption spectra of Cu_2O films ($\sim 2\mu\text{m}$) deposited at different electrolyte pH. Plots are normalized for comparison purpose. Absorption spectrum of FTO substrate is shown in the bottom. Tauc plots for bandgap calculation are presented in (b).

This effect is confirmed by fitting the absorption spectra using Tauc plots, as demonstrated in Figure 5-11b. In each case, the best fitting plots are obtained using an exponent of 1.5 corresponding to a direct forbidden transition, in agreement with the electronic properties of Cu_2O discussed in Section 3.3.2. By fitting the linear region of the plots (dashed lines), estimated bandgaps of 1.92, 1.82, and 1.70 eV are obtained at deposition pH of 9.5, 12.5, and 13.5 respectively. The first two values are consistent with typical reported bandgaps for Cu_2O , while the latter is noticeably smaller. This suggests that the improved

performance in devices with partially dissolved Cu_2O layers can be at least partially attributed to the broader absorption region, which would result in a higher light absorption efficiency and J_{SC} .

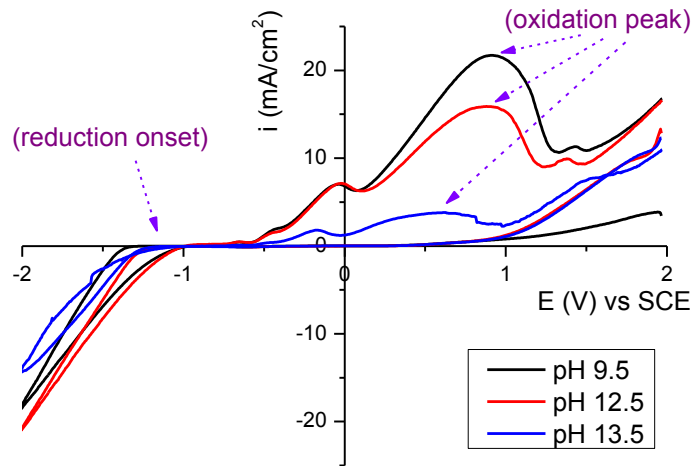


Figure 5-12: Cyclic voltammograms of Cu_2O films ($\sim 2\mu\text{m}$) deposited at different electrolyte pH.

The bandgaps of these films are also estimated using cyclic voltammetry (Figure 5-12). The calculated results show good agreement between the two techniques, as summarized in Table 5-5. In addition, it is also found from the cyclic voltammograms that the decrease in bandgap of Cu_2O films with dissolved and reformed morphology is mainly due to a shift in the valence band, as indicated by the position of the oxidation peak. This change in valence band position in theory reduces the maximum obtainable V_{OC} from the device, as discussed in Section 2.1.3, although the actual attained V_{OC} of the device is not expected to be affected by this factor since the V_{OC} is limited by the work function of the FTO anode rather than the Cu_2O valence band.

Table 5-5: Bandgap of Cu_2O thin films as measured by different techniques

E_g (eV)	pH 9.5	pH 12.5	pH 13.5
UV-vis absorption	1.92	1.82	1.70
cyclic voltammetry	2.08	1.92	1.72

It is also worth noting that the bandgap values measured using cyclic voltammetry is consistently larger than that using UV-vis absorption, as shown in Table 5-5. This discrepancy is known to be the result of the different mode of charge carrier generation/injection between the two techniques, as discussed in Section 3.3.2. However, at pH 13.5, the measured values are much closer to each other than

in other cases. This possibly implies that the behavior of the FTO/Cu₂O interface has been altered significantly due to dissolution and that the energy barrier at this interface is reduced as a result. This would potentially improve J_{SC} , V_{OC} and the fill factor of the device, although the actual bandgap of the Cu₂O thin film is unlikely to be affected.

Charge carrier concentration and mobility

The charge carrier concentration and mobility of the Cu₂O films deposited at different electrolyte pH, as obtained using the SCLC techniques with an FTO/Cu₂O/Al structure, are presented in Figure 5-13. As discussed in Section 3.3.2, the values obtained are the hole concentration and the mobility of the high-mobility charge carriers. Overall, a hole concentration on the order of $10^{14} \sim 10^{15} \text{ cm}^{-3}$ is found in all samples presented above, which agrees with reported range in typical electrodeposited Cu₂O thin films [47,63]. Also, the carrier concentration and mobility for films deposited at pH 9.5 and 12.5 are similar, while the carrier concentration is consistently lower and the mobility higher at pH 13.5. The effect is especially significant for the carrier mobility values in the 2- μm films typically used for device fabrication. The estimated carrier mobility in Cu₂O films deposited at pH 9.5 and 12.5 is $\sim 5 \text{ cm}^2/\text{Vs}$ and $\sim 30\text{-}50 \text{ cm}^2/\text{Vs}$ at pH 13.5, almost an order of magnitude higher. In addition, we also observe that the carrier mobility of the thin films tends to rise slightly with increased thickness. This suggests that the defects in the Cu₂O films are not distributed evenly within the film. More defects may be formed at the beginning of the electrodeposition process and decrease over time. The fact that the hole concentration is reduced in the pH 13.5 sample also indicates that the change in bandgap as noted in Section 5.4.1 is not due to the incorporation of Cu(II) species, which has been reported as a possible method for bandgap control without extrinsic doping [129].

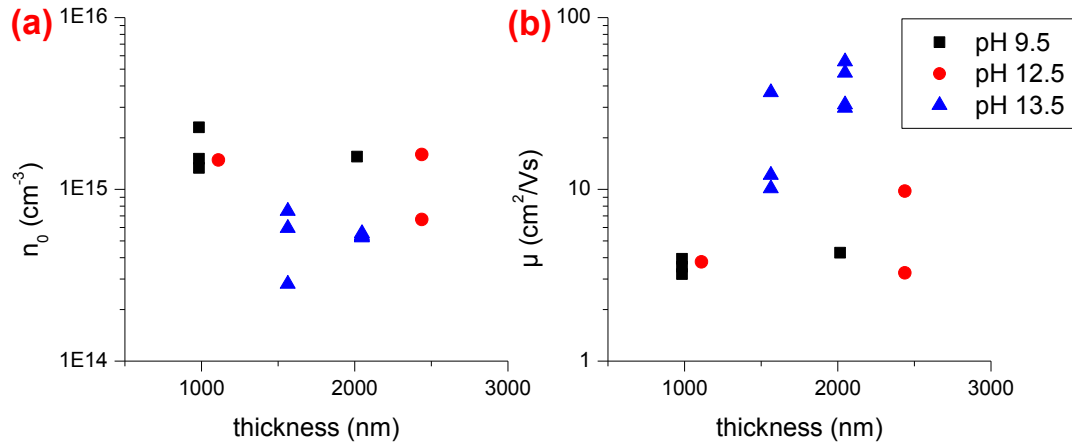


Figure 5-13: Charge carrier (a) concentration and (b) mobility of Cu_2O thin films deposited at different pH. Values are obtained using SCLC techniques with FTO/ Cu_2O /Al structure.

In addition, a negative correlation between carrier concentration and mobility is found in the films presented above, as shown in Figure 5-14. This agrees with previous reports on Cu_2O deposited using different techniques [35,137,198–200], as well as for other common semiconductors. The difference in charge carrier concentration and mobility in Cu_2O thin films deposited at high pH can be explained by its effect on the morphology. As the Cu_2O grains dissolve and reform, some grain boundaries may merge together, which could cause the reduction of the Cu defect and hole concentrations. However, at the same time, this could cause fewer traps to exist, thereby reducing the hole-electron recombination rate and improving the carrier mobility. If so, the high carrier mobility of the reformed Cu_2O films is the key factor contributing to the high J_{SC} observed in the corresponding devices.

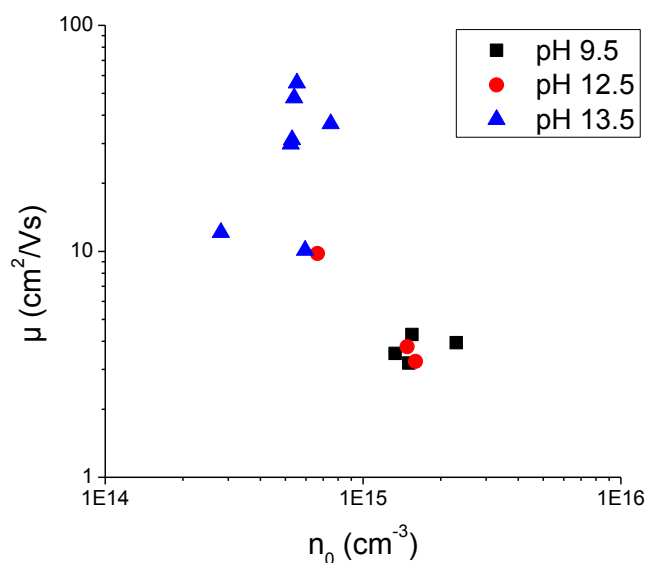


Figure 5-14: Correlation between hole concentration and mobility of Cu₂O thin films deposited at different electrolyte pH. Values are obtained using SCLC techniques with FTO/Cu₂O/Al structure.

Characterization of the Cu₂O films using SIMS has also been conducted in order to compare the Cu vacancies in the various samples. Figure 5-15a presents the SIMS profiles for samples deposited at pH 9.5 and 13.5 down to a depth of ~300 nm below the initial surface. While the amounts of Cu⁺ are similar in the two samples, a noticeable difference can be observed in the O²⁻ intensities. This effect can be seen more clearly by plotting the ratio of the sputtered Cu⁺ and O²⁻ intensities from the two samples in Figure 5-15b. Although the exact defect concentration is unknown, it is clear that the Cu:O ratio is considerably higher in the film deposited at pH 13.5, indicating a lower Cu vacancy concentration, as also shown in the SCLC data. In addition, the Cu:O ratio is found to decrease slightly as the sputter depth increases and moves closer to the FTO substrate. Such a trend suggests that the Cu vacancy concentration decreases as deposition continues and thickness increases, which is also consistent with that observed using the SCLC technique.

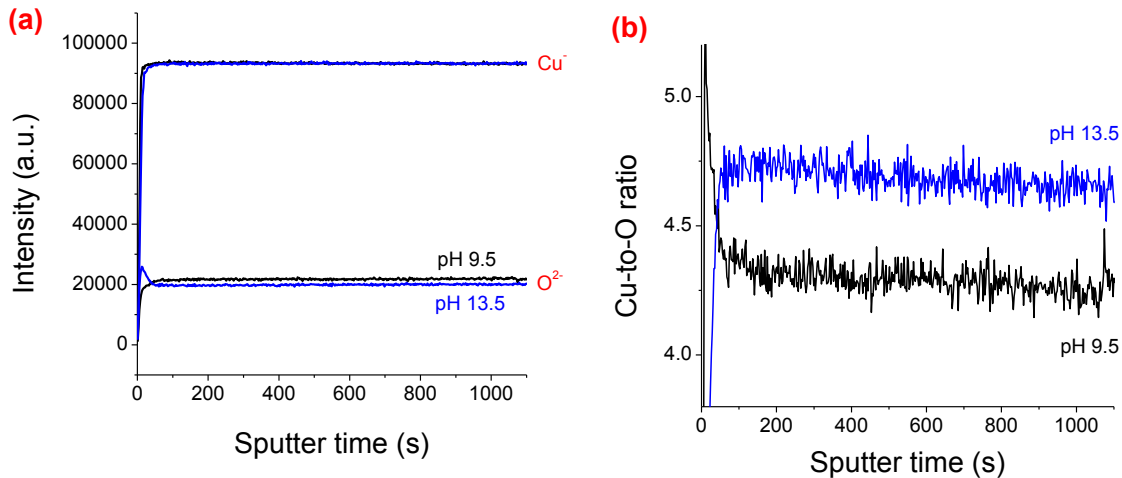


Figure 5-15: (a) SIMS profiles of Cu⁺ and O²⁻ intensities with sputter time and (b) Cu:O intensity ratios for samples deposited at pH 9.5 and 13.5

Furthermore, the hole mobility of films with $\sim 2\mu\text{m}$ thickness is measured using FTO/Cu₂O/Au structure. Figure 5-16a compares the measured mobility values using Al and Au top contacts. It is found that the mobility values obtained from the two measurements are within a similar range for the thin films deposited at pH 12.5, suggesting that the hole mobility is likely higher than the electron mobility, although the latter cannot be determined from available data. On the other hand for film deposited at pH 9.5 or 13.5, the mobility values measured using FTO/Cu₂O/Al structure are higher by an order of magnitude than with an Au top contact. This indicates that the values obtained using the FTO/Cu₂O/Al structure as presented in Figures 5-13 and 5-14 correspond to the electron mobility, and that the electrons have much higher mobility than holes for Cu₂O films deposited in these conditions. The electron and hole mobility of $\sim 2\mu\text{m}$ Cu₂O thin films are plotted in Figure 5-16b. It is found that the effect of dissolution is more significant on electron mobility than hole mobility. In particular, a noticeable decrease in hole mobility is observed as the pH increases from pH 12.5 to 13.5, indicating that there are other factors which have a negative impact on the hole mobility beside dissolution. One possibility is that the hole mobility in the Cu₂O thin films is higher in $\langle 111 \rangle$ -oriented crystals than in $\langle 100 \rangle$ orientation [173], and as the deformed film at pH 13.5 no longer has a preferred $\langle 111 \rangle$ orientation, the hole mobility would be negatively affected despite the more favorable grain structure.

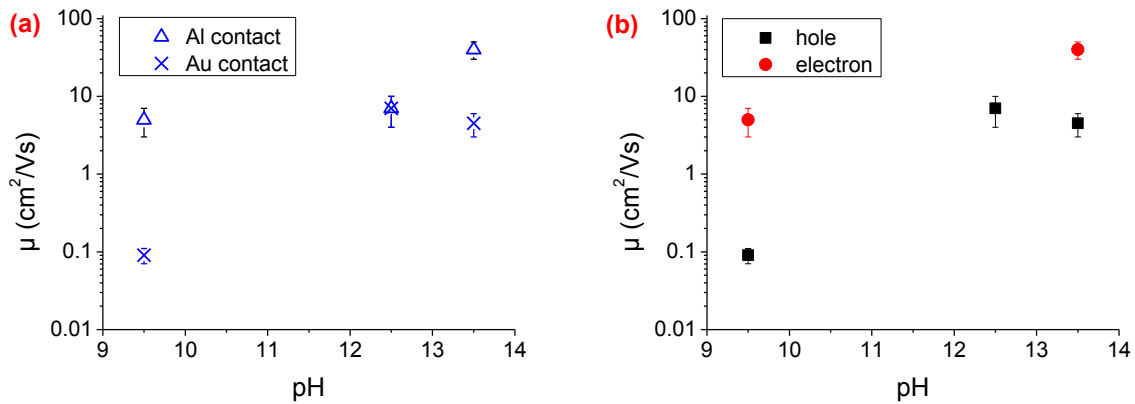


Figure 5-16: (a) Measured charge carrier mobility using different contact materials and (b) electron and hole mobility of Cu_2O thin films deposited at different pH.

In addition, in all three cases, the values of electron and hole mobilities in the same film are different by more than an order of magnitude. The Cu_2O films deposited at pH 9.5 and 13.5 have higher electron mobility, while hole mobility becomes higher at pH 12.5. This non-monotonic trend suggests that it is likely the electron and hole mobility in the Cu_2O films are being affected by different factors. The observed differences are also consistent with the front- and back- illuminated device results presented in Section 5.3.4. When the light is illuminated from the front of the device, more charge carriers are generated close to the n-type side of the device. The photogenerated electrons can easily reach the p-n interface, while the holes are required to travel through the Cu_2O film before reaching the anode. The opposite happens with back-illumination when more electrons than holes are required to travel a longer distance. Therefore, when the electron and hole mobilities are significantly different from each other, the performances of front- and back-illuminated devices will show a large difference. At pH 12.5, the hole mobility is higher than the electron mobility, thus the back-illuminated PCE is much lower than that the front-illuminated PCE, whereas the opposite is observed as pH 9.5 and 13.5 with higher electron mobility.

5.4.2 Limitations

As mentioned previously, the simple FTO/ Cu_2O /AZO structure has been selected in order to reduce possible sources of errors and most clearly determine the effect of Cu_2O morphology on device

performance. This device structure, while showing good reproducibility, is not considered the most efficient design for the Cu_2O solar cells. This section discusses several non-idealities that limit the device performance, as well as the potential techniques to address them.

Cu_2O film roughness

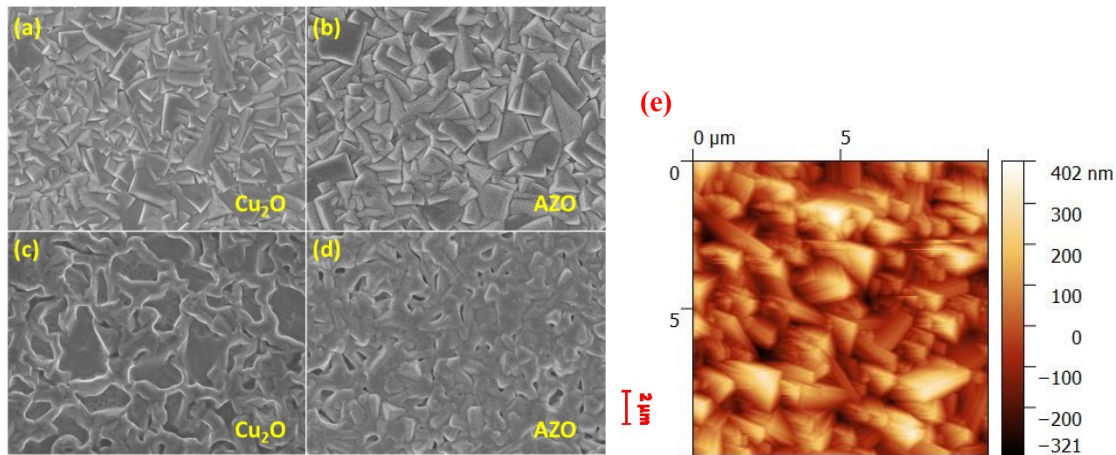


Figure 5-17: SEM images of Cu_2O and AZO surfaces used in devices with: (a, b) typical cubic Cu_2O morphology (0.2 M CuSO_4 + 3 M lactic acid, pH 12.5, 60°C, -0.65V, thickness $\sim 2\mu\text{m}$) and (c, d) typical dissolved and reformed morphology (0.2 M CuSO_4 + 3 M lactic acid, pH 13.5, 65°C, -0.72V, thickness $\sim 2\mu\text{m}$). AFM image for (a) is shown in (e)

Figure 5-17 presents the AZO layer on a 2- μm Cu_2O film with either cubic (Figure 5-17 a, b) or partially dissolved and reformed (Figure 5-17 c, d) morphology. In both samples, the Cu_2O surface appears to be relatively rough, with grain size on the micron scale. This is supported by the roughness values estimated using AFM technique. Figure 5-17e shows an AFM image of the sample corresponding to Figure 5-17a, which consists of features up to a few hundred nanometers and has an estimated roughness of ~ 111 nm. The roughness of the partially dissolved and reformed Cu_2O sample has not been measured although features with heights in the 1-micron range are observed, indicating an even rougher surface.

As a result, the thickness of the n-type AZO layer sputtered on top of Cu_2O is likely non-uniform since its average value is only 300 nm, which is on the same order as the Cu_2O grains on the surface. This is supported by the SEM images of the AZO films (Figures 5-17 b and d), in which some portions of the Cu_2O layer (corners of cubic grains) are still exposed looking down on the top of the AZO layer,

suggesting possible pinholes. An uneven n-type AZO layer likely contributes to the loss of J_{SC} and FF since this would significantly reduce the effective device area and shunt resistance because of pinhole formation. In addition, due to the higher roughness of the partially dissolved and reformed Cu_2O films, it is unlikely that cells fabricated using these films will have better AZO coverage than the films containing cubic Cu_2O grains.

Since both the surface morphology and bulk properties of the Cu_2O film are determined by the deposition conditions, it would be difficult to modify the deposition procedure in order to reduce the surface roughness only without affecting other aspects of the device performance. However, post-treatment methods such as chemical mechanical polishing may be helpful to resolve this issue. Alternative techniques such as ALD can also be used to deposit more uniform AZO layers [100].

Interfacial defects

In addition to the roughness effect, the chemical state at the Cu_2O/AZO also limits the performance of the resulting device. In particular, the formation of CuO and surface contamination are likely two key limitations. The former is a known issue during Cu_2O solar cell fabrication, as discussed in Section 2.2.2, but difficult to resolve without using all-vacuum processing or post-deposition treatment.

Figure 5-18 shows the SIMS profiles of C and OH^- of the Cu_2O thin film formed at pH 9.5 and 13.5. A noticeably higher carbon and hydroxide content is found at the surface of the as-deposited film, which is a clear indication that some organic compound is left at the surface of the Cu_2O film prior to AZO deposition, most likely lactate ions from the electrolyte used for electrodeposition. Similar result is found for all electrolyte pH and is considered to be a limitation of the device design. It is noted that while the carbon intensity diminishes to zero within 100 s sputter time, the presence of hydroxide is detected throughout the measurement for all samples, and the intensities are found to be vastly different even in the bulk of the thin films. This is likely due to the fact that the measurement of hydroxide is highly sensitive to the system pressure during the SIMS measurement process, and as a result different OH^- baseline may be found for each measurement. Therefore, although a clear presence of OH^- species is found on the

surface of all Cu_2O films, no conclusion can be drawn on their relative amounts based on available data. The presence of residual lactate at the Cu_2O surface would result in additional trap sites at the $\text{Cu}_2\text{O}/\text{AZO}$ interface, which significantly lowers the fill factor of the device. Possible methods to address this issue include ultrasonic cleaning of the Cu_2O surface prior to AZO deposition, as well as chemical mechanical polishing which also removes surface CuO and reduces film roughness.

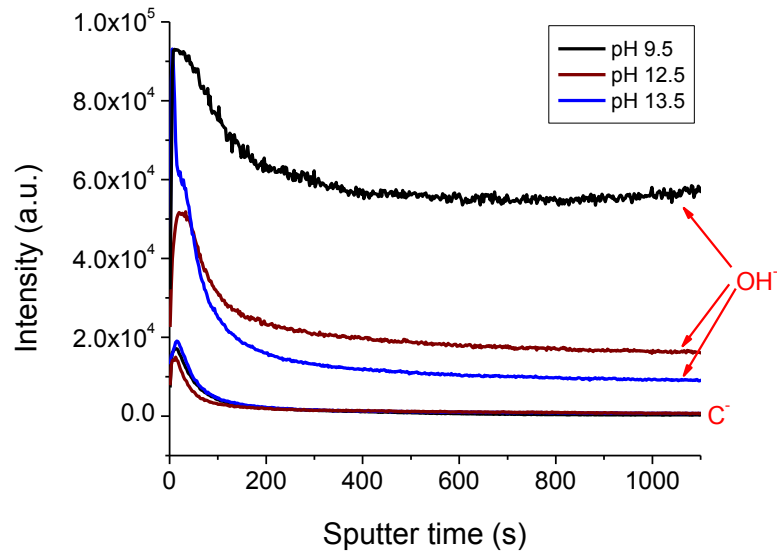


Figure 5-18: SIMS profiles of OH^- and C^- intensities with sputter time for Cu_2O films deposited at different electrolyte pH

Surface resistivity

Another possible limitation is the relatively high surface resistivity of sputtered AZO films in comparison with metals, which makes it less preferable as the top contact. For front-illuminated devices, the addition of a top contact will significantly lower the effective device area exposed to the incident light. On the other hand, no shadowing effect would occur in back-illuminated devices since the light is shone on the device from the FTO-side. In this section, we present the effect of depositing an Al contact (~100 nm) on top of the n-type AZO layer by thermal evaporation in an attempt to improve surface conductivity and probe contact.

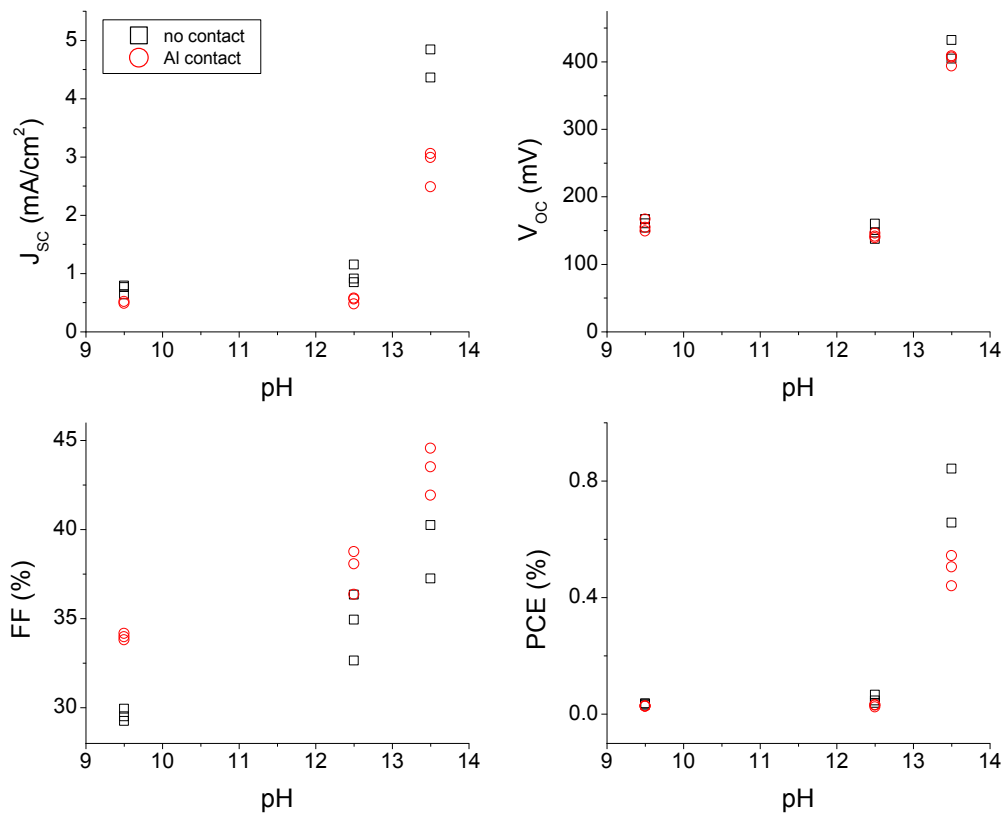


Figure 5-19: The effect of deposition pH on device performance for back-illuminated solar cells with and without an Al top contact.

Figure 5-19 compares the device performance of FTO/Cu₂O/AZO and FTO/Cu₂O/AZO/Al cells fabricated under otherwise identical conditions. The addition of the Al top contact appears to have little effect on the V_{OC} , whereas it tends to lower the J_{SC} and raise the FF in all devices. The deposition of Al as top contact for the Cu₂O/AZO devices investigated in this project is overall not recommended since the improvement of FF does not compensate the reduction in J_{sc} , especially in the higher-efficiency devices.

The drop in J_{SC} can be attributed to the slight mismatch in electronic energy levels at the AZO/Al interface. The work function of Al is reported to be between 4.1 and 4.3 eV, which places it slightly above the conduction band of ZnO (~ -4.4eV) in the energy band alignment. This would cause a significant loss of free electrons at the interface due to recombination. On the other hand, the higher FF likely arises due to the improved surface conductivity, as is the purpose of using an additional metallic top

contact. The effect of a non-uniform AZO layer, as discussed in Section 5.4.3, is significantly offset by the increase in surface conductivity.

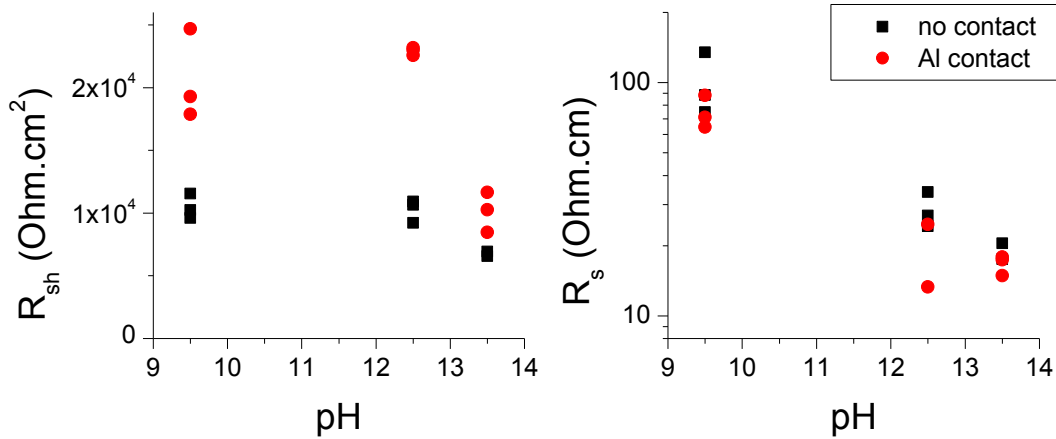


Figure 5-20: Effect of deposition pH on R_{sh} and R_s of back-illuminated solar cells with and without an Al top contact.

Measurement of the R_{sh} and R_s values for these devices also yields values that are consistent with these proposals. As shown in Figure 5-20, devices with Al top contacts exhibit lower R_s and higher R_{sh} overall, suggesting a significant improvement in the device architecture and that the loss in FF is one of the limitations of the FTO/Cu₂O/AZO cells structures that do not include a top contact layer. Consequently, the deposition of a top contact, possibly one with a slightly higher work function than Al, is another possible method to improve the performance of devices reported in this section.

5.5 Summary

In this chapter, solar cells fabricated using potentiostatically deposited Cu₂O and sputtered AZO are investigated. The pH during deposition of Cu₂O has the most prominent effect on the device performance. Performance measures including J_{SC} , V_{OC} and FF all improve significantly as the deposition pH increases. The optimal deposition conditions for this cell structure are found to be an electrolyte containing 0.2 M CuSO₄ and 3.0 M lactic acid adjusted to pH 13.4, temperature of 65°C and applied potential of -0.72 vs. SCE. The top device efficiency obtained is ~1.55%, which exceeds that reported in most previous studies on cells containing electrodeposited Cu₂O as the p-type material.

The reason for the improved efficiency is attributed to the partial dissolution and reformation of Cu_2O grains at high pH. This mechanism appears to improve the carrier mobility in the Cu_2O layer, as well as narrow the bandgap of the thin film. On the other hand, a low carrier concentration in Cu_2O , non-uniform AZO layer and low AZO surface conductivity are identified as some of the limitations in the above devices. In addition, when Cu_2O films are deposited at the same pH (12.5 or lower), the device efficiency improves as the fraction of grains with $\langle 111 \rangle$ -orientation increases.

Chapter 6. Alternative Procedures for Cu₂O Electrodeposition

6.1 Introduction

In Chapters 4 and 5, the effect of a number of variables on Cu₂O film morphology and device performance resulting quiescent electrolytes using constant potential has been studied. In this chapter, we investigate the use of less common electrodeposition procedures to produce the Cu₂O layers in solar cells, namely galvanostatic deposition, pulsed electrodeposition and deposition from stirred electrolytes, in order to further improve the electrodeposited Cu₂O film properties and corresponding device performance.

Parts of the results presented in this chapter (Section 6.3.3) are adapted from published work [185].

6.2 Galvanostatic Deposition

6.2.1 Background

Although both potentiostatic and galvanostatic deposition techniques often utilize DC current and lead to similar film morphologies [147,153,161], the latter has been less commonly used since it is normally expected that the film morphology can be better controlled by selection of the cathode potential. On the other hand, galvanostatic deposition tends to produce smoother films, especially during the initial stage of the deposition, which is preferred for solar cell applications [84].

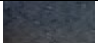







In terms of photovoltaic applications, Abdelfatah et al have compared the two modes of electrodeposition for the fabrication of Cu₂O/AZO solar cells and found that galvanostatic deposition tends to yield a better device fill factor, whereas constant applied potential leads to higher J_{SC} and V_{OC} levels [84]. However, Izaki et al have shown that the V_{OC} of Cu₂O/ZnO devices can be increased to as high as 590 mV and the PCE to ~1.28% by adjusting the applied current density during galvanostatic deposition [72].

6.2.2 Experimental

Galvanostatic electrodeposition of Cu_2O is performed in electrolytes containing 0.2 M CuSO_4 and 3 M lactic acid, adjusted to pH 12.5 with NaOH pellets using the standard three-electrode setup described in Section 3.2.1. The deposition temperature is maintained at either 40°C or 60°C. The potential transients are recorded during electrodeposition. All potentials are reported with reference to the SCE scale. The applied current density is calculated after deposition using the exact superficial deposit area. The metallic Cu content in the thin films is calculated using Eq. 3-2. Devices with Cu_2O film thickness $\sim 1.8\mu\text{m}$ – $2.3\mu\text{m}$ are fabricated and characterized as described in Section 5.2.1.

6.2.3 Results and Discussion

Table 6-1: Estimated thickness of Cu_2O films galvanostatically deposited from 0.2 M CuSO_4 + 3 M lactic acid electrolyte adjusted to pH 12.5.

T (°C)	i (mA/cm ²)	d _{Faraday} (nm)	d _{actual} (nm)	% Cu	Color
40	1.21	2339	2064	11.8%	
	0.96	2010	1898	5.3%	
	0.75	2321	2226	3.8%	
	0.38	1567	1541	1.5%	
60	1.08	1852	1820	1.6%	
	0.80	1660	1650	0.5%	
	0.65	2020	1979	1.9%	
	0.45	1896	1884	0.6%	

The films deposited at 40°C from the 0.2 M CuSO_4 + 3M lactic acid electrolyte at pH 12.5 tend to have a bluish tint at an applied current density higher than 0.5 mA/cm², as summarized in Table 6-1. This is clear evidence of the simultaneous formation of Cu_2O and Cu metal, as pure Cu_2O thin film is typically red in color. This conclusion is supported by a comparison between film thickness calculated from Faraday's Law using total charge and the actual deposit mass. Films with blue coloring have a significantly lower deposit mass than estimated from Faraday's Law, suggesting that a significant amount of Cu(0) is present in the film, as discussed previously in Section 3.2.1. On the other hand, films formed

at a lower current density of 0.38 mA/cm^2 , as well as as those deposited at $60 \text{ }^\circ\text{C}$ or higher appear to contain Cu_2O only.

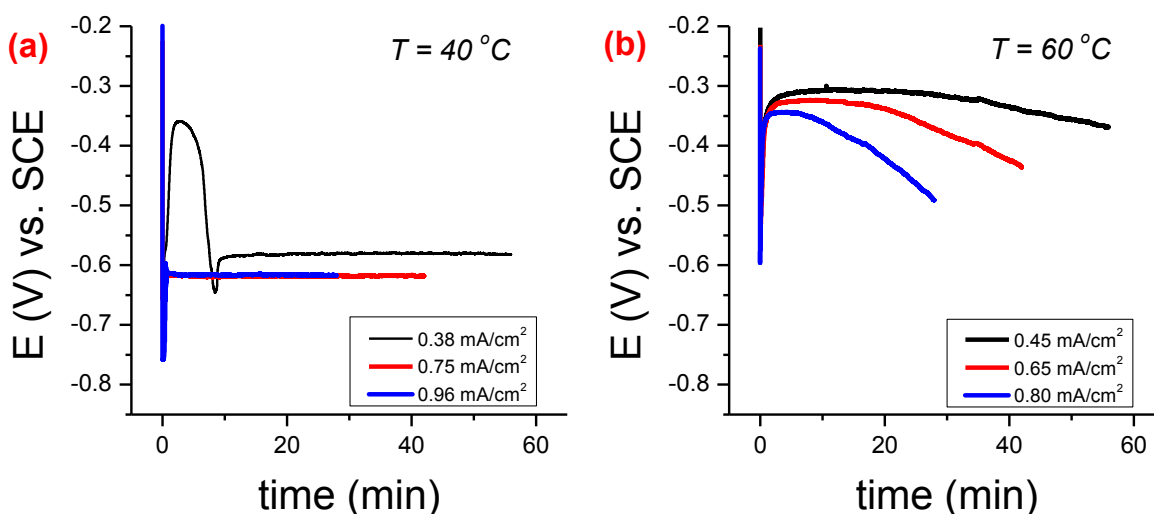


Figure 6-1: Potential transient curves during deposition of Cu_2O films in electrolyte containing $0.2 \text{ M CuSO}_4 + 3 \text{ M}$ lactic acid adjusted to pH 12.5 at different applied current densities and (a) 40°C and (b) 60°C .

Figure 6-1 shows the change in the working electrode potential during galvanostatic deposition of Cu_2O . For deposition at $40 \text{ }^\circ\text{C}$, the electrode potential reaches a steady state after a certain amount of time, similar to the behavior of the current density during constant potential deposition at relatively high applied potentials, as shown in Figure 4-4a. At an applied current density of 0.75 mA/cm^2 or higher, potential immediately rises to a spike before dropping and reaching a steady state after ~ 1 min of deposition. The fact that the potential remains constant thereafter indicates that the film resistance changes minimally as it grows thicker over the course of the 40 minute deposition. On the other hand, at a low current density of 0.38 mA/cm^2 , the electrode potential drops to a minimum value of -0.36 V following the initial rise, before rising again to a second peak value of -0.65 V and then settling down to the final steady state potential. The shape of the potential transient resembles that of the current transient for potentiostatic deposition at -0.6 V in $0.2 \text{ M CuSO}_4 + 3 \text{ M}$ lactic acid at pH 9.5 at $60 \text{ }^\circ\text{C}$, for which a small amount of Cu is found in the film (Figure 4-4 a, e). Furthermore, it is also noted that the steady state potentials observed at 40°C are more negative than the minimum potential required for the formation of

Cu metal in the same electrolyte and temperature. These results suggest that metallic Cu is formed during the deposition of all these samples at 40°C, including the one obtained at an applied current density of 0.38 mA/cm², for which no significant Cu formation is predicted using Faraday's Law (Eq. 3-2).

By comparison, the system does not reach a steady state potential by the end of the experiments conducted at 60°C, as shown in Figure 6-1b. After a similar initial spike, the electrode potential gradually becomes more negative over the duration of each experiment. Unlike at 40°C, where rapid potential changes are observed, the potential rise at 60°C is relatively slow even at a high applied current density above 1 mA/cm². The potentials measured at 60°C remain within the range for deposition of Cu₂O only, which agrees with the fact that we could find no evidence of Cu deposition on the basis of the SEM images and Faraday's law for the conditions investigated in this section.

Based on the results from potentiostatic experiments, the morphology of electrodeposited Cu₂O is strongly affected by the applied voltage. Therefore, the variation in potential during the galvanostatic experiments at 60°C likely causes the morphology to progressively change from the bottom to the top of the film. Also, as the process continues, the potential at the working electrode becomes more negative, which suggests that Cu formation is likely to occur when the deposition time is long enough, which is detrimental to device performance as mentioned in Section 5.2.2. This is confirmed by the preliminary device results fabricated using the conditions investigated in this section presented in Figure 6-2, where the device performance is noticeably degraded as the Cu content increases. In particular, for devices fabricated using the Cu₂O films deposited at 40°C, a Cu content of ~3.8% ($i = 0.74\text{mA/cm}^2$), both J_{SC} and V_{OC} are much lower comparing to devices with less Cu content. When Cu content is ~5% or higher, the devices no longer exhibit photovoltaic behavior ($i \sim 0.96\text{mA/cm}^2$). Furthermore, the V_{OC} values measured in the above devices are ~150 mV or lower regardless of deposition temperature, whereas the values obtained using potentiostatically deposited Cu₂O films from the same electrolyte composition and temperature are in the range of 190-220mV. The results of these experiments confirm that potentiostatic deposition provides better control of Cu₂O film morphology than does galvanostatic mode.

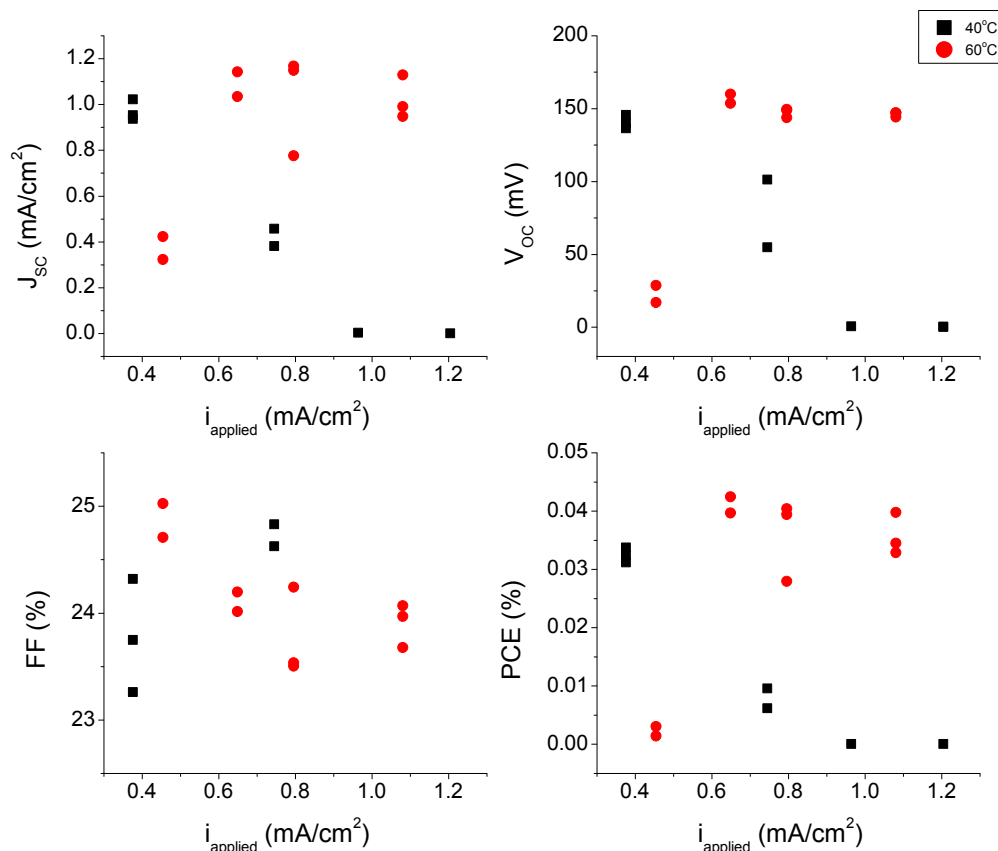


Figure 6-2: Cell characteristics for devices fabricated using galvanostatic Cu_2O films deposited in electrolyte containing 0.2 M CuSO_4 and 3 M lactic acid adjusted to pH 12.5 at different applied current densities (FTO/2 μm Cu_2O /250 nm AZO, front-illuminated)

6.3 Pulsed Potential Deposition

6.3.1 Background

Electrodeposition can be conducted using DC or pulsed techniques. Most of the reported studies on Cu_2O have been concerned with DC electrodeposition using either potentiostatic or galvanostatic techniques. A particular advantage of the use of pulsed techniques is that it has the potential to control the morphology of electrodeposits under ambient conditions without the need for additives. This can be particularly beneficial for electronic and photovoltaic applications where the presence of impurities in coatings and thin films is problematic.

Nevertheless, relatively little attention has been paid to the pulsed electrodeposition of Cu_2O . Compared to DC electrodeposition, pulsed electrodeposition can form thin films with better coverage and more uniform grain structure [201]. It has also been used to successfully modify film composition, morphology and porosity in other electrodeposition systems [202–204]. Gu et al. showed that unusual morphologies and structures such as flower-like Cu_2O particles can be obtained from a copper-citrate electrolyte using pulsed potentials [168], while Guo et al. reported that the Cu_2O grain size could be successfully tuned by square-wave voltammetry [205]. The use of pulsed Cu_2O electrodeposition as a method for filling an oxide nanostructure has also been reported [140,152,206]. However, the use of pulse waveforms for electrodeposition of Cu_2O from an alkaline copper-lactate electrolyte, which is a common system for the synthesis of p-type Cu_2O thin films for photovoltaic applications, has not been reported to the best of our knowledge.

6.3.2 Experimental

A similar experimental setup to that of DC electrodeposition, as detailed in Section 4.2, was used. The electrolyte contained 3.0 M lactic acid and CuSO_4 in the range from 0.1 to 0.4 M, with the pH adjusted to values between 9 and 12.5 using NaOH pellets. All deposition experiments were carried out at 60°C. Pulsed electrodeposition was conducted by applying square-wave potential pulses ranging between the open-circuit potential (OCP) as measured before the start of the process (termed the off-time) and different cathodic potentials (termed the on-time). The on- and off-times during these experiments were varied from milliseconds to minutes. In most cases, the total length of the on-time over the entire experiment was kept fixed at 7.5 minutes. When an extremely low pulse frequency was applied and the waveform consists of long pulses with on- and off-times of 2 minutes or longer, the experiment was conducted for 4 cycles and the total on-time exceeded 7.5 minutes. All potentials are reported with reference to the SCE scale. The samples were examined by XRD measurement to characterize the growth orientations of the Cu_2O films. The morphology of the samples was examined using SEM. Devices with

Cu₂O film thicknesses of ~1.8 μm – 2.1 μm were fabricated and characterized as described in Section 5.2.1.

6.3.3 Film morphology

All pulsed electrodeposition experiments in this section were conducted at pH between 9 and 10, a range in which the largest variation in film morphology is observed, as will be shown. At higher electrolyte pH, morphology from pulsed experiments is similar to that obtained from DC experiments.

Effect of pulsing frequency

The effect of frequencies ranging from 500 Hz to 1/600 Hz on Cu₂O film morphology during pulsed electrodeposition in 0.2M CuSO₄ and 3M lactic acid adjusted to pH 9.5 has been investigated. In each experiment, the input wave signal consists of potential steps to -0.5 V followed by one at the OCP (typically a value between -0.15 V and -0.21 V vs. SCE) at a duty cycle of 50%. When a very low frequency of 1/600 Hz is applied, the deposition experiment is continued for 4 cycles to ensure that enough cycles have been applied to observe any overall trend. Consequently, the total on-time of 20 minutes at this frequency is considerably longer than in the case of the other samples, for which a total on-time of 7.5 minutes is applied.

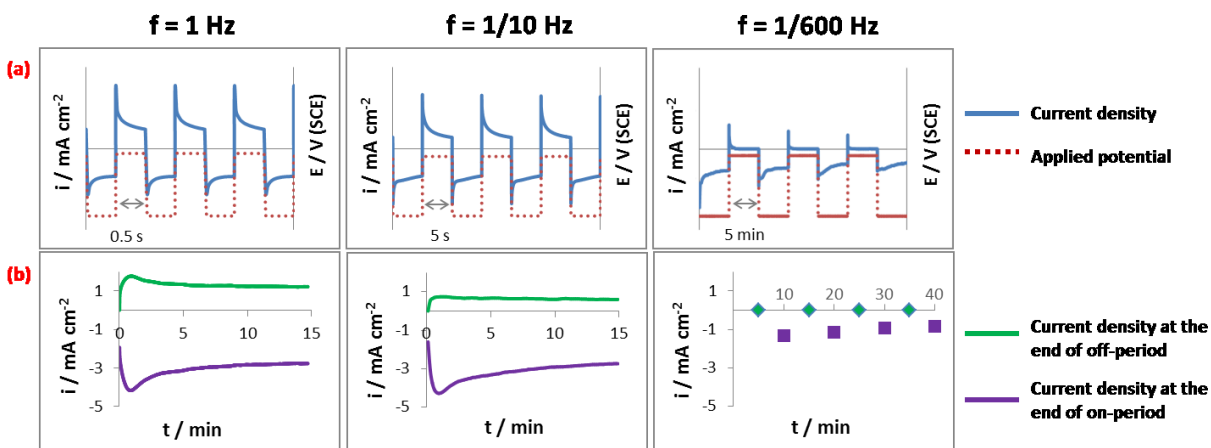


Figure 6-3: (a) Current transients during pulsed Cu₂O electrodeposition on FTO-glass substrate at 60°C and 50% duty cycle in electrolyte containing 0.2 M CuSO₄ – 3 M lactic acid adjusted to pH 9.5 at frequency 1, 1/10 and 1/600 Hz, respectively. Overall trends of the transients are shown in (b) by plotting the final current density during each individual pulse.

Some typical transient current responses are shown in Figure 6-3. The plots in Figure 6-3a show input potential waveforms (red dotted) and the resulting transient current responses (solid blue) during electrodeposition at frequencies of 1 Hz, 1/10 Hz and 1/600 Hz. The current response during each cycle is typical – an initial spike due to double layer charging/discharging as the potential is switched, followed by the more gradual faradaic component corresponding to reduction or oxidation. The magnitude of the current during the cathodic portion of each cycle always remains larger than the anodic portion, ensuring that a net deposition of Cu_2O is occurring. It is important to note that considerable anodic current can flow during the off-time since the potential applied during this portion of the pulse is the OCP based on the FTO electrode at the start of electrodeposition which is more positive than the OCP observed once Cu_2O has formed on the FTO surface. The decrease in current response during each cycle is more prominent at low frequencies when the pulses are longer. When the pulses are sufficiently long, the current density of the anodic parts gradually diminishes to zero during the off-time within a single pulse. The magnitude of the current is larger during the early cycles, but then gradually decreases as the process continues and eventually reaches a stationary state in both directions. The approach of the current response to a stationary state during the pulsed deposition experiments can be more clearly shown by plotting the respective current density at the end of the on- and off-period during each cycle versus the corresponding time. The results shown in Figure 6-3b reveal that a stationary condition is reached after about 5 minutes of pulsed deposition in the cases shown above.

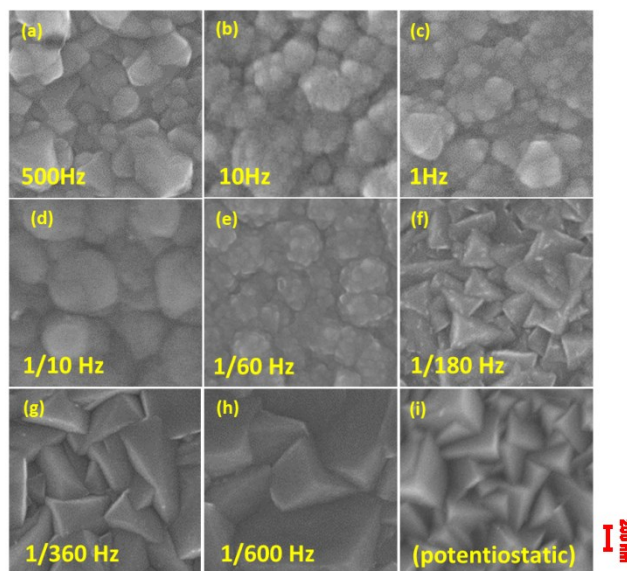


Figure 6-4: SEM images of Cu_2O films obtained by deposition on FTO-glass substrate at 60°C in electrolyte containing $0.2\text{ M CuSO}_4 - 3\text{ M lactic acid}$ adjusted to $\text{pH } 9.5$ with square-wave pulses of -0.5 V/OCP at frequencies: (a) 500 Hz , (b) 10 Hz , (c) 1 Hz , (d) $1/10\text{ Hz}$, (e) $1/60\text{ Hz}$, (f) $1/180\text{ Hz}$, (g) $1/360\text{ Hz}$, (h) $1/600\text{ Hz}$. Cu_2O film deposited under DC conditions at -0.5 V for 15 min is shown in (i) for comparison.

The surface morphologies of Cu_2O films formed at 50% duty cycle over the range of frequencies from $1/600\text{ Hz}$ to 500 Hz are shown in Figure 6-4. For comparison, an SEM image of a film formed by DC deposition at -0.5 V in the same electrolyte is also included (Figure 6-4i). As noted previously, cubic Cu_2O grains between ~ 200 and 500 nm tend to form under DC conditions. A comparison of the images in Figure 6-4 shows that the Cu_2O morphology increasingly diverges from that of the DC film as the pulse frequency increases. The truncated angular grains formed at the lowest frequencies of $1/600$ and $1/360\text{ Hz}$ are similar to (albeit slightly larger) those in the DC film (Figures 6-4 g, h). This observation is not surprising given that the conditions during pulsed electrolysis should approach that during DC polarization as the frequency decreases. With an increase in frequency to $1/180\text{ Hz}$, cubic Cu_2O grains are still produced, although they are somewhat smaller than that obtained at $1/600$ and $1/360\text{ Hz}$ (Figure 6-4f). However, when the frequency is raised further to $1/60\text{ Hz}$ and above (Figures 6-4 a-e), the Cu_2O coatings change dramatically and now consist of spherical grains that are relatively uniform in size ($\sim 500\text{ nm}$ or smaller). In some cases, these grains appear to be agglomerates of finer particles. A possible explanation for this behaviour becomes evident when the current responses during the potential pulses at the various

frequencies are examined. As shown in Figure 6-3, this analysis shows that the magnitudes of both the cathodic and anodic charges passed over the course of deposition increase as the pulse frequency is raised. It is noteworthy that a significant amount of anodic current flows during the off-periods at the higher frequencies, whereas it drops to very low levels at low frequencies. To gain further insight into the nature of the cathodic and anodic reactions occurring during these potential pulses, we estimated the mass of Cu_2O expected using Faraday's Law based on the difference in the cathodic and anodic charges over the course of each deposition experiment, assuming that the reduction of Cu(II) to Cu_2O and the re-oxidation of some of the Cu_2O back to Cu(II) are the only reactions that occur during the on- and off-times, respectively. In every case, the amount of Cu_2O so obtained closely matched the mass of the coating that was actually measured at the end of deposition. This result reveals that not only are Cu(II) reduction to Cu_2O and re-oxidation of some Cu_2O to Cu(II) the only cathodic and anodic processes that occur, but some of the Cu_2O formed during the on-times re-dissolves during the off-times. Thus, the change in Cu_2O morphology depending on pulse frequency may be related to events occurring during the off-times. One would expect dissolution to preferentially occur at higher energy sites in the Cu_2O coating such as sharp corners and edges, leaving behind more rounded and spherical features. This effect should be enhanced as the pulse frequency increases and more anodic current is generated during the off-times.

Furthermore, for Cu_2O films with the same grain shape, the particle size becomes smaller as the pulsing frequency is raised. This trend is clearly observed for the spherical grains formed at frequencies between 1/10 and 10 Hz (Figures 6-4 b-d) and for the cubic/angular grains formed between 1/60 and 1/600 Hz (Figures 6-4 f-h). The generation of finer-grained deposits by increasing frequency is a well-known effect and one of the intended purposes of pulsed methods [202,203]. However, this trend does not hold when comparing grains with the different morphologies. As shown by comparisons of Figures 6-4a and b as well as Figures 6-4 d and e, the particle size is significantly smaller in the sample obtained at the lower frequency when a change in particle shape has occurred.

Effect of duty cycle

The effect of duty cycle has been investigated by varying both the on- and off-times (t_{on} and t_{off}) during Cu_2O electrodeposition using square-wave pulses of -0.5 V/OCP . Overall, the shapes of the current transients reveal similar properties to those obtained with 50% duty cycles.

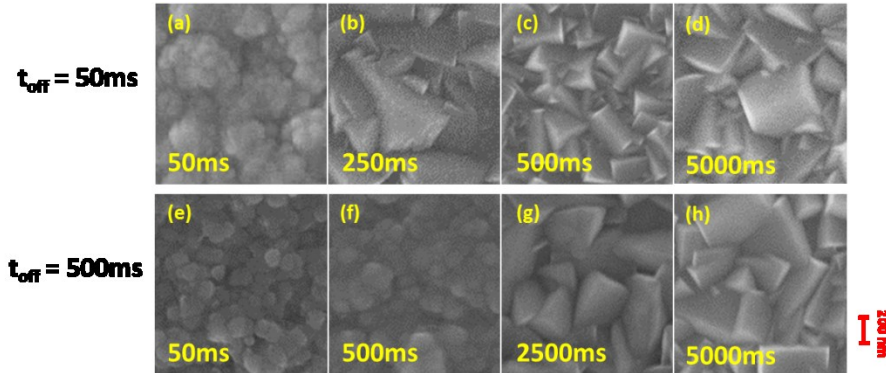


Figure 6-5: SEM images of Cu_2O films obtained by deposition on FTO-glass substrate at 60°C in electrolyte containing 0.2 M CuSO_4 - 3M lactic acid adjusted to $\text{pH } 9.5$ with square-wave pulses of -0.5 V/OCP and off-times t_{off} of (a-d) 50 ms and (e-h) 500 ms . Values of t_{on} are labelled on the images.

Figure 6-5 shows the surface morphology of Cu_2O films formed by varying the on-periods at off-times of 50 and 500 ms . For deposition with $t_{off} = 50 \text{ ms}$, a transition from spherical to cubic particles is observed as the duration of the on-period is prolonged (Figure 6-5 a-d). With $t_{on} = 50 \text{ ms}$, spherical particles less than 100 nm in diameter are obtained. Truncated cubic grains appear when the duration of the on-time reaches 250 ms . The grains change to well-defined cubes when the on-times rise above 500 ms . Although a similar trend in the change of morphology is observed for $t_{off} = 500 \text{ ms}$, the transition to cubic particles requires much longer on-times (Figure 6-5 e-h).

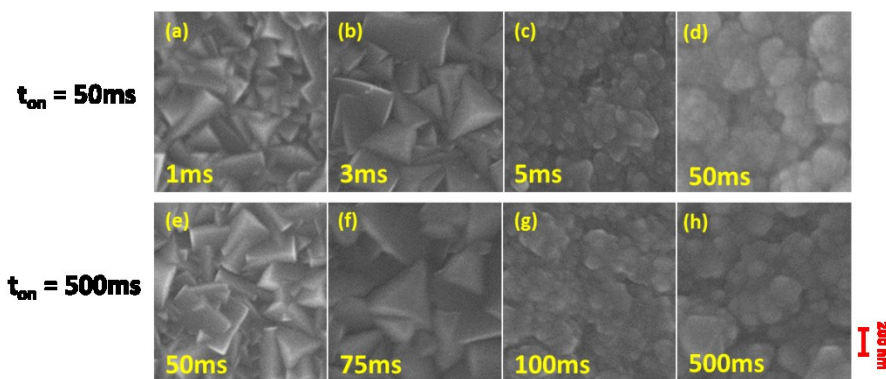


Figure 6-6: SEM images of Cu_2O films obtained by deposition on FTO-glass substrate at 60°C in electrolyte containing $0.2\text{M CuSO}_4 - 3\text{M}$ lactic acid adjusted to pH 9.5 with square-wave pulses of -0.5 V/OCP vs. SCE at on-times t_{on} of (a-d) 50 ms and (e-h) $t_{\text{on}} = 500\text{ ms}$. Values of t_{off} are labelled on the images.

The opposite trend is observed when t_{off} is increased at a fixed t_{on} of 50 ms or 500 ms (Figure 6-6). The grains are predominantly cubic at short off-times of 1 and 3 ms when t_{on} is 50 ms , but become spherical when the off-time is extended to 5 ms and above. At a t_{on} of 500 ms , a similar evolution of the morphology is observed, although it requires longer off-times. It should be recalled from the results discussed earlier that the formation of cubic Cu_2O grains is favoured during DC deposition at -0.5 V vs. SCE in the same electrolyte (Figures 6-4i). This observation is consistent with the effect of t_{off} shown in Figure 6-4 since the conditions during pulsed electrolysis would be expected to approach those of DC electrolysis as t_{off} approaches zero.

These trends with respect to changes in t_{on} and t_{off} at a given applied potential during the on-time are consistent with the explanation provided earlier for the effect of frequency on Cu_2O morphology. If the dissolution of Cu_2O during the off-times of -0.5 V/OCP square-wave pulses plays a crucial role in determining the film morphology, one would expect an increase in t_{on} at a fixed t_{off} to promote the formation of cubic grains, whereas an increase in t_{off} at a fixed t_{on} to favor more spherical grains. The importance of both the on-time and off-times is further evident in the images in Figure 6-5 which show that t_{off} has a large effect on Cu_2O morphology when t_{on} is relatively short at 50 and 500 ms , but relatively little impact when t_{on} is increased to as much as 5000 ms .

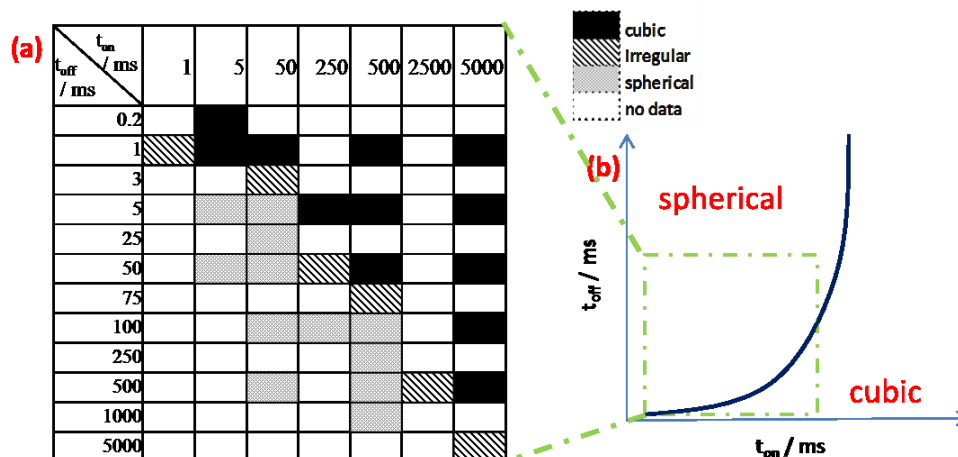


Figure 6-7: (a) Summary of effect of t_{on} and t_{off} on Cu_2O film morphology obtained by deposition on FTO-glass substrate at 60°C in electrolyte containing $0.2\text{ M CuSO}_4 - 3\text{ M}$ lactic acid adjusted to pH 9.5 with square-wave pulses of -0.5 V/OCP vs. SCE; (b) schematic curve delineating conditions for spherical and cubic morphology (rectangular region indicated by the green dashed lines corresponds to the conditions covered in Figure 6-7a). Diagram is not to scale and is intended for qualitative purposes only.

The combined effects of t_{on} and t_{off} on Cu_2O morphology during pulsed electrodeposition with on- or off-times of 5000 ms or less are summarized in Figure 6-7a. It is clearly shown that, as the duty cycle of the process becomes higher (i.e., large t_{on} relative to t_{off}), the formation of cubic particles is favoured. From the data collected, a cubic-only structure requires a duty cycle of 80% or higher at intermediate pulse periods between 5 ms and 5000 ms.

A diagram in t_{off} - t_{on} phase space can be drawn to delineate the conditions where the different morphologies are obtained. Figure 6-7b shows the conditions where the Cu_2O grains take the form of cubes or spheres. For our purposes, a cubic morphology is henceforth defined to be the one made up of cubic or truncated cubic particles, where distinct angles are observed. This diagram is not drawn to scale and is intended for qualitative purposes only. The rectangular region indicated by the green dashed lines corresponds to the range of conditions covered in Figure 6-7a. The solid curve delineates the transition between films with spherical and cubic morphologies. For conditions to the right of the curve, the grains tend to be cubic with well-defined angles and edges. On the other hand, the particles are less defined and

usually spherical or irregular in shape with few distinct angles when formed at on- and off-times found to the left of the curve.

It should be noted that the effect of duty cycle discussed above is only applicable to pulsing conditions at intermediate frequencies. As shown in the previous section, cubic morphology can be obtained at a 50% duty cycle when the pulses are sufficiently long. Hence, it is expected that a threshold value of t_{on} exists, above which the resulting morphology would be cubic regardless of the length of the off-time. The value of this threshold time should be close to the time required for well-defined cubic Cu_2O particles to form during potentiostatic DC electrodeposition at the same applied cathodic potential. As shown in Figure 4-11, this time should be in the range of 3-5 minutes for the conditions shown in this section. When the on-time is longer than this value, the condition would resemble a sequence of DC potentiostatic electrodeposition steps, with cubic grains being obtained at each stage.

Similarly, a threshold t_{off} value that causes a significant change in morphology should exist as well. This is inferred from the shape of the current transient curves shown in Figure 6-3a. When the system is held at OCP for a sufficiently long time, the anodic current density diminishes to zero by the end of the pulse. Once this stage is reached, no significant further change to the deposit morphology during the pulse would be expected. Therefore, for t_{off} that exceeds this threshold duration, any observed differences in morphology should depend entirely on the length of t_{on} . This threshold value of t_{off} can be estimated from the conditions at which the current during the off-time first decreases to zero by the end of a pulse. Based on the results of this study, this corresponds to a duration of ~2-3 minutes for this system.

Effect of other parameters

In this section, we examine the effects of other parameters on the orientation and morphology of Cu_2O films produced by pulsed electrodeposition.

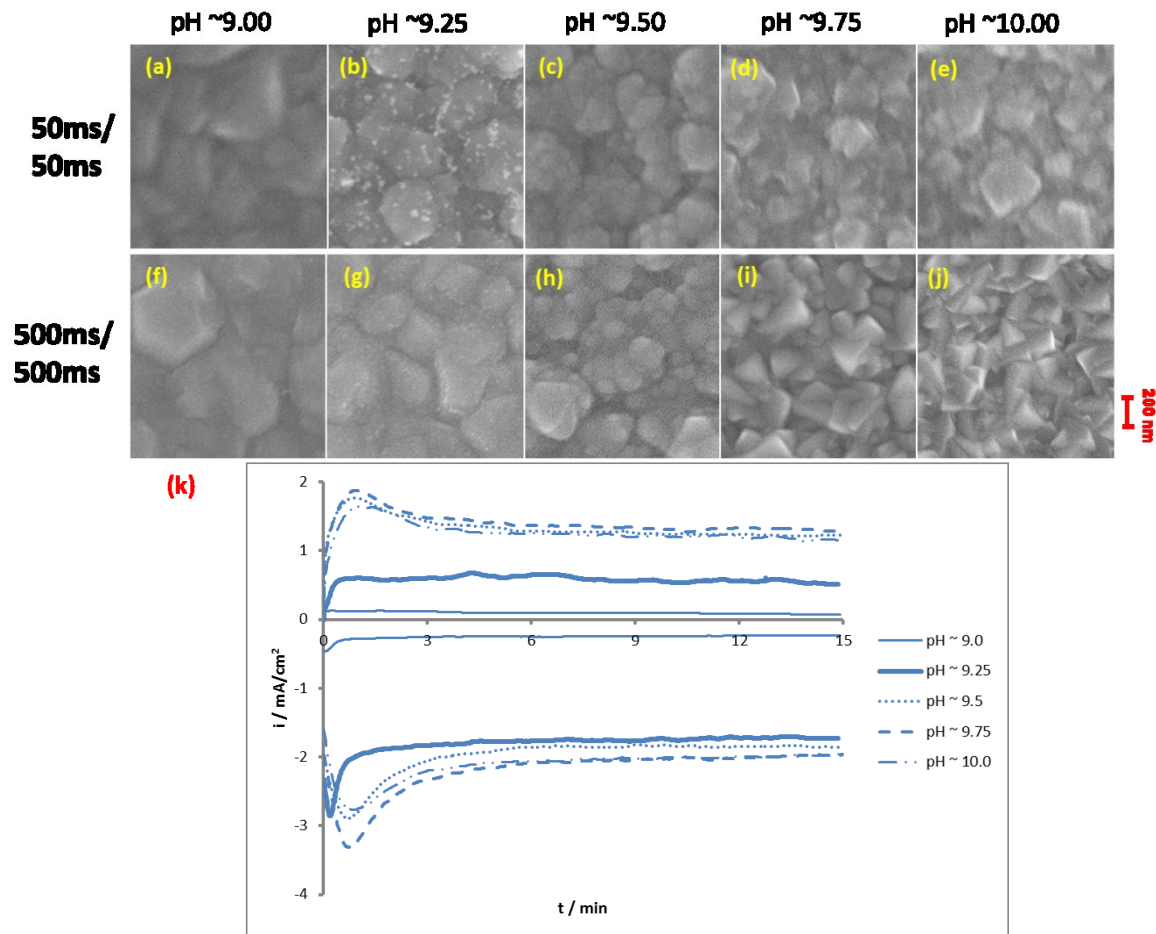


Figure 6-8: SEM images of Cu₂O films obtained by deposition on FTO-glass substrate at 60°C in electrolytes containing 0.2 M CuSO₄ – 3 M lactic acid adjusted to different pH with square-wave pulses of -0.5 V/OCP vs. SCE at the following on-/off-times: (a-e) 50 ms/50 ms and (f-j) 500 ms/500 ms. The cathodic and anodic current transients over the course of deposition at 500 ms/500 ms obtained by plotting the final current density of each individual pulse are shown in (k).

The effect of pH on the resulting morphology of Cu₂O films produced by pulsed electrodeposition is shown in Figure 6-8 a-j. In these experiments, the composition of the electrolyte is maintained at 0.2 M CuSO₄ and 3 M lactic acid and square-wave pulses of -0.5 V/OCP vs. SCE and on/off times of 50 ms/50 ms and 500 ms/500 ms are applied. The SEM images in Figure 6-8 a-j reveal a trend whereby the deposit grains change from spherical at pH 9 and 9.25 to cubic above pH 9.5. This result agrees with previous reports on the effect of electrolyte pH on the morphology of Cu₂O films produced under DC conditions (Section 4.3.6), indicating that it is not affected by the mode of electrolysis, as would be expected according to the explanation proposed in Section 4.4.2.

A particularly striking aspect is the very high sensitivity of morphology to pH over the narrow range from 9 to 10. Spherical grains predominate at pH 9.5, but only a small shift in pH to 9.8 is required for cubic grains to become dominant. On the other hand, grains that have irregular polyhedral shape are observed at pH 9.0 and 9.25. As the pH shifts from 9.5 in either direction, the grain shape becomes more angular, suggesting that the spherical grains are an intermediate phase between cubic and octahedral morphologies. Although distinct octahedral grains are not observed here, they are most likely to appear when the electrolyte pH is lowered below 9.0. It should be noted that these very large effects on Cu₂O morphology with only small changes in pH between 9 and 10 have also been reported previously during DC deposition [147,149,159].

However, comparison of the morphology with that obtained under DC conditions at the same pH clearly shows that the Cu₂O films deposited under pulsed conditions are noticeably more rounded, which according to our previous explanation could occur due to dissolution. To gain further insight into the effect of pH on the processes during pulse deposition, the variation of the current density during the on-time and off-time over the course of 15 minutes of deposition at various pH between 9 and 10 using square-wave pulses with amplitude -0.5 V/OCP vs. SCE and $t_{\text{on}}/t_{\text{off}} = 500 \text{ ms}/500 \text{ ms}$ is presented in Figure 6-8k. For convenience, only the current density at the end of the on- and off-periods during each cycle is plotted versus the corresponding time. These transients show that the net current over the course of deposition increases when the pH during deposition is raised from 9.0 to 9.25, but then decreases with a further rise to 9.5 and above. Of particular interest are the effects that pH has on the individual cathodic and anodic currents during the on- and off-times, respectively. Much less deposition occurs during the on-time at pH 9.0 than at the higher pH values, but the amount is largely unaffected by pH once it is varied between 9.25 and 10.0. Examination of the responses during the off-times indicates that the behaviour at pH 9.0 and at pH 9.5-10.0 mirrors the behavior observed during the on-time in that the anodic current is the lowest at pH 9.0 and highest at pH 9.5-10.0. However, an important difference is revealed in the case of the transient at pH 9.25. Whereas the cathodic current during the on-time at pH

9.25 is very similar to that at pH 9.5-10.0, the corresponding anodic current is about half that at the higher pHs. It is this difference that leads to the net cathodic current at pH 9.25 being the highest.

It does not seem reasonable to attribute these effects to the differences in the OH^- concentration alone over this pH range that appear so small in magnitude compared to the differences in the observed currents. Instead, they are likely related to the different crystal orientations formed depending on the pH. The trends observed in Figure 6-8k suggest that the deposition rate of Cu_2O grains with (100) orientation is slower than that of grains with (111) orientation. On the other hand, it appears from a comparison of the anodic currents at the various pHs that grains with cubic morphology and (111) orientation dissolve more readily than grains with spherical morphology and stronger (100) orientation. It is well recognized that the various crystal planes in Cu_2O have different tendencies to oxidize, although whether the (100) plane is more or less resistant to oxidation than (111) appears to depend on the way in which oxidation is carried out and the electrolyte composition and conditions [187,207–210].

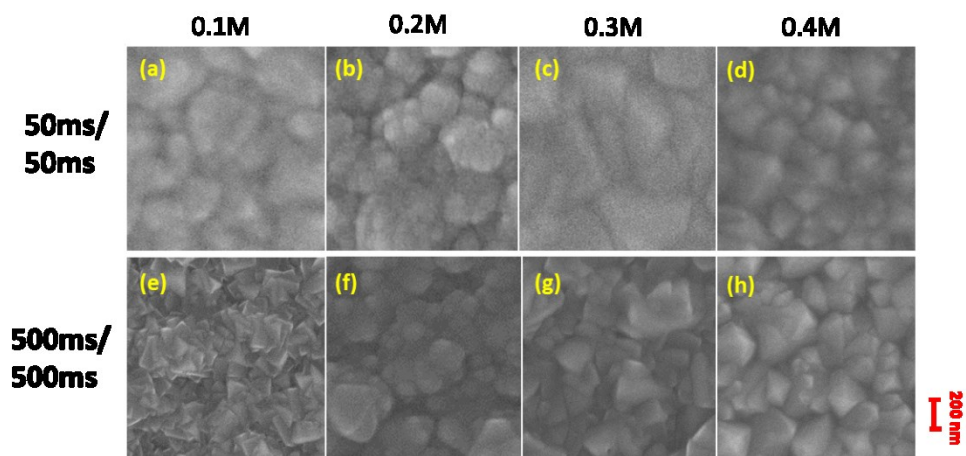


Figure 6-9: SEM images of Cu_2O films obtained by deposition on FTO-glass substrate at 60°C in electrolyte containing 3 M lactic acid and different CuSO_4 concentrations adjusted to pH 9.5 with square-wave pulses of -0.5 V/OCP vs. SCE at the following on-/off-times: (a-d) 50 ms/50 ms and (e-h) 500 ms/500 ms. The number above each image denotes the CuSO_4 concentration.

Figure 6-9 presents the surface morphology of Cu_2O films deposited from electrolytes containing CuSO_4 concentrations at pH 9.5 from 0.1 to 0.4 M using square-wave pulses of -0.5 V/OCP with on- and off-times of 50 ms/50 ms and 500 ms/500 ms. A clear transition from cubic to octahedral morphology is

observed as the CuSO_4 concentration increases from 0.1 M to 0.4 M for deposition with 500 ms/500 ms pulses.

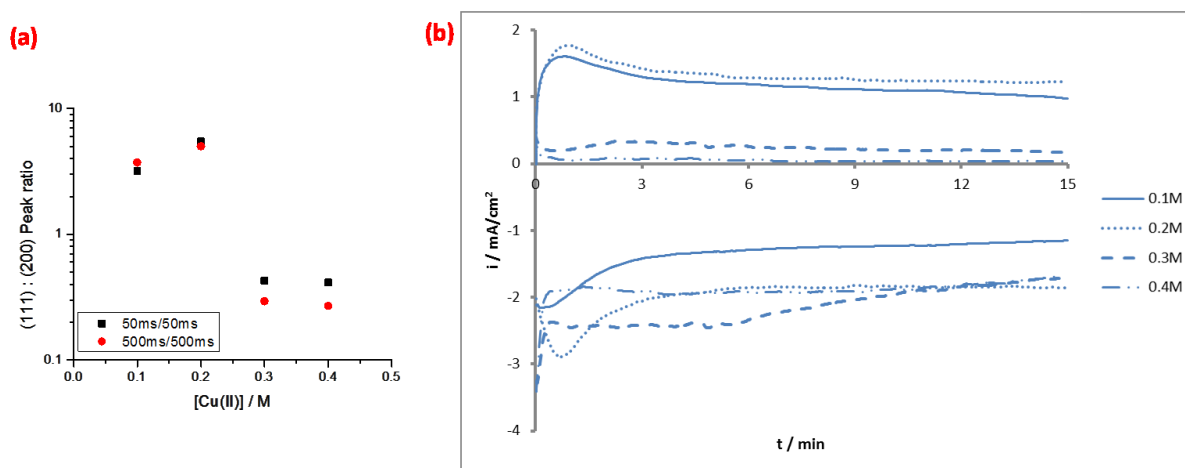


Figure 6-10: (a) Effect of $[\text{CuSO}_4]$ on (111):(200) peak intensity ratio from the XRD patterns of Cu_2O films obtained by deposition on FTO-glass substrate at 60°C in electrolyte containing 3 M lactic acid adjusted to pH 9.5 with square-wave pulses of $-0.5\text{V}/\text{OCP}$ vs. SCE and on-/off-times of 50 ms/50 ms and 500 ms/500 ms. (b) Effect of $[\text{CuSO}_4]$ on the cathodic and anodic current transients over the course of deposition at 500 ms/500 ms obtained by plotting the final current density of each individual pulse.

This trend is further assessed by measuring the (111):(200) peak intensity ratios from the XRD patterns of the Cu_2O films shown in Figure 6-10. The results presented in Figure 6-10a confirm the effect of $[\text{CuSO}_4]$ on morphology gleaned from the SEM images. When the CuSO_4 concentration during deposition is relatively high at 0.3 or 0.4M, the resulting crystals primarily exhibit $\langle 200 \rangle$ orientation, consistent with expectations based on the predominance of octahedral grains in the SEM images (Figures 6-9 c-d and g-h). A sharp change in morphology is observed when the CuSO_4 concentration is reduced to 0.1 or 0.2 M and the $\langle 111 \rangle$ orientation and cubic grain formation become dominant, again in agreement with the SEM images.

Further insight into this behaviour can be obtained by examining the cathodic and anodic current transients during the on- and off-times over the course of the deposition experiments conducted at the different CuSO_4 concentrations (Figure 6-10b). Most relevant to the crystal orientation is the behaviour during the on-time which shows the cathodic current increasing significantly as the CuSO_4 concentration rises from 0.1 to 0.2 M, but remaining largely unaffected by any further rise to 0.3 and 0.4 M. It is

particularly worth noting that this change occurs at a similar CuSO_4 concentration where the shift in preferred crystal orientation from $\langle 111 \rangle$ to $\langle 100 \rangle$ occurs.

It is noted that the trend observed in Figure 6-10 for the effect of $[\text{CuSO}_4]$ on film orientation is the opposite to previously observed for DC electrodeposition in the same electrolyte and temperature, as presented in Section 4.3.5 and Figure 4-7. This difference is likely related to the replenishment of CuLac_2 at the surface during the off-times. As discussed in Chapter 4, the surface concentration of CuLac_2 is dropping constantly during DC deposition due to transport limitation. This effect is reduced by the application of pulsed potentials, which provides time for the lactate ions at the surface to diffuse away and CuLac_2 complexes to be replenished from the bulk solution during the off-times. When the bulk concentration of CuLac_2 is relatively high, the $[\text{Cu(II)}]:[\text{OH}^-]$ ratio at the electrode surface remains in a range that favors $\langle 100 \rangle$ oriented growth, as opposed to a preference for $\langle 111 \rangle$ growth during DC electrodeposition. This agrees with the mechanism discussed in Section 4.4.2 relating the Cu:O ratio to the different growth orientation and also helps explain why the same trend does not hold during DC experiments.

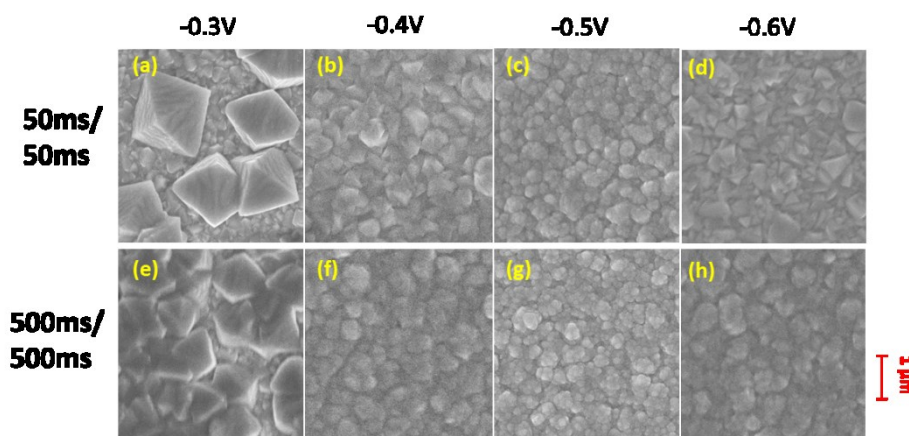


Figure 6-11: SEM images of Cu_2O films obtained by deposition on FTO-glass substrate at 60°C in electrolytes containing 0.2 M CuSO_4 – 3 M lactic acid adjusted to pH 9.5 with square-wave pulses having different cathodic potentials at the following on-/off-times: (a-d) 50 ms/50 ms and (e-h) 500 ms/500 ms. The potential during the off-time is maintained at the OCP. The number above each image denotes the cathodic potential.

The effect of the cathodic potential during the pulse on-times on the surface morphology of films obtained in electrolytes containing 0.2 M CuSO_4 – 3 M lactic acid adjusted to pH 9.5 is shown in Figure

6-11. The applied potential during the off-time is maintained at the OCP. Spherical/irregular grains tend to be formed at more negative potentials during both 50 ms/50 ms and 500 ms/500 ms pulses, whereas the morphology becomes more octahedral when a lower cathodic potential of -0.3 V is applied. In the case of 50 ms/50 ms pulses, large individual octahedral particles are evident. This observation is consistent with the trend observed under DC conditions in this study (Chapter 4) and previous ones that a shift in crystal orientation from the $\langle 100 \rangle$ direction to the $\langle 111 \rangle$ direction in grain morphology from octahedral to cubic tends to occur as the cathodic overpotential or current density increases. Furthermore, this behavior can be explained by considering the differences in surface energy among the various Cu_2O planes (Section 4.4.1).

A comparison of the effect of cathodic overpotential during DC and pulsed deposition indicates that the use of pulsed waveforms tends to reduce the growth in the $\langle 111 \rangle$ direction and promote growth in the $\langle 100 \rangle$ direction since distinct octahedral shapes are observed under pulsed conditions (Figure 6-11 a, e) at -0.3 V/OCP, whereas only irregularly shaped grains are obtained in DC electrodeposition at -0.3 V under otherwise identical conditions. Such a trend also agrees with the finding that distinct cubic grains are formed by DC deposition at a potential of -0.4V (Figure 4-4c), whereas only rounded and irregular grains are produced by pulsed deposition using the same on-time potential (Figures 6-11b, f). This difference is likely related to the effect of anodic dissolution on some of the Cu_2O grains during the off-time, as discussed in previous sections.

It is also worth noting that no evidence of Cu formation is found in the Cu_2O deposits formed at a cathodic potential of -0.6V, unlike the situation with DC electrodeposition at the same potential (Figure 4-4e). This observation that Cu_2O alone without Cu can be formed at more negative potentials using a pulsed waveform than that possible via DC electrodeposition reflects one of the advantages of pulsed methods. The formation of Cu at high cathodic potential is likely related to the availability of OH^- ions at the surface. Although the diffusion from bulk to the surface is much faster than that of CuLac_2 , the bulk concentration of OH^- is orders-of-magnitude lower than that of Cu(II) . Thus, when the potential becomes

negative enough during cathodic polarization, the OH^- concentration at the surface will reach zero before that of Cu(II) . In this case, the diffusion of OH^- ions from the bulk becomes rate-determining in the formation of Cu_2O . If OH^- is not available as a reactant, but Cu(II) is, Cu deposition should occur if the potential is sufficiently cathodic. Thus, when DC deposition is conducted at -0.6 V in a solution containing 0.2 M CuSO_4 and 3 M lactic acid and adjusted to $\text{pH } 9.5$, OH^- may become depleted enough for both Cu_2O and Cu to form. However, when the same potential is applied during the on-time of a pulsed waveform, enough OH^- is replenished in the vicinity of the electrode during the subsequent off-time that the OH^- concentration at the surface remains high enough during the on-time for Cu_2O deposition to still be dominant.

6.3.4 Device performance

In this section, devices are fabricated using pulse-deposited Cu_2O thin films from electrolytes containing $0.2\text{ M CuSO}_4 + 3.0\text{ M}$ lactic acid adjusted to $\text{pH } 9.5$ (-0.5 V/OCP) and 12.5 (-0.65 V/OCP) at 60°C with $500\text{ ms}/500\text{ ms}$ cycles. Devices fabricated using Cu_2O films deposited using constant applied potential under otherwise identical conditions are used as comparison. However, it is found that, with the Cu_2O thin film pulse-deposited from the $\text{pH } 9.5$ electrolyte, the resulting device show only minimal photovoltaic efficiency and a $\text{PCE} \sim 0\%$, indicating that this Cu_2O layer is not suitable in solar cells. The performance measures are listed in Table 6-2.

Table 6-2: Performance measures of devices fabricated with Cu_2O layers deposited using DC or pulsed waveform from electrolytes containing $0.2\text{ M CuSO}_4 + 3.0\text{ M}$ lactic acid at 60°C .

Device			J_{sc} (mA/cm^2)	V_{oc} (mV)	FF (%)	PCE (%)	R_{sh} ($\text{ohm}\cdot\text{cm}^2$)	R_{s} ($\text{ohm}\cdot\text{cm}^2$)
pH 9.5	DC (-0.5 V)	Front	0.255	214.7	23.3	0.013	1.59E+04	8.51E+02
		Back	0.288	247.3	25.9	0.018	1.97E+04	6.87E+02
	Pulsed (-0.5V/OCP , 500ms/500ms)	Front	<i>(No data available: device PCE is too low)</i>					
		Back						
pH 12.5	DC (-0.65 V)	Front	3.170	200.4	28.0	0.178	2.79E+03	4.51E+01
		Back	1.519	156.7	33.6	0.080	6.60E+03	2.62E+01
	Pulsed (-0.65V/OCP , 500ms/500ms)	Front	2.224	194.5	25.2	0.109	3.80E+03	9.81E+01
		Back	1.146	154.5	31.0	0.055	8.05E+03	6.15E+01

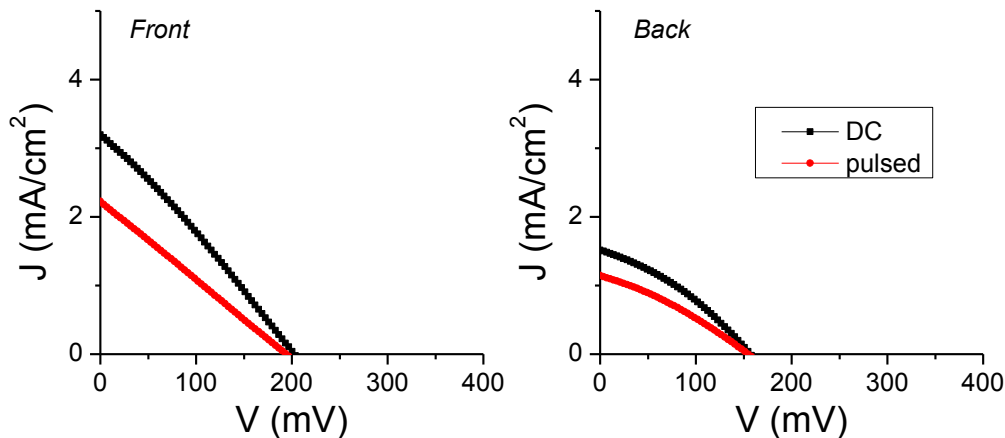


Figure 6-12: Front- and back-illuminated J-V curves for devices fabricated using potentiostatic DC (-0.65 V) or pulsed waveform (-0.65 V/OCP, 500 ms/500 ms). Cu_2O films are deposited from electrolytes containing 0.2 M CuSO_4 + 3.0 M lactic acid adjusted to pH 12.5 at 60°C.

Figure 6-12 shows the J-V curves of devices with Cu_2O layers deposited from the pH 12.5 electrolyte using either DC or pulsed waveform. It is clear from Table 6-2 and these plots that the performance is better in devices fabricated with Cu_2O layers produced using potentiostatic DC deposition than with the pulsed method. The V_{OC} does not vary significantly, which suggests that the bandgap and absorption coefficient of the Cu_2O thin film are not significantly altered by the application of the pulsed waveform. It is also noted that the devices made from pulsed Cu_2O films have much higher series resistance than those with DC-plated Cu_2O layers, indicating that the higher R_s is the source of the loss in FF.

The charge carrier concentration and mobility in the Cu_2O thin films that have been pulse-deposited (-0.5 V/OCP, 500 ms/500 ms) from electrolytes containing 0.2 M CuSO_4 + 3.0 M lactic acid adjusted to pH 9.5 at 60°C have been estimated using the SCLC technique. The carrier concentration in the pulsed sample is found to be on the order of 10^{16} cm^{-3} , almost an order of magnitude higher than that in thin films deposited at -0.5V from the same electrolyte and temperature. On the other hand, the carrier mobility is reduced to be in the range from 0.01 to 0.1 cm^2/Vs , more than two orders-of-magnitude lower than its DC counterpart (Figure 5-13b). This variation in film properties may be related to oxidation occurring during the off-time of pulsed electrodeposition, as discussed in detail in Section 6.3.3. While the oxidation species obtained during the off-time dissolves into the electrolyte, a fraction of them may

still remain on the surface at the beginning of the on-time, thus incorporated into the deposited film. This incorporation of Cu(II) in the Cu₂O thin film is likely the reason for the increase in Cu vacancies and therefore the hole concentration. At the same time, more trap sites are created as the defect density becomes higher, which lower the charge carrier mobility.

In summary, pulsed deposition has been demonstrated as a technique to induce Cu vacancy into the Cu₂O thin film. However, device performance using pulse-deposited Cu₂O layers is currently limited by the lower carrier mobility.

6.4 Use of Stirred Electrolytes

6.4.1 Background

During electrodeposition, agitation of electrolyte speeds up the transport of species to and from the electrode, thereby altering their surface concentrations and reducing the thickness of the depletion layer close to electrode surface. It also allows gas bubbles forming on the electrodes to be removed at a faster rate for processes involving gas evolution. The effect of stirring for the purpose of de-bubbling [211], removal of transport limitation [211], as well as morphology and composition control in the deposition of alloys and semiconductors [212–215] has been extensively studied in other deposition systems. As far as we know, no studies have been reported on the use of stirring during the electrodeposition of Cu₂O thin films although it has been reported by Xue et al. that the mode and speed of stirring influence the filling of Cu₂O particles into TiO₂ nanotubes [216].

6.4.2 Experimental

The electrodeposition of Cu₂O is carried out as described in Section 4.2. A magnetic stir bar is placed at the bottom of the flask for agitation. The same stirring speed is used for all stirred experiments. All potentials are reported with reference to the SCE scale. The samples are examined by XRD to characterize the growth orientations of the Cu₂O films. The morphology of the samples is examined using

SEM. Devices with Cu_2O film thickness $\sim 1.95\mu\text{m} - 2.1\mu\text{m}$ are fabricated and characterized as described in Section 5.2.1.

6.4.3 Film morphology

Similar to the pulsed electrodeposition data reported in Section 6.3, only films deposited at a relatively low pH (~ 9.5) show significant difference in morphology depending on whether the electrolyte is stirred or not. At pH 12.5 or 13.5, the morphologies formed under stirred and unstirred conditions are similar to each other.

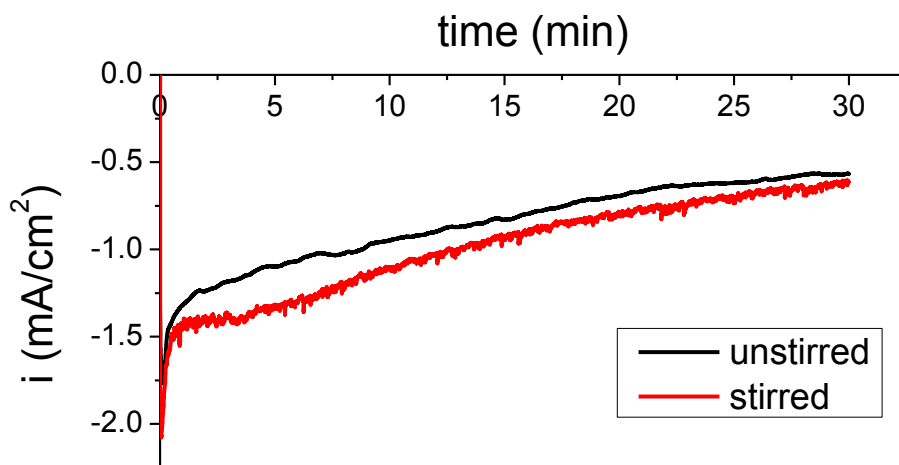


Figure 6-13: Current transient curves during electrodeposition of Cu_2O films at 60°C in electrolyte containing $0.2\text{ M CuSO}_4 + 3\text{ M}$ lactic acid adjusted to pH 9.5 at -0.5 V vs. SCE under stirred or unstirred conditions.

The current transient curves for Cu_2O films electrodeposited at 60°C under stirred or unstirred conditions in $0.2\text{ M CuSO}_4 + 3\text{ M}$ lactic acid adjusted to pH 9.5 at -0.5V are presented in Figure 6-13. The overall shapes are similar in both cases although a higher current density is observed when the electrolyte is being stirred, indicating a faster deposition rate overall.

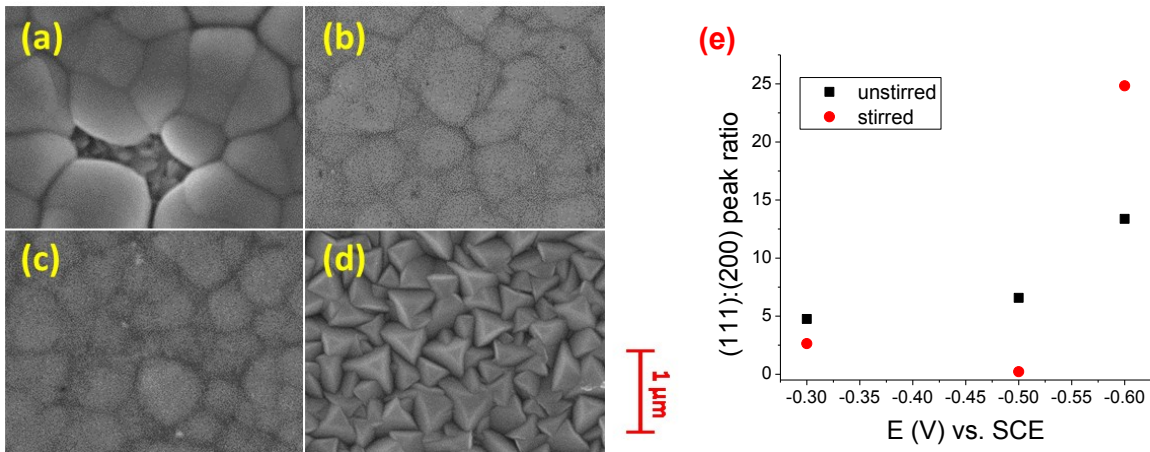


Figure 6-14: SEM images of Cu₂O films electrodeposited at 60°C in stirred electrolyte containing 0.2 M CuSO₄ + 3 M lactic acid adjusted to pH 9.5 at applied potentials of (a) -0.3, (b) -0.4, (c) -0.5 and (d) -0.6V vs. SCE. Deposition time is 15 min in cases. The effect of deposition potential on (111):(200) peak ratio of Cu₂O films obtained under stirred and unstirred conditions is presented in (e).

The morphology of Cu₂O films deposited in a stirred electrolyte at different potentials is shown in Figure 6-14. At a cathodic potential of -0.5V or more positive, the Cu₂O film consists of irregular, round grains with no clear edges and corners, similar to that formed in the same electrolyte at -0.3V in a quiescent electrolyte (Figure 4-4b). XRD patterns reveal that these films also have a much lower (111):(200) peak ratio than that deposited in an unstirred electrolyte, indicating a faster growth in the <100> direction.

The effect of stirring on the growth direction is similar to that observed by applying pulsed potentials and a similar explanation involving transport of reactant species to the electrode surface can be applied here. When the electrolyte is continually stirred during the deposition process, lactate ions close to the electrode surface can be removed at a much faster rate and hence allow CuLac₂ complexes to reach the surface more easily. As a result, the surface concentration of Cu(II) is kept at a level at which <100> growth orientation is favored over <111>. On the other hand, truncated cubic grains with a clear <111>-dominant orientation are observed at an applied potential of -0.6V. This indicates that the consumption of CuLac₂ is again fast enough for <111>-orientation to be favored as a result. It is also worth noting that the formation of Cu clusters is not observed at -0.6V in stirred electrolyte, again similar to the case of pulsed

potential deposition under similar conditions. As discussed in the previous section, this suggests that the transport of OH^- ions is also promoted by stirring.

Furthermore, rounded features are observed in samples deposited at an applied potential of -0.5V or lower in stirred electrolyte, whereas they are also formed at -0.3V in quiescent electrolyte. This suggests that stirring promotes the dissolution of Cu_2O during the deposition process.

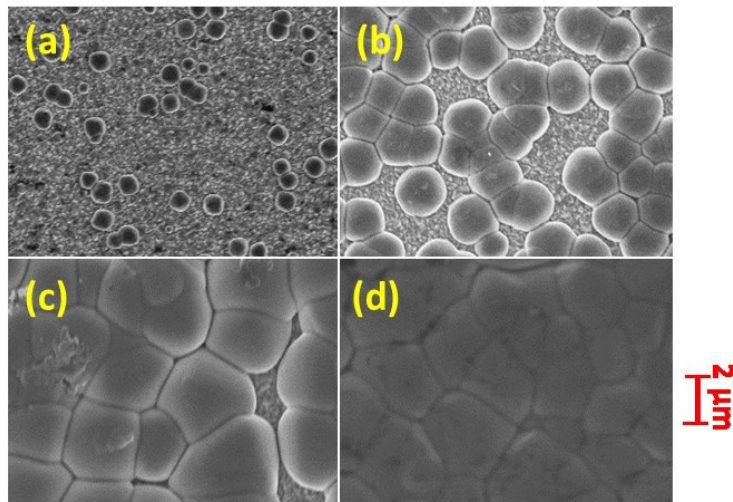


Figure 6-15: SEM images of Cu_2O films electrodeposited at -0.3 V and 60°C in stirred electrolyte containing $0.2\text{ M CuSO}_4 + 3\text{ M}$ lactic acid adjusted to $\text{pH } 9.5$ for different durations: (a) 3, (b) 15, (c) 45 and (d) 60 min.

Further examination of the evolution of morphology during Cu_2O electrodeposition in stirred electrolyte, is presented in Figure 6-15. Particles in the shape of spherical caps are formed within the first 3 minutes of the process (Figure 6-15a). They appear to expand in size as the process continues and eventually merge with each other (Figure 6-15 c, d). After that, the particles begin to grow primarily in the vertical direction and eventually evolve into columnar grains as shown Figure 6-15d. The fact that no significant change in grain shape and orientation is observed suggests that the surface concentrations of the relevant species do not change significantly over time. This is another indication that the process is not limited by transport under these stirred conditions, as opposed to the results obtained in the unstirred electrolyte at -0.5V , as shown in Figures 4-11 and discussed in Section 4.4.2.

6.4.4 Device performance

In this section, devices are fabricated using Cu_2O thin films from stirred electrolytes containing 0.2 M CuSO_4 + 3.0 M lactic acid adjusted to different pH. Devices fabricated using Cu_2O films in unstirred electrolytes are shown for comparison (parameters corresponding to these devices are presented in Section 5.3.4).

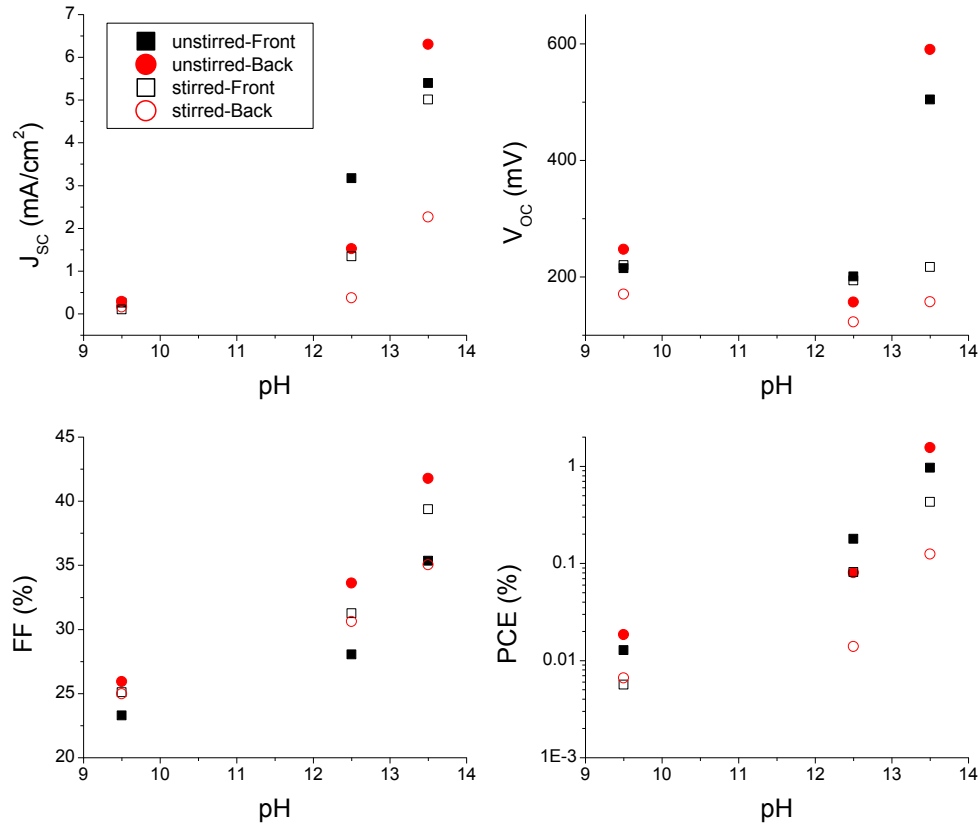


Figure 6-16: Performance of devices fabricated using Cu_2O layers deposited in stirred and unstirred electrolytes (0.2M CuSO_4 + 3.0M lactic acid) at different pH.

Figure 6-16 compares the performance of solar cells fabricated using Cu_2O deposited from stirred and unstirred electrolytes, under otherwise identical conditions. Stirring during Cu_2O deposition tends to reduce the PCE, J_{sc} and V_{oc} of the resulting devices under both front- and back-illumination. This effect differs from that obtained using potential pulsing where only J_{sc} is reduced, as shown in Figure 6-12. In particular, the J_{sc} and V_{oc} in back-illuminated devices decrease much more significantly than in front-

illuminated devices, which suggests that the electron mobility in the Cu_2O layer may have dropped considerably when deposited under stirred conditions. The J-V curves for the pH 13.5 samples are shown in Figure 6-17.

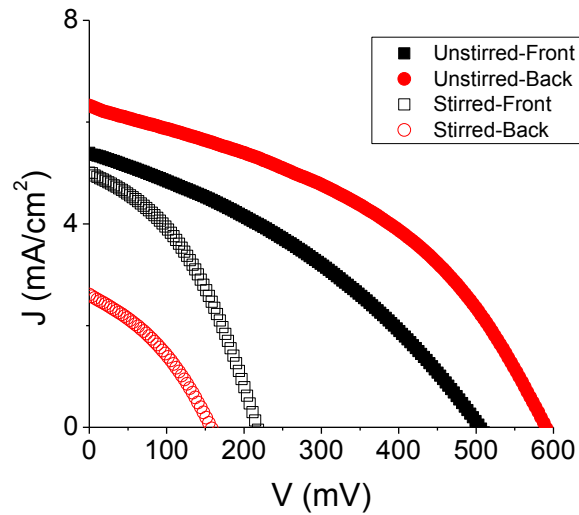


Figure 6-17: J-V curves for devices fabricated using Cu_2O layers deposited in stirred and unstirred electrolytes at pH 13.5 (0.2 M CuSO_4 + 3.0 M lactic acid) at 65°C .

Part of the cause for the lower performance may be attributed to the change in Cu_2O growth orientation in stirred electrolyte, as discussed in Section 6.4.3. Figure 6-18 shows the effect of deposition pH on the (111):(200) peak ratios of Cu_2O films under stirred and unstirred conditions. These results confirm that the shift in orientation from $\langle 111 \rangle$ direction to $\langle 100 \rangle$ occurs at both pH 9.5 and 12.5 although an obvious change in morphology is not observed in the latter case. The reduction of J_{SC} in devices fabricated using these Cu_2O films is consistent with the effect of pH on the orientation observed in quiescent electrolyte, as discussed in Section 5.3.1 and presented in Figure 5-1.

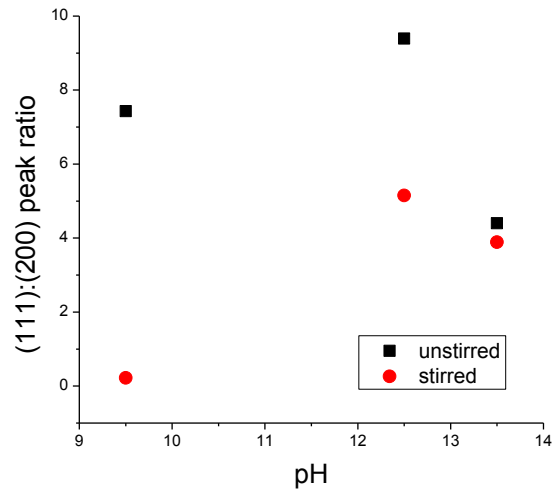


Figure 6-18: Effect of pH on the orientation of Cu₂O thin films deposited in stirred or unstirred electrolyte.

The carrier concentration and mobility of Cu₂O thin film deposited at pH 9.5 (0.2 M CuSO₄ + 3.0 M lactic acid, -0.5 V, 65°C) have also been measured using the SCLC technique. Similar to pulsed samples, the hole concentration is measured to be on the order of 10¹⁶, much higher than that obtained under unstirred conditions. On the other hand, carrier mobilities in the range 10⁻⁴ – 10⁻² cm²/Vs are measured in Cu₂O deposited in stirred electrolytes, which are several orders of magnitude lower than that obtained in an unstirred electrolyte under otherwise identical conditions (Figure 5-13b). The differences in carrier concentration and mobility suggest that the dissolution process observed during stirred electrodeposition occurs mostly due to oxidation instead of chemical dissolution. The same argument used to explain the effect of potential pulsing can be applied here. A significant amount of Cu(II) may be incorporated in the Cu₂O film causing the defect concentration to rise and the carrier mobility to drop. Comparison of the J_{SC} values in devices fabricated using Cu₂O layers deposited at pH 12.5 shows that they decrease in the following order: unstirred DC > unstirred pulsed > stirred DC, which is consistent with the relative carrier mobility in each film.

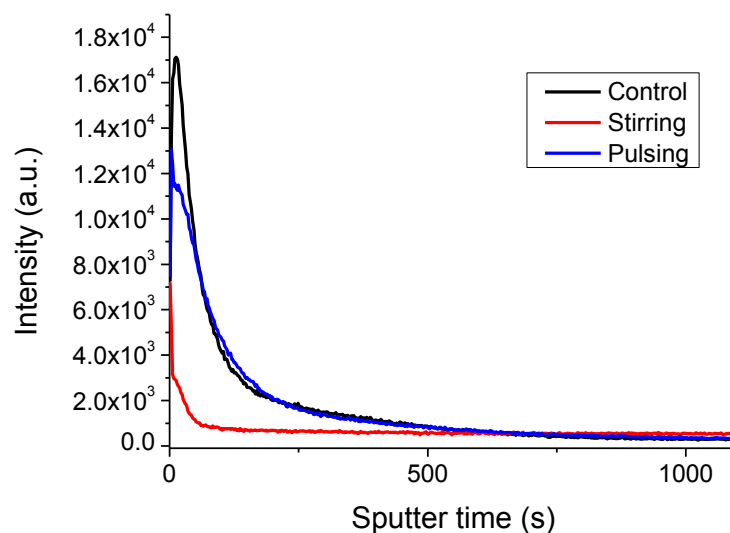


Figure 6-19: SIMS profiles of C^- intensity for stirring and pulsing (500ms/500ms) electrodeposition conditions from the pH 9.5 electrolyte. Result for DC deposition in quiescent electrolyte is shown as comparison.

It is also noted that significantly less organic contamination on the surface occurs for samples deposited in stirred electrolyte. Figure 6-19 shows the SIMS profiles of carbon in stirred and pulsed unstirred samples compared with DC deposition from quiescent electrolyte (0.3M $CuSO_4$ + 3M lactic acid, pH 9.5, $E_{app} = -0.5V$). The amount of carbon close to the film surface is found to be significantly smaller when it is formed under stirring conditions, whereas using a pulsed potential in an unstirred electrolyte the amount is similar to the unstirred DC experiment. This suggests that the effect of convection on the transport of lactate species is more significant than diffusion, which is also consistent with the observed trend in charge carrier mobility and device efficiency.

6.5 Summary

In this chapter, the use of galvanostatic deposition, pulsed potential deposition, as well as electrodeposition from stirred electrolyte as alternatives to potentiostatic DC deposition of Cu_2O thin films is investigated and the performance of the corresponding Cu_2O/AZO solar cells is characterized.

Galvanostatic deposition is found to be less suitable for solar cell fabrication due to the difficulty in preventing the co-deposition of Cu metal. On the other hand, evidence of dissolution during deposition is observed under both pulsed and stirred conditions although the mechanism is found to be oxidation instead of chemical dissolution. In both cases, the deposit morphology is found to differ from the typical polyhedral shapes observed at a lower pH of ~ 9.5 . Round features instead of angular ones tend to form. The reason for this is attributed to the lowering of transport limitations during the deposition process either by allowing more time for replenishment of reactants at the cathode surface or by enhancing convection. As a result, higher hole concentration is found than in films deposited under DC conditions. In terms of device performance, both procedures resulted in lower performance compared to DC deposition under similar conditions due to lower carrier mobility in the Cu_2O film.

Chapter 7. Chemical Deposition of ZnO

7.1 Background

Undoped ZnO is one of the most common n-type materials used in photovoltaic devices. Compared to AZO, undoped ZnO usually has lower conductivity, but can be deposited using a wider range of techniques, which have a large effect on the film properties as well as the resulting device performance [74]. Among these, solution-based processes such as electrodeposition and chemical growth are usually favored since they require milder operating conditions and are less damaging than sputtering to the Cu_2O surface. Furthermore, a variety of ZnO morphologies can be prepared using solution-based techniques, which has a large impact on solar cell performance due to effects on both the n-type ZnO layer [53,54,60] and the interlayer added for interfacial control [65,66,69].

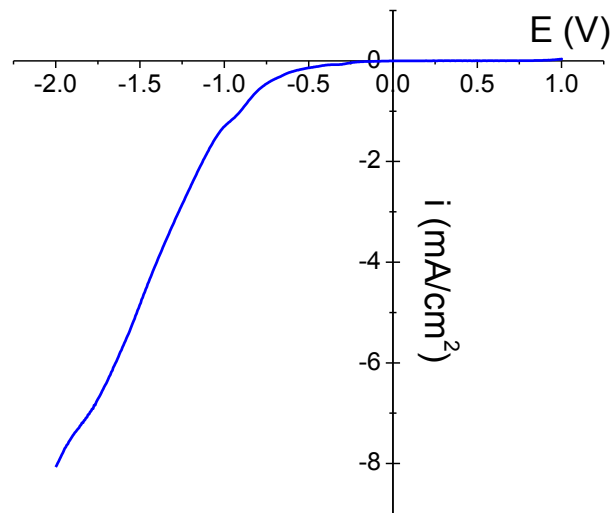
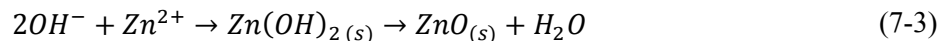


Figure 7-1: Linear sweep voltammogram obtained on FTO-coated glass substrates immersed in 0.05 M $\text{Zn}(\text{NO}_3)_2$ solution and 65°C

Similar to Cu_2O , ZnO can also be easily deposited by electrochemical deposition, usually involving the formation and dissociation of zinc hydroxide on the substrate surface. However, some problems that arise during the fabrication of $\text{Cu}_2\text{O}/\text{ZnO}$ make this technique less attractive. Firstly, the ZnO layer is

prone to dissolution in alkaline solutions, especially since the required thickness of ZnO in a solar cell is only a few hundred nanometers or thinner, whereas the electrodeposition of p-type Cu₂O is typically carried out in high pH, making it difficult to deposit Cu₂O onto ZnO thin films for device fabrication. This can be resolved by using a buffer layer [47] or applying a cathodic bias before placing ZnO thin films in the Cu₂O electrodeposition bath [68]. On the other hand, during the electrodeposition of ZnO on top of Cu₂O, the Cu₂O layer is easily reduced from the cathodic potential required for ZnO formation. Figure 7-1 shows an LSV plot obtained after immersing FTO in a 0.05 M Zn(NO₃)₂ solution at 65°C, which are typical conditions for ZnO electrodeposition. As shown by the position of the onset of cathodic current, the formation of ZnO begins to occur at ~ -0.5V vs. SCE, but a potential of -0.7V or more negative is required for the deposition to occur at an acceptable rate. However, from our previous experiments, the reduction of Cu₂O to Cu becomes significant when the potential reaches ~-0.6V as suggested by the Cu formation range in Figure 4-3. Previous studies have demonstrated that ZnO electrodeposition on Cu₂O or CuO can be achieved through careful control of deposition current [142], as well as more advanced techniques such as photo-assisted electrodeposition which lowers the required potential for ZnO formation [49].

On the other hand, the growth of ZnO on Cu₂O thin films by chemical methods is less difficult since the problem of Cu₂O reduction is mostly avoided. The chemical growth of ZnO is usually carried out in a solution containing Zn²⁺ ions and a hydroxide source such as hexamethylenetetramine (HMTA). Similar to electrodeposition, the formation of ZnO by chemical growth also involves the formation and dehydration of Zn(OH)₂ [217]:



During the process, the HMTA molecules in the solution are decomposed to formaldehyde and ammonia, which acts as a pH buffer in the solution and also supplies OH⁻ ions at a slow rate. The control of the

solution pH is important for the chemical deposition of ZnO since Zn(OH)_2 is likely to precipitate in solution if the pH rises too high [218].

An interesting and useful aspect of the chemical growth of ZnO thin film by the above method is that it can lead to the formation of highly oriented ZnO nanorods with controllable morphology. In particular, the aspect ratio of the nanorods can be varied by controlling the ratio of Zn^{2+} and HMTA in the chemical bath [219,220] as well as their total concentration [221,222]. In addition, ammonia or ammonium salts can be introduced into the solution for the formation of more complicated nanostructures [218].

In this section, the efficacy of using chemically grown ZnO films as an alternative to sputtered AZO for Cu_2O -based solar cells is investigated. In particular, the growth of ZnO nanorods from zinc nitrate/HMTA solutions is briefly examined. This is followed by a comparison of the performance of solar cells with $\text{Cu}_2\text{O}/\text{ZnO}$ heterojunctions formed by chemically depositing ZnO on electrodeposited Cu_2O thin films with that of $\text{Cu}_2\text{O}/\text{AZO}$ devices with identical Cu_2O films.

7.2 Experimental

Devices with $\text{Cu}_2\text{O}/\text{ZnO}$ architecture are fabricated by first electrodepositing Cu_2O thin films onto FTO substrates followed by chemical growth of ZnO on top of the Cu_2O surface. Cu_2O electrodeposition is carried out in electrolyte containing 0.2 M CuSO_4 + 3 M lactic acid adjusted to pH 12.5 or 13.4. The ZnO layers are then chemically deposited with or without a ZnO seed layer. To produce seed particles, a ZnO colloidal solution is prepared according to the following procedure previously reported in the literature [223,224]. This involves the preparation of two solutions A and B. Solution A contains 0.11 M zinc acetate dissolved in a 90% ethanol solution, while Solution B contains 0.40 M KOH dissolved in a 90% ethanol solution. Solution B is then added to Solution A drop-wise at 65°C over a ~15 minute time in order to form the ZnO colloid particles. The mixture is stirred for another 20 min and then refrigerated overnight. The ZnO particles formed this way have nominal size ~120 nm suspended in 90% ethanol solution with concentration ~0.04g/mL is used for dip-coating. These ZnO colloids are then deposited

onto the $\text{Cu}_2\text{O}/\text{FTO}$ substrate by dip-coating at a withdrawal rate of ~ 6 cm/min, as described by Alarfaj & Subahi [225]. The substrate is then dried in air at 120°C . The coating process is repeated on the same substrate for 1-10 cycles in order to ensure a uniform coverage.

Once the seed layer is formed, chemical deposition is carried out in $\text{Zn}(\text{NO}_3)_2 + 0.025$ M HMTA solutions with various concentrations adjusted to pH ~ 5 (using diluted nitric acid and NaOH solutions) at a temperature of 85°C . These experiments are conducted at concentrations varying from 0.075 M to 0.1 M $\text{Zn}(\text{NO}_3)_2$ and deposition times between 5 min and 1 hour. After deposition, the sample is rinsed with DI water and dried in air for ~ 30 min at 120°C .

Some samples are reserved for characterization of film morphology and orientation using SEM and XRD, while others are used to fabricate solar cell devices using the following procedure. The ZnO deposit on exposed FTO substrate is washed off using HNO_3 solution, and the edge of the ZnO/ Cu_2O deposit area is removed using Kapton thermal tape to prevent possible shorting. The sample is then dried in air for ~ 30 min at 120°C . Finally, the device area is defined with thermal tape and Al contacts are deposited on the outside of both FTO and ZnO layers by thermal evaporation. In these experiments, device performance is characterized using back-illumination.

7.3 Chemical growth of ZnO nanorods

7.3.1 XRD

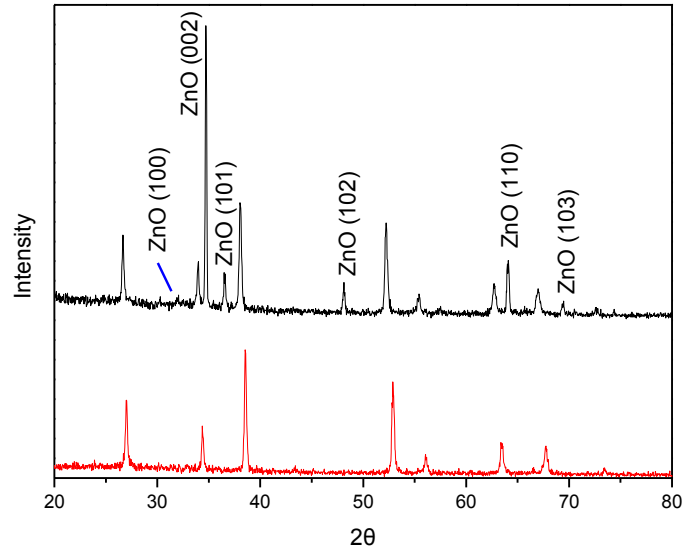


Figure 7-2: X-ray diffraction profile of a typical ZnO film chemically deposited on FTO-glass substrate. The bottom spectrum shows the profile of the FTO substrate for all experiments in this work.

All of the chemically grown ZnO films studied in this chapter have very similar X-ray diffraction spectra. A representative spectrum is presented in Figure 7-2. These data show that pure ZnO thin films are obtained in all cases and that four major peaks corresponding to ZnO orientations (002), (101), (102) and (110) appear. Among these, the relative intensities of (002) and (101) show the most significant variation as the deposition conditions are changed. Thus, the (002):(101) peak intensity ratio from the XRD spectra is used in the subsequent discussions as an indication of the growth orientation of ZnO thin films.

7.3.2 Effect of seed layer

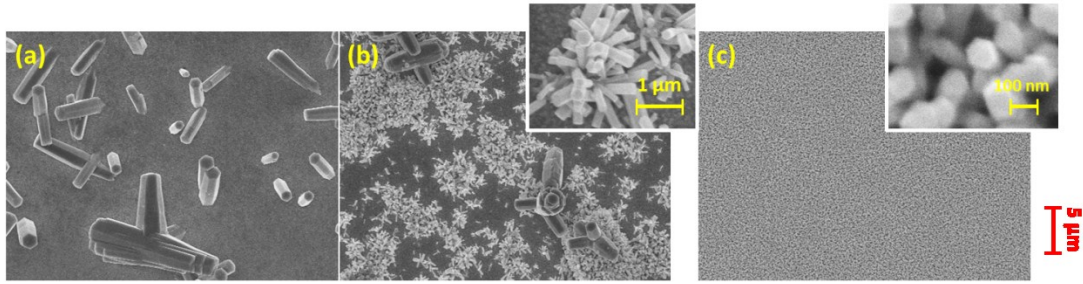


Figure 7-3: SEM images of ZnO thin films deposited on FTO-glass substrate from 0.025 M $\text{Zn}(\text{NO}_3)_2$ + 0.025 M HMTA solution at 85°C for 1 hour using different types of seed layer: (a) no seed layer, (b) ZnO powder (average diameter ~100nm), (c) ZnO colloids (average diameter ~120 nm). In each of the samples, 5 layers of seeds have been applied.

Figure 7-3 shows the morphology of ZnO thin films grown in 0.025 M $\text{Zn}(\text{NO}_3)_2$ + 0.025 M HMTA at 85°C on bare FTO or onto FTO coated with different seed layers. When no seed layer is coated, micron-sized ZnO particles with random orientation are formed, as shown in Figure 7-3a. The particles are sparse and do not form a continuous film. This is expected since ZnO is not expected to grow in any preferential direction or orientation on an FTO surface without pre-coated seeds. Since ZnO does not have a particularly strong affinity for the FTO surface, it deposits on the substrate surface with a frequency similar to that of the precipitation of ZnO particles in solution and so relatively few particles deposit on the substrate as the result. Using powdered ZnO as seed layer, flower-like nanorods of varied size form (Figure 7-3b). These nanorods appear to form in two distinct size ranges. Most ZnO particles have a diameter of 100nm or less and lengths in the range of ~1μm, as shown in the inset of Figure 7-3b. On the other hand, clusters of larger micron-sized ZnO rods are also observed, with dimensions similar to those that form in the absence of a seed layer. The appearance of these larger clusters is likely a result of an uneven seed layer coating when ZnO powder is used. When ZnO nanoparticle colloids form the seed layer, a relatively homogeneous coating of vertically aligned nanorods with average diameter ~80nm forms on the substrate (Figure 7-3c). As shown in the inset, these nanorods have hexagonal cross-section. The nanorods are not closely packed so that a spacing between nanorods is clearly observed.

When only a single seed layer is applied, some regions of the resulting ZnO film have noticeably fewer nanorods, which is a clear evidence of an uneven coating. However, once 3 seed layers or more have been applied, the coating becomes quite uniform. Thus, several dip-coating cycles are required to produce a uniform coating of ZnO nanoparticle seeds from the colloidal solution. Consequently, we coated the FTO substrate with 5 seed layers of ZnO colloids as a routine procedure before chemical deposition in all subsequent cases discussed in the following sections. It should also be noted that when more than one layer of ZnO colloids is coated onto the substrate, no difference in nanorod dimensions is observed when up to 10 layers are applied.

7.3.3 Effect of bath composition

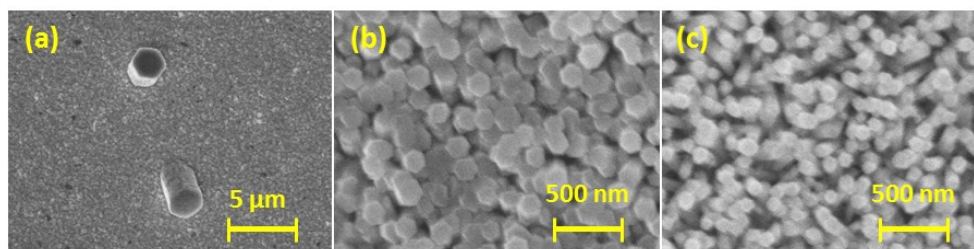


Figure 7-4: SEM images of ZnO thin films deposited on FTO-glass substrates at 85°C for 1 hour from 0.025 M $Zn(NO_3)_2$ + 0.025 M HMTA solution adjusted to pH:(a) 3, (b) 5, (c) 6.9 (unadjusted) with HNO_3 . All samples dip-coated with 5 layers of ZnO colloids as seed layer.

Figure 7-4 presents the morphology of ZnO films grown from solutions adjusted to different pH values with other conditions kept the same. The deposition rate is found to increase with solution pH up to pH 7, which is consistent with expectations as OH^- ions are required to form ZnO. At pH 3, only a few micron-sized hexagonal nanorods form on the FTO surface after 1 hour of deposition time (Figure 7-4a). When the pH is raised to pH 5 or 7, uniform nanorod arrays form (Figure 7-4 b, c). Furthermore, the average diameter of the ZnO nanorods is found to decrease as pH rises. The diameter of the few particles that form at pH 3 is found to be $\sim 2 \mu m$, decreases to $\sim 150 nm$ at pH 5 and to $\sim 80 nm$ at pH 6.9. The reason for this effect is unclear although the suggestion was made in a previous study that the nucleation and growth rates of ZnO nanorods can be controlled using solution pH [226]. No deposition is found on the substrate when the pH is raised to 8 or higher (SEM not shown here). This is consistent with the mechanism

proposed in [218] whereby a weakly acidic solution is required to promote the dehydration of $\text{Zn}(\text{OH})_2$ to ZnO .

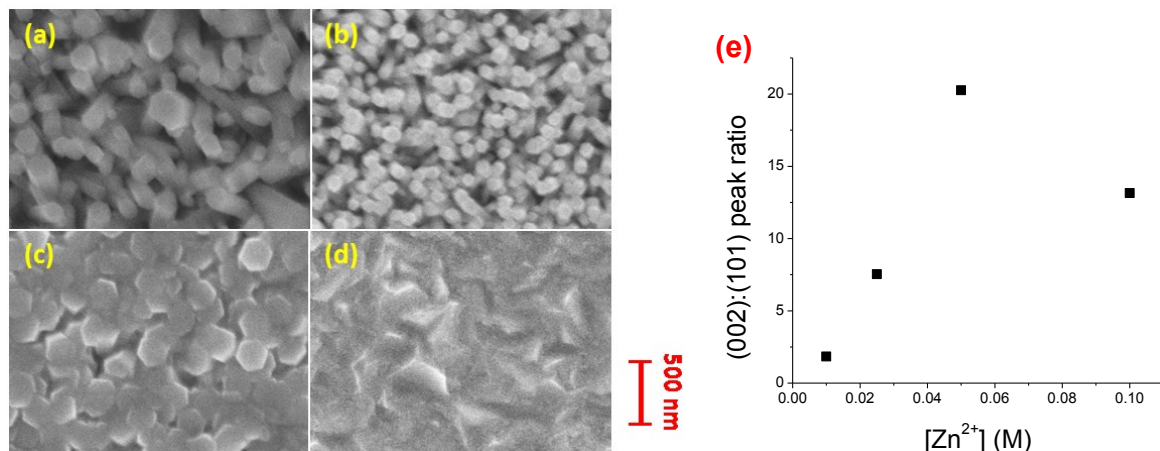


Figure 7-5: SEM images of ZnO thin films deposited on FTO-glass substrates at 85°C for 1 hour from solution containing 0.025 M HMTA and different $\text{Zn}(\text{NO}_3)_2$ concentrations: (a) 0.01, (b) 0.025, (c) 0.05 and (d) 0.10M adjusted to pH 5 using HNO_3 . The orientations of the resulting ZnO thin films are shown in (e). All samples dip-coated with 5 layers of ZnO colloids as seed layer.

Figure 7-5 a-d presents the effect of $[\text{Zn}^{2+}]$ on ZnO morphology. The ZnO morphology becomes more closely packed and less rod-like as $[\text{Zn}^{2+}]$ increases. Distinct nanorods are observed at $[\text{Zn}^{2+}]$ up to 0.025M, although the nanorod diameters appear to vary between ~50nm and 300nm at a low concentration of 0.01M (Figure 7-5a), whereas the distribution is relatively uniform at 0.025M (Figure 7-5b). Individual nanorods with hexagonal faces can still be distinguished at a 0.05M $\text{Zn}(\text{NO}_3)_2$ concentration, but they appear dislocated and appear to merge into each other to form a continuous film in some regions (Figure 7-5c). On the other hand, some spacing between individual nanorods is still visible although much smaller than at lower concentrations. When $[\text{Zn}^{2+}]$ is increased to 0.1M, a compact ZnO thin film with no visible holes in the structure forms. Rod-like structures are no longer present although hexagonal grains are still evident in the film. The preferred orientation of ZnO growth is shown in Figure 7-5e. Growth in the $\langle 002 \rangle$ direction is increasingly preferred as $[\text{Zn}^{2+}]$ rises to 0.05M, but then drops with a further increase to 0.1M when nanorods no longer are present.

These findings agree with those of previous studies [220,227] which attributed the formation of nanorods to the different surface energies of the ZnO planes. Since the (200) base of the hexagonal rods

has a more polar structure with higher surface energy [218] than the other faces, growth in the $\langle 200 \rangle$ direction is favored at lower $[\text{Zn}^{2+}]$. An increase in $[\text{Zn}^{2+}]$ should enhance the growth rates in both $\langle 200 \rangle$ and $\langle 101 \rangle$ directions. The data in Figure 7-5e indicate that the growth in $\langle 200 \rangle$ orientation increases more than $\langle 101 \rangle$ as the concentration increases reaching $\sim 0.05\text{M}$. When enough Zn^{2+} is added, growth in the $\langle 101 \rangle$ direction becomes significant enough that nanorods are no longer observed.

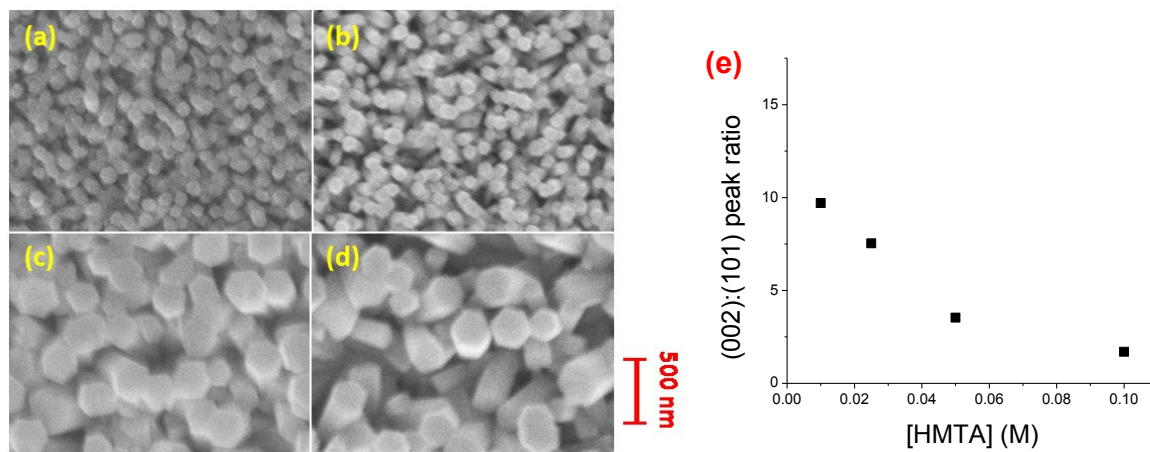


Figure 7-6: SEM images of ZnO thin films deposited on FTO-glass substrates at 85°C for 1 hour from solution containing 0.025 M $\text{Zn}(\text{NO}_3)_2$ and different HMTA concentrations: (a) 0.01, (b) 0.025, (c) 0.05 and (d) 0.10M adjusted to pH 5 using HNO_3 . The orientations of the resulting ZnO thin films are shown in (e). All samples dip-coated with 5 layers of ZnO colloids as seed layer.

The effect of $[\text{HMTA}]$ is presented in Figure 7-6. Similar to the effect of Zn^{2+} ions, an increase in HMTA concentration also causes larger nanorods to form, increasing in diameter from $\sim 50\text{nm}$ at 0.01 M HMTA to $\sim 250\text{nm}$ at 0.1M HMTA, while $[\text{Zn}^{2+}]$ is kept constant at 0.025M. However, one noticeable difference in behavior is that the spacing between the nanorods also increases with $[\text{HMTA}]$ so that the nanorods remain separated and loosely packed, whereas continuous films are formed at high $[\text{Zn}^{2+}]$ (Figure 7-5d). In addition, the (002):(101) peak intensity ratio decreases with an increase in $[\text{HMTA}]$ (Figure 7-6e), also reflecting an increased growth rate in the $\langle 101 \rangle$ direction. These observations agree with that of a previous study [220] that also shows the nanorod diameter to rise at higher $[\text{HMTA}]$. This trend is attributed to the higher $[\text{OH}^-]$ generated by the addition of more HMTA molecules.

7.4 Device performance

Although an ordered morphology such as nanorod arrays may improve charge transport properties in the ZnO layer, it is more important to have a continuous film. The Al contact deposited on top of the ZnO layer is only 100nm in thickness and so one would expect a spacing between nanorods to cause pinholes to form in the Al layer. Preliminary investigations using ZnO thin films made up of separated nanorods (obtained at 0.025 M-0.05 M Zn^{2+} , 0.025 M HMTA, 85°C, varied thicknesses) yield very low PCE, as expected based on the above reasoning and previous reports [59]. Therefore, a higher Zn^{2+} concentration of 0.075 or 0.1 M is used to deposit ZnO during device fabrication. As shown previously (Figure 7-5d), close-packed, slightly deformed nanorods form at 0.075 M, while compact films without any apparent alignment form at 0.1 M.

The thickness of the ZnO thin films is estimated from the side-view SEM images of them after deposition for 1 hour. Assuming a constant deposition rate, we estimate the deposition rates in solutions containing 0.025 M HMTA at 85°C to be ~300, ~500 and ~650nm for Zn^{2+} concentrations of 0.025M, 0.075M and 0.100M, respectively.

The performance of Cu_2O/ZnO devices with Cu_2O layers electrodeposited at pH 12.5 and 13.4 is shown in Figures 7-7 and 7-8, respectively. Overall, the highest efficiencies observed are ~0.03% with a Cu_2O layer deposited at pH 12.5 and ~0.27% at pH 13.4. The performance when Cu_2O is deposited at pH 12.5 is similar to that of $Cu_2O/AZO/Al$ devices with the same Cu_2O layer, but lower than that of the corresponding device fabricated at pH 13.4 (0.54% for $Cu_2O/AZO/Al$). In both cases, the maximum PCEs are obtained using ZnO films chemically deposited in solutions containing 0.075 M $Zn(NO_3)_2$, with an optimal thickness of 200-250 nm. This observation indicates that a close-packed nanorod morphology is preferred for device performance.

Furthermore, the performance measures are comparable to those achieved using AZO. When Cu_2O deposition is carried out at pH 12.5, the performance of the Cu_2O/ZnO devices is similar to that of the corresponding AZO devices with identical Cu_2O layers. At a deposition pH of 13.4, a slightly lower J_{sc}

value (2.4 mA/cm^2) is achieved than in $\text{Cu}_2\text{O}/\text{AZO}$ devices with the same Cu_2O layer (3.1 mA/cm^2), while the maximum V_{OC} and FF are similar. In particular, the similarity in the V_{OC} values obtained using the two device architectures suggests that the electronic band alignments in ZnO and AZO are similar.

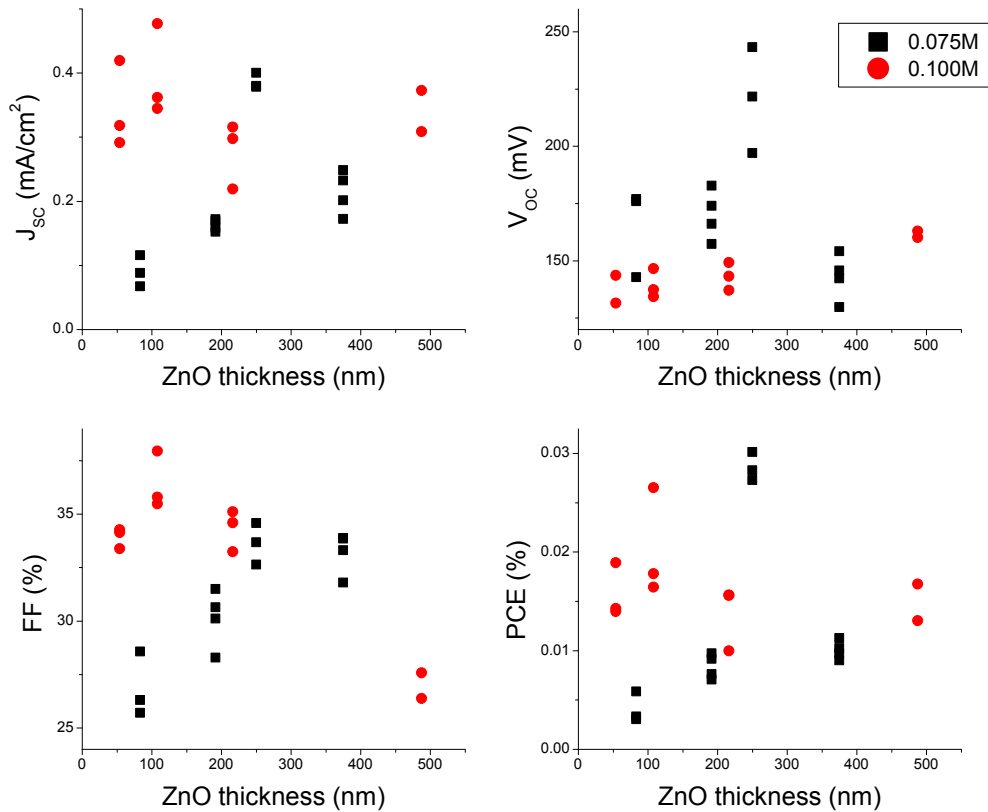


Figure 7-7: Performance measures of $\text{Cu}_2\text{O}/\text{ZnO}/\text{Al}$ devices fabricated using Cu_2O electrodeposited at 60°C and -0.65V from $0.2 \text{ M CuSO}_4 + 3 \text{ M lactic acid}$ at $\text{pH } 12.5$ and ZnO chemically deposited at 85°C from $\text{Zn}(\text{NO}_3)_2 + 0.025 \text{ M HMTA}$ with different Zn^{2+} concentrations.

The best performance variables are obtained when Cu_2O is electrodeposited at $\text{pH } 13.5$ (Figure 7-8). The maximum J_{SC} is obtained for a $\sim 200 \text{ nm}$ ZnO layer similar to the optimum AZO thickness in the $\text{Cu}_2\text{O}/\text{AZO}$ devices. V_{OC} is found to decrease with ZnO thickness, with the highest value observed at 80 nm . On the other hand, FF shows the opposite trend, with the optimal ZnO thickness estimated to be $\sim 380 \text{ nm}$ or higher. This mismatch in the preferred ZnO thickness depending on whether V_{OC} or FF is being

considered causes the PCE of Cu₂O/ZnO devices fabricated using Cu₂O deposited at pH 13.4 to have only half the efficiency of Cu₂O/AZO devices.

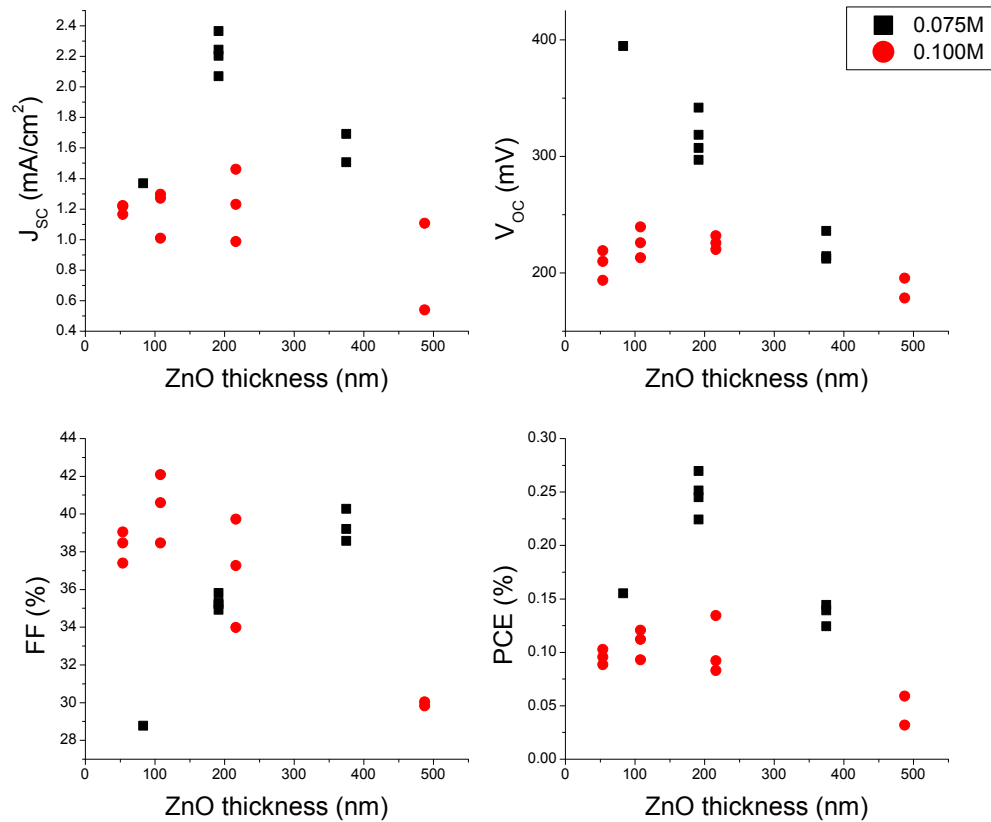


Figure 7-8: Performance measures of Cu₂O/ZnO/Al devices fabricated using Cu₂O electrodeposited at 65°C and -0.72V from 0.2 M CuSO₄ + 3 M lactic acid at pH 13.4 and ZnO chemically deposited from Zn(NO₃)₂ + 0.025 M HMTA at 85°C with different Zn²⁺ concentrations.

In summary, chemically grown ZnO thin films are shown to be a viable alternative to sputtered AZO, with the possibility of improvement because of more uniform n-type layer thickness. It has been demonstrated that similar cell performance measures in comparison to Cu₂O/AZO devices can be obtained in the resulting Cu₂O/ZnO devices although the highest PCE achieved is still lower. For future improvement, alternative procedures to modify ZnO film properties, such as doping or the addition of an electron extraction (n⁺) layer, should be explored in order to resolve the inconsistency in length scales observed in devices containing a high-mobility Cu₂O layer.

7.5 Summary

In this chapter, ZnO thin films are grown on both FTO and electrodeposited Cu₂O surfaces by chemical growth method. The effects of seed layers and solution composition are briefly investigated. <002>-oriented ZnO nanorods with various length and diameter are formed by adjusting growth parameters. Smooth ZnO thin films with no pinhole defects, which are favored for the fabrication of Cu₂O/ZnO solar cells, are also obtained. The performance of Cu₂O/ZnO devices using the aforementioned ZnO thin films as n-type material is not as high as that of devices with AZO layers. However, more uniform n-type layer thickness is obtained, and similar J_{SC} or V_{OC} values can be obtained individually, indicating good potential for improvement.

Chapter 8. Conclusions and Future Outlook

8.1 Conclusions

In this study, the electrodeposition of p-type Cu_2O thin films from copper-lactate electrolyte for the fabrication of oxide solar cells is investigated. The effects of parameters including applied potential, temperature, pH, copper concentration and lactate concentration on the Cu_2O film morphology and orientation are investigated. Different Cu_2O morphologies including common polyhedral grains and less common ones such as spherical and star-like shapes can be obtained by adjusting the deposition conditions. These effects are attributed to the combined effects of surface energy, atomic densities of Cu and O, adsorption and partial Cu_2O dissolution on the growth orientation and grain formation. It is found that the variation in growth orientation is mostly due to the relative rates of reaction and transport. When reaction kinetics is the limiting factor, $\langle 100 \rangle$ growth is preferred when the conditions are close to thermodynamic equilibrium. On the other hand, $\langle 111 \rangle$ -oriented growth is favored when transport rate is limiting. In other conditions, mixed orientations tend to be formed. In addition, dissolution effect becomes significant at high pH when the rate of dissolution is comparable to the rate of Cu_2O formation. Grain dissolution can also occur by oxidation in pulsed or stirred conditions, in which relaxed transport limitation is also observed.

In terms of device efficiency, it is found that the electrolyte pH during Cu_2O electrodeposition has the most prominent effect followed by film orientation. Performance variables including J_{sc} , V_{oc} and FF all improve significantly as the Cu_2O deposition pH increases due to improved carrier mobility and a smaller bandgap in the Cu_2O layer. The application of potential pulses or stirring of the electrolyte during Cu_2O deposition leads to films with higher carrier concentration and lower mobility, which reduce device efficiency compared to that achieved when the Cu_2O layer is deposited at constant potential under quiescent conditions. Finally, low carrier concentration in the Cu_2O layer, non-uniform AZO layer and low AZO surface conductivity are identified as some of the factors that limit device performance.

Chemically grown ZnO has also been investigated as a possible alternative for sputtered AZO in Cu₂O-based oxide solar cells. The performance of Cu₂O/ZnO devices is not as high as devices with AZO layers, though more uniform n-type layer thickness is obtained and similar cell performance variables can be obtained individually, indicating good potential for improvement.

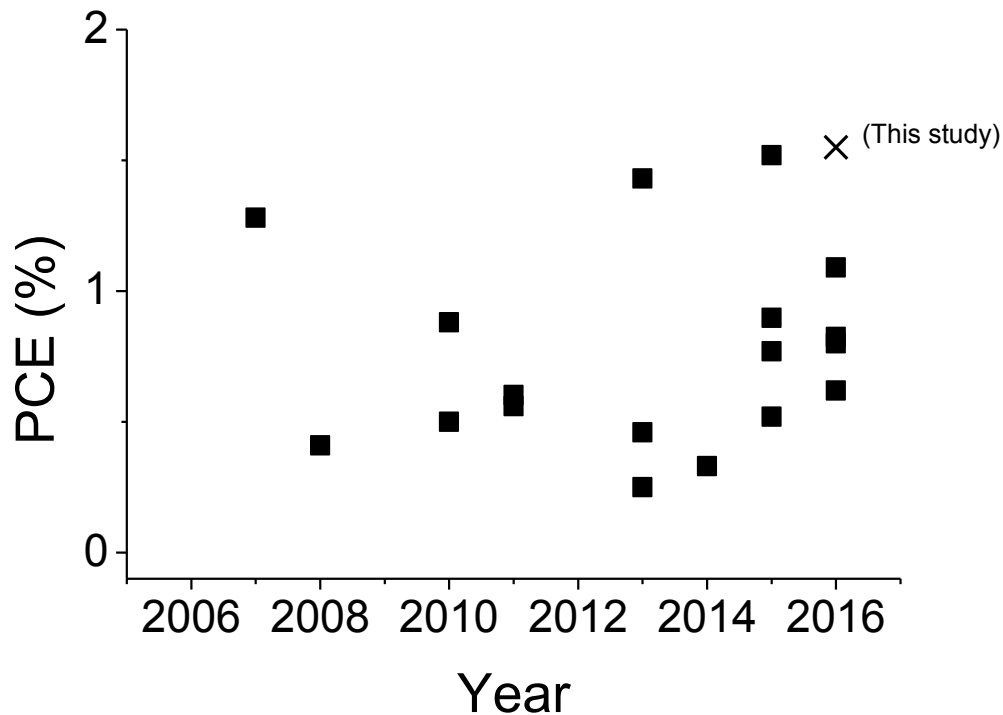


Figure 8-1: Reported efficiencies of Cu₂O/ZnO (doped or undoped) solar cells fabricated using electrodeposited Cu₂O thin films as p-type material without additional interlayers.

The major contributions of this study include:

- fabrication of Cu₂O/AZO solar cells containing electrodeposited Cu₂O thin films without addition layers that attain a PCE up to 1.55%. This is by far the highest efficiency obtained from devices that use the same deposition technique and structure (Figure 8-1).
- systematic investigation of the effect of deposition conditions in a typical copper-lactate system on p-type Cu₂O morphology and Cu₂O/AZO cell performance, with detailed discussion on the deposition mechanisms related to orientation control.

- discovery of the effect of partial dissolution of Cu_2O on film properties, as well as the improvement in carrier mobility and band structures. The improvements have been achieved by using electrolytes with pH 13 or higher, conditions that have not been investigated before for device fabrication.
- morphology control and improvement of hole concentration via less common electrodeposition procedures, namely the application of potential pulses to deposit Cu_2O and stirring, which have not been reported previously.

8.2 Recommended future research

1. Further investigations on the role of partial dissolution during Cu_2O electrodeposition

The dissolution of Cu_2O in alkaline environments is a relatively well-known process. However, to the best of our knowledge, its role during the electrodeposition of Cu_2O has not been reported. In this study, we found that the effect of dissolution becomes significant at a pH of ~ 13 and above and alters the morphology of Cu_2O thin films. More importantly, this dissolution and reformation process increases the carrier mobility and decreases the band gap of the Cu_2O thin film, which tends to improve the device efficiency of the oxide solar cells.

Consequently, it is recommended that a more detailed and systematic investigation on the dissolution process during the electrodeposition of p-type Cu_2O be performed. The origin of the change in charge carrier mobility and band structure should be determined and applied for better control of film properties. This would make it possible to obtain solar cell efficiency from electrodeposited films comparable to other, more energy intensive deposition techniques.

2. Design of a better procedure for measuring charge carrier mobility

Although hole mobility has been widely accepted as one of the key factors controlling the performance of Cu_2O -based solar cells, only a limited amount of data is available on the charge carrier mobility of electrodeposited Cu_2O thin films due to the difficulty in performing reliable measurements. Part of the

reason for this is that a conductive substrate is required for electrodeposition techniques, which makes the most common measurement based on the Hall effect difficult to perform. In addition, as far as we know, no electron mobility data have been reported before for electrodeposited Cu₂O thin films.

In this study, charge carrier mobilities were measured using the SCLC technique, which is more commonly used for organic semiconductors. This method can reliably yield the hole mobility of the films, but the electron mobility can only be roughly estimated in the cases where it is higher than the hole mobility. However, during the analysis, it is found that both hole and electron mobility can affect the device performance. In particular, for films that have undergone significant dissolution, the electron mobility can be as high as $\sim 50 \text{ cm}^2/\text{Vs}$, much higher than that expected from electrodeposited Cu₂O films, which resulted in a large increase in back-illumination efficiency. Consequently, an alternate more accurate measurement technique for the electron mobility of electrodeposited Cu₂O thin films should be used (e.g., time-of-flight mobility) in order to perform more in-depth studies of the mobility effect.

3. Further investigations on chemical growth of ZnO

In Chapter 7, devices fabricated from chemically grown ZnO as a replacement for sputtered AZO was briefly studied. Although the resulting device efficiency is much lower than that of Cu₂O/AZO devices using the conditions discussed, it must be acknowledged that the growth conditions of ZnO were not optimized. Nevertheless, we showed that the chemically deposited ZnO films have more uniform thickness than sputtered AZO and form fewer pinholes in the structure, which is considered one of the major limitations in the Cu₂O/AZO devices as discussed in Chapter 5. Furthermore, chemical deposition requires a much lower processing temperature than that does sputtering and is in general less energy-intensive and can be more easily scaled up. Therefore, if the film properties of chemically deposited ZnO can be made to be similar to those of sputtered AZO, the former technique would be more preferable. Thus, it is recommended that the chemical growth of ZnO be optimized as a possible alternative to AZO as the n-type material in Cu₂O-based solar cells.

4. Device optimization

This study focused on Cu_2O electrodeposition and the resulting effects on film and device properties. Thus, the substrate geometry is selected for ease of electrodeposition rather than for device performance optimization. It is very likely that some device efficiency has been sacrificed by use of a large substrate used for Cu_2O deposition. It is thus recommended that the device geometry and architecture be optimized in order to achieve higher and more consistent device performance using the same conditions discussed in this study.

Furthermore, only the most basic FTO/ Cu_2O /AZO structure has been investigated in this study for the purpose of simplifying the fabrication procedure. It may be possible for other techniques reported in the literature, as reviewed in Chapter 2, to improve the device PCE beyond the 1.55% level achieved in this study without significantly increasing the cost of fabrication. For example, gold can be used as the substrate instead of FTO and potentially increase the device V_{OC} by as much as 0.1V. An aluminium contact can be used in conjunction with a more uniform ZnO layer in order to improve surface conductivity and shunt resistance. Surface treatment of Cu_2O or modified AZO deposition procedure can be used to minimize the formation of CuO at the interface as discussed in Section 2.2.2. Finally, the device can be further optimized by the addition of n+ and p+ layers to improve the charge transport properties.

5. Other applications

It has been demonstrated that Cu_2O films with high mobility, high carrier concentration and atypical morphology can be obtained by modifying the electrodeposition procedure. Some of these efforts led to improved solar cell performance, while others were less successful. However, some of the Cu_2O film properties obtained in this study may be desirable in other applications such as photocatalysis, water splitting, gas sensing and transistors. Deposition on flexible substrates may also be possible by adjusting the electrochemical and/or solution conditions.

References

1. Green, M. A., Emery, K., Hishikawa, Y., Warta, W. & Dunlop, E. D. Solar cell efficiency tables (version 48). *Prog. Photovoltaics Res. Appl.* **24**, 905–913 (2016).
2. Avrutin, V., Izyumskaya, N. & Morkoç, H. Semiconductor solar cells: Recent progress in terrestrial applications. *Superlattices Microstruct.* **49**, 337–364 (2011).
3. Chiba, Y. *et al.* Dye-Sensitized Solar Cells with Conversion Efficiency of 11.1%. *Jpn. J. Appl. Phys.* **45**, L638–L640 (2006).
4. Huynh, W. U., Dittmer, J. J. & Alivisatos, A. P. Hybrid Nanorod-Polymer Solar Cells. *Science (80-.)*. **295**, 2425 LP-2427 (2002).
5. Günes, S., Neugebauer, H. & Sariciftci, N. S. Conjugated polymer-based organic solar cells. *Chem. Rev.* **107**, 1324–38 (2007).
6. Scharber, M. C. *et al.* Design Rules for Donors in Bulk-Heterojunction Solar Cells—Towards 10 % Energy-Conversion Efficiency. *Adv. Mater.* **18**, 789–794 (2006).
7. Liu, M., Johnston, M. B. & Snaith, H. J. Efficient planar heterojunction perovskite solar cells by vapour deposition. *Nature* **501**, 395–8 (2013).
8. Hossain, M. I. & Alharbi, F. H. Recent advances in alternative material photovoltaics. *Mater. Technol. Adv. Perform. Mater.* **28**, 88–97 (2013).
9. Drobny, V. F. & Pulfrey, D. L. Properties of reactively-sputtered copper oxide thin films. *Thin Solid Films* **61**, 89–98 (1979).
10. Olsen, L. C., Addis, F. W. & Miller, W. Experimental and theoretical studies of Cu₂O solar cells. *Sol. Cells* **7**, 247–279 (1982).
11. Olsen, L. C., Bohara, R. C. & Urie, M. W. Explanation for low-efficiency Cu₂O Schottky-barrier solar cells. *Appl. Phys. Lett.* **34**, 47 (1979).
12. Rakhshani, A. E. Preparation, characterization and photovoltaic properties of cuprous oxide-A review. *Solid-State Electr.* **29**, 7–17 (1986).
13. Katayama, J., Ito, K., Matsuoka, M. & Tamaki, J. Performance of Cu₂O/ZnO Solar Cell Prepared By Two-Step Electrodeposition. *J. Appl. Electrochem.* **34**, 687–692 (2004).
14. Ishizuka, S. *et al.* Polycrystalline n-ZnO/p-Cu₂O heterojunctions grown by RF-magnetron sputtering. *Phys. Status Solidi* **1**, 1067–1070 (2004).
15. Tanaka, H., Shimakawa, T., Miyata, T., Sato, H. & Minami, T. Electrical and optical properties of TCO–Cu₂O heterojunction devices. *Thin Solid Films* **469–470**, 80–85 (2004).
16. Minami, T., Tanaka, H., Shimakawa, T., Miyata, T. & Sato, H. High-efficiency oxide heterojunction solar cells using Cu₂O sheets. *Japanese J. Appl. Physics, Part 2 Lett.* **43**, (2004).
17. Caglar, Y. *et al.* Synthesis and characterization of (CuO)_x(ZnO)_{1-x} composite thin films with tunable optical and electrical properties. *Thin Solid Films* **520**, 6642–6647 (2012).
18. Cao, C. *et al.* Fabrication of a novel heterostructure of Co₃O₄-modified TiO₂ nanorod arrays and its enhanced photoelectrochemical property. *J. Alloys Compd.* **550**, 137–143 (2013).
19. Shinde, S. S., Bansode, R. A., Bhosale, C. H. & Rajpure, K. Y. Physical properties of hematite α -Fe₂O₃ thin films: application to photoelectrochemical solar cells. *J. Semicond.* **32**, 13001 (2011).

20. Rühle, S. *et al.* All-oxide photovoltaics. *J. Phys. Chem. Lett.* **3**, 3755–3764 (2012).
21. Seidel, J. *et al.* Efficient photovoltaic current generation at ferroelectric domain walls. *Phys. Rev. Lett.* **107**, 1–4 (2011).
22. Choi, T., Lee, S., Choi, Y. J., Kiryukhin, V. & Cheong, S. W. Switchable ferroelectric diode and photovoltaic effect in BiFeO₃. *Science (80-.)*. **324**, 63–66 (2013).
23. Masudy-Panah, S. *et al.* Titanium doped cupric oxide for photovoltaic application. *Sol. Energy Mater. Sol. Cells* **140**, 266–274 (2015).
24. Grondahl, L. O. & Geiger, P. H. A new electronic rectifier. *J. Am. Inst. Electr. Eng.* **46**, 215–222 (1927).
25. Wick, R. & Tilley, S. D. Photovoltaic and Photoelectrochemical Solar Energy Conversion with Cu₂O. *J. Phys. Chem. C* **119**, 26243–26257 (2015).
26. Markvart, T. & Castañer, L. in *Pract. Handb. Photovoltaics Fundam. Appl.* (eds. Markvart, T. & Castañer, L.) 71–93 (Elsevier, 2003, 2003). doi:10.1016/B978-185617390-2/50005-2
27. Shockley, W. & Queisser, H. J. Detailed Balance Limit of Efficiency of p-n Junction Solar Cells. *J. Appl. Phys.* **32**, 510 (1961).
28. Vos, a De. Detailed balance limit of the efficiency of tandem solar cells. *J. Phys. D. Appl. Phys.* **13**, 839–846 (1980).
29. Shpaisman, H., Niiitsoo, O., Lubomirsky, I. & Cahen, D. Can up- and down-conversion and multi-exciton generation improve photovoltaics? *Sol. Energy Mater. Sol. Cells* **92**, 1541–1546 (2008).
30. Nolan, M. & Elliott, S. D. The p-type conduction mechanism in Cu₂O: a first principles study. *Phys. Chem. Chem. Phys.* **8**, 5350–5358 (2006).
31. Raebiger, H., Lany, S. & Zunger, A. Origins of the p-type nature and cation deficiency in Cu₂O and related materials. *Phys. Rev. B - Condens. Matter Mater. Phys.* **76**, (2007).
32. Porat, O. & Riess, I. Defect chemistry of Cu_{2-y}O at elevated temperatures. Part II: Electrical conductivity, thermoelectric power and charged point defects. *Solid State Ionics* **81**, 29–41 (1995).
33. Wijesundera, R. P., Gunawardhana, L. K. A. D. D. S. & Siripala, W. Electrodeposited Cu₂O homojunction solar cells: Fabrication of a cell of high short circuit photocurrent. *Sol. Energy Mater. Sol. Cells* **157**, 881–886 (2016).
34. Ergen, O., Gibb, A., Vazquez-Mena, O., Regan, W. R. & Zettl, A. Metal insulator semiconductor solar cell devices based on a Cu₂O substrate utilizing h-BN as an insulating and passivating layer. *Appl. Phys. Lett.* **106**, (2015).
35. Minami, T., Miyata, T. & Nishi, Y. Relationship between the electrical properties of the n-oxide and p-Cu₂O layers and the photovoltaic properties of Cu₂O-based heterojunction solar cells. *Sol. Energy Mater. Sol. Cells* **147**, 85–93 (2016).
36. Lee, S. W. *et al.* Improved Cu₂O-based solar cells using atomic layer deposition to control the Cu oxidation state at the p-n junction. *Adv. Energy Mater.* **4**, 1–7 (2014).
37. Minami, T., Nishi, Y. & Miyata, T. Effect of the thin Ga₂O₃ layer in n⁺-ZnO/n-Ga₂O₃/p-Cu₂O heterojunction solar cells. *Thin Solid Films* **549**, 65–69 (2013).
38. Minami, T., Nishi, Y., Miyata, T. & Nomoto, J. High-Efficiency Oxide Solar Cells with ZnO/Cu₂O Heterojunction Fabricated on Thermally Oxidized Cu₂O Sheets. *Appl. Phys. Express* **4**, 62301 (2011).

39. Zhang, J. *et al.* Fabrication of Two Types of Ordered InP Nanowire Arrays on a Single Anodic Aluminum Oxide Template and Its Application in Solar Cells. *J. Mater. Sci. Technol.* **31**, 634–638 (2015).
40. Hussain, S. *et al.* Fabrication and photovoltaic characteristics of Cu₂O/TiO₂ thin film heterojunction solar cell. *Thin Solid Films* **522**, 430–434 (2012).
41. Hasuda, K., Takakuwa, O. & Soyama, H. Effect of load current density during the production of Cu₂O/Cu solar cells by anodic oxidation on film quality and output power. *Solid. State. Electron.* **91**, 130–136 (2014).
42. Hsu, Y. K., Wu, J. R., Chen, M. H., Chen, Y. C. & Lin, Y. G. Fabrication of homojunction Cu₂O solar cells by electrochemical deposition. *Appl. Surf. Sci.* **354**, 8–13 (2015).
43. McShane, C. M., Siripala, W. P. & Choi, K. S. Effect of junction morphology on the performance of polycrystalline Cu₂O homojunction solar cells. *J. Phys. Chem. Lett.* **1**, 2666–2670 (2010).
44. Han, K., Han, X. & Tao, M. Fabrications and Characterization of Electrodeposited Cu₂O p-n Homojunction Solar Cells. *Photovolt. Spec. Conf. (PVSC), 2010 35th IEEE* 3334–3337 (2010).
45. Zhai, H. *et al.* Novel fabrication of copper nanowire/cuprous oxidebased semiconductor-liquid junction solar cells. *Nano Res.* **8**, 3205–3215 (2015).
46. Chatterjee, S., Saha, S. K. & Pal, A. J. Formation of all-oxide solar cells in atmospheric condition based on Cu₂O thin-films grown through SILAR technique. *Sol. Energy Mater. Sol. Cells* **147**, 17–26 (2016).
47. Zhang, L. *et al.* Inorganic Solar Cells Based on Electrospun ZnO Nanofibrous Networks and Electrodeposited Cu₂O. *Nanoscale Res. Lett.* **10**, 465 (2015).
48. Soundaram, N., Chandramohan, R., Valanarasu, S., Thomas, R. & Kathalingam, A. Studies on SILAR deposited Cu₂O and ZnO films for solar cell applications. *J. Mater. Sci. Mater. Electron.* **26**, 5030–5036 (2015).
49. Zamzuri, M., Sasano, J., Mohamad, F. B. & Izaki, M. Substrate type <111>-Cu₂O/<0001>-ZnO photovoltaic device prepared by photo-assisted electrodeposition. *Thin Solid Films* **595**, 136–141 (2015).
50. Elfadill, N. G., Hashim, M. R., Chahrour, K. M., Qaeed, M. a. & Bououdina, M. The influence of Cu₂O crystal structure on the Cu₂O/ZnO heterojunction photovoltaic performance. *Superlattices Microstruct.* **85**, 908–917 (2015).
51. Chen, X. *et al.* Three-dimensional ordered ZnO/Cu₂O nanoheterojunctions for efficient metal-oxide solar cells. *ACS Appl. Mater. Interfaces* **7**, 3216–3223 (2015).
52. Siol, S. *et al.* Band Alignment Engineering at Cu₂O/ZnO Heterointerfaces. *ACS Appl. Mater. Interfaces* acsami.6b07325 (2016). doi:10.1021/acsami.6b07325
53. Abd-Ellah, M., Thomas, J. P., Zhang, L. & Leung, K. T. Enhancement of solar cell performance of p-Cu₂O/n-ZnO-nanotube and nanorod heterojunction devices. *Sol. Energy Mater. Sol. Cells* **152**, 87–93 (2016).
54. Hsu, Y. K., Lin, H. H., Chen, M. H., Chen, Y. C. & Lin, Y. G. Polarity-dependant Performance of p-Cu₂O/n-ZnO Heterojunction Solar Cells. *Electrochim. Acta* **144**, 295–299 (2014).
55. Lin, P. *et al.* Enhanced photoresponse of Cu₂O/ZnO heterojunction with piezo-modulated interface engineering. *Nano Res.* **7**, 860–868 (2014).
56. Hsu, Y., Lin, H., Wu, J., Chen, M. & Chen, Y. p-Cu₂O thin film on n-ZnO nanorods for solar cell.

- RSC Adv.* **4**, 7655–7659 (2014).
57. Marin, A. T. *et al.* Novel atmospheric growth technique to improve both light absorption and charge collection in ZnO/Cu₂O thin film solar cells. *Adv. Funct. Mater.* **23**, 3413–3419 (2013).
 58. Cheng, K. *et al.* Interface engineering for efficient charge collection in Cu₂O/ZnO heterojunction solar cells with ordered ZnO cavity-like nanopatterns. *Sol. Energy Mater. Sol. Cells* **116**, 120–125 (2013).
 59. Gershon, T. S. *et al.* Improved fill factors in solution-processed ZnO/Cu₂O photovoltaics. *Thin Solid Films* **536**, 280–285 (2013).
 60. Fujimoto, K., Oku, T., Akiyama, T. & Suzuki, A. Fabrication and characterization of copper oxide-zinc oxide solar cells prepared by electrodeposition. *J. Phys. Conf. Ser.* **433**, 12024 (2013).
 61. Perng, D. C., Chen, J. W., Kao, T. T. & Chang, R. P. Cu₂O growth characteristics on an array of ZnO nanorods for the nano-structured solar cells. *Surf. Coatings Technol.* **231**, 261–266 (2013).
 62. Chen, L., Wang, C. & Lu, S. Annealing Effects of Sputtered Cu₂O Nanocolumns on ZnO-Coated Glass Substrate for Solar Cell Applications. *J. Nanomater.* **2013**, 1–7 (2013).
 63. Musselman, K. P., Marin, A., Schmidt-Mende, L. & MacManus-Driscoll, J. L. Incompatible Length Scales in Nanostructured Cu₂O Solar Cells. *Adv. Funct. Mater.* **22**, 2202–2208 (2012).
 64. Hussain, S. *et al.* Fabrication and Electrical Characterization of p-Cu₂O/n-ZnO Heterojunction. *J. Nanosci. Nanotechnol.* **12**, 1967–1971 (2012).
 65. Chen, J.-W., Perng, D.-C. & Fang, J.-F. Nano-structured Cu₂O solar cells fabricated on sparse ZnO nanorods. *Sol. Energy Mater. Sol. Cells* **95**, 2471–2477 (2011).
 66. Musselman, K. P. *et al.* Strong efficiency improvements in ultra-low-cost inorganic nanowire solar cells. *Adv. Mater.* **22**, E254-8 (2010).
 67. Wang, R.-C. & Lin, H.-Y. Simple fabrication and improved photoresponse of ZnO–Cu₂O core–shell heterojunction nanorod arrays. *Sensors Actuators B Chem.* **149**, 94–97 (2010).
 68. Cui, J. & Gibson, U. J. A Simple Two-Step Electrodeposition of Cu₂O/ZnO Nanopillar Solar Cells. *J. Phys. Chem. C* **114**, 6408–6412 (2010).
 69. Yuhas, B. D. & Yang, P. Nanowire-based all-oxide solar cells. *J. Am. Chem. Soc.* **131**, 3756–61 (2009).
 70. Jeong, S. & Aydil, E. S. Heteroepitaxial growth of Cu₂O thin film on ZnO by metal organic chemical vapor deposition. *J. Cryst. Growth* **311**, 4188–4192 (2009).
 71. Jeong, S. S., Mittiga, A., Salza, E., Masci, A. & Passerini, S. Electrodeposited ZnO/Cu₂O heterojunction solar cells. *Electrochim. Acta* **53**, 2226–2231 (2008).
 72. Izaki, M. *et al.* Electrochemically constructed p-Cu₂O/n-ZnO heterojunction diode for photovoltaic device. *J. Phys. D. Appl. Phys.* **40**, 3326–3329 (2007).
 73. Hsueh, T.-J. *et al.* Cu₂O/n-ZnO nanowire solar cells on ZnO:Ga/glass templates. *Scr. Mater.* **57**, 53–56 (2007).
 74. Minami, T., Miyata, T., Ihara, K., Minamino, Y. & Tsukada, S. Effect of ZnO film deposition methods on the photovoltaic properties of ZnO–Cu₂O heterojunction devices. *Thin Solid Films* **494**, 47–52 (2006).
 75. Zhang, D. ., Liu, Y. ., Liu, Y. . & Yang, H. The electrical properties and the interfaces of Cu₂O/ZnO/ITO p–i–n heterojunction. *Phys. B Condens. Matter* **351**, 178–183 (2004).

76. Gershon, T., Musselman, K. P., Marin, A., Friend, R. H. & MacManus-Driscoll, J. L. Thin-film ZnO/Cu₂O solar cells incorporating an organic buffer layer. *Sol. Energy Mater. Sol. Cells* **96**, 148–154 (2012).
77. Xie, J., Guo, C. & Li, C. M. Interface functionalization with polymer self-assembly to boost photovoltage of Cu₂O/ZnO nanowires solar cells. *Int. J. Hydrogen Energy* **39**, 16227–16233 (2014).
78. Hsu, Y.-K. *et al.* Electrochemical growth and characterization of a p-Cu₂O thin film on n-ZnO nanorods for solar cell application. *RSC Adv.* **4**, 7655 (2014).
79. Fujimoto, K., Oku, T. & Akiyama, T. Fabrication and Characterization of ZnO/Cu₂O Solar Cells Prepared by Electrodeposition. *Appl. Phys. Express* **6**, 86503 (2013).
80. Lee, Y. S. *et al.* Atomic layer deposited gallium oxide buffer layer enables 1.2V open-circuit voltage in cuprous oxide solar cells. *Adv. Mater.* **26**, 4704–4710 (2014).
81. Ievskaya, Y., Hoye, R. L. Z., Sadhanala, A., Musselman, K. P. & MacManus-Driscoll, J. L. Fabrication of ZnO/Cu₂O heterojunctions in atmospheric conditions: Improved interface quality and solar cell performance. *Sol. Energy Mater. Sol. Cells* **135**, 43–48 (2015).
82. Mittiga, A., Salza, E., Sarto, F., Tucci, M. & Vasanthi, R. Heterojunction solar cell with 2% efficiency based on a Cu₂O substrate. *Appl. Phys. Lett.* **88**, 22–24 (2006).
83. Minami, T., Nishi, Y., Miyata, T. & Abe, S. Photovoltaic Properties in Al-doped ZnO/non-doped Zn_{1-x}Mg_xO/Cu₂O Heterojunction Solar Cells. *ECS Trans.* **50**, 59–68 (2013).
84. Abdelfatah, M. *et al.* Effect of Potentiostatic and Galvanostatic Electrodeposition Modes on the Basic Parameters of Solar Cells Based on Cu₂O Thin Films. *ECS J. Solid State Sci. Technol.* **5**, Q183–Q187 (2016).
85. Abdelfatah, M. *et al.* Fabrication and characterization of low cost Cu₂O/ZnO:Al solar cells for sustainable photovoltaics with earth abundant materials. *Sol. Energy Mater. Sol. Cells* **145**, 454–461 (2016).
86. Niu, W., Zhou, M., Ye, Z. & Zhu, L. Photoresponse enhancement of Cu₂O solar cell with sulfur-doped ZnO buffer layer to mediate the interfacial band alignment. *Sol. Energy Mater. Sol. Cells* **144**, 717–723 (2016).
87. Minami, T., Miyata, T. & Nishi, Y. Efficiency improvement of Cu₂O-based heterojunction solar cells fabricated using thermally oxidized copper sheets. *Thin Solid Films* **559**, 105–111 (2014).
88. Lee, Y. S. *et al.* Nitrogen-doped cuprous oxide as a p-type hole-transporting layer in thin-film solar cells. *J. Mater. Chem. A* **1**, 15416 (2013).
89. Noda, S., Shima, H. & Akinaga, H. Cu₂O/ZnO Heterojunction Solar Cells Fabricated by Magnetron-Sputter Deposition Method Films Using Sintered Ceramics Targets. *J. Phys. Conf. Ser.* **433**, 12027 (2013).
90. Septina, W. *et al.* Potentiostatic electrodeposition of cuprous oxide thin films for photovoltaic applications. *Electrochim. Acta* **56**, 4882–4888 (2011).
91. Kuo, C.-L. *et al.* The synthesis and electrical characterization of Cu₂O/Al:ZnO radial p-n junction nanowire arrays. *Nanotechnology* **20**, 365603 (2009).
92. Chou, S.-M., Hon, M.-H., Leu, I.-C. & Lee, Y.-H. Al-Doped ZnO/Cu₂O Heterojunction Fabricated on (200) and (111)-Orientated Cu₂O Substrates. *J. Electrochem. Soc.* **155**, H923 (2008).
93. Miyata, T., Minami, T., Tanaka, H. & Sato, H. Effect of a buffer layer on the photovoltaic

- properties of AZO/Cu₂O Solar Cells. *Proc. SPIE* **6037**, 603712-603712-10 (2005).
94. Nishi, Y., Miyata, T. & Minami, T. Electrochemically deposited Cu₂O thin films on thermally oxidized Cu₂O sheets for solar cell applications. *Sol. Energy Mater. Sol. Cells* **155**, 405–410 (2016).
 95. Al-Ghamdi, A. A. *et al.* Composite metal oxide semiconductor based photodiodes for solar panel tracking applications. *J. Alloys Compd.* **650**, 692–699 (2015).
 96. Abdelfatah, M. *et al.* Fabrication and characterization of flexible solar cell from electrodeposited Cu₂O thin film on plastic substrate. *Sol. Energy* **122**, 1193–1198 (2015).
 97. Wee, S. H., Huang, P.-S., Lee, J.-K. & Goyal, A. Heteroepitaxial Cu₂O thin film solar cell on metallic substrates. *Sci. Rep.* **5**, 16272 (2015).
 98. Tanaka, H., Shimakawa, T., Miyata, T., Sato, H. & Minami, T. Effect of AZO film deposition conditions on the photovoltaic properties of AZO-Cu₂O heterojunctions. *Appl. Surf. Sci.* **244**, 568–572 (2005).
 99. Chen, S. *et al.* An electrochemical constructed p-Cu₂O/n-ZnO heterojunction for solar cell. *J. Alloys Compd.* **644**, 378–382 (2015).
 100. Lee, Y. S. *et al.* Ultrathin Amorphous Zinc-Tin-Oxide Buffer Layer for Enhancing Heterojunction Interface Quality in Metal-oxide Solar Cells. *Energy Environ. Sci.* **6**, 2112–2118 (2013).
 101. Nishi, Y., Miyata, T. & Minami, T. The impact of heterojunction formation temperature on obtainable conversion efficiency in n-ZnO/p-Cu₂O solar cells. *Thin Solid Films* **528**, 72–76 (2013).
 102. Wong, L. M. *et al.* Growth of Cu₂O on Ga-doped ZnO and their interface energy alignment for thin film solar cells. *J. Appl. Phys.* **108**, 33702 (2010).
 103. Pavan, M. *et al.* TiO₂/Cu₂O all-oxide heterojunction solar cells produced by spray pyrolysis. *Sol. Energy Mater. Sol. Cells* **132**, 549–556 (2015).
 104. Kardarian, K. *et al.* Effect of Mg doping on Cu₂O thin films and their behavior on the TiO₂/Cu₂O heterojunction solar cells. *Sol. Energy Mater. Sol. Cells* **147**, 27–36 (2016).
 105. Hussain, S. *et al.* Cu₂O/TiO₂ nanoporous thin-film heterojunctions: Fabrication and electrical characterization. *Mater. Sci. Semicond. Process.* **25**, 181–185 (2014).
 106. Ruhle, S. *et al.* Combinatorial solar cell libraries for the investigation of different metal back contacts for TiO₂-Cu₂O hetero-junction solar cells. *Phys. Chem. Chem. Phys.* **16**, 7066–7073 (2014).
 107. Ichimura, M. & Kato, Y. Fabrication of TiO₂/Cu₂O heterojunction solar cells by electrophoretic deposition and electrodeposition. *Mater. Sci. Semicond. Process.* **16**, 1538–1541 (2013).
 108. Li, D. *et al.* Prototype of a scalable core-shell Cu₂O/TiO₂ solar cell. *Chem. Phys. Lett.* **501**, 446–450 (2011).
 109. Vequizo, J. J. M., Zhang, C. & Ichimura, M. Fabrication of Cu₂O/Fe-O heterojunction solar cells by electrodeposition. *Thin Solid Films* **597**, 83–87 (2015).
 110. Jayakrishnan, R. Photovoltaic response of Cu₂O/In₂S₃ hetero-structure grown on Cu substrate. *Mater. Sci. Semicond. Process.* **16**, 1608–1612 (2013).
 111. Elfadill, N. G., Hashim, M. R., Chahrour, K. M. & Mohammed, S. A. Electrochemical deposition of Na-doped p-type Cu₂O film on n-type Si for photovoltaic application. *J. Electroanal. Chem.* **767**, 7–12 (2016).

112. Elfadill, N. G., Hashim, M. R. & Thabit, K. A. T. The role of using seed-layer assisted electrodeposition method on the growth and the photovoltaic properties of p-Cu₂O/n-Si heterojunctions. *J. Mater. Sci. Mater. Electron.* **26**, 985–991 (2014).
113. Khan, M. A., Septina, W., Ikeda, S. & Matsumura, M. An inorganic/organic hybrid solar cell consisting of Cu₂O and a fullerene derivative. *Thin Solid Films* **526**, 191–194 (2012).
114. Yu, Y.-Y., Chien, W.-C. & Wang, Y.-J. Copper oxide hole transport materials for heterojunction solar cell applications. *Thin Solid Films* 1–7 (2016). doi:10.1016/j.tsf.2016.04.001
115. Shen, W. *et al.* Simple solution-processed CuO_x as anode buffer layer for efficient organic solar cells. *Mater. Sci. Eng. B* **200**, 1–8 (2015).
116. Hossain, M. I., Alharbi, F. H. & Tabet, N. Copper oxide as inorganic hole transport material for lead halide perovskite based solar cells. *Sol. Energy* **120**, 370–380 (2015).
117. Zuo, C. & Ding, L. Solution-Processed Cu₂O and CuO as Hole Transport Materials for Efficient Perovskite Solar Cells. *Small* **11**, 5528–5532 (2015).
118. Johnson, F. *et al.* Sputtered metal oxide broken gap junctions for tandem solar cells. *Sol. Energy Mater. Sol. Cells* **132**, 515–522 (2015).
119. Nejand, B. A., Ahmadi, V., Gharibzadeh, S. & Shahverdi, H. R. Cuprous Oxide as a Potential Low-Cost Hole-Transport Material for Stable Perovskite Solar Cells. *ChemSusChem* **9**, 302–313 (2016).
120. Chatterjee, S. & Pal, A. J. Introducing Cu₂O thin films as a hole-transport layer in efficient planar perovskite solar cell structures. *J. Phys. Chem. C* **120**, 1428–1437 (2016).
121. Türck, J. *et al.* Copper (I) Oxide (Cu₂O) based back contact for p-i-n CdTe solar cells. *Prog. Photovolt Res. Appl.* **24**, 1229–1236 (2016).
122. Ho Song, S., Aydil, E. S. & Campbell, S. A. Metal-oxide broken-gap tunnel junction for copper indium gallium diselenide tandem solar cells. *Sol. Energy Mater. Sol. Cells* **133**, 133–142 (2015).
123. Lee, S., Kim, D. H. & Kim, T. W. Enhancement of the power conversion efficiency for inverted polymer solar cells due to an embedded Cu_xO interlayer formed by using Cu(I) acetate and Cu(II) acetate. *J. Sol-Gel Sci. Technol.* **67**, 105–111 (2013).
124. Cheng Siah, S., Seog Lee, Y., Segal, Y. & Buonassisi, T. Low contact resistivity of metals on nitrogen-doped cuprous oxide (Cu₂O) thin-films. *J. Appl. Phys.* **112**, 84508 (2012).
125. Stevanović, V., Zakutayev, A. & Lany, S. Composition dependence of the band gap and doping in Cu₂O-based alloys as predicted by an extension of the dilute-defect model. *Phys. Rev. Appl.* **2**, 1–11 (2014).
126. Subramanian, A. *et al.* Non-equilibrium synthesis, structure, and opto-electronic properties of Cu_{2-2x}Zn_xO alloys. *J. Mater. Sci.* **50**, 1350–1357 (2015).
127. Meyer, B. K., Merita, S. & Polity, A. On the synthesis and properties of ternary copper oxide sulfides (Cu₂O_{1-x}S_x). *Phys. status solidi - Rapid Res. Lett.* **7**, 360–363 (2013).
128. Zakutayev, A., Stevanovic, V. & Lany, S. Non-equilibrium alloying controls optoelectronic properties in Cu₂O thin films for photovoltaic absorber applications. *Appl. Phys. Lett.* **106**, (2015).
129. Song, Y. & Ichimura, M. H₂O₂ Treatment of Electrochemically Deposited Cu₂O Thin Films for Enhancing Optical Absorption. *Int. J. Photoenergy* **2013**, 738063 (2013).
130. Pouloupoulos, P. *et al.* Intense Quantum Confinement Effects in Cu₂O Thin Films. *J. Phys. Chem.*

- C **115**, 14839–14843 (2011).
131. Matsuzaki, K. *et al.* Epitaxial growth of high mobility Cu₂O thin films and application to p-channel thin film transistor. *Appl. Phys. Lett.* **93**, 202107 (2008).
 132. Minami, T., Nishi, Y. & Miyata, T. Impact of incorporating sodium into polycrystalline p-type Cu₂O for heterojunction solar cell applications. *Appl. Phys. Lett.* **105**, 1–6 (2014).
 133. Upadhyay, S. *et al.* Experimental and first-principles theoretical studies on Ag-doped cuprous oxide as photocathode in photoelectrochemical splitting of water. *J. Mater. Sci.* **49**, 868–876 (2014).
 134. Akimoto, K. *et al.* Thin film deposition of Cu₂O and application for solar cells. *Sol. Energy* **80**, 715–722 (2006).
 135. Wilson, S. S. *et al.* Interface stoichiometry control to improve device voltage and modify band alignment in ZnO/Cu₂O heterojunction solar cells. *Energy Environ. Sci.* **7**, 3606–3610 (2014).
 136. Ikenoue, T., Sakamoto, S.-I. & Inui, Y. Fabrication and characterization of Cu₂O, ZnO and ITO thin films toward oxide thin film solar cell by mist chemical vapor deposition method. *Phys. Status Solidi C* **118**, 1237–1239 (2014).
 137. Gan, J., Venkatachalapathy, V., Svensson, B. G. & Monakhov, E. V. Influence of target power on properties of Cu_xO thin films prepared by reactive radio frequency magnetron sputtering. *Thin Solid Films* **594**, 250–255 (2015).
 138. Kuo, C.-H. & Huang, M. H. Morphologically controlled synthesis of Cu₂O nanocrystals and their properties. *Nano Today* **5**, 106–116 (2010).
 139. Bao, H. *et al.* Shape-dependent reducibility of cuprous oxide nanocrystals. *J. Phys. Chem. C* **114**, 6676–6680 (2010).
 140. Iida, C., Sato, M., Nakayama, M. & Sanada, A. Electrodeposition of Cu₂O Nanopyramids Using an Anodic Aluminum Oxide Template. *Int. J. Electrochem. Sci.* **6**, 4730–4736 (2011).
 141. Tan, Y. *et al.* Controllable fabrication and electrical performance of single crystalline Cu₂O nanowires with high aspect ratios. *Nano Lett.* **7**, 3723–3728 (2007).
 142. Lee, J. & Tak, Y. Selective electrodeposition of ZnO onto Cu₂O. *Electrochem. Commun.* **2**, 765–768 (2000).
 143. Ogwu, A. A. *et al.* An investigation of the surface energy and optical transmittance of copper oxide thin films prepared by reactive magnetron sputtering. *Acta Mater.* **53**, 5151–5159 (2005).
 144. Stareck, J. E. Electrodeposition of Cuprous Oxide and Bath Therefor. (1943).
 145. Bijani, S. *et al.* Study of the nucleation and growth mechanisms in the electrodeposition of micro- and nanostructured Cu₂O thin films. *J. Phys. Chem. C* **115**, 21373–21382 (2011).
 146. Lee, J. & Tak, Y. Epitaxial growth of Cu₂O (111) by electrodeposition. *Electrochem. Solid-State Lett.* **2**, 559–560 (1999).
 147. Zhou, Y. C. & Switzer, J. A. Galvanostatic electrodeposition and microstructure of copper (I) oxide film. *Mater. Res. Innov.* **2**, 22–27 (1998).
 148. Siegfried, M. J. & Choi, K. S. Directing the architecture of cuprous oxide crystals during electrochemical growth. *Angew. Chemie - Int. Ed.* **44**, 3218–3223 (2005).
 149. Wang, L. C., de Tacconi, N. R., Chenthamarakshan, C. R., Rajeshwar, K. & Tao, M. Electrodeposited copper oxide films: Effect of bath pH on grain orientation and orientation-

- dependent interfacial behavior. *Thin Solid Films* **515**, 3090–3095 (2007).
150. Santamaria, M., Conigliaro, G., Di Franco, F. & Di Quarto, F. Photoelectrochemical Evidence of Cu₂O/TiO₂ Nanotubes Hetero-Junctions formation and their Physicochemical Characterization. *Electrochim. Acta* **144**, 315–323 (2014).
 151. Tsui, L. K. & Zangari, G. Modification of TiO₂ nanotubes by Cu₂O for photoelectrochemical, photocatalytic, and photovoltaic devices. *Electrochim. Acta* **128**, 341–348 (2013).
 152. Assaud, L., Heresanu, V., Hanbücken, M. & Santinacci, L. Fabrication of p/n heterojunctions by electrochemical deposition of Cu₂O onto TiO₂ nanotubes. *Comptes Rendus Chim.* **16**, 89–95 (2013).
 153. Mahalingam, T. & Sanjeeviraja, C. Galvanostatic deposition of Cu₂O layers through the electrogeneration of base route. *J. Mater. Sci. Lett.* **17**, 603–605 (1998).
 154. Morales, J. *et al.* Electrodeposition of Cu₂O: An Excellent Method for Obtaining Films of Controlled Morphology and Good Performance in Li-Ion Batteries. *Electrochem. Solid-State Lett.* **8**, A159 (2005).
 155. Shinagawa, T. *et al.* Controllable Growth Orientation of Ag₂O and Cu₂O Films by Electrocrystallization from Aqueous Solutions. *Cryst. Growth Des.* **13**, 52–58 (2013).
 156. Huang, M. C. *et al.* Temperature dependence on p-Cu₂O thin film electrochemically deposited onto copper substrate. *Appl. Surf. Sci.* **301**, 369–377 (2014).
 157. Mizuno, K. *et al.* Structural and Electrical Characterizations of Electrodeposited p-Type Semiconductor Cu₂O Films. *J. Electrochem. Soc.* **152**, C179 (2005).
 158. Bijani, S., Martínez, L., Gabás, M., Dalchiele, E. A. & Ramos-Barrado, J. R. Low-temperature electrodeposition of Cu₂O thin films: Modulation of micro-nanostructure by modifying the applied potential and electrolytic bath pH. *J. Phys. Chem. C* **113**, 19482–19487 (2009).
 159. Rakhshani, A. E. & Varghese, J. Surface texture in electrodeposited films of cuprous oxide. *J. Mater. Sci.* **23**, 3847–3853 (1988).
 160. Liang, R. M., Chang, Y. M., Wu, P. W. & Lin, P. Effect of annealing on the electrodeposited Cu₂O films for photoelectrochemical hydrogen generation. *Thin Solid Films* **518**, 7191–7195 (2010).
 161. De Jongh, P. E., Vanmaekelbergh, D. & Kelly, J. J. Cu₂O: Electrodeposition and Characterization. *Chem. Mater.* **11**, 3512–3517 (1999).
 162. Golden, T. D. *et al.* Electrochemical Deposition of Copper(I) Oxide Films. *Chem. Mater.* **8**, 2499–2504 (1996).
 163. Liu, R., Oba, F., Bohannon, E. W., Ernst, F. & Switzer, J. A. Shape Control in Epitaxial Electrodeposition: Cu₂O Nanocubes on InP(001). *Chem. Mater.* **15**, 4882–4885 (2003).
 164. Mahalingam, T., Chitra, J. ., Chu, J. & Sebastian, P. . Preparation and microstructural studies of electrodeposited Cu₂O thin films. *Mater. Lett.* **58**, 1802–1807 (2004).
 165. Switzer, J. A., Kothari, H. M. & Bohannon, E. W. Thermodynamic to kinetic transition in epitaxial electrodeposition. *J. Phys. Chem. B* **106**, 4027–4031 (2002).
 166. Oshero, A., Zhu, C. & Panzer, M. J. Role of solution chemistry in determining the morphology and photoconductivity of electrodeposited cuprous oxide films. *Chem. Mater.* **25**, 692–698 (2013).
 167. Zhu, C., Oshero, A. & Panzer, M. J. Surface chemistry of electrodeposited Cu₂O films studied by

- XPS. *Electrochim. Acta* **111**, 771–778 (2013).
168. Gu, Y. e., Su, X., Du, Y. & Wang, C. Preparation of flower-like Cu₂O nanoparticles by pulse electrodeposition and their electrocatalytic application. *Appl. Surf. Sci.* **256**, 5862–5866 (2010).
 169. Laidoudi, S. *et al.* Growth and Characterization of Electrodeposited Cu₂O Thin Films. *Semicond. Sci. Technol.* **28**, 115005 (2013).
 170. Siegfried, M. J. & Choi, K. S. Electrochemical crystallization of cuprous oxide with systematic shape evolution. *Adv. Mater.* **16**, 1743–1746 (2004).
 171. Siegfried, M. J. & Choi, K. Elucidating the Effect of Additives on the Growth and Stability of Cu₂O Surfaces via Shape Transformation of Pre-Grown Crystals. *J. Am. Chem. Soc.* **128**, 10356–10357 (2006).
 172. Riveros, G. *et al.* Study of the electrodeposition of Cu₂O thin films from DMSO solution. *J. Electrochem. Soc.* **160**, D28–D33 (2013).
 173. Zamzuri, M., Mohamad, F. B. & Izaki, M. Electrodeposited<111>-oriented Cu₂O Photovoltaic Device with Al:ZnO. *J. Surf. Finish. Soc. Japan* **66**, 544–545 (2015).
 174. Helander, M. G., Greiner, M. T., Wang, Z. B., Tang, W. M. & Lu, Z. H. Work function of fluorine doped tin oxide. *J. Vac. Sci. Technol. A* **29**, 11019 (2011).
 175. Park, J., Shin, J., Cha, S. & Park, J. Deposition-temperature effects on AZO thin films prepared by RF magnetron sputtering and their physical properties. *J. Korean Phys. Soc.* **49**, 584–588 (2006).
 176. Minami, T., Tanaka, H., Shimakawa, T., Miyata, T. & Sato, H. High-Efficiency Oxide Heterojunction Solar Cells Using Cu₂O Sheets. *Jpn. J. Appl. Phys.* **43**, L917–L919 (2004).
 177. Tauc, J. in *Opt. Prop. Solids Pap. from NATO Adv. Study Inst. Opt. Prop. Solids Held August 7--20, 1966, Freiburg, Ger.* (eds. Nudelman, S. & Mitra, S. S.) 123–136 (Springer US, 1969). doi:10.1007/978-1-4757-1123-3_5
 178. Viezbicke, B. D., Patel, S., Davis, B. E. & Birnie, D. P. Evaluation of the Tauc method for optical absorption edge determination: ZnO thin films as a model system. *Phys. Status Solidi* **11**, n/a-n/a (2015).
 179. Davis, E. A. & Mott, N. F. Conduction in non-crystalline systems V. Conductivity, optical absorption and photoconductivity in amorphous semiconductors. *Philos. Mag.* **22**, 0903–0922 (1970).
 180. Bredas, J. L., Silbey, R., Boudreaux, D. S. & Chance, R. R. Chain-length dependence of electronic and electrochemical properties of conjugated systems: polyacetylene, polyphenylene, polythiophene, and polypyrrole. *J. Am. Chem. Soc.* **105**, 6555–6559 (1983).
 181. Stefanaki, E. C., Valassiadis, O., Hatzikraniotis, E. & Paraskevopoulos, K. M. Hall Effect and Resistivity Measurements in Films Grown on Conductive Substrate. in *28th Panhellenic Conf. Solid State Phys. Mater. Sci.* **2**, 6–7 (2012).
 182. Lamri Zeggar, M., Messaoudi, M., Aida, M. S. & Attaf, N. Gap states density measurement in copper oxide thin films. *Mater. Sci. Semicond. Process.* **45**, 32–35 (2016).
 183. Murgatroyd, P. N. Theory of space-charge-limited current enhanced by Frenkel effect. *J. Phys. D. Appl. Phys.* **3**, 308 (1970).
 184. Chan, H.-K. in *Ferroelectr. - Charact. Model.* (ed. Lallart, M.) (InTech, 2011). doi:10.5772/946
 185. Yang, Y., Li, Y. & Pritzker, M. Control of Cu₂O Film Morphology Using Potentiostatic Pulsed

- Electrodeposition. *Electrochim. Acta* **213**, 225–235 (2016).
186. Bohannon, E. W., Shumsky, M. G. & Switzer, J. A. Epitaxial Electrodeposition of Copper (I) Oxide on Single-Crystal Gold (100). *Communications* 2289–2291 (1999). doi:10.1021/cm990304o
 187. Soon, A., Todorova, M., Delley, B. & Stampfl, C. Thermodynamic stability and structure of copper oxide surfaces: A first-principles investigation. *Phys. Rev. B* **75**, 1–9 (2007).
 188. Scarano, D. *et al.* FTIR study of the interaction of CO with pure and silica-supported copper (I) oxide. *Surf. Sci.* **411**, 272–285 (1998).
 189. Jones, P. M., May, J. A., Reitz, J. B. & Solomon, E. I. Electron Spectroscopic Studies of CH₃OH Chemisorption on Cu₂O and ZnO Single-Crystal Surfaces: Methoxide Bonding and Reactivity Related to Methanol Synthesis. *J. Am. Chem. Soc.* **120**, 1506–1516 (1998).
 190. Wu, W., Feng, K., Shan, B. & Zhang, N. Orientation and Grain Shape control of Cu₂O Film and the Related Properties. *Electrochim. Acta* **176**, 59–64 (2015).
 191. Gou, L. & Murphy, C. J. Solution-Phase Synthesis of Cu₂O Nanocubes. *Nano Lett.* **3**, 231–234 (2003).
 192. Shang, Y. & Guo, L. Facet-Controlled Synthetic Strategy of Cu₂O-Based Crystals for Catalysis and Sensing. *Adv. Sci.* **2**, n/a-n/a (2015).
 193. Zhang, D. F. *et al.* Delicate control of crystallographic facet-oriented Cu₂O nanocrystals and the correlated adsorption ability. *J. Mater. Chem.* **19**, 5220–5225 (2009).
 194. Beverskog, B. & Puigdomenech, I. Revised Pourbaix Diagrams for Copper at 25 to 300°C. *J. Electrochem. Soc.* **144**, 399 (1997).
 195. Giri, S. D. & Sarkar, A. Electrochemical Study of Bulk and Monolayer Copper in Alkaline Solution. *J. Electrochem. Soc.* **163**, H252–H259 (2016).
 196. Nakahara, S., Ahmed, S. & Buckley, D. N. A Model for Spontaneous Morphology Change in Electrodeposited Metal Films during Room-Temperature Aging. *Electrochem. Solid-State Lett.* **10**, D17–D21 (2007).
 197. Ruan, S. & Schuh, C. A. Kinetic Monte Carlo simulations of nanocrystalline film deposition. *J. Appl. Phys.* **107**, (2010).
 198. Lee, Y. S., Winkler, M. T., Siah, S. C., Brandt, R. & Buonassisi, T. Hall mobility of cuprous oxide thin films deposited by reactive direct-current magnetron sputtering. *Appl. Phys. Lett.* **98**, 192115 (2011).
 199. Matumura, H., Fujii, A. & Kitatani, T. Properties of High-Mobility Cu₂O Films Prepared by Thermal Oxidation Temperatures of Cu at Low. *Jpn. J. Appl. Phys.* **35**, 5631–5636 (1996).
 200. Li, J. *et al.* Probing defects in nitrogen-doped Cu₂O. *Sci. Rep.* **4**, 7240 (2014).
 201. Pagotto, S. O., de Alvarenga Freire, C. M. & Ballester, M. Zn–Ni alloy deposits obtained by continuous and pulsed electrodeposition processes. *Surf. Coatings Technol.* **122**, 10–13 (1999).
 202. El-Sherik, A. M., Erb, U. & Page, J. Microstructural evolution in pulse plated nickel electrodeposits. *Surf. Coatings Technol.* **88**, 70–78 (1997).
 203. Zhu, D., Lei, W. N., Qu, N. S. & Xu, H. Y. Nanocrystalline Electroforming Process. *CIRP Ann. - Manuf. Technol.* **51**, 173–176 (2002).
 204. Chandrasekar, M. S. & Pushpavanam, M. Pulse and pulse reverse plating—Conceptual,

- advantages and applications. *Electrochim. Acta* **53**, 3313–3322 (2008).
205. Guo, X., Lv, W. & Li, X. Y. Additive-free shape-invariant nano-to-micron size-tuning of Cu₂O cubic crystals by square-wave voltammetry. *J. Phys. Chem. C* **118**, 11062–11077 (2014).
 206. Li, G., Liang, W., Xue, J., Liu, Y. & Liang, X. Electrochemical preparation and photoelectric properties of Cu₂O-loaded TiO₂ nanotube arrays. *J. Wuhan Univ. Technol. Sci. Ed.* **29**, 23–28 (2014).
 207. Wu, L., Tsui, L., Swami, N. & Zangari, G. Photoelectrochemical Stability of Electrodeposited Cu₂O Films. *J. Phys. Chem. C* **114**, 11551–11556 (2010).
 208. Sui, Y. *et al.* Synthesis of Cu₂O nanoframes and nanocages by selective oxidative etching at room temperature. *Angew. Chemie - Int. Ed.* **49**, 4282–4285 (2010).
 209. Hua, Q. *et al.* Morphological evolution of Cu₂O nanocrystals in an acid solution: Stability of different crystal planes. *Langmuir* **27**, 665–671 (2011).
 210. Hua, Q., Chen, K., Chang, S., Ma, Y. & Huang, W. Crystal plane-dependent compositional and structural evolution of uniform Cu₂O nanocrystals in aqueous ammonia solutions. *J. Phys. Chem. C* **115**, 20618–20627 (2011).
 211. Tseng, B. *et al.* Influence of de-bubbling on crystal structure and magnetic properties of electrodeposited CoNiP layers. in *2015 IEEE Magn. Conf.* 1 (2015).
 212. Atapattu, H. Y. R., De Silva, D. S. M., Pathiratne, K. A. S. & Dharmadasa, I. M. Effect of stirring rate of electrolyte on properties of electrodeposited CdS layers. *J. Mater. Sci. Mater. Electron.* **27**, 5415–5421 (2016).
 213. Kuznetsov, V. V., Vinokurov, E. G. & Kudryavtsev, V. N. Effect of hydrodynamic electrolysis conditions on the kinetics of cathodic processes in chromium(III) sulfate electrolytes. *Russ. J. Electrochem.* **36**, 756–760 (2000).
 214. Gomez, E., Ramirez, J., Valles, E. & Vallez, E. Electrodeposition of Co-Ni alloys. *J. Appl. Electrochem.* **28**, 71–79 (1998).
 215. Kruglikov, S. S., Kudriavtsev, N. T. & Vorobiova, G. F. On the mechanism of levelling by addition agents in electrodeposition of metals. *Electrochim. Acta* **10**, 253–261 (1965).
 216. Xue, J.-B., Shen, Q.-Q., Li, G.-L. & Liang, W. Preparation and photoelectric property of different morphologies Cu₂O loaded on TiO₂ nanotube arrays films. *Chinese J. Inorg. Chem.* **29**, 729–734 (2013).
 217. Wang, M. *et al.* Synthesis of well-aligned ZnO nanorod arrays with high optical property via a low-temperature solution method. *J. Cryst. Growth* **291**, 334–339 (2006).
 218. Tong, Y. *et al.* Growth of ZnO Nanostructures with Different Morphologies by Using Hydrothermal Technique. *J. Phys. Chem. B* **110**, 20263–20267 (2006).
 219. Wang, S.-F. *et al.* Effects of Preparation Conditions on the Growth of ZnO Nanorod Arrays Using Aqueous Solution Method. *Int. J. Appl. Ceram. Technol.* **5**, 419–429 (2008).
 220. Akgun, M. C., Kalay, Y. E. & Unalan, H. E. Hydrothermal zinc oxide nanowire growth using zinc acetate dihydrate salt. *J. Mater. Res.* **27**, 1445–1451 (2012).
 221. Vayssieres, L., Keis, K., Lindquist, S.-E. & Hagfeldt, A. Purpose-Built Anisotropic Metal Oxide Material: 3D Highly Oriented Microrod Array of ZnO. *J. Phys. Chem. B* **105**, 3350–3352 (2001).
 222. Vayssieres, L. Growth of arrayed nanorods and nanowires of ZnO from aqueous solutions. *Adv.*

- Mater.* **15**, 464–466 (2003).
223. Liu, D. & Kelly, T. L. Perovskite solar cells with a planar heterojunction structure prepared using room-temperature solution processing techniques - supporting information. *Nat. Photonics* **8**, 133–138 (2013).
224. Son, D.-Y., Bae, K.-H., Kim, H.-S. & Park, N.-G. Effects of Seed Layer on Growth of ZnO Nanorod and Performance of Perovskite Solar Cell. *J. Phys. Chem. C* **119**, 10321–10328 (2015).
225. Alarfaj, E. & Subahi, A. The influence of external magnetic field on the structural and optical properties of nanocrystalline ZnO thin films prepared by dip coating method. *Superlattices Microstruct.* **86**, 508–517 (2015).
226. Pal, U. *et al.* Synthesis and optical properties of ZnO nanostructures with different morphologies. *Opt. Mater. (Amst)*. **29**, 65–69 (2006).
227. Baeten, L. *et al.* Tuning the dimensions of ZnO nanorod arrays for application in hybrid photovoltaics. *ChemPhysChem* **13**, 2777–2783 (2012).